Functionalization of two-dimensional nanomaterials based on graphene

Yu-Pu Lin

Aix-Marseille Université
Ecole Doctorale de Physique et Sciences de la Matière (ED 352)

Thèse

pour l'obtention du grade de Docteur de l'Université Aix-Marseille
Mention: Matière condensée et Nanosciences

Functionalization of two-dimensional nanomaterials based on graphene

Presentée par:

Yu-Pu LIN

Soutenue publiquement le 18 septembre 2014, devant le jury composé de:

Rapporteurs :	Laurent Simon	IS2M, CNRS
	Robert Sporken	Université de Namur
Examinateurs :	Pierre Mallet	Institut Néel, CNRS
	Christophe Bichara	CINaM, CNRS
Invité :	Laurent Roux	Ion Beam Services
Directeur de thèse :	Jean-Marc Themlin	Aix-Marseille Université
Co-directeur de thèse :	Younal Ksari	Aix-Marseille Université

Thèse réalisée au sein de l'Institut Matériaux Microélectronique Nanosciences de Provence
IM2NP - UMR CNRS 7334 & Universités d'Aix-Marseille et de Toulon
Avenue Escadrille Normandie Niemen - Case 142 - 13397 Marseille Cedex 20 (France)

"Nature has a great simplicity and therefore a great beauty."
—Richard P. Feynman

Acknowledgements

First of all, I wish to express my gratitude to my supervisor, Prof. Jean-Marc Themlin, for giving me the opportunity to work on this interesting subject, for leading me into the fascinating world of research by sharing his knowledge and experiences, and, especially, for giving me support and constant encouragement all along the past three years.

I owe a great debt of gratitude to many colleges of the Nanostructuration team for their support in the completion of this thesis. I would like to express my sincere thanks to Dr. Younal Ksari, my co-supervisor, for his support in my experimental work and article writing. I would like to give a large thanks to Dr. Luca Giovanelli for shearing his knowledge in spectroscopic analysis and in Igor Pro, and most importantly for lending me his car, which give me the opportunity to visit the region of Provence. I would like to express my sincere thanks to Prof. Mathieu Abel for another great work we have done together, namely "*Self-assemble monolayer of melamine on Cu(111)*", which I didn't incorporate in this thesis. And, I would also like to thank all the members of Nanostructuration team, including all senior and junior PhD students, and especially Dr. Mathieu Koudia, for their valuable help and insightful discussions in many scientific and technical subjects.

Furthermore, there are several persons who I owe a deep appreciation for their important contributions in this thesis. Many thanks to Dr. Laurent Simon who has spent lots of time teaching me and demonstrates to me about the STM technique, and to Dominique Aubel and Samar Garreau for ARUPS and XPS measurements. Many thanks to our industrial collaborators: Ion Beam Services (IBS), including Dr. Lauren Roux, Yohann Spiegel and Gaël Borvon, for their support in the nitrogen implantation experiments.

I would also like to thank all the financial supports of this thesis and research project. I would like to thank CNRS and Région PACA for the co-funding of my PhD contract (BDO), with the local industrial support of IBS. And I would like to thank the ANR project "ChimiGraphN" for the financial support in most of my research activities.

Finally, I would like to thank my family and friends for giving their full support in my academic pursuits. Thanks to my dad, I have become a responsible man and learned to not be afraid of the challenges in my life. Thanks to my mom, I have learned to be always grateful of every day we live. I would also like to thank Prof. Chii-Don Ho and Prof. Yu-Chi Chang, close friends and colleagues of my father, who were also a great support in my academic pursuits. And, I would like to thanks my girlfriend, Camille, for her love, for her constant believes in me, and for always standing beside me.

I would like to end with my special thanks *in advance* to anyone who is reading this thesis for your patience and I hope you will enjoy it.

Résumé étendu en français

Fonctionnalisation de Nanomatériaux Bidimensionnels à Base de Graphène

Les systèmes bidimensionnels (2D) représentent une nouvelle famille de matériaux possédant des propriétés électroniques et quantiques extrêmes dues à leur nature. Le graphène, composé d'une seule monocouche d'atomes de carbone en hybridation sp^2 et structuré en nid d'abeille (figure 1a), en est l'archétype le plus étudié depuis la dernière décennie. Son interêt découle de ses propriétés extrêmes, par exemple sa très bonne conductivité, grande résistance mécanique et chimique, haute conductivité thermique, pour les-quelles il est considéré très avantageux pour de multiples applications, notamment pour remplacer les semi-conducteurs à base de Si pour la réalisation des futurs dispositifs électroniques. Cependant, le graphène est un semi-conducteur à gap nul (situé entre les deux cônes de Dirac au point K de sa zone de Brillouin (figure 1b)) ce qui est peu favorable pour fabriquer les circuits logiques. Son caractère peu réactif et son épaisseur d'un seul atome compliqunte la modification de ses propriétés par les méthodes conventionnelles. En vue de valoriser le graphène vers d'autres applications potentielles, il est donc indispensable de trouver des méthodes adéquates pour maitriser ses propriétés électroniques ainsi que sa réactivité chimique. Cette thèse est donc menée dans le but d'explorer différentes méthodes efficaces pour "fonctionnaliser" le graphène.

Cette étude de la fonctionnalisation du graphène se base principalement sur la monocouche de graphène épitaxiée sur le carbure de silicium (SiC), un semi-conducteur à grand gap, qui permet de préserver les propriétés électroniques du graphène sans avoir besoin de le transférer sur un autre substrat (ex. SiO_2/Si). L'épitaxie du graphène est réalisée par le recuit du SiC et la sublimation du Si à $\sim$1200°C sous ultravide (UHV), laissant une surface riche en carbone qui peut se reconstruire en monocouche(s) de graphène. Ces monocouches de graphène sont ensuite étudiées *in situ* par la spectroscopie de photoémission inverse (IPES), la spectroscopie de

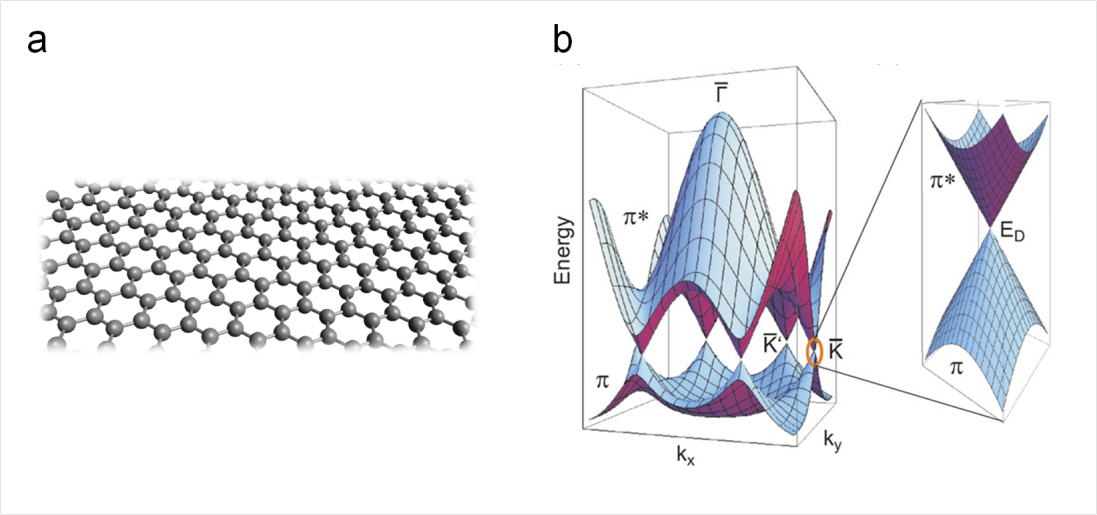

Figure 1: (a) Representation du monocouche de graphène en nid d'abeille. (b) Structure électronique de la bande π du graphène dans l'espace réciproque avec les deux cônes de Dirac au point K.

courant total (TCS), le diffraction d'électrons lents (LEED) et la spectroscopie d'électron Auger (AES), et *ex situ* par la photoémission en rayons X (XPS) et la spectroscopie Raman, pour révéler leur propriétés électroniques, structurales et leur composition chimique. L'IPES, un instrument peu commun, permet l'accès aux états inoccupés par l'injection d'électrons de basse énergie (6-22 eV), et la détection des photons émis lors de transitions radiatives des électrons incidents vers des états inoccupés plus proches du niveau de Fermi (E_F). Le principe du fonctionnement de l'IPES est schématisé dans la figure 2.4 La dispersion des bandes de conduction en $k_{||}$ est aussi accessible par la résolution angulaire en IPES (ARIPES). Plus de détails sur la fabrication et caractérisation du graphène vierge sont présentés dans le chapitre 3, et les méthodes expérimentales dans le chapitre 2.

Concernant la fonctionnalisation, l'incorporation d'atomes d'azote dans le graphène est réalisée à l'aide de sources d'azote à base de plasma (chapitre 4). Deux sources différentes sont étudiées dans cette thèse : (i) un canon à ions/atomes *in situ* générés par un plasma excité par des micro-ondes en conditions de résonance cyclotron électronique (MW-ECR); (ii) un implanteur industriel *ex situ* à basse énergie équipé d'un plasma en radiofréquence (RF), fabriqué et opéré par la société Ion Beam Services (IBS). Figure 3a montre la la configuration expérimentale de (i). L'influence des conditions du plasma, les énergies et espèces d'azote exposés, la procédure

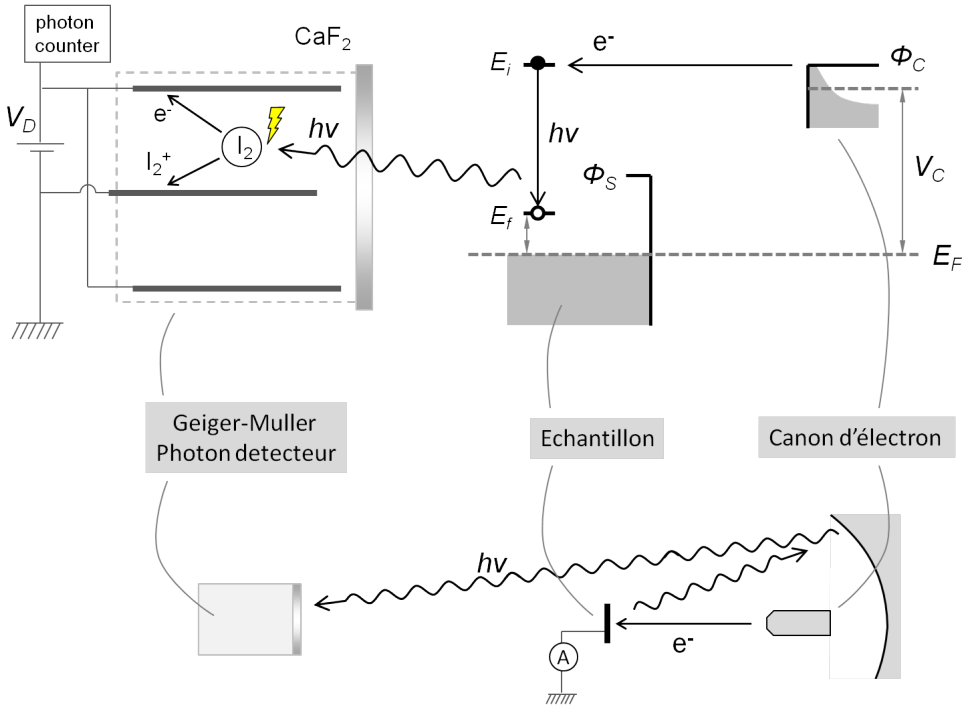

Figure 2: Le principe du fonctionnement de l'IPES (en haut) et la représentation de la configuration expérimentale (en bas).

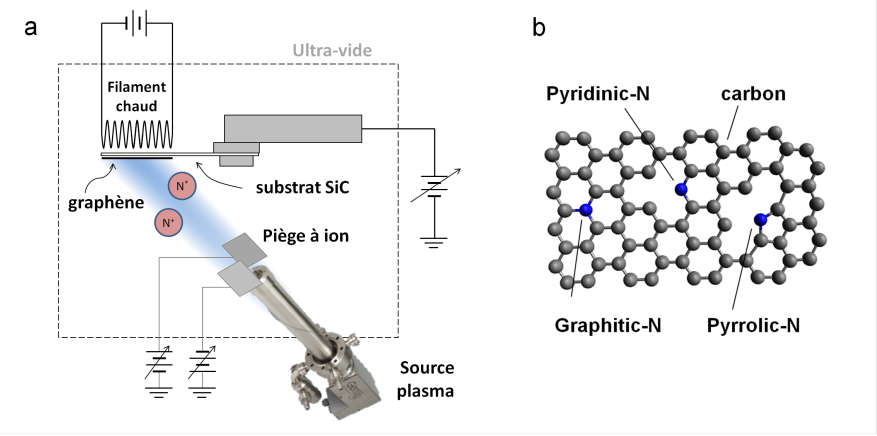

Figure 3: (a) La représentation de la configuration expérimentale (*in situ*) pour l'incorporation de l'azote. (b) Les principaux configurations du graphène incorporé dans le graphène.

de dopage, ainsi que l'épaisseur du graphène de départ sont également étudiés. Les images LEED montrent que la structure cristallographique du graphène se dégrade rapidement en fonction de la dose, mais il peut heureusement être réparé dans une certaine mesure en maintenant l'échantillon à chaud (∼850°C) pendant le bombardement. Plus précisément, la structure de graphène est sévèrement endommagée après une dose d'environ 1×10^{15} ions/cm^2 (35 eV) à température ambiante (RT), alors qu'elle est bien préservée sous une dose de 4×10^{15} ions/cm^2 (35 eV) à 850°C.

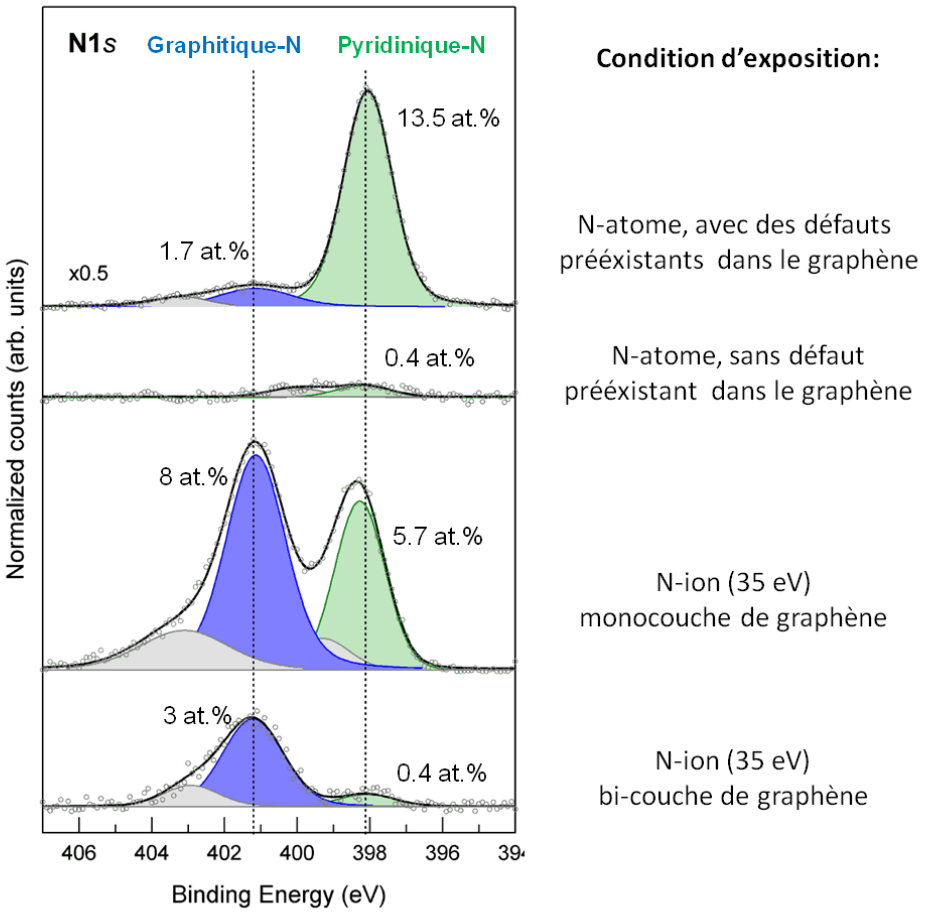

Figure 4: Les spectra XPS N1*s* représantatifs des chantillons de graphène dpoé d'azote étudiés dans cette thèse.

Les analyses des niveaux de cœur de N1s par XPS montrent qu'il est possible de contrôler la configuration des liaisons des azotes substitués dans le graphène, par l'énergie et les espèces d'azote incidentes, et aussi via l'épaisseur du graphène de départ (figure 4). L'incorporation d'azotes pyridiniques (pyridinique-N), liés à 2 C et situés à côté d'une lacune (figure 3b), est favorisée par des espèces d'azote de très basse énergie (atomes N thermalisés) jusqu'à 13 at.%, mais dépend de la présence de défauts préexistants. Les azotes graphitiques (graphitique-N, figure 3b), liés à 3 C, substituent efficacement les carbones du graphène en utilisant des ions d'azote (N-ion) entre 20 et 35 eV. La création de défauts due au bombardement d'ions, qui favorise l'incorporation des pyridinique-N, peut être restreinte sur un graphène d'épaisseur égale ou supérieure à 2 monocouches, ce qui mène à une concentration majoritaire de graphitique-N (3 at.% contre 0.4 at.% de pyridinique-N). Ces résultats expérimentaux sont en bon accord avec les études théoriques qui prédisent une énergie minimale de 15-22 eV et une énergie optimale de 50 eV pour activer la substitution dans le graphène, ainsi qu'une réactivité plus élevée pour une monocouche de graphène (plus faible pour une multicouche).

L'analyse ARIPES des structures électroniques du graphène dopé par N-ion (ex. d'une dose de 4×10^{15} ions/cm^2 à 35 eV sur une bi-couche de graphène) montre un décalage de ses niveaux inoccupés vers E_F ($\sim$0.5 eV), donc un dopage de type-n, ainsi qu'une diminution de la vitesse de Fermi (v_F), obtenue par l'analyse de la dispersion des états π^*. Compatible avec les études théoriques, cette modification de la structure électronique est attribuée aux graphitique-N (3 at.%) incorporés, mais cependant l'efficacité de dopage électronique reste relativement faible. Plus précisément, le transfert de charge d'un graphitique-N vers le graphène est d'environ 0.06-0.1 électron/atome dabsle cas d;une monocouche de graphène, alors que d'autres travaux ont estimé un transfert de charge de 0.5-0.6 électron/atome. Ce phénomène est attribué à la présence de sites de dopage complexes, composés de plusieurs azotes proches l'un de l'autre, ce qui rend le dopage moins efficace, un phénomène également révélé dans des études théoriques.

La substitution par l'azote est susceptible d'être confinée dans la première couche de graphène. Ceci est justifié par XPS et par l'étude du dopage d'azote sur une multicouche de graphène sur SiC(000$\bar{1}$), la face carbone de SiC. Les multicouches de graphène épitaxiées sur cette surface sont désorientées l'une l'autre, et chacune garde les propriétés d'une monocouche de graphène isolé. Après l'incorporation d'azote, seul le graphène de surface (désorienté du SiC) est affecté, montrant un dopage de type-n par ARIPES. Le graphène du dessous (aligné au SiC) reste non dopé. Concernant les

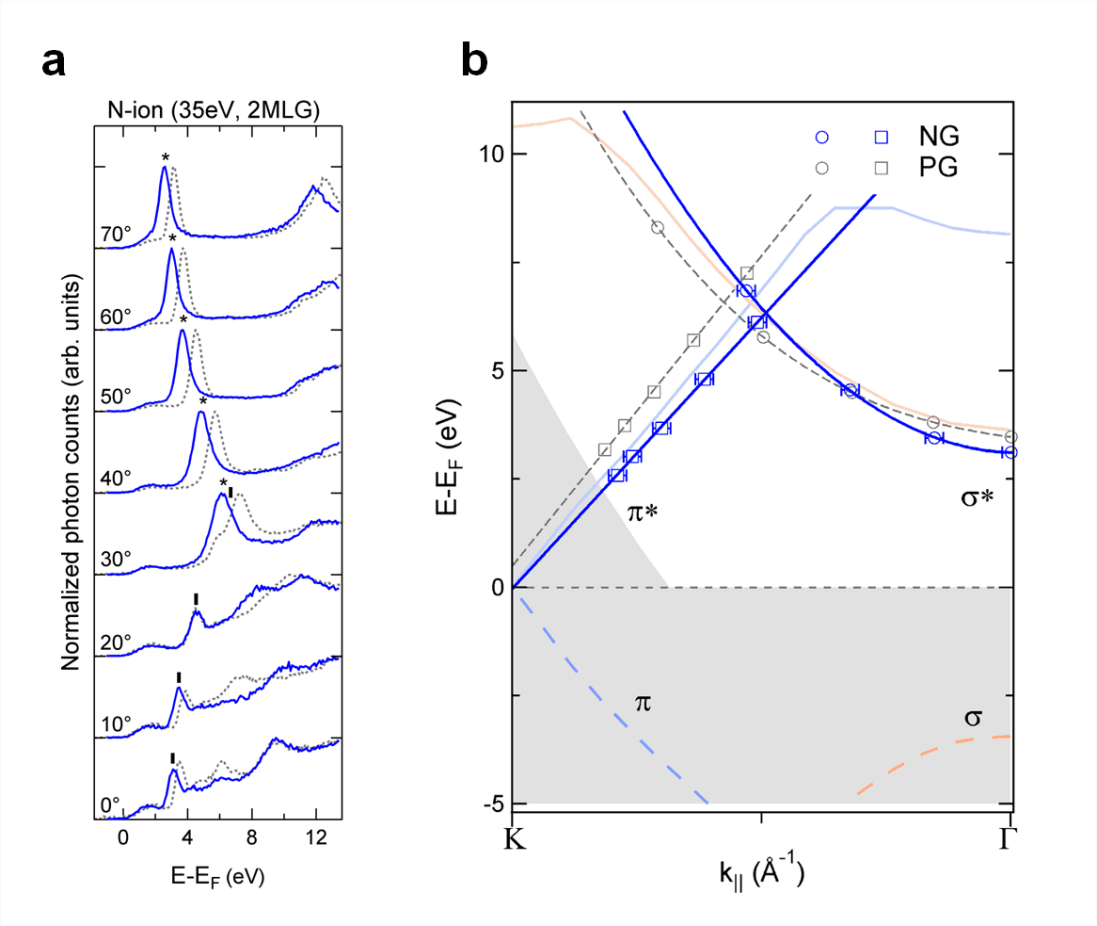

Figure 5: (a) Spectres de l'IPES du bi-couche de graphène en fonction de l'angle d'incidence. (b) La structure du bande du graphène dopé d'azote (bleu, et vièrge en gris) en dispersion en $k_{||}$ dans la direction $\Gamma - K$.

études des bandes de valence et l'imagerie des défauts du graphène dopé par l'azote, des mesures très préliminaires sont présentées. Les premières images de microscopie à effet tunnel (STM) à basse température confirment la présence des sites de dopage d'azote complexes.

Dans le chapitre 5, la fonctionnalisation du graphène par l'hydrogénation est étudiée sur la couche tampon de graphène (BLG) sur SiC(0001), connue également comme la reconstruction $(6\sqrt{3} \times 6\sqrt{3})R30°$, riche en carbone. Conformément aux études précédentes, l'hydrogénation de cette surface à haute température (∼700°C) permet l'intercalation de H sous le BLG, saturant les liaisons pendantes de Si et cassant les liaisons C-Si entre BLG et SiC. La substitution des liaisons C-Si, qui sont la cause de la destruction du caractère conducteur de graphène pour le BLG, transforme le BLG en une monocouche de graphène quasi-autoportante (QFSG), attestée par la présence des états π^* dans les spectres ARIPES. L'hydrogénation de BLG à RT, au contraire, forme des liaisons C-H sur la surface. Comme le montrent les spectres ARIPES et AES, les liaisons pendantes de Si restantes à l'interface sont également saturées, très probablement par la formation de nouvelles liaisons C-Si entre un BLG plus ondulé et le SiC. Les représentations des structures du H-BLG. Le caractère fortement-isolant du H-BLG qui contraste avec la haute conductivité du QFSG nous donne l'opportunité de suggérer un nouveau concept de fabrication de dispositifs à base de graphène sur SiC. Des pistes de QFSG pourraient être tracées entre H-BLG sans graver le graphène mais via un gradient local de température du BLG durant l'hydrogénation, par exemple avec un faisceau laser focalisé.

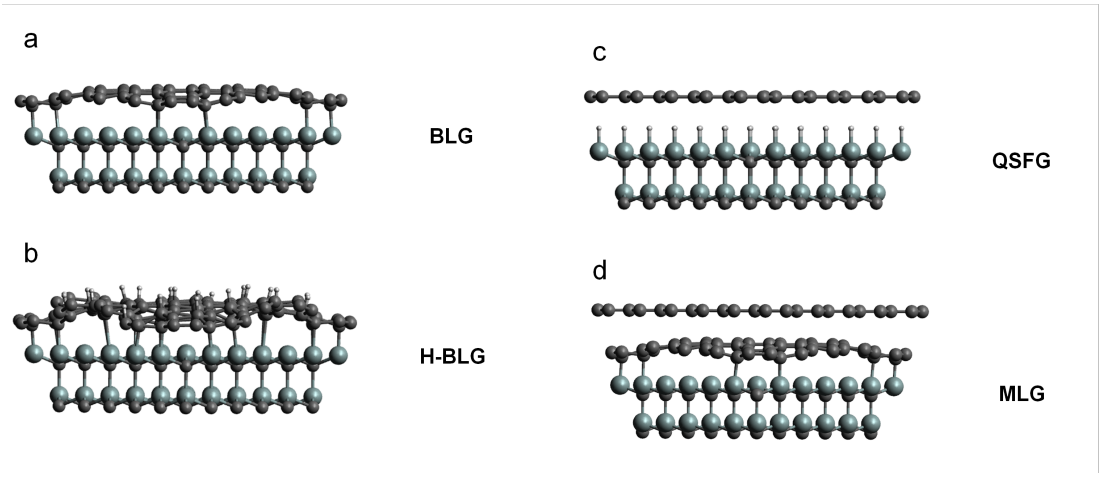

Figure 6: Modèle des structures de graphène sur SiC: BLG, H-BLG, QFSG et MLG.

Dans la dernière partie expérimentale (chapitre 6), la réaction/couplage entre des molécules π-conjugué et les graphène vierge et fonctionnalisé est étudiée. Trois molécules sont utilisées, à savoir le C_{60}, PTCDA et PTCDI. Les états inoccupés des molécules physisorbées sont légèrement modifiés en passant du graphène vierge au graphène dopé d'azote. Les réactions entre les molécules de PTCDA et PTCDI et le graphène sont observées après l'exposition aux électrons de basse énergie (<50 eV). Les molécules semblent perdre leurs groupes d'oxyde et/ou d'azote, et forment alors des liaisons covalentes avec le graphène. Par contre, on n'a pas pu distinguer une différence notable de réactivité des molécules sur le graphène dopé ou non-dopé dans les conditions étudiées. Cependant, ces résultats préliminaires seront utiles dans le cadre du projet ANR "ChimiGraphN", qui envisage des réactions de type Diels-Alder induites par une pointe STM pour greffer des molécules adéquates sur les zones riches en électrons du graphène dopé-n. En résumé, nous avons étudié et démontré l'efficacité de différentes méthodes (dopage d'azote et hydrogénation) aptes à fonctionnaliser le graphène en modifiant ses propriétés électroniques et sa réactivité chimique. Les connaissances acquises dans cette thèse permettront une meilleure maîtrise des propriétés des matériaux 2D comme le graphène. Elles faciliteront le développement de nouvelles applications à base de graphène, notamment en nano-électronique.

Contents

Chapter 1

Introduction

Our life has become more and more convenient and amazing to date thanks to the invention of transistor after the discovery of semiconductors in the field of solid-state physics. Si-based semiconductor, firstly demonstrated in 1954, is still the most widespread material for the fabrication of digital devices to date. It has induced an exponential development of electronic devices, integrated circuits (IC), and relevant applications. To increase the efficiency and the calculation speed of these devices, more transistors were integrated inside the same IC, which, as predicted by Moore's law, would double its number every 18 months. This prediction has been quite accurate but till recently, as the devices start to scale-down to the nano-scale. When the width of the transistor channel gets close to a few nanometers, the effects of the edges, defects and impurities, and more importantly the quantum effects are amplified, which can severely restrain the device performances. The behavior of carriers inside these nano-scale devices would largely depend on their quantum character relative to the dimension of the employed materials and their intrinsic properties. Thus, as the dimension of the devices narrows down, good quality and high performance of the devices become more and more difficult to obtain when using conventional materials and manufacturing methods, such as in Si-based semiconductors.

To go over these difficulties, a large variety of methods and materials have been proposed to manufacture advanced nano-scaled electronic devices, including carbon nanotubes, III-V types nano-wires and self-assembled monolayers, to replace conventional Si-based ones. The discovery of graphene and the demonstration of its ultimate properties, namely extremely high mobility, high chemical stability and high thermal conductivity, have immediately promoted it to become one of the best candidates for the realization of next-generation electronic devices. The two dimensional structure and one-atom thickness of graphene favor the fabrication of nano-scale devices, as well as the design of particular quantum properties. It has also shown the potential of large-surface mass production, by using chemical-vapor deposition assisted epitaxy.

However, the absence of an energy gap in the graphene electronic band structure, its semi-metallic character, restrains its applications in electronics devices, *e.g.* in transistor-based logic devices, which require a low off-current. Its relative chemical inertness also limits the modification of graphene using conventional methods. In order to break through these obstacles and to realize future graphene-based devices, finding proper ways to tune the properties of graphene, such as gap-opening and electronic doping, is the most urgent task. In addition, for these applications, a high quality graphene with controllable thickness on a non-metallic substrate, such as mono- or multi-layer graphene epitaxially grown on semi-insulating SiC substrates, is also much preferred.

In this thesis, entitled "the functionalization of two-dimensional nano-materials based on graphene", a practical study of the functionalization of graphene is presented. The principal works accomplished in this thesis include: (i) the fabrication and characterization of monolayer graphene on SiC surfaces, (ii) the nitrogen doping of graphene via plasma-based methods, (iii) the hydrogenation of graphene and (iv) the interaction of semiconducting organic molecules with the functionalized graphene. Actually, in connection with the ANR project "ChimiGraphN", one of the aims of this thesis is to support the study of the chemisorption of molecules on graphene epitaxially grown on SiC by enhancing the reactivity of graphene via nitrogen doping. The properties of pristine and functionalized graphene samples are investigated using various spectroscopic methods, especially the angle-resolved inverse photoemission spectroscopy (ARIPES), one of the expertise of our team, which gives access to the unoccupied electronic structure of the material. Other spectroscopic techniques, such as core-level photoemission spectroscopy, are also involved. The "ChimiGraphN" project also gives me the opportunity to access different analytic instruments, such as angle-resolved photoemission spectroscopy (ARPES) and low-temperature scanning tunneling microscopy (LT-STM), to enrich our study on the functionalization of graphene.

The content of this thesis is divided in seven chapters. In this first chapter, the background knowledge and the state of the art of the studied material, the graphene, are briefly introduced. The principal properties of graphene are presented, following by a general review of the fabrication process of graphene monolayer(s). It reveals the importance of this work and explains the exploration paths, *e.g.* the graphene grown on SiC. It ends with the summary of the state of art on the functionalization of graphene, and points out important issues that we try to solve in this thesis.

In the second chapter, a general description of the numerous experimental methods involved in this thesis is presented. It includes the working environment of the experiment, a ultra-high vacuum (UHV) system, the sample preparation methods and equipments, such as nitrogen plasma source and atomic hydrogen source. The working principles of the employed analysis instruments and techniques, especially ARIPES, target current spectroscopy (TCS), low-energy electron diffraction (LEED), Auger electron spectroscopy (AES) and X-ray photoemission spectroscopy (XPS) are also presented.

To investigate the functionalized graphene, a good understanding of the starting material, the pristine graphene, is necessary. The analyzed results may also vary from one to another instrument due to different experimental configurations and conditions. Thus, in the third chapter, we show the study of the pristine graphene monolayer(s) using our proper instruments mentioned above. Besides inspecting its conduction band structure, we also demonstrate the methods used to determine the quality and thickness of the pristine graphene.

The fourth chapter reports the main results of this thesis, the functionalization of graphene via nitrogen doping using plasma-based techniques. An extended study on the nitrogen doping processes and the properties of the nitrogen-doped graphene (NG) is presented. It includes the use of two different nitrogen plasma sources, and the graphene grown on the two opposite sides of SiC, Si-face and C-face. The obtained NG samples are investigated in various aspects, such as their electronic properties, atomic structures, and chemical environments.

In the fifth chapter, we show the study of hydrogenation on the buffer layer graphene, a graphene layer covalently bound to SiC. We demonstrate that hydrogen may significantly alter graphene properties in distinct ways when using different processing temperatures, which involves the saturation of the remaining Si dangling bonds at the SiC subsurface. It either transforms the buffer layer into a more insulating material or into a quasi-free standing graphene layer. We further propose a possible process to manufacture graphene-based devices without etching the graphene film based on selective hydrogenation intercalation.

The sixth chapter is devoted to a preliminary study of π-conjugated molecules interacting with pristine and doped graphene. Three different molecules, C_{60}, PTCDA and PTCDI are deposited onto the pristine and nitrogen-incorporated graphene. The interactions between the molecules and the two types of 2D solids are revealed by their electronic structure. Chemical bonding of the molecules with graphene is also primitively demonstrated by low-energy electron exposure.

Finally, the last chapter summaries the experimental results and conclusions deduced from these results. Key issues involving the graphene functionalization processes using the studied methods are presented. They give convenient reference with valuable indications for further investigations using similar processes, hopefully expected to boost the development of graphene-based devices.

1.1 Graphene

Carbon, one of the few elements known since antiquity, exists in different forms or allotrope. Some of them were discovered for long time such as diamond and graphite, in 3D crystal structures, some discovered in the late 20th century, like fullerenes and nanotubes, also described as 0D and 1D forms, as illustrated in figure 1.1a-d. Each of them possesses much different properties. The missing 2D allotrope of carbon (figure 1.1e), the so called graphene, has been discovered only recently and immediately

attracted extensive interests. The successful isolation of a single-layer graphene has been firstly demonstrated by Geim *et al.* using a top-down approach: the exfoliation of graphite crystal [1]. Since then, the graphene has become one of the most studied material in the world, with a stunning increase in the publications demonstrating its unique properties and large variety of applications.

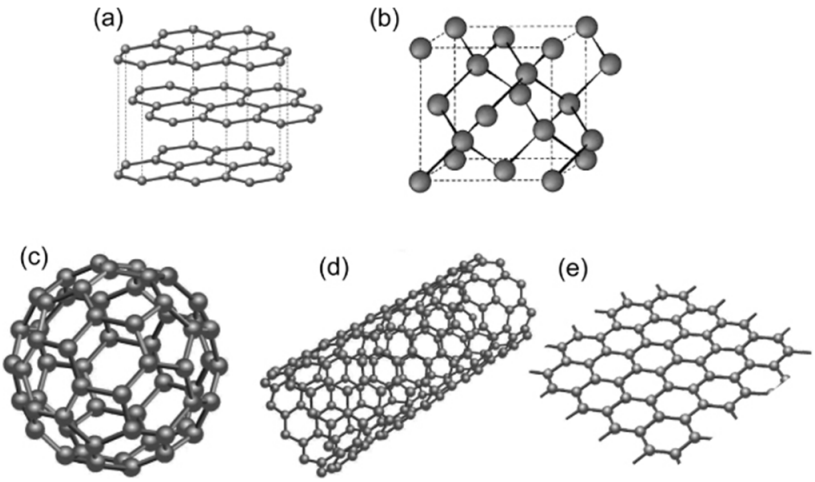

Figure 1.1: Ordered carbon allotropes in (a,b) 3D (graphite and diamond), (c) 0D (C_{60}), (d) 1D (carbon nanotube) and (e) 2D (graphene) form. Figure reprinted from Ref. [2].

1.1.1 Two-dimensional nanostructure

Graphene is a particular two-dimensional material composed of a single layer (or few layers) of carbon atoms closely bonded in sp^2 configuration that forms the well-known honeycomb nanostructure. Since its discovery in 2004, graphene has attracted extensive interests in the past few years due to its outstanding physical, electronic, thermal and mechanical properties [1, 3–5]. However, the theoretical study of graphene has begun long before that. It was employed as the starting point for all calculations on graphite [6], carbon nanotubes and fullerenes because of its simple hexagonal units. It was also assumed, in the point of view of thermodynamics, that a 2D crystalline material like graphene is unstable under ambient conditions [7]. Nevertheless, the stability of graphene can be attained thanks to the strong sp^2 bonding between carbon atoms reducing the thermal fluctuations, *i.e.* long-range rippling, and defects in graphene at relatively low level [8].

1.1.2 Electronic properties

One of the major reasons justifying that graphene has attracted such attention is its unique electronic properties linked to its specific π-conjugated 2D structure. The first approach for the electronic structure of graphene was realized by Wallace using tight-binding approximation, in 1947 [6]. The most interesting property is that the band dispersions in wave vector $k_{\parallel}$ is practically linear near the K point of the Brillouin Zone (BZ) of graphene lattice and forms two opposite cone shapes with no gap, as shown in figure 1.2. The cones are known as Dirac cones, and their crossing point at the K point, which energy equals to the Fermi level (E_F) for a free-standing graphene, is called the Dirac point. The linear dispersion of the energy band close to K point makes the electrons near the Dirac point behave like massless fermions, relativistic particle better described by the Dirac equation for spin 1/2 particles. The equation describing this linear dispersion relation is:

$$E = \hbar v_F \sqrt{k_x^2 + k_y^2} \tag{1.1}$$

Here the Fermi velocity $v_F \sim 10^6$ m/s, the wavevector k is measured from the Dirac points, and E is the energy relative to the Dirac point.

These unique electronic properties lead to the remarkable high electron/hole mobilities of graphene at room temperature, with reported values over 15,000 $\mathrm{cm}^2 \cdot V^{-1} \cdot s^{-1}$ [8]. The dominant scattering mechanism for the electron transport in graphene should be defect scattering rather than carrier scattering, since the mobility have been shown to be nearly independent of temperature between 10 K and 100 K [9]. Moreover, the electronic properties of graphene are very sensitive to the substrate due to its large surface area and 2D structure. For a quasi-free-standing graphene, such as graphene flakes transferred on SiO_2, the graphene is relatively isolated and the mobility is much higher than a graphene strongly coupled with a substrate, such as epitaxial graphene on SiC. For the latter, the graphene is doped and possess higher electron density, but the fluctuations or the defects due to the substrate induce additional phonons increasing the scattering of electrons.

Despite numerous demonstrations, the manipulation of graphene electronic properties and its applications are restrained at experimental stage due to intrinsic issues, such as the zero gap at the K point. This is especially critical for electronic devices, which prefer to have a band gap near the E_F. Methods to open a gap at the Dirac point of graphene have been proposed by using graphene nano-ribbons, applying strain or doping the graphene layer(s) [11–13]. Though, more applicable techniques are still in demand.

1.1.3 Synthesis of graphene

Multiple approaches, including physical and/or chemical processes, each with different advantages, have been demonstrated to obtain mono- or few-layer(s) of graphene in

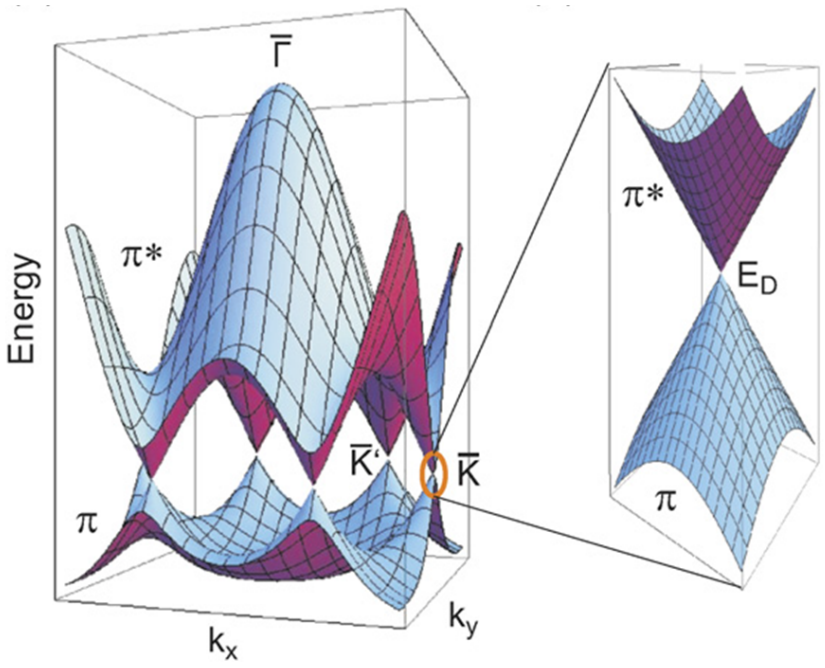

Figure 1.2: The graphene π and π^* band dispersions based on tight-binding approximation of Wallace [6]. in three-dimension representation. The right part of the figure shows the zoom of the Dirac cone at K point of graphene BZ. Figure reprinted from Ref. [10].

the past few years. Some of them have been well developed and even already commercialized. Four of the most commonly employed syntheses methods are briefly presented in the following, namely epitaxy on SiC, mechanical exfoliation, chemical vapor deposition (CVD) and reduction of graphene oxide. In this thesis, we have chosen to study the graphene obtained via the epitaxy on SiC. By comparing with other three methods, we show that the epitaxial graphene on SiC is the most favorable process for this study, since we are interested in its electronic and chemical properties.

Epitaxy on SiC

Silicon Carbide is a semi-transparent, large band gap, and semi-conducting material used in electronics devices. Producing graphene through UHV annealing of SiC surface is thus an attractive approach especially for semiconductor industry since the graphene obtained on SiC do not require to transfer onto other substrate for the following device fabrication. Beside the advantage in application, this approach also offers a good control on the thickness of epitaxial graphene.

When a SiC substrate is heated under UHV, Si atoms sublimate from the SiC surface and induce different surfaces reconstructions depending on the concentration of the Si and C atoms on the surface. For example, Si(0001) have surface reconstructions like (3×3), $(\sqrt{3} \times \sqrt{3})R30°$ and $(6\sqrt{3} \times 6\sqrt{3})R30°$, for a Si-rich to C-rich surface (see chapter 3). At higher temperature of about 1200°C, Forbeaux *et al* have shown that few layers of graphite (or graphene) are grown on the Si(0001) surface, which is actually the first reported practical approach to obtain graphene [14]. It was until later that the epitaxial graphene on SiC was better studied [15, 16].

More specifically, when annealing a SiC(0001) surface to about 1050°C in UHV, a $(6\sqrt{3} \times 6\sqrt{3})R30°$ reconstruction can be obtained on the surface. This reconstruction consists of a graphene-like honeycomb structure strongly bound to the SiC substrate, where 20-30% of carbon atoms are kept in sp^3 hybridization and covalently bonded with the Si atoms at the SiC subsurface [10]. The nanostructure of this C-rich reconstruction is illustrated in figure 1.3. This C-rich layer is also called the buffer layer (or zero-layer) of graphene (BLG). By further annealing to about 1200°C, Si atoms at the interface further sublimate and the BLG becomes detached from the SiC substrate, forming a single layer of graphene. Simultaneously, another BLG is formed under the first graphene layer. Repeating this process with increasing annealing temperature will generate double or multi layers of graphene. A schematic representation of the graphene grown on the surface of SiC is shown in figure 1.3.

A similar procedure is proposed for the C-terminated SiC$(000\bar{1})$ face in UHV, which results in few layer of graphene stacking with orientational disorder [17]. Due to the absence of BLG on the SiC$(000\bar{1})$ surface and the unusual rotational stacking of graphene, epitaxial graphene layers on SiC$(000\bar{1})$ are quasi-decoupled from each other and each monolayer behaves as an electronically isolated single-layer graphene. However, the

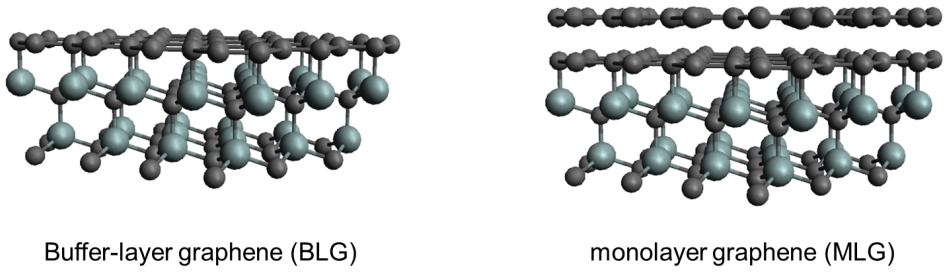

Figure 1.3: Schematic representation of the buffer-layer of graphene and monolayer graphene grown on SiC(0001) surface.

graphene grows much faster on C-face, which makes it more difficult to control the actual thickness of this epitaxial graphene.

Recently, the epitaxy of graphene on SiC(000$\bar{1}$) has been realized in a vapor phase of ambient Ar. It requires higher annealing temperature (∼1600°C) but permits improved thickness homogeneity and a much larger size up to wafer-scale. The principal concept is to reduce the sublimation rate of Si at nearly equilibrium conditions, which enables the surface reconstruction to be fully completed and homogeneous before the formation of graphene on the SiC surface [18].

Mechanical Exfoliation

Mechanical exfoliation is the most simple and direct way to obtain high quality, single layer of graphene. It is realized by a simple peeling process starting from commercially available highly oriented pyrolytic graphite (HOPG) sheet. It follows by rubbing the peeled-off graphite layers on SiO_2/Si substrate until obtaining single or few layers of graphene flakes lying on the surface. These thin flakes can then be washed off from the adhesive substrate in acetone and transferred to a silicon wafer for study.

This method was firstly demonstrated by Geim *et al.* in 2004, which led to the explosive attention on graphene [1]. The simplicity of the method gives access to numerous exciting discoveries of graphene properties. However, it is limited by its low production, small flakes sizes of graphene (about few μm^2), and defects due to chemical oxidation of the graphite.

Improved approaches have been proposed to increase the production and quality of the resulting graphene. It has been demonstrated that graphite could be exfoliated in a solution assisted with ultrasounds to produce defect-free monolayer graphene (MLG). The proposed solutions include N-methyl-pyrrolidone [19], sodium dodecylbenzene sulfonate [20], and sodium cholate [21], which have similar surface energy with

graphene to facilitate the exfoliation. The difficulties rest in preventing the cost and the contamination from the exfoliation solvent.

Chemical vapor deposition

With the aim of using industrial familiar processes, the synthesis of graphene through chemical vapor deposition (CVD) have been developed [22]. During CVD, a mix of reactant gases flows in the reaction chamber where the substrate (usually a metallic one) is heated at high temperature. The thin-film product is formed on the surface and the residue gases are pumped out. For the production of graphene, one usually uses carbon-containing gaseous sources, such as CH_4 or C_2H_2, to generate reactions on a metal surface, such as Ni or Cu [23, 24].

The choice of the reactive gas has little effects on the graphene preparation but the choice of the substrate can be divided in two major categories with different growing mechanisms. One is to use the nickel-like metals, which produces graphene by dissolving carbon in the substrate and follows by a precipitation of carbon on the surface that forms graphene layer(s) after cooling the metal substrates [23]. The other is based on the copper-like metals, which produces the graphene layers through a super saturation of carbon species at the surface due to its lower carbon solubility [25]. Recently, the production of graphene via CVD method has been realized using different substrates, such as SiC, for better homogeneity than its epitaxial counterparts, or using plasma-enhanced CVD for lower temperature and higher productivity [26].

The advantages of the CVD method are its large-size scalability and a lower preparation temperature. It is also much easier to introduce dopants in graphene by a simple addition of dopant-containing reacting gas, such as NH_3 gas for nitrogen doping. However, though the thickness of graphene is not difficult to control, the obtained graphene film needs to be transferred on other substrate to be electrically isolated, which is a very critical process for semiconductor applications as impurities could easily contaminate the graphene.

Reduction of graphene oxide

The reduction of graphene oxide, firstly demonstrated by Stankovich *et al.* in 2006 [27], is an approach that provides a simple, low-temperature and low-cost method to produce graphene-based thin flakes. The idea of this method is also to separate graphene layers from graphite, a top-down method. It is realized by first oxidizing the graphite in a solution of oxidants, including concentrated sulfuric acid, nitric acid and potassium permanganate. Due to the addition of oxygen-containing function groups, graphene oxides can be easily exfoliated in water into stable monolayer sheets, for example, using ultrasonic treatment. The graphene oxide sheets are then chemically reduced and precipitated into graphene monolayer flakes. The commonly used reducing agents are hydrazine and sodium borohydrate [28]. The reduction of graphene oxide through thermal annealing to 1050°C can also produce graphene monolayer with nearly 80%

yield. However, this approach usually creates much vacancies and structural defects during the synthesis, making it less favorable in electronics applications.

1.1.4 Defects in graphene

Except the latter chemically derived route, most graphene synthesis methods can produce graphene layers with minimal structural defects, thanks to its strong and stable sp^2 bonding structure. Though, the defects in graphene are still important elements in terms of tailoring the electronic and/or chemical properties of graphene. The presence of defects changes the distribution of electrons in the graphene structure that alters the local electronic structure. They also work as scattering center for electron waves and cause the decrease of carrier mobility in graphene. Principal types of point defects, since they are more related to the subject of this thesis, are briefly presented in the following.

First, the Stone-Wales defect, is when two carbon atoms turn 90° in-plane and makes four hexagons to transform into two heptagons and two pentagons, as shown in figure 1.4 [29]. It is a point defect without any addition or removal of carbon atom. It has a formation energy of ∼5 eV with a kinetic barrier of 10 eV [30]. Calculations show that the presence of Stone-Wales defects opens a local band gap, up to 0.3 eV in graphene [31].

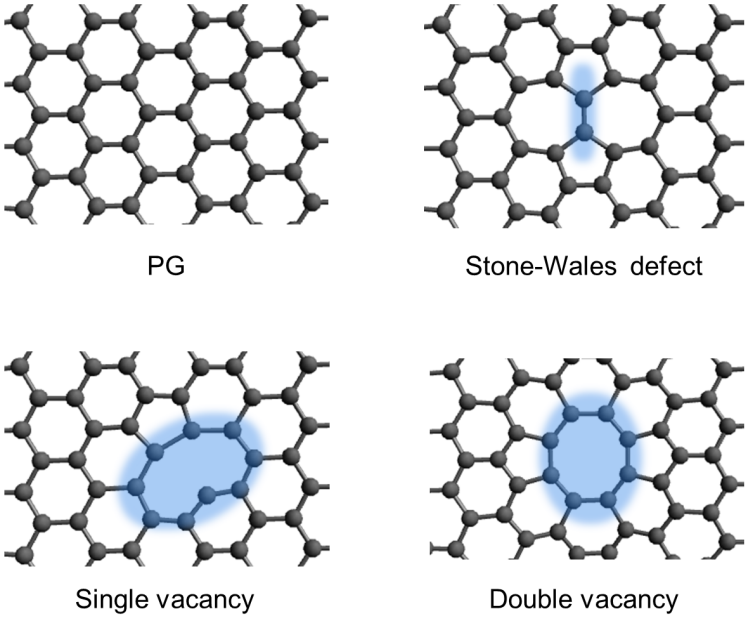

Figure 1.4: Representation of principal defects of graphene: Stone-Wales defect, single vacancy and double vacancy.

Table 1.1: Point defects in graphene - Overview of common point defects in graphene with their theoretical formation and migration energies. Values taken from Ref [29]

defect type	configuration [additional atom]	formation energy (eV)	migration energy (eV)
Stone-Wales	55-77 [0]	4.5-5.3	10
single vacancy	5-9 [-1]	7.3-7.5	1.2-1.4
double vacancy	5-8-5 [-2]	7.2-7.9	7
	555-777 [-2]	6.4-7.5	6
adatom	[+1]	6-7	0.4
inverse SW	57-57 [+2]	5.8	-

The other in-plane defect in graphene system is the C vacancy. Single C vacancy usually leaves an unsaturated dangling bond and a pentagon after defect relaxation (figure 1.4). It has a formation energy of ∼7.5 eV and modifies the local density of states. It also has a low migration barrier of ∼1.3 eV, which enables the migration of single vacancy at relatively low temperatures of 100-200°C [32]. During the migration, it may encounter other vacancy defects and combine into a multiple vacancies site, such as double vacancy, which has different types of configurations, all having a formation energy around 7 eV [29]. When it forms double vacancy, as shown in figure 1.4, the defect becomes more stable due to the decrease of total formation energy from 15 eV (2×7.5 eV) to ∼7 eV. It also becomes less mobile due to higher migration barrier (6-7 eV).

Adatoms, instead, only exist with the deformation of 2D graphene structure, or need to jump out the hexagonal plane. It usually has very low migration barrier (∼0.3 eV), and can travel rapidly at room temperature [29]. Though, due to low energy barrier, adatom-like defects are usually less stable and can be easily repaired.

The different point defects presented above are summarized in table 1.1. They are solely intrinsic defects since no other element is involved. However, when different atoms are introduced in graphene system creating extrinsic defects, the electronic properties of graphene may be further altered. The careful control of these defects can provide more possibilities to the usage of the graphene, which are further discussed in the next section.

1.2 Functionalization of graphene

Since the successful isolation of graphene, numerous applications, including nano-electronics, catalysis, gas detection, and hydrogen storage, have been proposed and demonstrated [33–36]. Graphene electronic devices are particularly anticipated to replace their Si-based counterparts. However, this technology is restrained by the diffi-

culties in tailoring the electronic properties of graphene with traditional methods due to its one-atom thickness, low reactivity and the zero gap at the Dirac point [37]. In order to tailoring the electronic properties of the pristine graphene (PG), various doping approaches have been proposed.

Generally, the doping of graphene can be classified into two categories. The first is electrical doping through simple charged carrier transfer. It occurs when applying a gate electrode voltage [38], by depositing metallic cluster [39] or via substrate-induced doping [13, 40]. The other one is chemical doping, which induces the doping of graphene via chemical routes (*i.e.* involving the formation of chemical bondings), such as substitutional doping with heteroatoms [41], hydrogenation, or molecular doping [42]. Among these doping mechanisms, three of them, involved in this thesis, are discussed in more details in the following, *i.e.* the substrate-induced doping, the molecular doping and the substitutional doping.

1.2.1 Substrate-induced doping

It is well known that a charge transfer or an induced dipole occurs at the junction of two different materials and modifies the electronic structure at the interface. When it happens between a 2D materials of only one- (or few-) atom-thick and a substrate, such as graphene on SiC, the electronic states perturbation at the interface will influence the entire 2D material, comparable to the doping of the material [10]. This substrate-induced doping is especially obvious if the 2D materials interact strongly with the underneath substrate, e.g. in the case of metallic or semiconducting substrate.

The graphene grown on SiC, studied in this thesis, is a typical case for substrate-induced doping. It has been revealed that the graphene is intrinsically electron doped (n-doped) by the underneath $(6\sqrt{3} \times 6\sqrt{3})R30°$ surface reconstruction, also known as BLG, as shown in figure 1.5a,b. According to angle-resolved photoemission spectroscopy measurements, the negative charges are transferred to the graphene and brings the E_F to ∼0.4 eV above the Dirac point [16].

To obtain a "neutral" graphene on SiC or other doping substrate, two routes are possible. That is, either via the intercalation of a decoupling agent between the graphene and the substrate, or the addition of a compensation doping by an other method. For the former, the intercalation of hydrogen at high temperature can effectively isolate the graphene from the SiC substrate [43]. More specifically, activated hydrogen atoms can diffuse through the graphene layer at considerably high temperature (>700°C) and passivate the Si dangling bonds and Si-C bonds at the interface. The BLG is thus decoupled from the substrate and becomes a quasi-free-standing graphene (QFSG) monolayer, as also shown in figure 1.5c. From a single layer graphene on SiC (SLG), a free-standing bi-layer graphene can also be obtained (figure 1.5d). As for the compensation of substrate-induced doping, Riedl *et al.* have found that the adsorption of n-type organic molecules with high electron affinities, e.g. F_4-TCNQ, on graphene

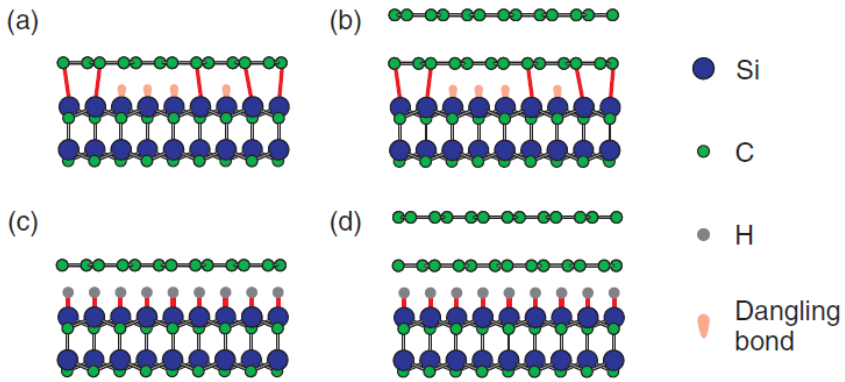

Figure 1.5: Schematic representation of graphene growth on SiC(0001). (a) a BLG, (b) a MLG, (c) a QFSG, (d) a QSFG bilayer. Figure reprinted from Ref. [43].

surface can also compensate the doping of SiC substrate, which brings back the E_F to the Dirac point [10].

Some substrates induce little doping onto graphene, such as SiO_2 or C-face of SiC. Graphene on these substrates are nearly electronically neutral and may be n-type or p-type doped using different methods, facilitating the application in semiconductor industry. However, the substrate-induced doping is still very useful if properly used.

1.2.2 Molecular doping

Molecular doping, employing donor or acceptor-type molecules adsorbed on the surface (some classify it as surface transfer doping) [44], is effective especially in the case of two-dimensional (2D) nanomaterials, like graphene thanks of its large surface area. Depending on the functional groups of the adsorbed molecules on graphene surface, the molecule can withdraw or donate electrons to the graphene, effectively doping it p- or n-type, respectively. For example, water, NO_2 and tetrafluoro-tetracyanoquinodimethane (F_4-TCNQ) molecules cause p-type doping, while NH_3 causes a n-type doping of graphene [1, 35, 43]. Since the adsorbed molecules should remain non-ionized at these levels of charge transfer, the molecular doping may involve some kinds of chemical bonds but weaker than covalent ones. This approach can not only find use in electronics but is also interesting for gas detection application, as the resistivity of graphene strongly varies with the doping caused by the adsorbed molecules.

1.2.3 Hydrogenation

Hydrogenation of graphene is similar to molecular doping since H atom is adsorbed on the graphene surface like a molecule (except at the edge of graphene sheet, which is a much different case). But it does not induce excess carriers and is covalently

bonded to graphene different to other physisorbed molecules. The hydrogenation of graphene transforms the bonded carbon atom from sp^2 into sp^3 hybridization. The disruption of the sp^2 structure changes the local electronic properties of graphene and may open a small band gap [45]. The complete hydrogenation of graphene results in a new 2D material called graphane [46, 47]. Its structure is shown in figure 1.6, where all carbon atoms are bonded with a hydrogen while turning into sp^3 configuration. The graphane was estimated to be an insulating 2D material with a large band gap of ∼3.5 eV obtained from density functional theory (DFT), or 5.4 eV by *GW* approximation [48]. More details are introduced in chapter 5.

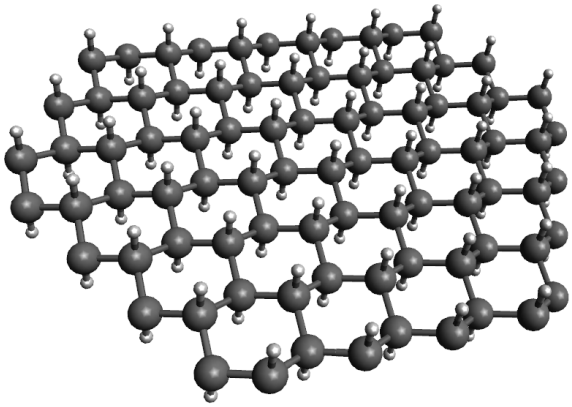

Figure 1.6: Schematic representation of graphane in the chair conformation. The carbon atoms are shown in gray and the hydrogen atoms in white balls.

1.2.4 Substitutional doping

The substitutional-like doping, which aims to replace carbon atoms in the honeycomb lattice of graphene by hetero-atoms providing (or taking away) electrons to the graphene [49], appears more favorable in many applications. One of the most commonly used substitutional-like doping is to incorporate nitrogen in the graphene structure. Nitrogen atoms provide excess valence electrons when replacing carbon atoms, doping the graphene into n-type. In contrary, if the substitution is made by acceptor-like boron atoms, the graphene becomes p-type.

Generally, there are three principal doping configurations for the substitutional-like nitrogen doping in graphene, as also shown in figure 1.7.

- Pyridinic-N: N atom in sp^2 configuration bonded with two carbon in a hexagonal ring next to a single vacancy.
- Pyrrolic-N: N atom in sp^2 configuration forming a pentagonal ring with the neighbor C next to a vacancy.

- Graphitic-N: N atom in sp^2 configuration bonded to three carbon atoms.

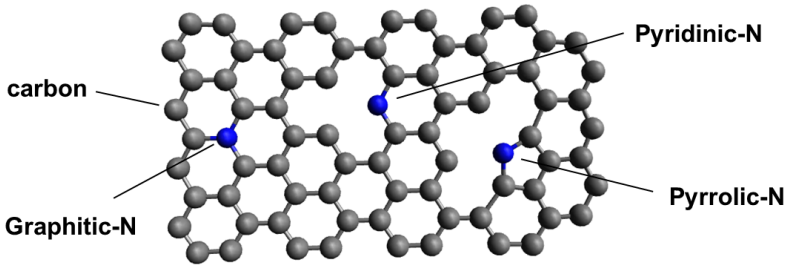

Figure 1.7: Schematic representation of the three principal configurations of doping nitrogen: Pyridinic-N, Pyrrolic-N and Graphitic-N

Usually, the configurations of the doping nitrogen are identified using core level photoemission spectroscopy (XPS). In XPS, the binding energy of N1s core levels of pyridinic-N, pyrrolic-N and graphitic-N, are located around 398.3 eV, 399.8 eV and 401.2 eV, respectively [50]. The configuration of the doping nitrogen can be further examined using scanning tunneling microscope [41, 51, 52]. The local electron density perturbation induced by the doping nitrogen can also be revealed using scanning tunneling spectroscopy [41, 52]. For example, it shows that ∼50-60% of the excess electrons provided by a graphitic-N are delocalized over several nanometers, implying a local n-type doping.

The *ab initio* computed formation energy of these configurations have been reported by Lv *et al* [51]. It shows that the formation energy of a graphitic-N and a pyridinic-N are only ∼0.2 eV and ∼3.4 eV *wrt* PG, respectively. The large difference is due to the creation of a single vacancy next to the pyridinic-N. If we compare to the formation energy of a single or double vacancy, 7-7.5 eV [32], the presence of a pyridinic-N actually stabilizes the single vacancy system. Thus, the presence of defects during the substitutional doping, especially vacancies, is very critical and should be taken into consideration for both calculations and experiments. One should also consider the high probability to find complex doping configuration consisting of multiple doping nitrogen atoms, which may influence the electronic properties of graphene differently [53]. However, the properties of these complex doping configurations are still poorly studied.

Many approaches have been proposed to incorporate nitrogen into the honeycomb structure of graphene. The first reported method is the direct synthesis by chemical vapor deposition (CVD) [49]. It is realized by the simple addition of nitrogen-containing molecules, NH_3, into reactant gases during the graphene growth by CVD. This method mainly produces graphitic-N and induces a n-type doping to the graphene [51].

Some post-doping methods have also been proposed, such as thermal annealing in a NH_3 atmosphere and nitrogen-based plasma treatment [54, 55]. These methods

usually produce pyridinic-N, especially the former method. Theoretically, it induces a negligible doping relative to a single vacancy since the nitrogen do not provide excess electrons in this configuration but only modifies the local electron density distribution. A local *p*-type doping may be found at either single C vacancy and pyridinic-N sites, which is due to the C vacancy defect but not due to the incorporated nitrogen atom. However, the actual doping configuration may be more complex (*e.g.* with multiple N atoms and multiple vacancies defects), as some of them are energetically more stable, and may modify local electronic properties differently than expected [53]. For example, as described earlier, two single vacancies tends to merge into a double vacancy, which exhibit a relatively neutral doping.

The identification of the general doping level of the prepared nitrogen-doped graphene (NG) can be performed via two methods. One is to directly inspect its valence-band (or conduction band) electronic structure using photoemission spectroscopy (or IPES) to define the position of E_F corresponding to its Dirac point. The other is to measure its conductivity under a varied gate voltage. The later needs to transfer the graphene on particular substrates, e.g. SiO_2/Si, and deposit metal contacts for the electrical measurements. Raman spectroscopy also provides information about the doping of graphene with the development of defect-related modes [50]. Sometimes, it shows a small red shift of the graphene-based peaks for n-type doping, and a blue shift for p-type, due to the variation of charge density in the graphene [56]. Though, the band-shifting of Raman spectra actually indicates the stiffening or smoothing of the phonon, which is caused by more complex effects than the mere electronic doping.

The successful demonstrations of the graphene doping, especially with nitrogen, have launched the developments of large varieties of applications. Nitrogen-doped graphene is regarded as a potential candidate for metal-free cathode of fuel cells due to the electron-accepting ability of N atom in graphene (large density of unoccupied states near E_F) [57, 58]. It has been shown that NG, prepared via the reduction of graphene oxide, exhibits efficient oxygen-reduction reaction with high stability and good electrical properties [59]. As for semiconductor applications, it has been shown that the doping of nitrogen may open a band gap beside the n-type doping, which transforms the graphene into an extreme high-mobility 2D semiconductor [49]. However, being highly critical to the electronic properties of NG, the control of the structural quality, the doping concentration and configurations become the major issue toward practical applications [50]. The NG has also attracted great attention as a potential anode material in lithium ion batteries and as ultra-capacitors thanks to its large surface area and excellent electrical properties. [60]. Finally, the disturbed local electron density caused by the doping nitrogen permits higher local reactivity and may enable an easier "grafting" of the graphene, which is highly immune for PG. This may provide much more possibilities of using the NG, such as highly effective catalyst, patterned functional area, etc.

Different doping methods result in various configurations of doping nitrogen and favor different applications [50]. However, despite the numerous studies, only few of

them have been able to alter or to control the creation of any specific configuration of the doping nitrogen, i.e. to be able to fabricate pyridinic-N rich or graphitic-N rich by a simple changing of doping conditions [61]. One of the goal of this thesis is to study the creation mechanisms of the doping nitrogen, and to find an easy way to control the resulting configuration of the dopant.

Chapter 2

Experimental Methods

Many experimental methods are involved in this thesis due to the complexity of the studied systems. In order to give a general information on the applied methods, this chapter summarizes the principal experimental methods and instruments involved in this work. It includes the working environment, a UHV system, the sample preparation methods and the general description of the analysis techniques.

2.1 UHV system

The principal experiments carried out in this work are performed in our UHV system, including the preparation of graphene samples, the functionalization of graphene, and a part of the sample characterizations. The use of a UHV system is very important for the study of material surface, especially for nano-structured surfaces whose properties may be critically modified with minimum structural changes. For example, assuming 100% adsorption efficiency, the material surface may be fully covered by molecules of the residual gas after one second at a pressure of 10^{-6} mbar. In contrast, the UHV, at a base pressure in the 10^{-10} mbar range, can ensure a clean surface for several hours ($> 10^4$ seconds), which is long enough to acquire the necessary information from the studied surface. The UHV also enables a long mean free path for the electrons and molecules, and a low ionization probability of the residual gas near a high-voltage source. This permits a proper function of the characterization techniques used in this thesis, since most of them collect or emit electrons to acquire the information from the surface.

The configuration of our UHV system is presented in figure 2.1. To obtain UHV, the system is constructed principally with a stainless steel body, all metal seals, copper gaskets, glass windows, and some molybdenum (or tantalum) parts that require to sustain high temperature. Three pumping levels are used in the system. First, a scroll type mechanical pump is used to attain 10^{-3} mbar with a minimum contamination. Then, a turbo pump is used to attain a higher vacuum of 10^{-7} mbar, which enables

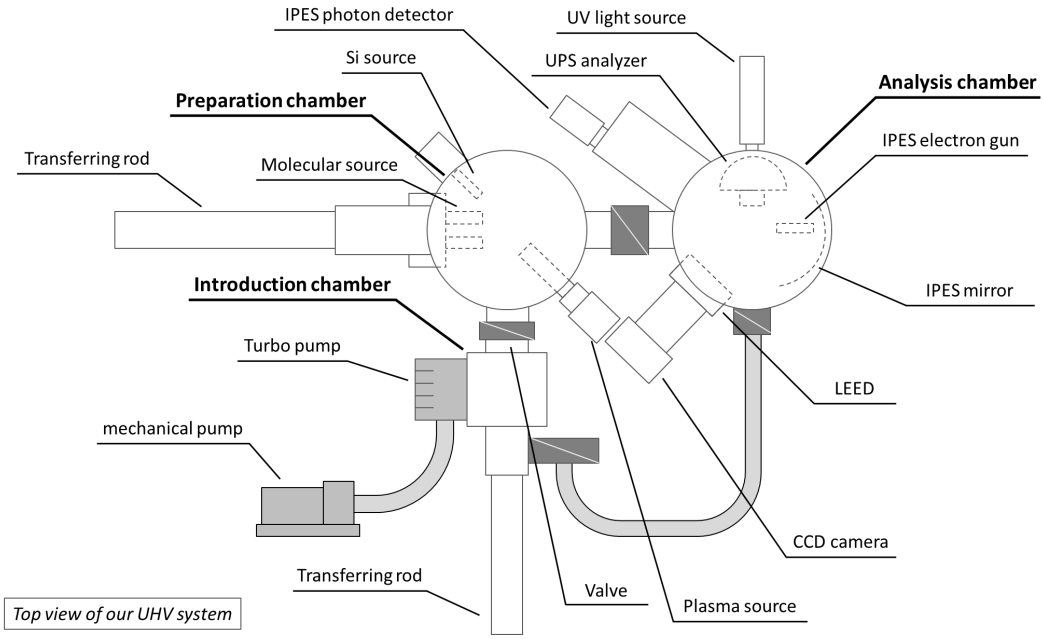

Figure 2.1: Schematic representation of our UHV system viewed from the top

some treatments on the sample or some preliminary functional tests of the system. And finally, several ion pumps combined with titanium sublimation pumps are used to attain 10^{-10} mbar or better. Each time after the system is brought to air, the system is backed for 48 hours during pumping stages to desorb residual gases adsorbed on the inside walls.

The UHV system is separated by vacuum valves into two big and one small chamber, namely the preparation chamber, the analysis chamber, and the introduction chamber. The preparation chamber is equipped with a heating filament, a plasma source, a silicon evaporator and two molecular evaporators, as shown in figure 2.1 and 2.2. The base pressure is measured by a Variant IMG-300 inverted magnetron cold cathode type gauge. A mass spectrometer is also mounted on the top of the chamber to identify the composition of the residual atmosphere. The analysis chamber consists of an IPES, a LEED/AES and a ultra-violet photoemission spectroscope (UPS). Details of these analytical instruments are described later, in section 2.3.

2.2 Sample fabrication and functionalization

Figure 2.2 shows the main configuration of the preparation chamber. When working in the preparation chamber, the sample is hold from one end by a sample holder. The heating filament can be brought to the rear of the sample for sample annealing. The

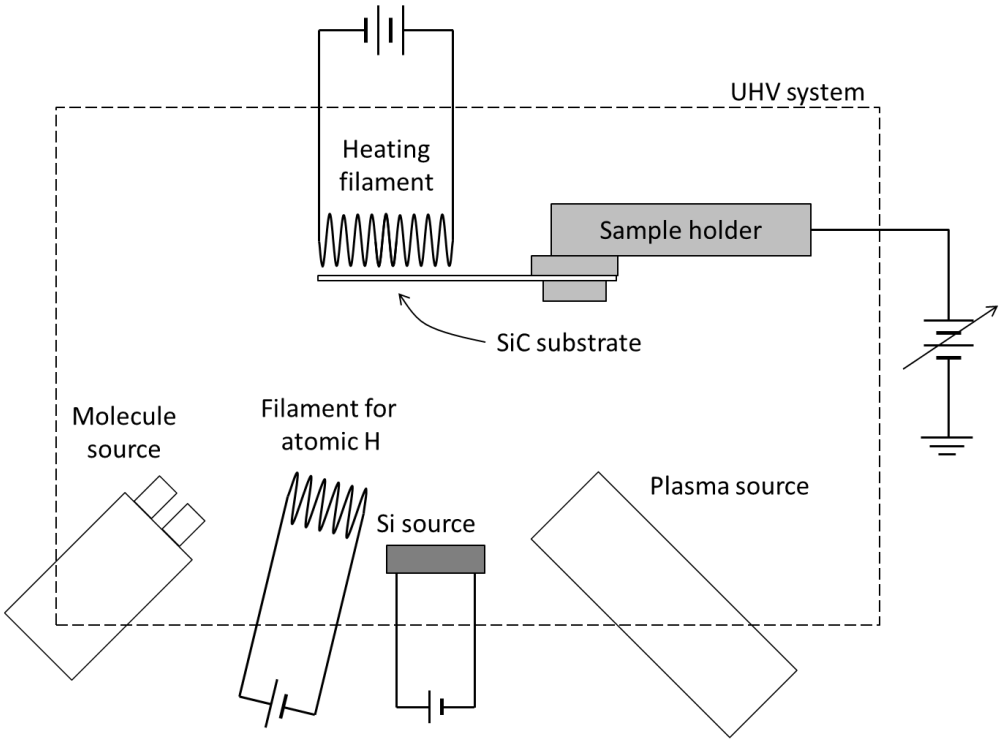

Figure 2.2: Sketch of the main configuration in the preparation chamber.

fixed end of the sample will cause a temperature gradient during the annealing. Though, the annealing temperature is kept homogeneous enough within 4-6 mm starting from the loose end. The joule heated Si source and the filament of atomic H source are placed ∼5 cm away from the sample. The plasma source and the molecular sources (Knudsen cell) are placed ∼10 cm away from the sample, and are targeted to the sample with a 45° incident angle.

2.2.1 Epitaxial growth of graphene on SiC

Graphene samples were prepared from n-type Si-face 6H-SiC(0001) (or C-face 6H-SiC(000$\bar{1}$)) wafers provided by NovaSiC. The SiC surfaces were chemically polished by the manufacturer and are ready for the epitaxy of graphene. The studied samples are cut into a rectangular shape with a dimension of about 4×15 mm before introducing in UHV system. A newly introduced sample is first annealed in UHV at ∼700°C for 1 hour to degas and to get rid of surface impurities. In order to obtain better homogeneity with minimum defects, the samples are then annealed, at about 850°C for Si-face SiC or 950°C for C-face, under a low Si flux for 20-30 min until the formation of a (3×3) or a (2×2) surface reconstruction, respectively. The success of this step ensures the surface quality of SiC substrate with minimum impurities, *i.e.* free of native oxide, as checked by XPS and AES. This is followed by subsequent annealing steps, each exhibiting another SiC surface reconstruction (see chapter 3), to keep the homogeneity of the surface structure.

The graphene monolayer is obtained by a final annealing at ∼1150°C for about 10-15 min, regarding the size of the studied sample. A BLG, a monolayer graphene (both at Si-face) or a multilayer graphene can be obtained by slightly varying the annealing time or temperature. The quality of the pristine graphene sample is verified *in situ* by LEED and IPES. The number of graphene layers is calibrated *ex situ* by Raman spectroscopy. More details are presented in chapter 3.

In our system, the annealing of the SiC sample is performed by bringing the hot filament to the back side of the suspended sample, as close as ∼1.5 mm. The thermal radiation annealing by the filament brings the sample up to about 900°C. The annealing temperature can be further increased by polarizing the sample positively to bombard the sample with electrons emitted from the hot-filament. The annealing temperature is estimated by comparing with the value reported in literature, at which different SiC reconstructions are obtained, or calibrated using an external pyrometer. The Si flux is provided by Joule heating of a small piece of Si wafer.

2.2.2 Atomic hydrogen exposition

In this thesis, the atomic hydrogen used for the hydrogenation of graphene is generated by thermal activation (or decomposition) of H_2 molecules using a hot tungsten filament heated to about 2000°C and placed ∼50 mm in front of the sample. The partial pressure of the molecular hydrogen is controlled by a leak valve, which is connected to

a high purity H_2 container. The hydrogen molecules in the chamber are only activated (or decomposed) when hitting the hot filament. A fraction of these activated hydrogen diffuses toward the nearby sample for the hydrogenation of the sample.

The setup of an atomic hydrogen source is usually quite different from one to another, which affects the hydrogenation efficiency of graphene. Parameters, especially the exposition time, are hardly comparable between different works. As reference, the typical working conditions, for the hydrogen intercalation in our system, is ∼36,000 L (1.3×10^{-5}mbar×1 hr.), while hot the filament and the sample are held at 2000°C and 700°C, respectively.

2.2.3 Plasma exposition

The preparation chamber is equipped with a Tectra Gen2 microwave plasma source working at the electron-cyclotron-resonance condition (ECR-MW) [62]. A representation sketch of the plasma source is presented in figure 2.3. An external magnetron source is used for the generation of microwaves at 2.45 GHz and a magnet is used to deflect the electrons generated by the inserted energy in a circular path. The plasma is generated inside a quartz cup filled with the required gas at low pressure, usually around 5×10^{-5} mbar. Electron cyclotron resonance can be reached at the appropriate microwave frequency and magnetic field. This method results in a spiral trajectory of the electrons with high kinetic energy, which permits a much higher plasma density, high cracking efficiency, and low self-bias. Though, the plasma generated from reactive gas, such as O_2, H_2 or N_2, would consist of a larger proportion of neutral and ionized monomers *wrt* conventional RF plasma [62].

The plasma diffuses from the gas inlet at the rear part (right side in figure 2.3) to the beam exit at the front part (left side in figure 2.3). A hollow BN aperture/extractor is placed at the beam exit, confining most of the plasma inside the source but enabling a beam of activated neutrals and ions to be emitted toward the sample. A pair of parallel metal plates is placed at the outlet of the source, namely the ion trap, and voltages with opposite sign (up to ±5 kV) can be applied to prevent most of the ions to reach the sample.

The plasma source can work in two distinct modes. In the ion mode, the source emits downstream plasma constituted by a mixture of low-energy ions and neutrals thermalized by the BN aperture. In the atom mode, it emits only thermalized neutrals by turning on the ion trap. The mean ion energy in the downstream plasma is determined by the plasma potential, which is around 20 eV [62]. During exposure, the source is operated at a constant power and is maintained at a working pressure of 5×10^{-5} mbar. The resulting output ion flux is of the order of 4×10^{12} ions·s^{-1}·cm^{-2}, and the atom/neutral flux is estimated to be over 2.5×10^{15} atoms·s^{-1}·cm^{-2} according to the manufacturer (based on the oxidation rate of a target metal surface) [62]. The kinetic energy of the incident ions on the sample can be altered by the sample bias voltage. Applying positive or negative bias allows the retarding or accelerating of the

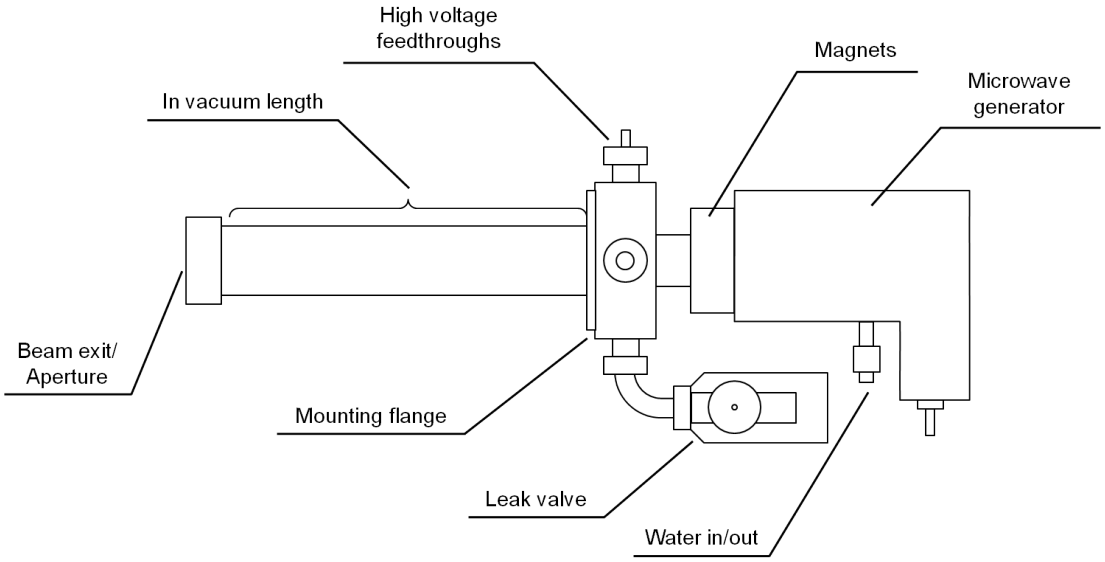

Figure 2.3: Schematic representation of the ECR-MW plasma source

incident cations. The kinetic energy of emitted ions can also be controlled by the potential of the anode for the high-energy region (> 50 eV). In this work, the plasma source is principally used to dope graphene with various nitrogen species, e.g. low-energy ions and/or activated atoms. It helps us to study the mechanisms of NG synthesis.

2.2.4 Molecular source

The molecular source installed in our UHV system consists of two cylindrical molybdenum crucibles. The diameter of the cylindrical molybdenum crucibles is about 2.5 mm, and is placed 50 mm from the sample with an incident angle of 45°. Each crucible has a thermocouple connected at its bottom to monitor the temperature of the molecules loaded inside the crucible. They are heated by two separated hot filaments, or by electron bombardment when polarizing the crucible. A tantalum foil is placed between the two crucibles to screen the thermal radiation of the opposite filament. A manual shutter is placed in front of the molecule source to control the deposition. The deposition rate can be monitored by a quartz crystal microbalance (QCM) placed close to the sample.

2.3 Characterization techniques

In this thesis, a number of analytical techniques have been used with the aim to characterize the final graphene products and to identify important experimental parameters. Most of the studied samples are prepared in our own UHV system and analyzed with the *in situ* instruments. These techniques include angle-resolved inversed

photoemission spectroscopy (ARIPES), low-energy electron diffraction (LEED), Auger electron spectroscopy (AES) and ultra-violet photoemission spectroscopy (UPS). In order to gather complementary information, some analyses are performed with *ex situ* instruments. The main techniques used were X-ray photoemission spectroscopy (XPS), Raman spectroscopy and scanning tunneling microscopy (STM).

IPES and UPS are applied to investigate the electronic structure of the studied graphene. LEED is used to reveal the crystallographic structure (shape and size of the surface unit cell) of the sample surface, especially used to control the preparation of graphene monolayer from the SiC substrate. AES and XPS are used to obtain information of the chemical composition and environments. Raman spectroscopy is used to identify the bonding and the layer thickness of the graphene. STM is used to study the local atomic structure of nitrogen-doped graphene.

One very important parameter to keep in mind, when interpreting the results from the *ex situ* techniques, is that the samples have been exposed to ambient air prior to the measurements. Even though the graphene has low reactivity and can mostly be recovered after a heat treatment in UHV, it still might impact our results when comparing to the literature. Nevertheless, most of the results presented in this thesis are reproducible by repeating the experiment twice or more.

2.3.1 Inverse photoemission spectroscopy

The interest of using IPES is its ability to probe the unoccupied states of the electronic structure of the target material. The working principle is the inverse way of photoemission. First, electrons with a specific kinetic energy are emitted toward the target. After entering the target by coupling with a higher empty state, the electron may lose its energy by emitting a photon filling an unoccupied state close to the Fermi level (E_F) [63]. The emitted photons from this transition are then collected and counted.

There exists two different IPES systems to analyze the inverse photoemission. One by variable incident electron energy with fixed photon energy detector, namely isochromatic mode IPES. The other uses a dispersive grating to analyze varied photon energies by keeping the incident electron energy constant.

Experimental setup

In this thesis, the isochromatic mode of IPES is used. The working principle and the representation scheme of our IPES system are shown in figure 2.4. The electron gun emits electrons toward the sample with a variable energy. The energies used in this thesis are around 6 eV to 22 eV. The electron transmitted to the sample will fall from a higher initial state to a lower unoccupied state closer to E_F. It simultaneously emits a photon with an energy corresponding to the energy difference between the initial state energy (E_i) and the final state energy(E_f). An elliptical mirror then collects and

reflects the photons emitting from the sample, which is placed at one of the focal points of the mirror, toward a bandpass photon detector situated at the other focal point.

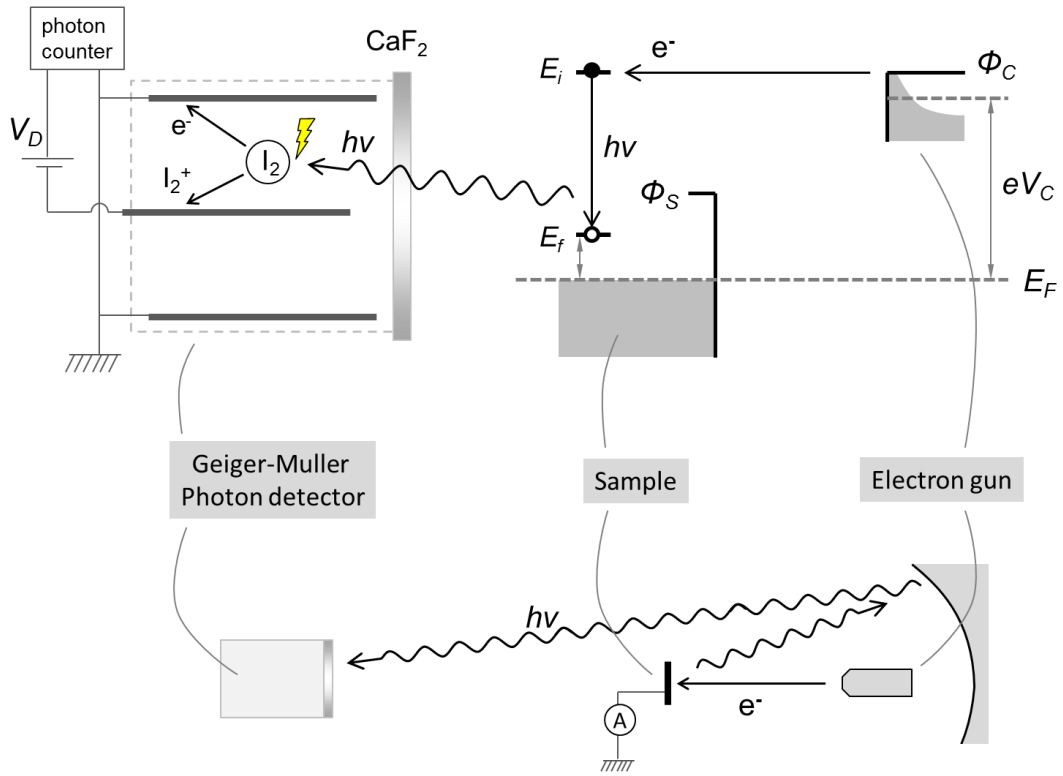

Figure 2.4: The working principle (top part) and the representation scheme (bottom part) of the IPES system.

The photon detector is a Geiger-Müller type detector adapted by Dose for IPES instruments [64, 65]. It consists of a CaF_2 window and a cylinder with a probing stick placing at its axis but electrically isolated from the cylinder. The CaF_2 window, which is transparent for photons below 10.2 eV, works as a low-pass filter. The cylinder is filled with a mix of iodine gas, with a partial pressure equal to the vapor pressure of several iodine crystals, and helium gas of several millibars. If a photon with energy $h\nu > 9.23$ eV enters the cylinder, it will generate the following photochemical reaction:

$$I_2 + h\nu \rightarrow I_2^+ + e^- \tag{2.1}$$

When applying a high voltage of about 300 - 450 V to the probing stick at the center, the electrons created by the ionization reaction will be accelerated toward it, generating a sudden increase of the current that is detectable after amplification. The minimum photon energy required for the reaction thus works as a high-pass filter. Together

with the low-pass property of a CaF_2 window, the entire setup works as a bandpass detector for photons with an energy of 9.7±0.40 eV. The transmission and the ionization probability spectra of the detector are shown in figure 2.5.

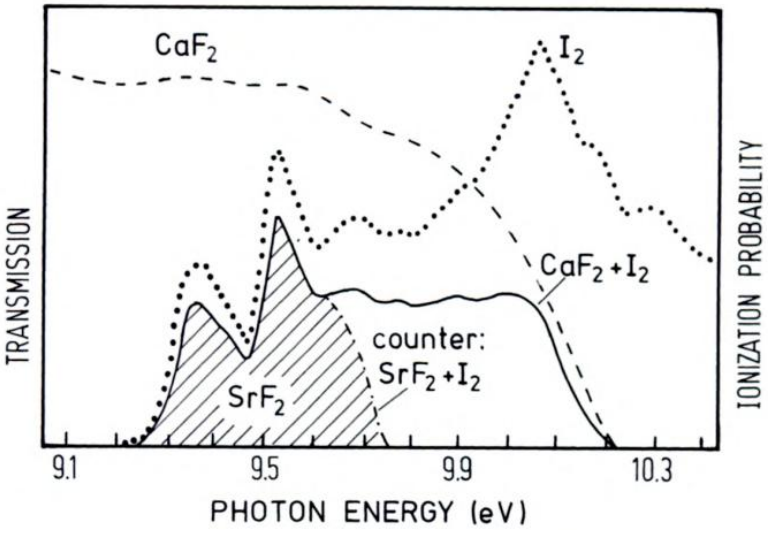

Figure 2.5: The transmission of the CaF_2 window and the ionization probability spectra of I_2 gas of the IPES detector. Figure adapted from Ref. [66].

Data acquisition

The amplified impulsions are counted by a National Instrument NIDAQMx acquisition card, with 32 input ports, 4 analogical output and two 10 Mhz counters. The data acquisition is controlled by a home-made program written in Igor Pro, which is presented in details in the thesis of F. Bocquet [67]. The interface panel and a standard IPES spectrum of graphene recorded by this program are shown in figure 2.6. The photon counts are normalized by the current absorbed by the sample. For the statistics and to reduce the noise, an average of multiple sweeps (5-10 sweeps) is performed for a single IPES spectrum. The total acquisition time for one IPES spectrum is about 0.5 hour.

To analyze IPES spectra, it is important to define the right position of E_F corresponding to the potential of the cathode of electron gun. To do this, we need to measure precisely the starting edge of a IPES spectrum of a metal since the lowest unoccupied state possible is at E_F. It also requires a well prepared metal target. Because if measuring a material with a band gap near the E_F, the starting edge of the spectrum is the bottom of conduction band instead of E_F. Figure 2.7 shows how we define E_F in this work, namely by measuring a clean polycrystalline tantalum foil with IPES. The tantalum sample was prepared by heating to over 1500°C in UHV. The exact position of E_F is defined by the maximum of the first derivative of the spectral starting edge,

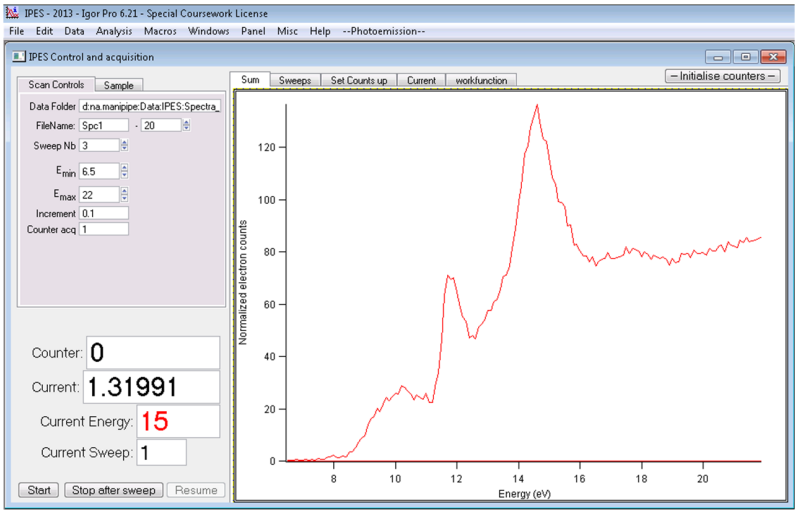

Figure 2.6: The interface of the IPES acquisition program recording a spectrum of PG.

which is 8.5 eV in this case. The work function of the cathode can be extracted from the position of E_F using the following equation:

$$h\nu = E_i - E_f = eV_C + \phi_C \tag{2.2}$$

For $h\mu = 9.7$ eV and $eV_C = 8.5$ eV, the work function of the cathode, ϕ_C, is 1.2 eV.

The presence of a background in the IPES spectra, as shown for example in figure 2.6, is a general effect. It is due to the inverse photoemission caused by inelastic electrons, which have lower initial energies. For the data acquisition, we assume that the E_i equals to the monochromatic incident electron energy defined by the potential of the cathode plus its work function. However, in general case, some electrons emitted by the cathode may undergo inelastic collisions and loose part of its energy before emitting a photon, which cause a diversion of the E_i and generate the background signal.

Characteristics of inverse photoemission

It should be noted that the efficiency of inverse photoemission is much lower than the direct photoemission, in the case of UPS and XPS for example. The efficiency difference of these two techniques can be defined with the following equation, from Ref. [68].

$$r \equiv \left(\frac{d\sigma}{d\Omega}\right)_{IPES} \left(\frac{d\sigma}{d\Omega}\right)^{-1}_{PES} = \frac{\omega^2}{c^2 k_e^2} \tag{2.3}$$

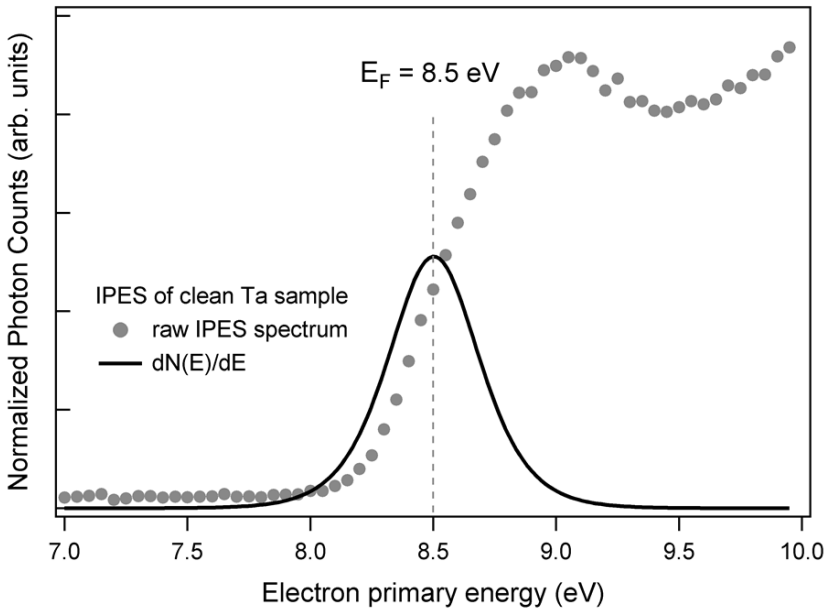

Figure 2.7: Example of defining E_F position with the IPES spectrum of a clean tantalum sample.

In the equation, $\hbar\omega$ is the energy of the emitted photon, c is the light velocity, and k_e the wave vector of the incident electron. For a typical case of inverse photoemission, r, the efficiency ratio of IPES to PES, is as small as about 10^{-5}. In addition, in order to minimize the electron beam dispersion, due to the space charge effect, before it hits the target, the electron gun needs to be placed as close as possible to the target. Hence, the electron gun must be small in order not to shadow photons emitted from the sample but highly-efficient to get sufficient inverse photoemission signal. The electron gun used in our IPES follows the design of Erdman and Zipf [69], as also shown in figure 2.8.

Owing to the conservation of the parallel component of the electron wave-vector when it crosses the surface barrier, the location of the optical transitions can be located in the entire reciprocal space, making IPE a powerful $k_\parallel$-resolved spectroscopy known as KRIPES (or ARIPES) [68]. The ARIPES gives access to a range of unoccupied electronic states, in particular the states close to the Fermi level, and for 2D materials like graphene, it allows to map their energy dispersion $E_n(k)$ throughout the Brillouin zone (BZ), although not completely (see chapter 3). Its angular resolution is obtained by rotating the sample around an axis parallel to the surface plane and perpendicular to the fixed electron beam. In this way, the precise $E(k_\parallel)$ dispersion of unoccupied states can be followed along high-symmetry directions, *e.g.* Γ-K or Γ-M, in the graphene BZ. The reliability of the spectra is verified by performing ARIPES using another configuration, *i.e.* rotating the electron gun around the fixed sample. The precision of

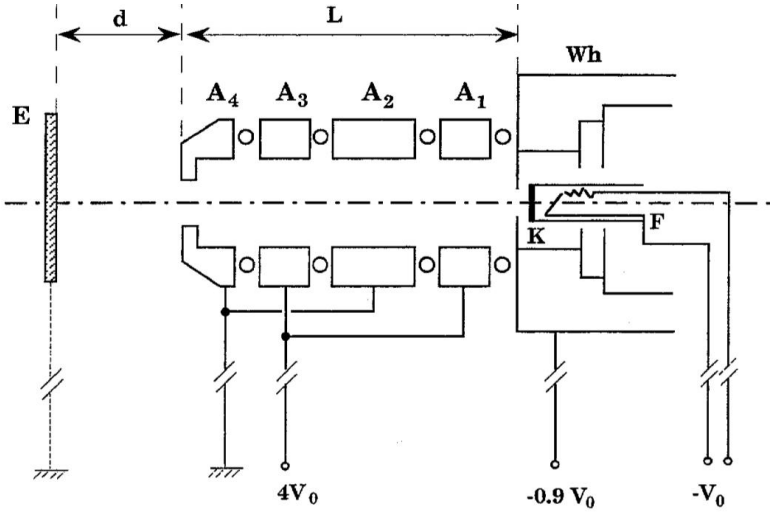

Figure 2.8: Scheme of the electron gun used in our IPES system. The small circles represent the sapphire balls that isolate each electric lens. Figure reprinted from Ref. [67].

the incident angle is 0.1°. As for the azimuth of the sample, it can be adjusted by the diffraction spot of LEED to make sure the incident electrons have the correct lattice wave vector orientation.

It should be mentioned that the effect of a residual magnetic field is especially sensitive in ARIPES experiments. Indeed, the incident low-energy electrons are easily deviated even with the small terrestrial (or environmental) magnetic field, which is in the range of several hundred mG. For example, if an electron with a kinetic energy of 10 eV, emitted toward the sample at 50 mm away, suffers a perpendicular magnetic field of 100 mG, the electron incident angle at the sample will have a deviation of about 2°, which will result in very different surface wave vector $k_{||}$, especially when working at grazing angles. In order to minimize the deviation caused by the magnetic field, three pairs of coils are installed in the three perpendicular axis around our IPES system to compensate the terrestrial and the environmental magnetic field. The residual field at the trajectory of the incident electron is below 5 mG, which deviates electrons of 10 eV by less than 0.1° (a negligible difference of the respective $k_{||}$).

2.3.2 Target current spectroscopy

Target (or total) current spectroscopy (TCS) is another surface spectroscopic technique particularly useful in materials characterization when band-structure effects play a decisive role. It provides information about unoccupied states above the work function. The setup of a TCS experiment is very simple. A beam of low energy (0-20 eV) electrons is directed perpendicular to the studying sample in UHV. The electrons then interact with the sample following an inelastic-scattering model proposed by Komolov

and Chadderton [70]. Finally, the TCS signal is obtained by monitoring the derivative of absorbed (transmitted) current with respect to the incident energy using simple modulation or lock-in amplification techniques.

TCS has several additional advantages, such as low electron energies, low beam current, high surface sensitivity, and low cost [71]. Particularly, the technique has already found application in the studies of work function, chemi- and physisorption, epitaxy, inter-band transitions, densities of states, excitons, impurity atom excitation, plasmons and radiation damage [70]. In practice, TCS is often coupled with IPES because the low-energy-providing electron gun of IPES can also be used for TCS measurements. It provides complementary information to IPES technique, such as those listed above.

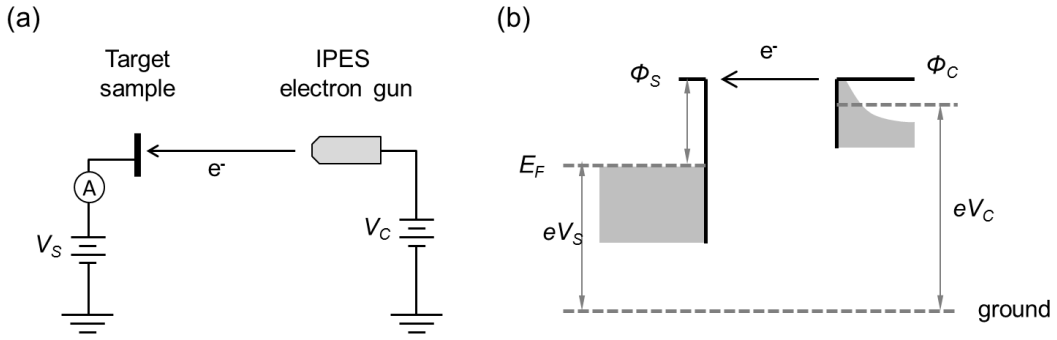

Figure 2.9: (a) The sketch of the setup for work function measurement by TCS. (b) The representative energy diagram of the measurement setup.

In this thesis, TCS is principally employed to measure the work function of the studied samples. The representative sketch of the TCS measurement setup is shown in figure 2.9a. Due to low emission current of the electron gun at low primary energy of 2-5 eV (the region where the work function locates), both the sample potential (V_S) and the electron primary energy are brought to higher potential during the measurement. Here, the V_S is brought to about 9 V. Thus, the normal incident electrons, with primary energy (eV_C) of 11-14 eV, are retarded to lower incident energy (2-5 eV) during the measurement. A graphite surface (multilayer graphene) is used as a reference for the work function measurement by TCS. A representative spectrum, as recorded, is shown in figure 2.10, where the absorbed current starts to increase at about 12.3 eV. In this thesis, the value of work function is determined by the location of the first derivative maximum of absorbed current *(dI(E)/dE)*, which is 12.4 eV in this case. The actual value of the work function can be calculated with the following equation derived from the energy diagram of figure 2.9b.

$$\phi_S = eV_C + \phi_C - eV_S \tag{2.4}$$

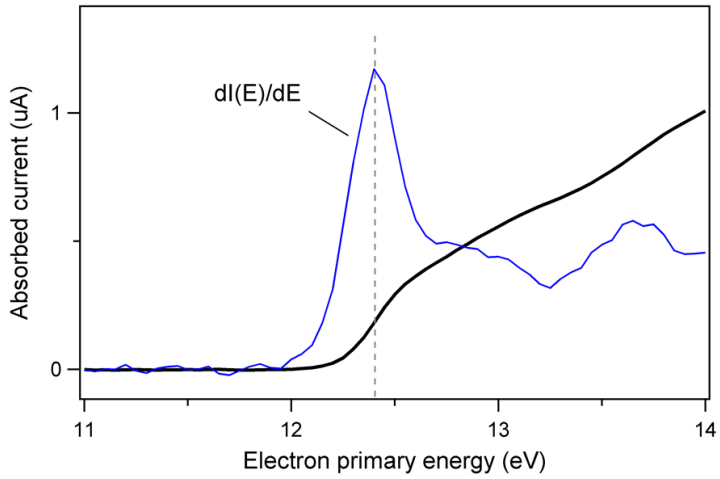

Figure 2.10: Typical TCS spectrum of PG at the low-energy threshold. The thin blue curve shows the first derivative of the absorbed current wrt. the primary energy.

For V_C = 12.4 V, ϕ_C = 1.2 eV (obtained from E_F measurement of IPES) and V_S = 9.0 V, the work function of the graphite sample ϕ_S is 4.6 eV, in good agreement with the value reported in the literature [72].

2.3.3 Low energy electron diffraction

Low energy electron diffraction (LEED) is one of the most simple and widely spread techniques for the determination of the surface structure of crystalline materials. Different to the common diffraction methods used for the study of crystal lattices, e.g. x-ray diffractometer (XRD), LEED uses, as emission source, a beam of low energy electrons in the range of 20 to 200 eV, which couples more importantly with the surface structure. The diffracted electrons are then collected and visualized by a fluorescent screen, which shows the diffraction pattern of the material surface.

The LEED results can be analyzed in two ways. The first is a qualitatively way, in which one measures the position of the diffraction spots with respect to the primary electron energy. The dimension and the rotation alignment of the surface crystalline structure can be revealed using the Bragg's Law ($2dsin\theta = n\lambda$) and the de Broglie hypothesis ($\lambda = h/\sqrt{2mE}$). The second is the quantitative way, which analyzes the intensity variation of diffraction spots with respect to the primary energy ($I_{LEED} - V$). When a stacking of different crystalline layers is close to the surface, it produces multiple scattering, where each layer can be identified by its different $I_{LEED} - V$ curves.

The reason that LEED possesses a high surface sensitivity is because low energy electrons interacts much strongly with the material than x-ray. Thus, the information

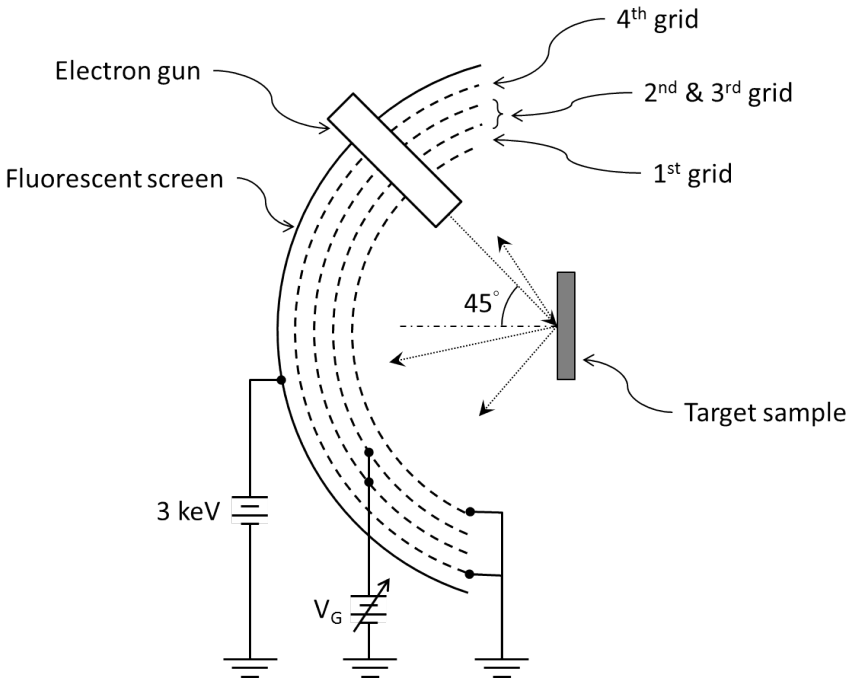

Figure 2.11: The diagram of our LEED setup, showing the electron gun, the three grids and the fluorescent screen.

gathered from the diffracted electrons mostly comes from the surface structure. The penetration of the electrons can be derived by calculating the decay of the primary electron beam energy I_0, as expressed as below.

$$I(d) = I_0 \times e^{-d/\Lambda(E)} \tag{2.5}$$

Here d is the penetration depth and $\Lambda(E)$ denotes the inelastic mean free path, defined as the traveling distance of an electron before its intensity decays by the factor $1/e$. For electrons with primary energy (E_p) of 20-200 eV, they have a low penetration depth (or short inelastic mean free path) of about 5-10 Å, that can be dependent of the target material [73].

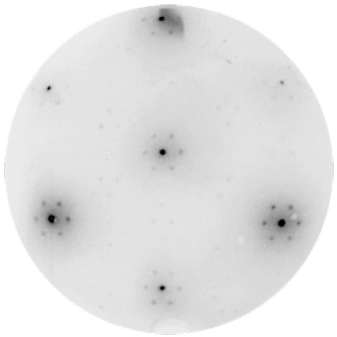

Figure 2.12: A typical LEED diffraction pattern from a sample of monolayer graphene on SiC. The image is taken at a primary electron energy = 100 eV.

The diagram of our LEED setup is shown in figure 2.11. The entire LEED is installed in the UHV analysis chamber. A series of hemispherical grids and a fluorescent screen are placed in front of the sample. An electron gun pierces through these grids and emits electrons toward the target at an incident angle of 45°. A retarding field is provided by the second and third grids to repulse undesired secondary electrons. The diffracted elastic electrons are finally collected by the fluorescent screen polarized at ∼3 keV. A charged-coupled device (CCD) camera is placed behind the fluorescent screen (outside the UHV chamber) to record the diffraction pattern. A typical LEED result recorded by CCD camera from the graphene on SiC is shown in figure 2.12. It shows a bright (1×1) pattern of the graphene with faint $(6\sqrt{3} \times 6\sqrt{3})R30°$ spots from the BLG/SiC interface.

Riedl *et al.* have reported that the thickness of the graphene can be determined by semi-quantitatively analyzing the LEED image of the graphene on SiC(0001). As shown in figure 2.13, the intensity of the diffraction varies with the incident electron energy, and also with the surface structure. Thus, at a particular primary energy (E_P), one can identify the number of graphene layer(s) by measuring the relative intensity between the graphene and the SiC diffraction spots. With E_P=126 eV at normal incident,

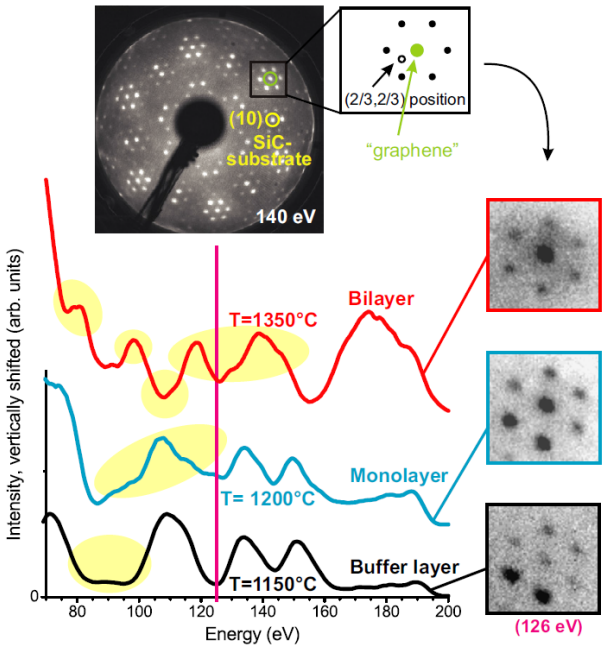

Figure 2.13: LEED spot intensity spectra *wrt.* primary energy for different numbers of epitaxial graphene layers: BLG, monolayer and bilayer graphene. Figure reprinted from Ref. [10].

the MLG on SiC shows an equal intensity for both diffraction spots. However, these results cannot be applied directly to determine the graphene thickness using our 45° incidence LEED setup (see section 3.1.1). The 45° incident angle of our LEED provides a more surface sensitive property, and also gives slightly different results compared to the literature that principally apply normal incident electron, especially for these quantitative analysis.

2.3.4 Auger electron spectroscopy

The Auger electron spectroscopy (AES) is an analytical technique used specifically to study the chemical composition of surface layers of a sample using the Auger effect. The latter is an electronic process of a exited atom with an empty core state (so called a core hole), which is filled by an outer shell electron and emits another outer-shell electron. More specifically, as shown in figure 2.14a, a surface atom is excited by an incident electron, typically with an energy in the range of 1-10 keV, removing a core shell electron from the system and leaving a core hole. The core hole is then filled by an electron of the outer shell through an interstate transition, loosing energy equal to the energy difference between the two states. This transition energy can be coupled to a second outer-shell electron, which will be emitted from the atom if the available energy is greater than the orbital binding energy. This emitted electron, the so called Auger electron, gives information about the state-to-state transitions of the atom by analyzing its energy, which permit the identification of the chemical nature of the atom.

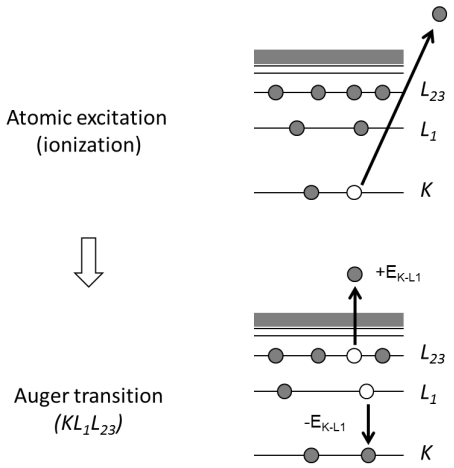

Figure 2.14: Diagram of the working principle of Auger effect. Example of the KL_1L_{23} Auger transition.

The Auger effect requires at least three electrons, so systems with fewer electrons, such as H and He, cannot emit Auger electrons. Moreover, to identify the different transitions involving the Auger process especially in heavy atoms, the Auger process is named after the three involved shells. For example, if the first exited electron is from the core shell, K, the transiting and emitting electrons are from L_1 and L_{23}, the Auger transition is called KL_1L_{23} transition, as also shown in figure 2.14b. The kinetic energy of this Auger electron (KE_{Auger}), which does not depend on the kinetic energy of the incident electrons, can be expressed with the following equation.

$$KE_{Auger} = E_K - E_{L1} - E_{L2} \tag{2.6}$$

Typically, the energy of the Auger electrons are in the range of 50 eV to 3 keV, and at these values, the escape depth of the electrons are localized within a few nanometers of the sample surface, giving the surface sensitivity of AES. There are two common ways to analyze the energy of the emitted Auger electron. One is using a cylindrical mirror analyzer (CMA) with an electron gun placed at its axis. In the detection unit, Auger electrons are multiplied by an electron multiplier and the signal is sent to data processing electronics. The other one is to use the hemispherical grid of LEED as retarding field analyzer and collecting Auger electrons using the outer screen.

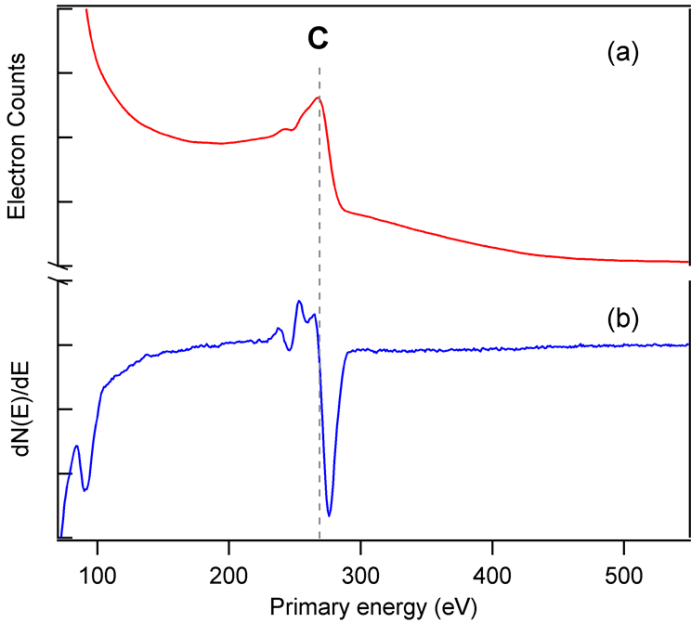

Figure 2.15: (a) AES spectrum of a MLG on SiC(0001) in electron counts *wrt* primary energy. (b) The same spectrum in differential form ($dN(E)/dE$).

The peak position of Auger electron counts *wrt* primary energy gives the energy of a particular Auger transition, which may be addressed to a particular atom, as shown

in figure 2.15a. The peak area leads to the concentration of the atom. Though, the AES spectra are generally expressed in the differential form: $dN(E)/dE$, which is the first derivative of the number of Auger electrons *wrt* the electron energy, as shown in figure 2.15b. This is because it is possible to measure the spectra directly in this form, and also gives a better sensitivity for detection. In $dN(E)/dE$ the energy of the Auger transition is the mean of the positive and negative peaks position. Though, in practice, the position of the negative peak is given. As for the composition ratio of the atoms, it can be derived from the intensity difference between the two peaks. However, the Auger effect is not the only mechanism available for atomic relaxation. The total transition rate, after the ionization of the atom, is a sum of the non-radiative (Auger) and radiative (photon emission) processes. To calculate the precise atomic concentration, the Auger electron yield for at specific incident energy should be taken into consideration. Generally, the Auger yield decreases with increasing atomic number (Z), and the x-ray yield becomes greater than the former for heavier atoms. For K-level based transitions, Auger effects are dominant for $Z < 15$ while for L- and M-level transitions, AES data can be measured for $Z \leqq 50$.

In our system, the AES is coupled with LEED, using a four-grids retarding field analyzer as shown in figure 2.11. The same electron gun is employed for AES by increasing the primary energy from 100-200 eV to 1-3 keV. The Auger electrons are analyzed using the potential of the second and third grid as a high-pass filter and the screen of LEED, positively polarized, as electron collector. The collecting current is amplified and converted to voltaic signal by a home-made pre-amplifier (figure 2.16), and the modulated signal is then analyzed using a lock-in amplifier. Differently to the CMA-based AES, this retarding field type AES gives a spectrum of emitted current. The first derivative of the spectra gives us the number of emitting Auger electron, and the second derivative (2f) gives the differential form of the AES signal, $dN(E)/dE$.

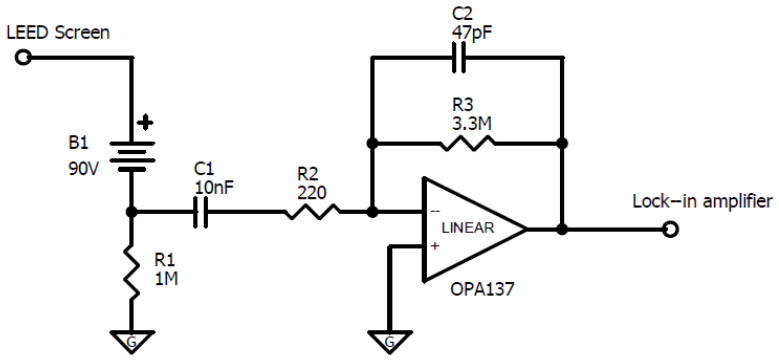

Figure 2.16: Circuit diagram of the home-made pre-amplifier for AES

During this thesis, we have changed the entire set of controlling and signal-analyzing electronics, which enabled us to add an interface program based on Igor to control the

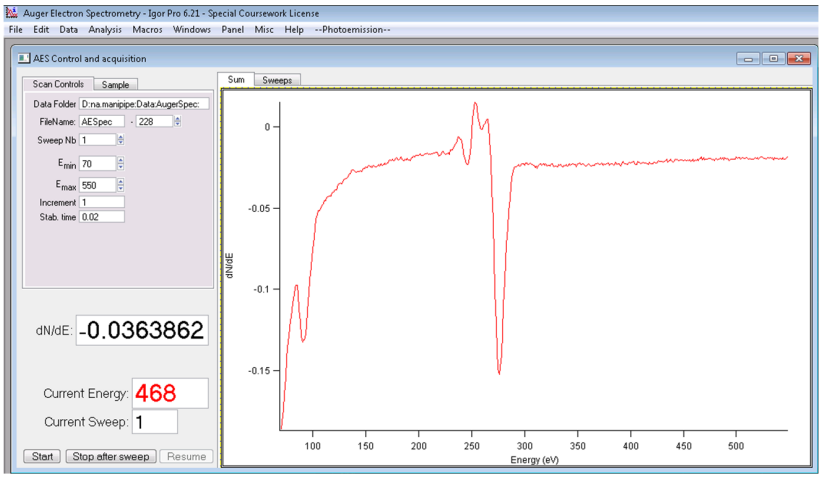

Figure 2.17: The interface of the AES acquisition program recording an AES spectrum of PG on SiC

AES system and record AES spectra through the computer, similar to those used in IPES and mass spectroscopy. A new CeB_6 cathode and the home-made pre-amplifier were also installed to obtain a better signal-to-noise ratio. The former provides a high incident current of 3-10 μA on the sample. The later amplify the signal of the order of $\sim 10^3$. The interface program and a typical AES spectrum of graphene on SiC is shown in figure 2.17. Details on the AES acquisition program can be found in appendix (p. 157).

2.3.5 Ultra-violet Photoemission Spectroscopy

The ultra-violet photoemission spectroscopy (UPS) is a commonly used technique to study the electronic structure of materials. Complementary to IPES revealing unoccupied states, it measures the occupied states of a material. It employs UV photons to excite valence band electrons of the material and obtains its valence band structure by analyzing the energy of these photoelectrons.

Many physical properties of a material can be deduced from its electronic structure making UPS and IPES very useful for the studies of nanomaterials. The advantage of performing both IPES and UPS *in situ* is to obtain a complete electronic structure with a minimal contamination.

The UPS, in our system, employs helium plasma as UV light source. By varying the plasma intensity, it is possible to obtain either a He(I) emission ($h\nu = 21.2$ eV) or a He(II) emission ($h\nu = 40.8$ eV). The UV light is directed on the target sample, which

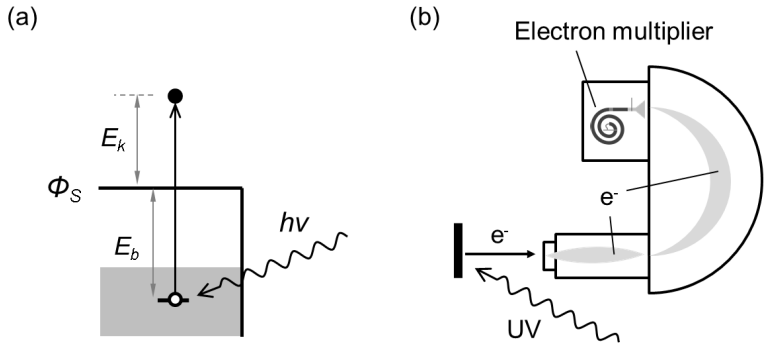

Figure 2.18: (a) The working principle of UPS. (b) The experimental setup of the UPS and the trajectory of photoelectrons.

incident angle is negligible for a momentum-resolved UPS since the momentum of a photon is negligible in a photoemission process. Though, the UPS spectra may still be affected due to prolongation effects and photoemission diffraction effects. When a UV photon couples with the sample, an atom is ionized and emits a photoelectron, which possess a kinetic energy E_k expressed by the equation:

$$E_k = h\nu - E_B \tag{2.7}$$

Here $h\nu$ is the energy of the incident photon energy, and E_B is the binding energy *wrt* vacuum level of the initial state of the photoelectron. A representation of this process is shown in figure2.18a. The emitted photoelectron is then collected, focused and retarded by a series of electrostatic lenses before entering the hemispherical analyzer. The electron is finally energy resolved and counted by a hemispherical analyzer with an electron multiplier at the exit. A schematic view of our UPS setup is shown in figure 2.18b. Details on the pre-amplifier and the interface program can be found in to the work of F. Bocquet [67]. A micro-channel plate detector can be mounted instead of electron multiplier, which is usually found in the case of angle-resolved photoemission spectroscopy (ARPES). It enables the resolution of energy (E_k) and wave vector ($k_{\|}$) of photoelectrons at the detection unit. In such configuration, a large region of the electronic structure of the material can be acquired simultaneously.

However, despite numerous trials, our UPS is still unable to work correctly due to a delicate issue. To reduce the effect of the magnetic field on electron trajectory in IPES, a magnetic field compensation system is used. A mu-metal shield that protects the hemispherical analyzer from magnetic fields was also removed since it perturbs the local magnetic field of the IPES system. Nevertheless, the magnetic field inside the hemispherical analyzer is not perfectly compensated which may cause the malfunction

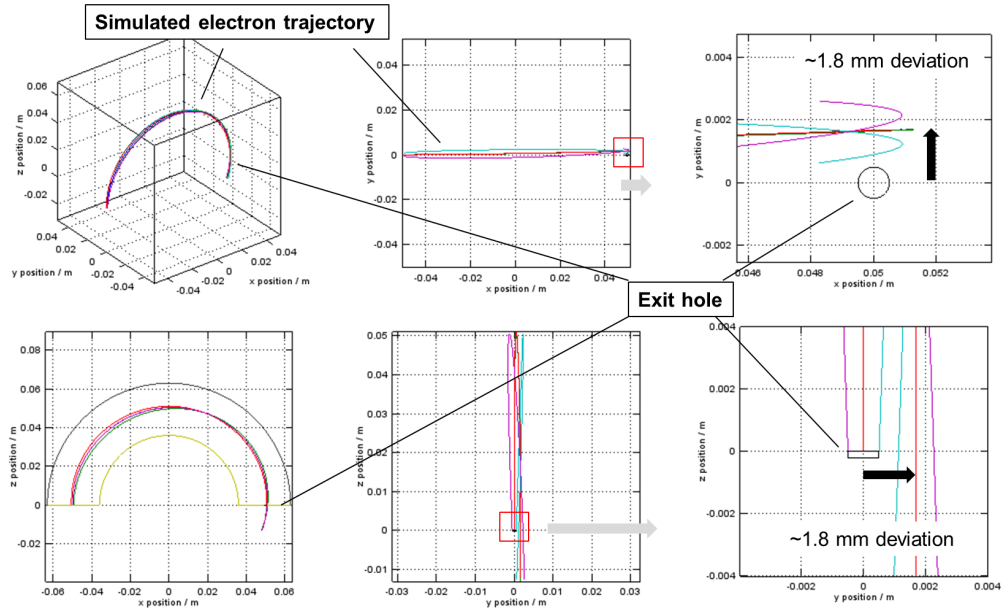

Figure 2.19: Simulated electron trajectory inside a hemispherical analyzer under a residual magnetic field of $B_x = 50$ mG, $B_y = 50$ mG, $B_z = 0$ mG: The pass energy is 25 eV, mean radius of the analyzer is 50 mm.

of the analyzer since it is even more sensitive to the magnetic field. A simple simulation of the electron trajectories inside the hemispherical analyzer with the presence of a residual magnetic field is shown in figure 2.19. For a residual magnetic field of 50 mG and pass energy of 25 eV inside the hemisphere, the photoelectrons that were expected to come out from the hemisphere will actually deviate 1.8 mm away from the exit hole. This explains why no electron can be counted while every element of the analyzer works correctly. The details of the simulation program are described in appendix 7. To resolve the problem, we have planned to optimize the magnetic field compensation, or to install an outer hemispherical analyzer, away from the IPES, to enable the installation of a mu-metal shield, which is not yet accomplished by far.

2.3.6 X-ray photoemission spectroscopy

The working principle of X-ray photoemission spectroscopy (XPS) is similar to the UPS counterpart, except that a X-ray light source is used instead of UV. The energy of the photons is much higher in the case of XPS, *e.g.* Al Kα X-ray with photon energy of 1486.7 eV. These high-energy photons permit the ionization of core level electrons, which give quantitative information about the elemental compositions and their chemical states. The analysis of these core-level electrons uses the same hemispherical analyzer and signal-acquiring electronics as for UPS. In our case, an Omicon EA 125 hemispherical analyzer is employed for most of the measurements.

Some issue should be paid attention to in XPS measurements. When analyzing the element composition, the photoemission cross-sections of different elements should be taken into consideration. To increase the energy resolution, a monochromator can be added in the source and different parameters can be applied for the hemispherical analyzer, such as pass energy and entrance/exit slits dimension. To increase the sensitivity for a particular sample or to avoid the staking of AES and XPS peaks, different X-ray sources can be applied, such as magnesium X-ray at 1253 eV, or much others using synchrotron radiation source. In this thesis, we used the common Al Kα X-ray at 1486.7 eV, and the XPS spectra are presented *wrt* the binding energy, taking E_F as the reference.

It should be noted that, all the XPS setups involved in this thesis are located in different UHV systems. That means that all the XPS measurements presented in the following are performed *ex situ*. Since it requires to take out the sample to ambient air before entering in the other one, a thermal annealing of the sample (at $\sim 550°C$ in UHV) is generally proceeded before the XPS measurements to remove any physisorbed impurities contaminated during the transfer.

2.3.7 Raman Spectroscopy

Raman spectroscopy is a vibrational spectroscopy technique providing information about the chemical bonding. It is based on inelastic scattering (also called Raman scattering) of a monochromatic laser radiation, usually in the near-infrared, visible

or near-ultraviolet range. Differently to the common infrared spectroscopy (IR) obtaining information from the direct absorption of the vibrational states, the Raman spectroscopy measures the energy difference of the incident photon and the same after inelastic scattering. Since it is a scattering-based technique, the biggest advantage of Raman spectroscopy is that a minimum sample preparation, and ambient air environment is required.

When an incident photon couples with the material, there are two possible inelastic scattering processes, Stokes and anti-Stokes, which intensities are much weaker than the elastic scattering (Rayleigh scattering). Stokes radiation occurs when the incident light looses energy, and anti-Stokes is when it gains energy from the system related to the vibrational energy levels in the electronic ground state of the system. The anti-Stokes radiation is even less intense than Stokes radiation because only molecules that are vibrationally excited prior to irradiation can give rise to the anti-Stokes line(s). Hence, in Raman spectroscopy, the Stokes scattering are usually measured. The signal might be disturbed if the sample shows strong fluorescence at the incident wavelength, which can be avoided by selecting a proper incident light. The obtained Raman spectrum are usually expressed in the wavenumber difference between Rayleigh (elastic) and Stokes (inelastic) scattering, also known as Raman shift.

Raman spectroscopy has been widely used in the characterization of graphene due to its simple, intense and largely informative vibrational modes [74, 75]. It is especially applied to determine the thickness and the quality of graphene layer(s) [74]. Figure 2.20a shows a typical Raman spectrum of the edge of a monolayer graphene, which shows the three most intense Raman process, D, G and G' (or 2D). The origin of these processes can be described with the sketch shown in figure 2.20b. First, the G-band process, located around 1580 cm^{-1}, is associated with the doubly degenerate in-plane optical phonon mode (E_{2g}) at the Brillouin zone (BZ) center, Γ. It is the sole first order Raman scattering process in graphene. The D- and 2D-bands, appearing around 1350 and 2700 cm^{-1}, originate from second-order Raman processes, as shown in figure 2.20b. They come from in-plane transverse optical phonons (iTO) near the K point of BZ, specifically the breathing modes of the hexagonal ring [75]. The D-band requires the activation of a defect and a iTO phonon. As for the 2D-band, the process is originated by two phonons with opposite wave vectors, where momentum conservation is satisfied. No defects are required for the activation of 2D-mode, thus it is always present in high quality graphene. The number of graphene layers is usually determined by either the position of the 2D-band (shifting due to the splitting of 2D mode for multiple layers) [74], or by the intensity ratio of 2D- and G-bands, $I(2G)/I(G)$. The quality of the graphene can be verified by the vicinity of D-band. There are also other modes with much less intensity, which give additional information about defects and other properties of graphene presented in the literature [75, 76].

In this thesis, the Raman spectroscopy is performed at IM2NP at University of Toulon with the support of Prof. Valmalette. The spectrometer is a HORIBA Jobin Yvon's LabRAM 800HR system, which can be coupled with an atomic-force microscopy

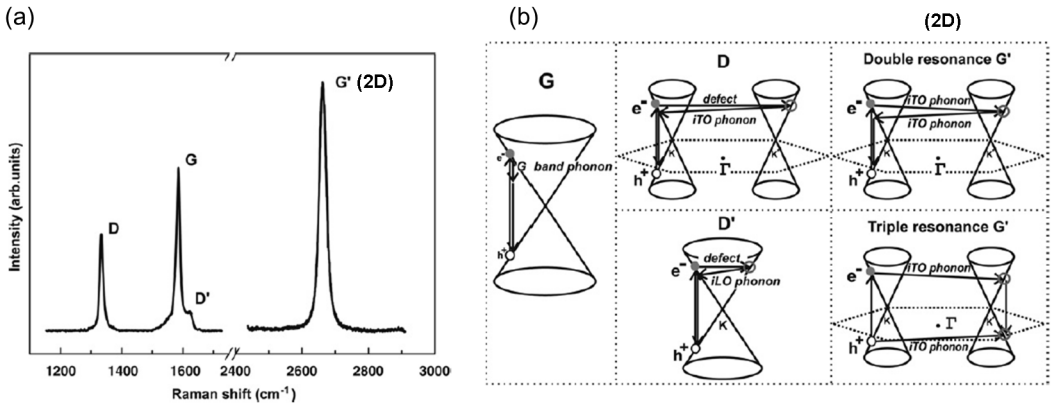

Figure 2.20: (a) Standard Raman spectrum at the edge of a graphene monolayer. (b) Principal phonon modes in graphene. Figure reprinted from Ref. [75].

(AFM) to perform tip-Enhanced Raman Spectroscopy. Though, only the standard Raman spectroscopy was used in this work. All the Raman spectra are obtained using a 514 nm argon laser with an incident power of 360 μW at the sample.

2.3.8 Scanning tunneling microscopy

The Scanning tunneling microscope (STM) was invented by G. Binnig and H. Rohrer in 1981, who earned the Nobel Prize of physics in 1986 for the development of this powerful instrument. It is an electronic microscope based on the concept of quantum tunneling. It gives access to the imaging of the studied surface at an atomic scale. The surface of the material is imaged using a scanning tip, usually made of tungsten or Pt/Ir alloy, brought very close to the surface, typically in the 4-7 Å range. Information is usually acquired from the position of the scanning tip at constant tunneling current and electric potential (bias) between the surface and the scanning tip.

Three important elements are required for the realization of a good STM instrument. First, the apex of the tips needs to be, ideally, only one atom thick to give the atomic resolution by interacting with the atoms of the surface. Second, the proper use of piezoelectric material, usually made of PZT (Lead Zirconium Titanate), enables us to control the XY and height position of the tip and to attain the atomic precision. And last, an electronics with a feedback loop to acquire information and to control the tip simultaneously while scanning the surface, for example when working in constant current mode imaging. A vibration-free (or spring-supported) stage is also important since a minimum vibration of the stage will cause the vibration of the tip, reducing the imaging resolution.

The STM has additional functions such as the manipulation of surface atoms/-molecules and the measurement of the local electronic structure at atomic scale. Dif-

ferent methods of manipulating the surface have been proposed, such as moving atoms or molecules on the surface and generating a reaction at a precise location [77]. The technique to measure the local electronic structure is called scanning tunneling spectroscopy (STS). It is used to probe the local density of electronic states (LDOS) and the band gap of the surface at the atomic scale. The spectroscopy is done either by performing I-V measurement at a particular location and tip distance, or by acquiring multiple constant-current images at many different tip-sample biases. The tunneling conductance, dI/dV, is derived from the relation of the tunneling current versus tip-sample bias. For ideal assumptions, the tunneling conductance is directly proportional to the sample DOS. Thus, a plot of LDOS as a function of energy can be obtained by STS.

The STM have been recently used for the study of surface- and nano-science, because it can actually "visualize" an atomic structure and even manipulate local species as small as an atom. In this thesis, the STM is principally used to study the defects created by the incorporation of nitrogen in the graphene layer. The STM/STS experiments are performed *ex situ* at IS2M in the team directed by Dr. Laurent Simon, the principal coordinator of the "ChimiGraphN" project. The measurements are carried out at a low temperature of 77K using a cryogenic LT-STM. Prior to any measurements, the studied samples are annealed at 800°C (or higher) to remove any adsorbed impurity on the surface. The STM is controlled via Nanonis SPM Control system, and the STS measurements are assisted by a SignalRecovery 7280 lock-in amplifier.

Chapter 3

Pristine graphene

In order to study the functionalization of graphene, it is very important to carefully prepare and characterize the pristine samples in the first place. Since the graphene consist in a layer of carbon atoms in sp^2 configuration forming a π-conjugated honeycomb structure, methods sensitive to these properties are usually applied to detect the presence of graphene. These methods include structural analysis (*e. g.* LEED and STM), chemical analysis (*e. g.* AES and XPS) and electronic properties measurements(*e. g.* IPES or ARUPS).

In this chapter, the fabrication of pristine graphene samples and their characterization using the techniques presented in chapter 2 are summarized. It should be noted that the analysis results in this work may be somewhat different to the literature due to actual experimental setups and the details of the preparation procedure. The investigation of the epitaxial graphene prepared on the Si-terminated SiC(0001) and C-terminated SiC(000$\bar{1}$) surface are both presented. In section 3.2, we show that the graphene grown on SiC(000$\bar{1}$) is not the most appropriate for our following study due to the various orientations of the top graphene layer that complicate the angle-resolved IPES measurements. It is also difficult to control the actual graphene coverage and thickness on C-face. Thus, the principal investigation in this thesis pertains to the epitaxial monolayer graphene on the SiC(0001) surface.

3.1 Graphene on Si-terminated SiC(0001) surface

As introduced in sections 1.1.3 and 2.2.1, the surface of SiC(0001) demonstrate different reconstructions as we deposit and sublimate Si atoms from the surface at increasing temperatures until the formation of graphene (or graphite). To ensure the quality of the epitaxy, the preparation of the graphene on SiC(0001) in UHV is proceeded step by step following these reconstruction stages, as shown in figure 3.1. We first obtain a (1×1) LEED image by degassing the bare SiC(0001) sample at $\sim$500°C, namely $(1 \times 1)_{SiC}$. The sample is then annealed at 850°C under a Si flux until the

formation of the (3×3) surface structure. This Si-rich surface is constituted by a Si ad-layer covered with some organized Si tetramers on the top of the outermost Si-C bilayer of SiC. At higher annealing temperature of about 950 °C, a moderately Si-rich reconstruction can be obtained showing a $(\sqrt{3} \times \sqrt{3})R30°$ diffraction pattern (figure 3.1). It is constructed by Si adatoms occupying T_4 sites on the top of the first Si-C bilayer. Finally, by a sequential annealing to ∼1050°C and ∼1150°C for about 10-15 min each, we obtain a $(6\sqrt{3} \times 6\sqrt{3})R30°$ reconstruction (the BLG), and the (1×1) structure of graphene (denoted as $(1 \times 1)_G$ in the following), respectively. The results of the resulting pristine graphene (PG) on SiC(0001) are discussed in the following.

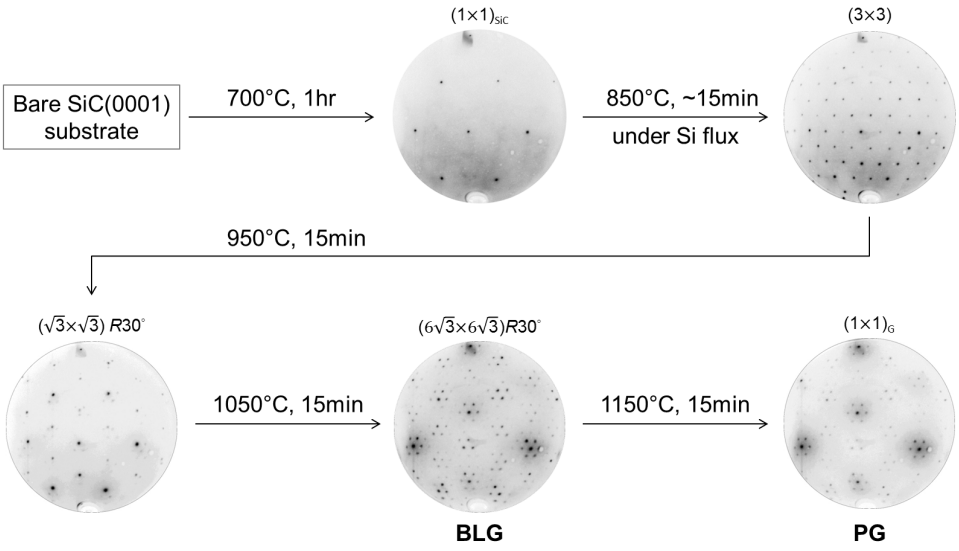

Figure 3.1: Sketch of the process flow of graphene preparation on SiC(0001) by thermal annealing in UHV. Each step is represented by its surface reconstruction revealed by LEED (E_p = 100 eV).

3.1.1 Determination of the graphene thickness

In order to keep the graphene away from impurities during the analysis and before the following functionalizing process, *in situ* analyses are preferable. In this thesis, we use *in situ* LEED, IPES and AES for the preliminary characterization of the pristine graphene. These results are compared to *ex situ* methods for complemented characterization of the epitaxial graphene samples.

Detecting graphene with *in situ* LEED

The actual structures of the epitaxial graphene samples are revealed by LEED. Figure 3.2 shows the LEED images of the SiC(0001) surface annealed at 1050°C for 15 min, at 1150°C for 15 min, 20 min and 25 min, respectively. These four samples are later identified as BLG, one monolayer graphene (1MLG), 2MLG and 3MLG, using Raman spectroscopy and IPES. Sketches of their structure are shown in figure 3.3 for information. As shown in figure 3.2, the $(1 \times 1)_G$ spots of graphene are observed as soon as one obtains the $(6\sqrt{3} \times 6\sqrt{3})R30°$ reconstruction. This is the evidence that the $(6\sqrt{3} \times 6\sqrt{3})R30°$ reconstruction is the "first" graphene layer forming on SiC(0001) surface, although it is strongly bound to the SiC substrate. The $(6\sqrt{3} \times 6\sqrt{3})$ diffraction pattern is due to the commensuration between BLG and SiC. As we will show later, this graphene layer has the right lattice parameter but does not exhibit the electronic properties of an isolated graphene. Thus, it is called the BLG [16].

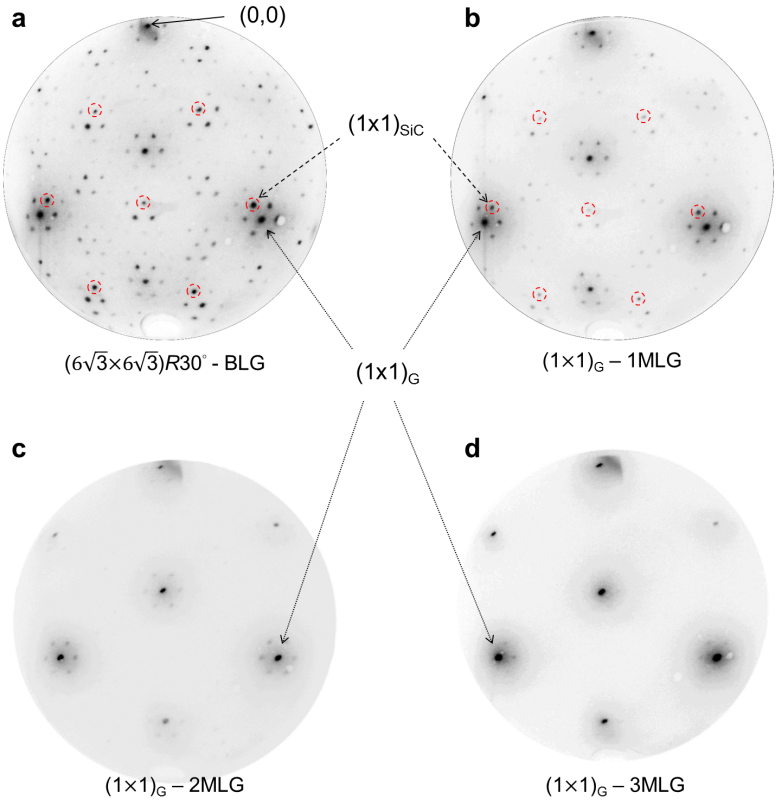

Figure 3.2: LEED images (E_p = 100 eV) of (a) a BLG, (b) a MLG, an estimated (c) 2MLG and (d) 3MLG on SiC(0001). The $(1 \times 1)_G$ spots in each image are pointed out by the arrows. The $(1 \times 1)_{SiC}$ spots are indicated by dashed circles.

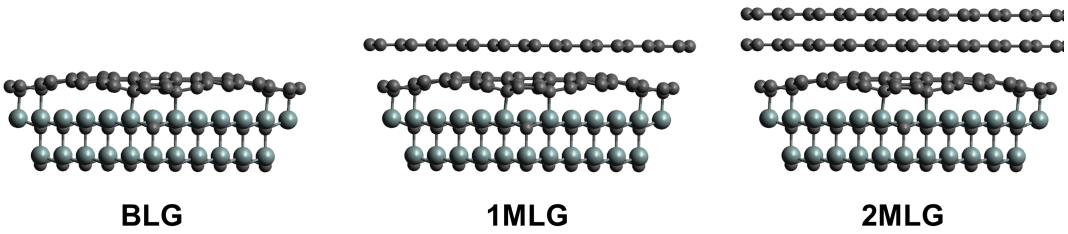

Figure 3.3: Structural representation of BLG, 1MLG and 2MLG on SiC(0001).

The $(1 \times 1)_G$ spots are enhanced with the formation of isolated monolayer graphene (MLG), as shown in figure 3.2b. They are further enhanced with increasing graphene thickness, while the $(6\sqrt{3} \times 6\sqrt{3})R30°$ pattern simultaneously vanishes. As reported in the literature (see section 2.3.3), the relative intensity between the $(1 \times 1)_{SiC}$ and $(1 \times 1)_G$ spots indicate the actual number of graphene layer [16]. However, due to the peculiar incident angle of 45° of our LEED (see section 2.3.3), we cannot directly apply these former results as references to determine the graphene thickness with our LEED. Figure 3.2c and d show the LEED images of the 2 and 3 monolayer graphene (2MLG and 3MLG) samples, prepared by a slightly higher temperature and longer annealing. The intensity of the $(1 \times 1)_G$ spots is even more pronounced than for MLG sample, but is difficult to quantify using image processing. The thickness of these two samples is determined by the assistance of *in situ* IPES and *ex situ* Raman spectroscopy analysis, providing a more precise determination of graphene thickness, as discussed below. It should be noted that no other diffraction spots emerges with increasing thickness other than the original $(1 \times 1)_G$ spots from the first layer. This indicates that the graphene layers grown on SiC(0001), the Si-terminated face, are azimuthally oriented to the same direction, unlike the graphene layers grown on SiC$(000\bar{1})$, which have multiple orientations, as discussed in the next section.

Determination of the graphene thickness using IPES and Raman spectroscopy

Being very sensitive to the outer surface layer, the IPES allows a reliable determination of the graphene thickness. Though, it would need to be calibrated using another method to ensure its accuracy. In this work, the Raman spectroscopy, which is commonly used for the determination of graphene thickness, is taken as a reliable reference for the thickness estimation using IPES. However, the analysis of the Raman spectra of graphene on SiC is more complicated than for the graphene on other substrates. Taking the Raman spectrum of PG on SiC(0001) for instance, the Raman modes of the SiC substrate are very complex and superposed with some Raman modes of graphene, as shown in figure 3.4. More precisely, the G and D bands of graphene (see section 2.3.7)

are superposed with the Raman features of the SiC substrate. Fortunately, the 2D band is located out of the prominent SiC features, at ∼2720 cm^{-1} for PG. In addition, the Raman signal contributed by SiC can be mostly subtracted from the graphene/SiC one, leaving only the Raman signal of graphene layer. As shown in figure 3.4, the subtracted Raman spectrum shows a well-developed G band at ∼1590 cm^{-1}, which was nearly undetectable in the raw spectrum. This method was first proposed by Röhr *et al.* [56], and followed by the study of Lee *et al.* to determine precisely the graphene thickness on SiC using the 2D band in the graphene Raman spectrum, as shown in figure 3.5 [78].

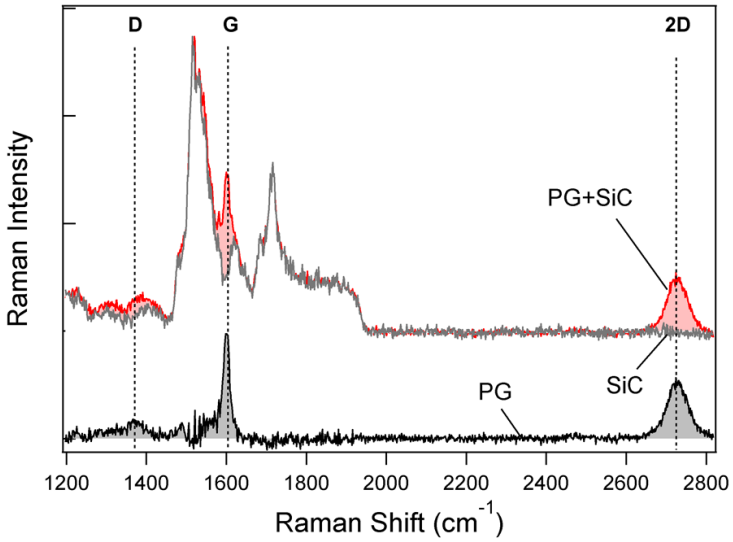

Figure 3.4: Example of the Raman spectra of PG obtained from the subtraction of the raw spectrum (PG+SiC) and the spectrum of the SiC substrate.

Figure 3.6a shows the Raman spectrum of BLG, 1MLG, 2MLG and 3MLG. For BLG sample, both G and 2D bands are absent, showing the lack of π-conjugate structure in BLG. For the other three samples, the 2D band positions (and full-wave half maximum, FWHM) are 2724 (58), 2733 (65), 2745 (70) cm^{-1}, respectively, corresponding well to 1MLG, 2MLG and 3MLG on 6*H*-SiC(0001) according to Ref [78]. Figure 3.6b,c shows the corresponding IPES spectra of these four samples taken at normal and 70° incidence, respectively. At normal incidence (figure 3.6b), five distinct features are found in these four spectra, namely peak A, B, C, E and H. Peak A is assigned to a surface state related to Si dangling bonds at the BLG/ SiC interface (see chapter 5 for more details). Peak B, C, H are assigned to unoccupied states related to σ*, SiC bulk and indirect transitions of π* at M point of graphene BZ. More details of these three features are discussed in the next subsection. Peak E is absent for BLG and MLG but it shows up at 2MLG and is further enhanced at 3MLG. Simultaneously, the intensity of the SiC-related peak C attenuates with increasing graphene thickness. Peak E is

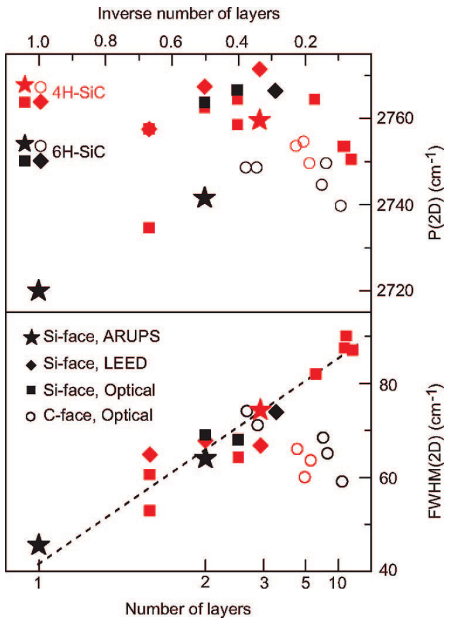

Figure 3.5: The position (and FWHM) of the Raman 2D band of graphene grown on SiC samples as a function of the inverse number (number) of layers. The different symbols refer to the different methods used to identify the layer thickness. Figure reprinted from Ref. [78].

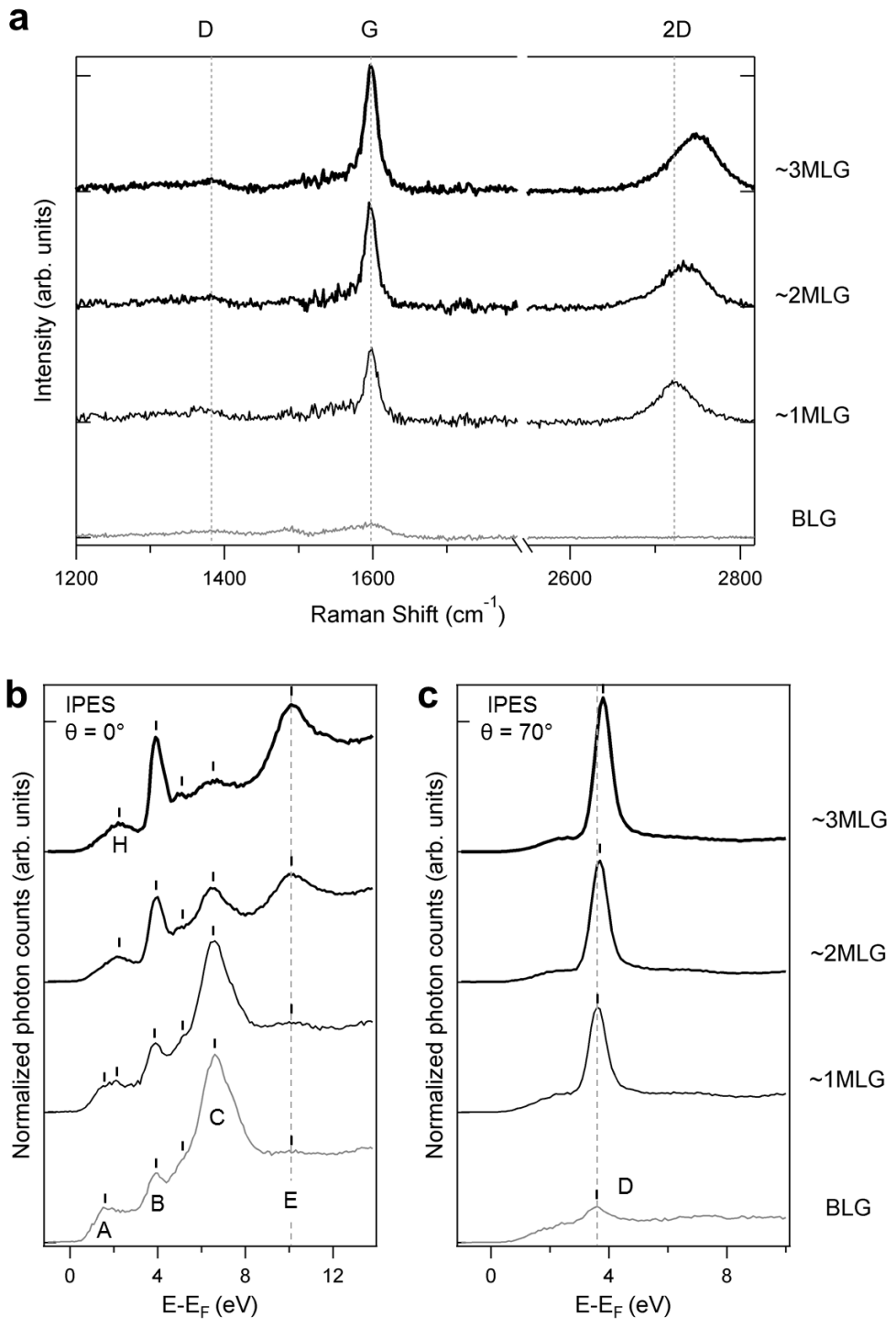

Figure 3.6: (a) Raman spectra, (b) normal incidence, and (c) 70° incidence IPES spectra of BLG, 1MLG, 2MLG and 3MLG.

thus attributed to thickness-dependent interlayer transition states since its intensity increases with graphene thickness. By comparing with Raman spectroscopy results, we may determine the graphene thickness using the relative intensity of peak C and peak E in the IPES spectrum of graphene. Since both MLG and BLG lack of peak E, the presence of peak D in IPES spectra obtained at grazing incidence is used to differentiate them, as shown in figure 3.6c. Peak D is assigned to π^* states of graphene (discussed in more detail in the next subsection), which are annihilated in BLG due to a strong covalent bonding with the SiC substrate (see chapter 5).

Many studies determine the thickness of graphene by the splitting of the π band of graphene at the Dirac cone using ARPES [16, 79]. The band splitting is due to interlayer interactions when graphene layers are Bernal-stacked, such as for exfoliated graphene and for the studied epitaxial graphene on SiC(0001). However, the same method is not applicable for IPES. This is because the access to the π^* states near the Dirac point of graphene (K point in graphene BZ) is forbidden using the actual isochromatic IPES working at ∼9.7 eV (see more details in the following). The splitting of the π^* states of multilayer graphene is much less resolved away from K point, as shown in figure 3.6c, where roughly only one π^* band can be observed, as also observed on graphite thin-film [14]. On the other hand, a shift of the π^* states is observed with increasing thickness. This is because the epitaxial graphene is initially n-doped by the BLG/SiC surface, but the effective doping is reduced in the top layers when the graphene becomes thicker. However, since the study of the functionalization of graphene is expected to modify the position and dispersion of the π^* band, it is inappropriate to use its position as a thickness index. We thus use an alternate way, *i.e.* by inspecting both the intensity of peak D and E in IPES spectra, to determine the thickness of graphene.

3.1.2 Unoccupied electronic structure of graphene on SiC(0001)

Figure 3.7 shows the ARIPES spectra of the BLG and 1MLG *wrt* the incidence angle θ along Γ-K in the graphene BZ. The evolution of the highly-dispersive sharp peak, peak D, at large incident angles for the MLG surface distinct it from the BLG one. These sharp peaks are assigned to the unoccupied π^* states of the graphene [14], the evidence of an extended conjugated structure consisting of C atoms in a sp^2 configuration. Thus, based on the unoccupied electronic structure, only the MLG behaves as an isolated graphene. Even though possessing a similar structure like graphene as revealed by LEED and a σ^*-related states as discussed below, the electronic properties of BLG are disturbed by its strong coupling with the SiC substrate through Si-C covalent bonds. Because of this, the $(1 \times 1)_G$ surface, the MLG on SiC, is used as the starting sample for the study of chemical doping of graphene, namely the pristine graphene (PG) in the following. As for the BLG, it is further studied by hydrogenation, as shown in chapter 5, where we demonstrate that BLG can retrieve its graphene-like character via the intercalation of hydrogen [43].

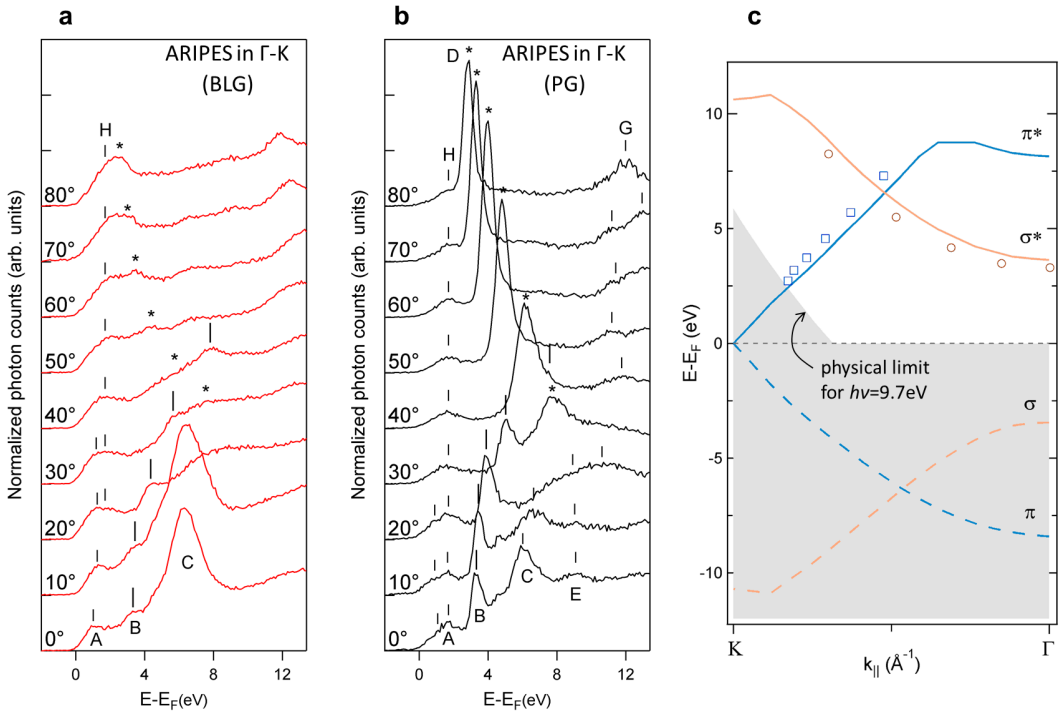

Figure 3.7: The ARIPES spectra of (a) BLG and (b) PG along Γ-K direction *wrt* electron incident angle. (c) Electronic band structure of graphene around E_F. Straight and dashed lines are *ab initio GW* calculation results extracted from Ref. [80]. Square and circle symbols represent experimental results on PG. The shadowed area delimits a forbidden region for an IPES spectrometer working at fixed photon energy around 9.7 eV.

Besides the prominent π^* states at high incidence, the IPES spectra of BLG and PG also show other features, especially at normal incidence, as shown in figure 3.7. The closest to the Fermi level, peak A, located at ∼1.1 eV, shows little dispersion along Γ-K. It is assigned to the interface states due to Si DBs located between the BLG and SiC substrate, which nature will be discussed in more detail in chapter 5. Peak B, located at ∼3.3 eV, disperse away from E_F with increasing angle. It is assigned to σ^* states of the C-C bonds [14], which are still present in BLG although the $\pi*$ states are absent. Peak C, located at about 6 eV, is attributed to the bulk SiC [14]. It shows a dispersion away from E_F with increasing angle but is quickly attenuated over 20°. Peak H, located at about 2 eV, is observed for an incidence above 20° with a negligible dispersion. It is assigned to an indirect transition to the high density of states (DOS) of π^* band at M point of graphene BZ (at ∼2 eV above E_F), as also observed for few layers of graphene and graphite [14]. Though the BLG have no π^* band, a large DOS at this energy is still found at M point of graphene BZ, as revealed by ARPES [81].

Figure 3.7c shows the $k_{\|}$ dispersion of the measured σ^* and π^* states of PG on SiC(0001) along Γ-K, compared to the theoretical band structure of graphene. The theoretical band structure is extracted from Ref. [80], which is obtained by *GW* approximation. The experimental data are obtained from the ARIPES spectra of PG in figure 3.7b. The position of σ^* and π^* states are determined by adjusting a sum of Gaussian curves after subtracting a background base line from the raw data. The measured σ^* states show a polynomial-like dispersion in $k_{\|}$ along Γ-K. The π^* states show a quasi-linear dispersion toward K point, where it should construct the upper Dirac cone. Both experimentally obtained σ^* and π^* dispersion show good agreement with the theoretical band structure. Though, as mentioned earlier, the access to the K point in IPES is forbidden due to the analyzing photon energy, ∼9.7 eV, as shown by the shadowed region in figure 3.7c. Indeed, the minimum energy (*wrt.* E_F) that can be reached by an incident electron (E_i) to allow radiative transition to a given final-state energy (E_f) is proportional to the square of the parallel component of the crystal momentum ($k_{\|}$), as shown by the following equation:

$$E_f = W_\phi - h\nu + E_i = W_\phi - h\nu + k_{\|}^2\left(\frac{\hbar^2}{2m_e sin^2\theta}\right) \tag{3.1}$$

in which W_ϕ stands for the target work function, $h\nu$ is the emitted photon energy, θ is the electron incident angle and m_e is the electron mass. At the large $k_{\|}$ value of the K point, the minimum final-state energy (E_f) is largely above E_F for $h\nu = 9.7$ eV (figure 3.7c). Thus, the unoccupied states near E_F at the K point could only be reached by larger photon energy. For the study of doped graphene, we can still appreciate the magnitude of n-type (or p-type) doping by observing the shift of the π^* band away from K.

One may notice that the position of the extrapolated line at K point, e.g. ∼0.48 eV above E_F for PG, actually differs from the expected Dirac point position, which is about -0.4 eV for monolayer graphene on SiC [10]. This is partly because the actual

dispersion of the π^* band of graphene is not perfectly linear between the Dirac point and larger $k_{\parallel}$ values away from K. The dispersion slope of the π^* band varies due to intrinsic electron coupling effects, such as correlation effects, trigonal warping and final-state energy [80, 82]. It may also be produced by substrate-induced doping effect [83]. These effects induce a systematic error to the estimated Dirac point position using a simple linear extrapolation from experimental points away from K. However, regardless of the exact position of the Dirac point, the determination of the *relative* position of the Dirac point using this method still appears reliable.

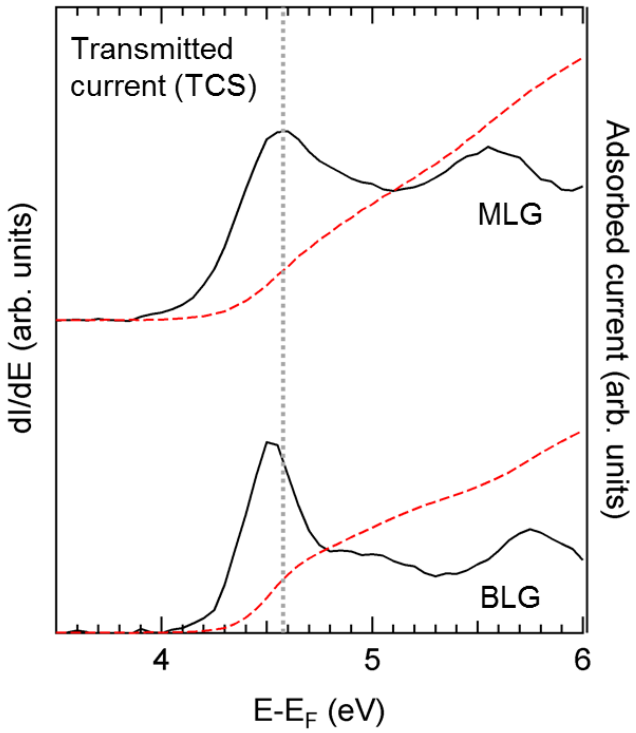

Figure 3.8: TCS spectra of BLG and MLG on SiC. The spectra are displayed in the first derivative of the transmitted current *wrt*. the incident electron energy.

Figure 3.8 shows the TCS spectra, *i.e.* the transmitted current (dashed line) *wrt* incident electron energy and their first derivative (solid line), of the BLG and MLG on SiC(0001) surface. The maximum of the first derivative at the lowest threshold indicates the magnitude of the surface work function. As shown in the figure, the work functions of the BLG and MLG on SiC(0001) revealed by TCS are 4.53 ±0.05 eV and 4.58 ±0.05 eV, respectively. This is close to the value of an isolated graphene (4.66 eV) reported in the literature [84].

3.1.3 Chemical analysis

AES (*in situ*)

Figure 3.9a shows the AES spectra of the Si-rich to C-rich SiC(0001) surfaces at E_P = 1200 eV. From top to bottom are the AES spectrum of (3×3), $(\sqrt{3} \times \sqrt{3})R30°$, BLG and MLG surfaces. The O KLL Auger mode at ∼502 eV is absent for the AES spectrum of the (3×3). It clearly shows that the native oxides are successfully removed from the surface using the sample preparation procedure presented in the beginning of this section. The Si/C Auger intensity ratio, $(Si/C)_{AES}$, for the (3×3) surface is about 28 using our AES setup. As for the $(\sqrt{3} \times \sqrt{3})R30°$, it is ∼8.5. As shown in figure 3.9b, both Si-rich surfaces show negligible C-sp^2 feature at about 253 eV, as indicated by an arrow.

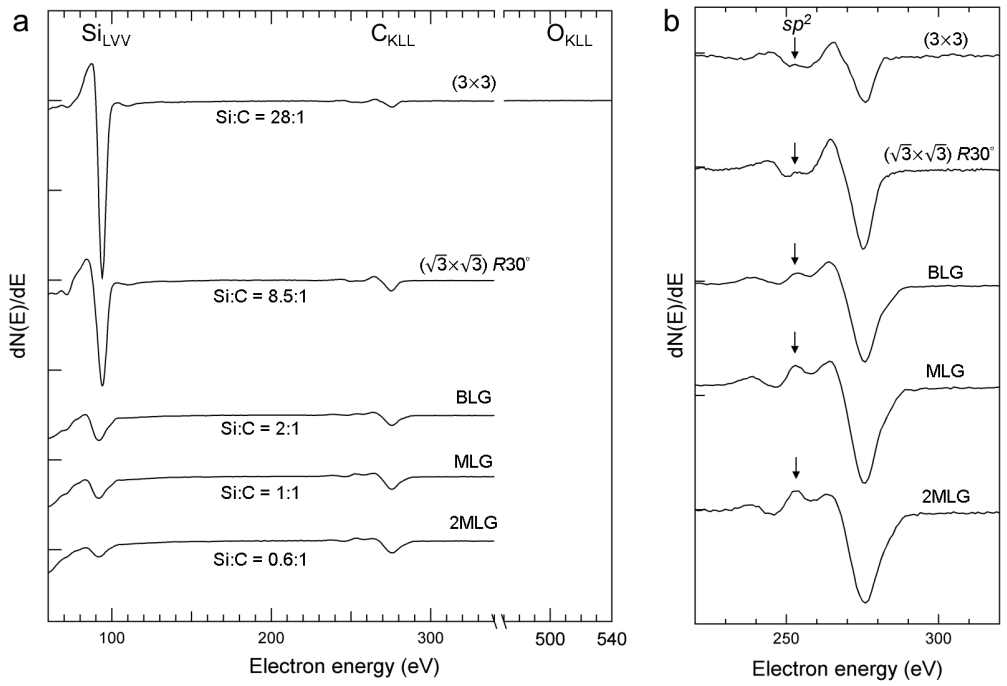

Figure 3.9: (a) AES spectra of the SiC(0001) surface during each steps of the graphene epitaxy procedure. (b) The enlarged C KLL features of these studied surfaces.

For BLG and MLG, the AES spectra show a $(Si/C)_{AES}$ of ∼2 and ∼1, respectively. Besides, the C-sp^2 feature starts to emerge for the BLG surface and is further enhanced in the spectrum of MLG. It indicates that the BLG actually contains C atoms in a sp^2 configuration, which agrees with the assumption that the BLG is a graphene layer covalently bonded to SiC [43].

Though the AES provides a rapid and surface-sensitive analysis for the elemental analysis of the surface atoms, the low resolution of Auger electrons restrain its capability to analyze the chemical shift of any particular element. Concerning the studies of graphene grown on SiC and other SiC surface reconstructions, both Si and C atoms have several different chemical states, which possess valuable information regarding the actual surface structure. Thus, in order to reveal more information on the chemical shifts, high-energy-resolution core-level spectrometry, such as XPS is required.

XPS (*ex situ*)

Figure 3.10 shows the core-level spectra, C 1*s* and Si 2*p*, of the PG on SiC. The spectra are taken with a monochromatic Al X-ray at 1486.6 eV with a pass energy of 10 eV inside the hemispherical analyzer, which provide a spectral resolution of ∼0.6 eV. Figure 3.10a shows the Si 2*p* spectrum of PG. The spectrum consists of a 2*p* 1/2 and a 2*p* 3/2 peaks showing only the contribution of the bulk Si atoms. The C 1*s* spectrum (figure 3.10b) shows several features located around the binding energy (BE) of 283-287 eV. It is composed of a sharp peak (C_{SiC}) at 283.8 eV that is assigned to the contribution of the carbon atoms in SiC bulk in sp^3 configuration [10]. The contribution of the graphene layer is located at higher binding energy of 284.7 eV due to its sp^2 configuration. Two other components located at 285.3 eV and 285.8 eV are attributed to the BLG at the interface. It reveals the fact that the BLG consists of a mix of sp^2 and sp^3 hybridized carbon atoms. However, the composition of these two configurations in the BLG (sp^2:sp^3) varies from 1:2 to 2:1 in different reported works [10, 85]. The reason might due to the limited resolution of the XPS, the different curve fitting methods applied, and the possible existence of complex interface structure, *i.e.* different BLG/SiC interfaces with varied Si:C concentrations. More details are discussed in chapter 5. A fifth peak located at 286.4 is attributed to oxidized carbon species (C-O). This is due to the inevitable ambient air exposure during the sample transferring for the *ex situ* experiment, which remains in the sample even after a 600°C pre-annealing in UHV before performing XPS measurements.

3.2 Graphene on C-terminated SiC(000$\bar{1}$) surface

Following the study of graphene grown on the Si-face of SiC, this section shows the fabrication and characterization of the graphene grown on the C-face of SiC. A similar process of Si sublimation in UHV is applied to grow epitaxial graphene layers on the C-face SiC(000$\bar{1}$). As shown in figure 3.11, the epitaxial-ready SiC(000$\bar{1}$) substrate is first degassed at 700°C for 1 hr. It is then annealed at 900°C under Si flux for 20 min to remove native oxide until obtaining a clean, Si-rich, (2 × 2) surface observed using LEED, namely $(2\times2)_{Si}$. By further annealing at 950°C, a (3×3) surface reconstruction is obtained. After annealing at 1000° for 10 min, a LEED pattern consisting of arcs and points, made of multiple graphene (1 × 1) spots in various orientations and a mix

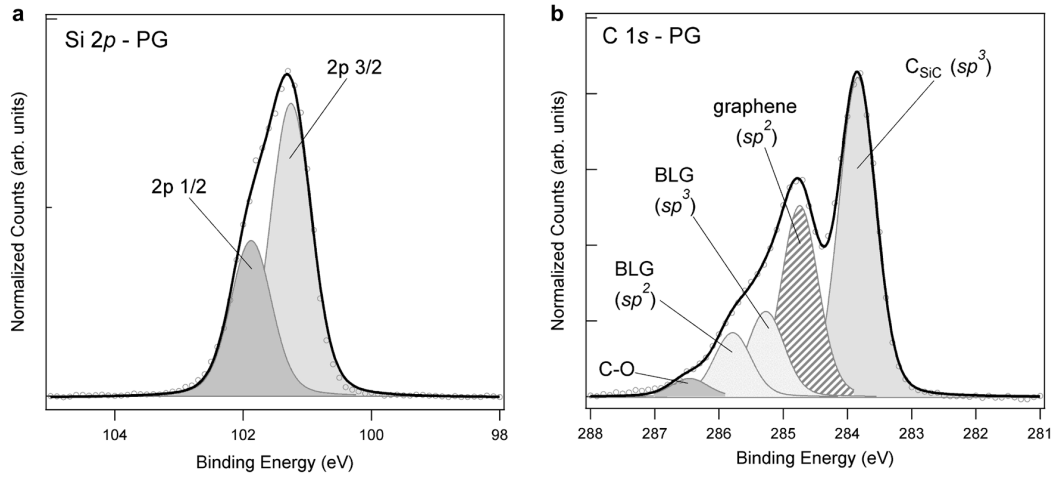

Figure 3.10: (a) Si*2p* and (b) C*1s* XPS spectra of the PG on SiC (0001).

of (3×3) and (2×2) pattern of SiC reconstructions, are obtained. The arcs/spots of graphene (G) are further enhanced with an additional $(1 \times 1)_{SiC}$ pattern of SiC bulk, after an annealing at 1050° for 5 min. After a final anneal at ∼1200°C for 5 min, only the diffraction pattern of graphene (G) remains.

Figure 3.12a and b shows the entire AES spectra and their C_{KLL} features of each reconstruction (or surface structure) during the graphene epitaxy on the SiC C-face: $(2 \times 2)_{Si}$, (3×3), (3×3)+G, (1×1)+G and G. The sp^2-related feature (as indicated by the arrow), emerges as the graphene diffraction pattern shows up. Its intensity relative to the main C peak grows much faster than for the graphene grown on the Si-face. The Si:C intensity ratio decreases to 1:9 when the diffraction pattern of the SiC substrate is vanished. The complex diffraction pattern of graphene grown on the C-face, which consists of arcs and spots, and the much higher C concentration on the surface as revealed by AES, indicates the formation of a multilayer graphene with multiple rotational disorder.

As shown above, the graphene grows much faster and at lower temperature on C-face SiC than on Si-face due to a more efficient Si sublimation. The C-face SiC also exhibits different surface reconstructions than the Si-face at high temperature. To lower the graphene growth rate on C-face, the graphene have been demonstrated to grow under a partial pressure of Ar or Si flux in a furnace (section 1.1.3) [18]. Though, regardless of the epitaxial method, UHV, furnace or under partial pressure, the graphene grown on C-face SiC usually results in a multilayer graphene (from 3-4 layers up to >10 layers) with a large orientation disorder, as shown in figure 3.13. Besides, while the graphene grown on SiC(0001) is *n*-doped due to the strong coupling between the BLG and the Si-terminated surface, the multi-layer graphene grown on C-face SiC$(000\bar{1})$ exhibits each layer as an unperturbed quasi-isolated graphene monolayer. It shows a

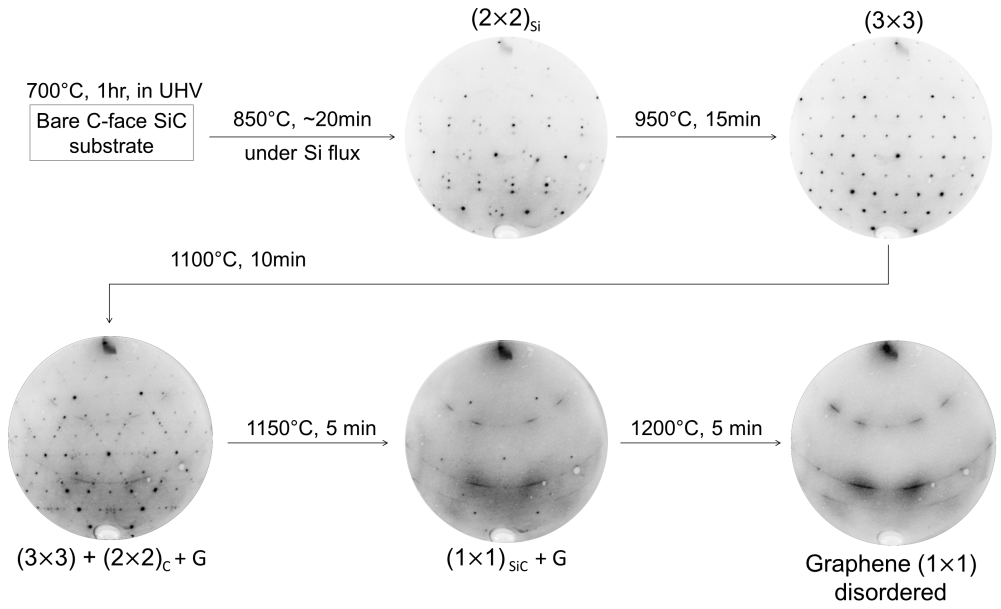

Figure 3.11: Sketch of the process flow of graphene preparation on SiC(000$\bar{1}$) by thermal annealing in UHV. Each step is represented by its surface reconstruction revealed by LEED.

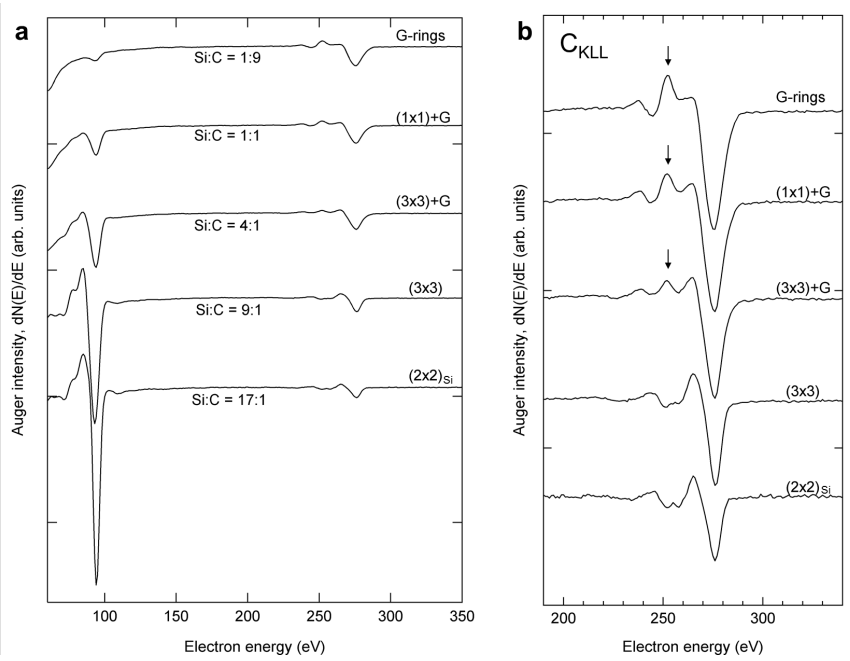

Figure 3.12: (a) AES spectra of each reconstruction during the graphene epitaxy on C-face SiC: $(2 \times 2)_Si$, (3×3), (3×3)+G, (1×1)+G and G. (b) The zoom of the C_{KLL} features of these spectra.

single π band at the linear dispersed Dirac cone [86], and even shows exceptionally high room temperature mobility (>200,000 cm^2/V s) [87]. It is preferred for the study of quantum effects of single layer graphene but causes difficulties if studying with angle- or momentum-resolved spectroscopy.

Peculiar character of the graphene on SiC(000$\bar{1}$)

The debate over the nature of the graphene, *e.g.* its isolated-graphene character and its orientation disorder, has been started since it was obtained on the SiC C-face. Many research groups have used different methods to reveal the actual structure of this isolated-graphene-like multilayer graphene grown on the SiC C-face. Most of them propose that the multilayer graphene consists of adjacent sheets that are rotated relative to each other but has generally one orientation by sheet, as revealed by X-ray diffraction results [88]. This model explains well the reason of observing an isolated-graphene-like character for each graphene layer. However, others have reported recently the observation of multi domains being randomly oriented, using micro-LEED, on the graphene grown under Ar ambient on the SiC C-face [89]. Though, their ARPES results show single π-cone for each domain, *i.e.* the isolated-graphene character. The most plausible explanation might be the presence of both cases, *i.e.* the presence of multiple domains, and in each domain the adjacent graphene sheets are disoriented *wrt* each nearby layer.

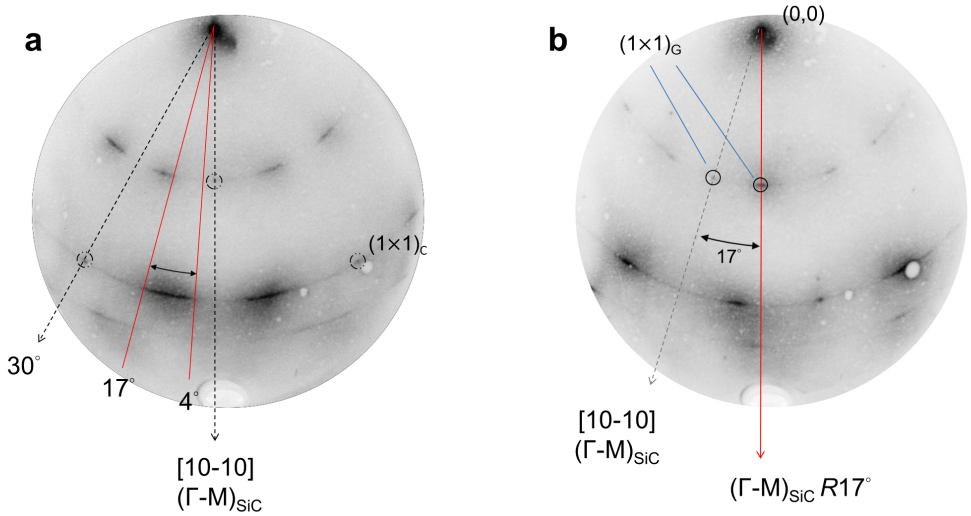

Figure 3.13: LEED image of PG grown on the C-face of SiC oriented to (a) the Γ-M direction of SiC, and (b) 17° *wrt* Γ-M_{SiC}.

The orientational disorder of the multilayer graphene can be identified by its LEED pattern. For example, figure 3.13a shows the LEED image of a multilayer graphene

grown on the C-face SiC(000$\bar{1}$), with a set of small arcs and single spots. The spots are situated at the same position than the $(1 \times 1)_G$ of the graphene grown on the Si-face,*i.e.* rotated 30° *wrt.* the SiC (1×1) spots, the SiC [10$\bar{1}$0] direction (or Γ-M$_{SiC}$). On the other hand, the arcs are rotated ±4°-17° from the [10$\bar{1}$0] direction. It should be noted that the orientation disorder of the multilayer graphene reported in the literature varies from one to another source, especially for the disorientation close to the [10$\bar{1}$0] direction. Some studies observed an azimuthal distribution peak at about 2.2° [88], others observed a wider distribution from 2° to 10° [86] or 6° to 13° [90]. The nature of this variation in the disordering angles is, however, still not quite understood to date.

Unoccupied electronic structure of graphene on SiC(000$\bar{1}$)

The orientational disorder of the graphene layers grown on SiC(000$\bar{1}$) causes serious difficulties for probing the graphene unoccupied states using our actual ARIPES technique. Different to the more commonly-used ARPES systems, which usually possess a 2D detector permitting to resolve photoelectrons with multiple emitting angles and azimuths (large $k_{\parallel}$ range), the ARIPES only resolve one particular angle along a single azimuth at a time. Thus, one has to take a large number of experiments in order to find the orientation of the topmost graphene layer, *i.e.* to find the correct azimuth for band dispersion measurement in the high symmetry direction, Γ-K or Γ-M. In addition to the difficulty to determine the graphene orientation, other characteristics of the actual ARIPES also make it unfavorable for the characterization of graphene grown on SiC(000$\bar{1}$), *i.e.* the relative low resolution and large probing area. The energy and angle resolution of the actual IPES is about 0.4 eV and 1°, respectively. As for the probing area of IPES, it is in the order of 10 mm^2, determined by the incident electron beam and the focal point of the mirror. When probing multiple disoriented domains of graphene with ARIPES, it may not be able to resolve the presence of multiple π* band of graphene, making it even more difficult to determine the high symmetry direction of graphene. Even if the azimuth is correctly selected for a particular graphene sheet to probe its π* band, the π* bands of other disoriented graphene may also contribute to the final spectrum. The resulting spectrum may show a broader π* states due to the low resolution and makes it difficult to determine the energy of the π* states.

In order to reduce the effect of graphene layer disorientation during ARIPES measurement, we prepared a PG sample grown on the SiC C-face with a fewer number of layers (FLG), which LEED image is shown in figure 3.13b. It should be noted that the arcs in the LEED image of FLG are shorter than for its multilayer counterpart (figure 3.13a), indicating that the orientation of these graphene layers are more concentrate with a maximum at about 17° from Γ-M$_{SiC}$ (Γ-M$_{SiC}R17°$). The ARIPES spectra of the PG along Γ-M$_{SiC}$, which should be resulting from the spots in figure 3.13b, and along Γ-M$_{SiC}R17°$, resulting from the arcs, are shown in figure 3.14a and b.

At low incident angle, the ARIPES spectra of PG on the SiC C-face along Γ-M$_{SiC}$ and Γ-M$_{SiC}R17°$ show little difference. At large incidence, the π* states are more

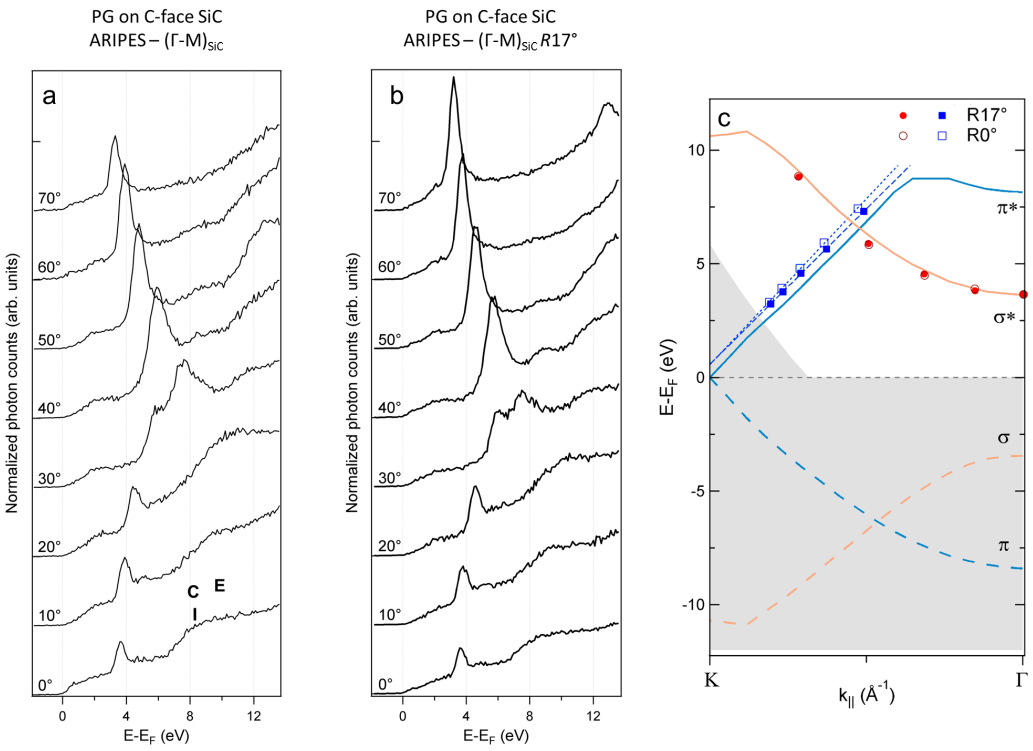

Figure 3.14: The ARIPES spectra of PG grown on the C-face of SiC (a) along Γ-M_{SiC}, and (b) rotated by 17°. (c) The corresponding k-dispersion of their σ^* and π^* states.

pronounced for those taken along Γ-M$_{SiC}R17°$ than those along Γ-M$_{SiC}$. This may be because the graphene that is oriented at 17° occupies larger domains than those oriented along Γ-M$_{SiC}$ (0°), or because the former are on the top layer and the later are underneath. The $k_{\|}$-dispersions of σ* and π* states along graphene Γ-K for both 0° and 17° oriented graphene are shown in figure 3.13c. The dispersions of σ*, hollow and fill circle for 0° and 17°, respectively, are identical for both orientations. The dispersion of π* states, hollow and filled square for 0° and 17°, show a slight difference in their slope but their linear extrapolations (dotted and dashed line for 0° and 17°) along Γ-K point of graphene BZ end at the same value at the K point. The slope difference may be due to the contribution of slightly disoriented graphene flakes, as revealed by the arcs observed by LEED, on the ARIPES spectra taken at 17°. The value of the linear extrapolation at the K point is ∼0.6 eV. It is slightly higher that for the PG grown on the Si-face (∼0.48 eV), indicating that the graphene grown on C-face is less n-doped by the SiC substrate, in accordance with the literature [91]. The difference between these two (0.12 eV) is, however, smaller than expected (∼0.4 eV), which should be due to the non-linear dispersion of π* band away from K point, as discussed in subsection 3.1.2.

By comparing to the IPES spectra of PG grown on the Si-face (figure 3.7b), the SiC substrate related features (peak C) are much attenuated for the IPES spectra of PG on the C-face, which should be due to the multilayer structure of PG grown on the C-face screening the underneath SiC substrate. Though being multilayer, the peak E located at ∼10 eV, which intensity is dependent to graphene thickness, seems less pronounced than what is expected for such multilayer structure. For PG on the Si-face, the SiC feature (peak C) is attenuated for a graphene thicker than 4ML including the BLG layer while peak E is well pronounced, as shown in figure 3.4. For PG on the C-face, instead, peak C is attenuated but peak E is not much pronounced. This may be due to the disorientation of graphene layers grown on the C-face SiC that restrains the formation of the graphite-interlayer-related state, peak E. This also implies that the graphene layers grown on C-face SiC are mostly electronically isolated from each other, while the multilayer graphene on Si-face behaves more like a graphite thin film by showing a more pronounced interlayer-related state.

Figure 3.15a shows the TCS spectra of PG grown on the Si-face (top panel) and the C-face (bottom panel), which reveal their work functions. The work function of PG on Si-face is 4.58 eV as also shown in subsection 3.1.2. On the other hand, the work function of PG on C-face is 4.93 eV, which is about 0.35 eV higher than the former. The difference in work function can be explained by the n-type doping induced by the SiC substrate for the graphene grown on the Si-face, which, according to the literature, brings the E$_F$ at about 0.4 eV above the Dirac point of graphene. As also illustrated in figure 3.15b, the n-type doping of graphene on the Si-face may decrease the work function of the graphene for about 0.35 eV. For the graphene on the C-face, which should remain undoped, the work function is larger.

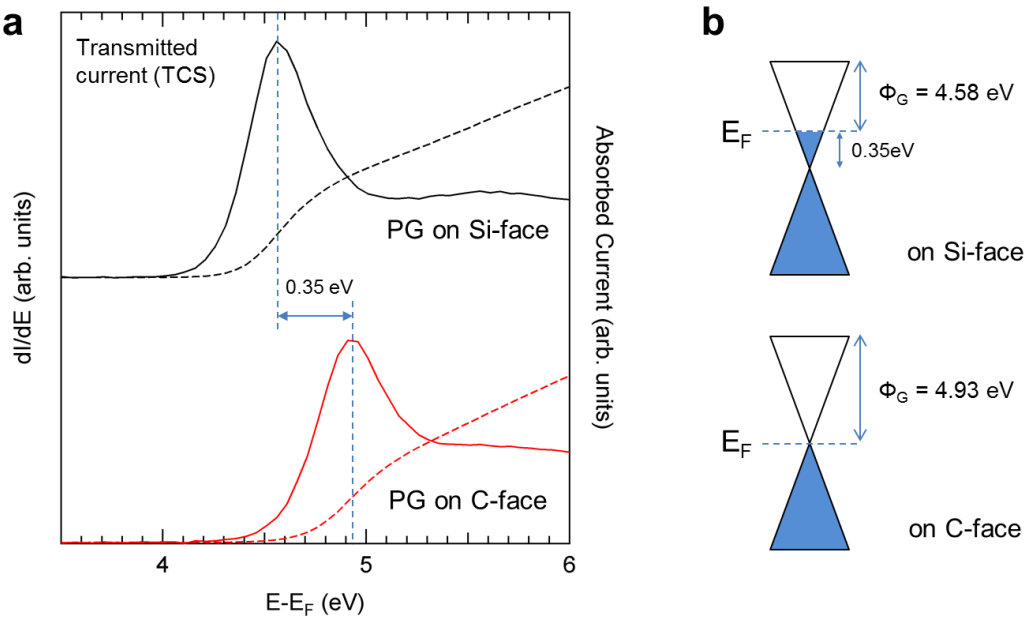

Figure 3.15: (a) TCS spectra of PG grown on the Si- and C-faces. The transmitted current *wrt* the incident electron energy are shown by dashed lines, and their first derivative in solid lines. (b) Schematic illustration of the nature of the substrate-induced n-type doping

3.3 Summary

In this chapter, we presented the main characteristics of the pristine graphene grown on either Si-terminated SiC(0001) surface and on C-terminated SiC(000$\bar{1}$) surface. The processes to grow graphene layer(s) on both SiC(0001) and (000$\bar{1}$) surface follow a series of annealing steps, where each step is monitored by its surface reconstruction using LEED. For PG grown on SiC(0001), we are able to control the thickness of the epitaxial graphene layer(s), either a buffer-layer, a monolayer, a bilayer or a multi-layer graphene on SiC(0001), all perfectly oriented at 30° *wrt* the hexagonal lattice of SiC(0001). Beside using LEED, the thickness can be accurately verified using IPES and (*ex situ*) Raman spectroscopy. We also present the chemical characteristics of the PG, *i.e.* its Auger electron and core-level photoemission spectra, which confirm that a BLG structure containing C atoms in sp^2 configuration is formed at the interface between the epitaxial graphene layer(s) and the SiC(0001) substrate. As for the C-face SiC(000$\bar{1}$), we show that the graphene layers grow much faster on the C-rich surface, and only multilayer graphene sample is obtained. These multi-layers are disoriented, as revealed by LEED, and are decoupled from each other, as evidenced by a less developed interlayer-related states in the IPES spectra. Finally, the angular-resolved unoccupied states are studied for the graphene grown on both Si- and C-face of SiC. Their principal unoccupied states, σ^* and π^* bands, are identified and their dispersions along $\Gamma - K$ primitively agree with the theoretical approximation results. All the above characteristics of the pristine samples are used as important benchmark values for the following study of functionalized graphene.

Chapter 4

Nitrogen doped graphene by plasma exposure

The core spirit of this thesis, the study of the graphene functionalization, is presented in this and the following chapters. Different methods, including chemical doping, hydrogenation and molecular doping, were applied to alter the electronic and chemical properties of the pristine graphene prepared on the SiC surface. In this chapter, the chemical doping of graphene is investigated through its doping species, doping process, chemical environment of the incorporated atoms and their impacts on its electronic properties.

Substituted nitrogen atom is one of the most widely studied species for the chemical doping of graphene. Since its size and bond length with C atom (N-C) are the closest to that of a C atom and a C-C bond in graphene, the N atom is logically the most favorable candidate to replace a C atom in the honeycomb lattice of graphene with a minimum structural perturbation. By substituting a C atom in the graphene lattice, a N atom modifies the local electronic and chemical properties of graphene by providing one extra valence electron. The impact to the electronic and chemical properties of graphene by this additional electron is strongly dependent to the chemical environment of the doping nitrogen, as they are usually found in different bonding configurations with (or without) the presence of neighboring vacancy, *i.e.* pyridinic-N or graphitic-N (see section 1.2.4). For example, the local electron density is increased near the graphitic-N doping site due to the delocalized additional electrons. As for the pyridinic-N site, the extra electron is confined at the pyridinic-N, thus induces little changes to the property of graphene, as predicted by the theoretical simulations [53]. Boron atom is another promising candidate for the substitution of carbon in graphene, as introduced in section 1.2.4. Though, due to the lack of appropriate gas phase boron source (common boron sources usually possess other elements, *e.i.* BF_3 and B_2H_6), the study of the chemical doping of graphene in this thesis is focused on nitrogen doping.

The nitrogen-doped graphene (NG) has been demonstrated to exhibit superior performance over the pristine graphene in several applications, such as in field-effect transistor devices, batteries, fuel cells, super-capacitors, and bio-sensors [3, 34, 49, 60, 92, 93]. Accordingly, different approaches have been demonstrated to fabricate NG, such as direct synthesis via CVD on a metal substrate, thermal annealing in nitrogen-containing atmosphere and various plasma based treatments, as also introduced in section 1.2.4. However, there is only a very limited number of works dedicated to the N doping of epitaxial graphene grown on SiC, and most of them consist of simulations. The experimental realizations of NG on SiC are still in the early stage of development, and additional efforts are necessary in order to obtain control and reproducibility of graphene chemical doping by N atoms.

Plasma-assisted nitrogen doping is a particular interesting process to fabricate NG for electronics applications. Besides being an industrial familiar technique, it has exceptional high throughput, potentially spatial selectivity, and can be performed regardless of the substrate (unlike the direct synthesis by CVD). It is also a highly versatile process, which can be altered by changing the feeding gas, the plasma characteristics, and by selecting the incident species, such as N ions or N atoms. Thus, the plasma-based process is a perfect match for the study of nitrogen doping on graphene and for the fabrication of graphene-based devices, especially when they are prepared on the semi-insulating SiC substrate.

Different to other reported works of nitrogen doping of graphene using ion/atomic irradiation [54, 94, 95], we concentrate the present study on the low-energy region (E_k < 50 eV). Experimental study of this low-energy region is rarely reported, usually only using atomic nitrogen with thermal energy [52]. The actual mechanism of the nitrogen doping via ion/atomic irradiation is yet poorly understood. Based on theoretical evaluation of the displacement threshold energy of C atoms in graphene, the minimum required energy for an N ion to knock a C atom out of its sp^2-hexagonal lattice is about 15-22 eV, depending on the simulation method [96]. The statical approach indicates the lowest possible displacement energy of C atom in graphene (15 eV), and the dynamical approach (22 eV) should more likely overestimate that value. The actual value should be between these two, maybe closer to the lower limit since the thermal ripping of the graphene layer (increasing curvature) also leads to lower displacement threshold. Furthermore, the atomistic simulations predict an optimum substitutional probability, the incident energy that dope graphene the most efficiently, at 50 eV for nitrogen doping [97]. At higher incident energy, the probability of unfavorable vacancy creation increases rapidly. Therefore, in order to introduce nitrogen in the graphene with minimum secondary damage, the use of low-energy species ($<$50 eV) is much preferred, which again supports the need of experimental study on the nitrogen doping of graphene using these seldom used low-energy species.

In this chapter, the nitrogen doping processes are primary studied on the graphene grown on the SiC(0001) surface (Si-face) using an ECR-MW plasma source mounted on our UHV system. We will focus on: (i) the doping species, (ii) the ion energy,

(iii) the temperature effect, and (iv) the presence of preexisting defects. The electronic and chemical properties of the resulting NG are mainly investigated using ARIPES and XPS. This study is complemented by two other subjects. The first one is the study of NG prepared on SiC(000$\bar{1}$), because the PG grown on the two sides of SiC substrate exhibits different properties, as shown in chapter 3. The second is the doping process using an industrial radio-frequency (RF) plasma-based implanter produced by Ion Beam Services (IBS, Rousset, France), also involved in this thesis project. The different characteristics of the plasma source may lead to the generation of different activated species, which helps to enrich the study of plasma-based nitrogen doping processes.

4.1 *In situ* nitrogen doping of graphene grown on SiC Si-face

The *in situ* plasma-based nitrogen source used in this study is a Tectra Gen2 ECR-MW plasma source, which is mounted in our preparation chamber, as shown in figure 4.1. The working principle of the plasma source is briefly described in section 2.2.3. The plasma conditions for nitrogen doping are generally maintained identical for every experiment, as described in the following. The working pressure in the UHV chamber is kept at $\sim 5.2\times10^{-5}$ mbar and the plasma power is fixed by the magnetron current at 15 mA. The typical plasma potential is about 20 V, and the ion energy distribution is about $\pm$ 15 V at this low energy [62]. The high plasma density induced by ECR consists of a large proportion of neutral and ionized monomers, as introduced in section 2.2.3. The nitrogen plasma may passively streams out of the source and diffuses toward the target, or it can be actively extracted by applying an extractor grid bias (fixed at 50 V in this work).

The nitrogen plasma stream consist of both neutral N species (with a high proportion of monomers), and charged particles (N ions and electrons). The neutral N species are mostly thermalized through the collisions with the BN aperture grid. The energy of the ions are determined by the plasma potential ($\sim$20V), anode voltage (kept grounded in this work), and the applied sample bias (used to vary incident ion energy in this work). Different from radio-frequency plasma, much higher densities of neutral species can be obtained in microwave-ECR plasma. Molecules like N_2 are dissociated with higher efficiency, leading to the emission of ionized as well as neutral monomers (N^+, $N^{\cdot}$), which are effective for reactive processes [62]. A $\pm$5 kV bias can be applied to the ion trap (see section 1.2.4) to remove charged particle, especially N ions, from the plasma stream, which becomes a neutral flow of thermalized N atoms. In general, this plasma source can be used in a versatile way by selecting different emitting N species and also varying the energy of the N ions with the sample bias. More specifically, when activating the ion trap, the source works in "atom mode" (N-atom), emitting only thermalized neutral N species to the target; when working without ion trap, namely

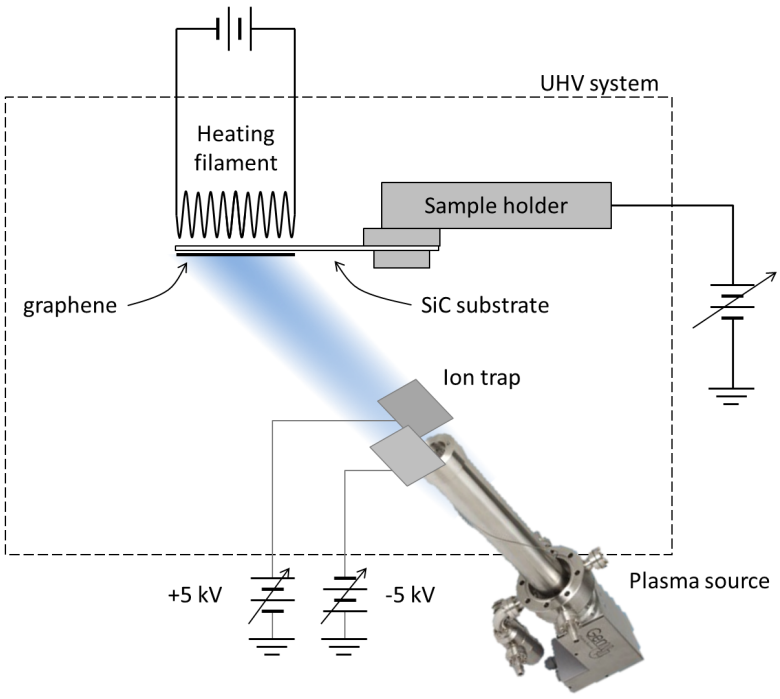

Figure 4.1: Sketch of the setup for the plasma-based nitrogen doping process.

the "ion mode" (N-ion), the plasma source emits all species in the plasma, *i.e.* both N ions and neutral N atoms, where the incident energy of the former is controlled by the target bias.

The annealing of the target sample during (or after) nitrogen doping is another feature studied in this work, as shown in figure 4.1. Besides removing physically adsorbed species at the surface, it has been reported that high temperature annealing removes the less-stable doping nitrogen in the graphene [98]. On the other hand, point defects, such as single vacancy, may migrate, annihilate or transform into the more stable double vacancy at higher temperature [29]. These effects show the importance of studying the annealing effect during the nitrogen doping process on graphene. It is also expected that NG fabricated at higher temperature are able to auto-repair the structural damage of the graphene due to irradiation and to become chemically more stable, thus much reliable for the applications.

4.1.1 Atomic nitrogen doping

We begin by showing the study of the *in situ* nitrogen doping of graphene using the species with lowest energy, the thermalized N atoms. The pristine graphene used in the following studies is grown on SiC(0001) except especially mentioned. By using the atom mode of the ECR-MW plasma source, only nitrogen atoms (or neutral species) may reach the sample, N-ions with higher energy are deviated from the original plasma stream by the ion trap (see section 2.2.3). They are mostly thermalized to very low energies (<0.1 eV), which may induce a minimum structural damage to the graphene monolayer during the plasma exposure. These thermalized neutral species are presumed to have insufficient energy to knock out and substitute carbon atoms in the graphene lattice but, being chemically active, they may be able to dope the graphene with the presence of defects (*e.g.* vacancy). In addition, we should also consider that a small amount of the emitting neutral species may have higher energy, such as non-thermalized atoms or accelerated ions that are neutralized before being deviated by the ion trap, and may be able to create defects during atomic nitrogen (N-atom) exposition.

Chemical analysis

Figure 4.2 shows the N 1*s* XPS spectra of the studied NG samples that are exposed to the nitrogen plasma source in atom mode, namely N-atom in the following. From the top to the bottom are the spectra of NG samples exposed to N-atom for 10 min at RT, 10 min at 850°C, 60 min at RT and 60 min at 850°C, which are equivalent to a dose of $\sim 1.5 \times 10^{18}$ atoms/cm^{-2} for the two former samples and $\sim 9 \times 10^{18}$ atoms/cm^{-2} for the last two samples.

As shown in figure 4.2, for 10 min N-atom exposure, only a small amount of pyridinic-N are introduced in the graphene layer, *i.e.* ∼0.8% and ∼0.7% when processed at RT and 850°C, respectively. The percentages shown here are the atomic

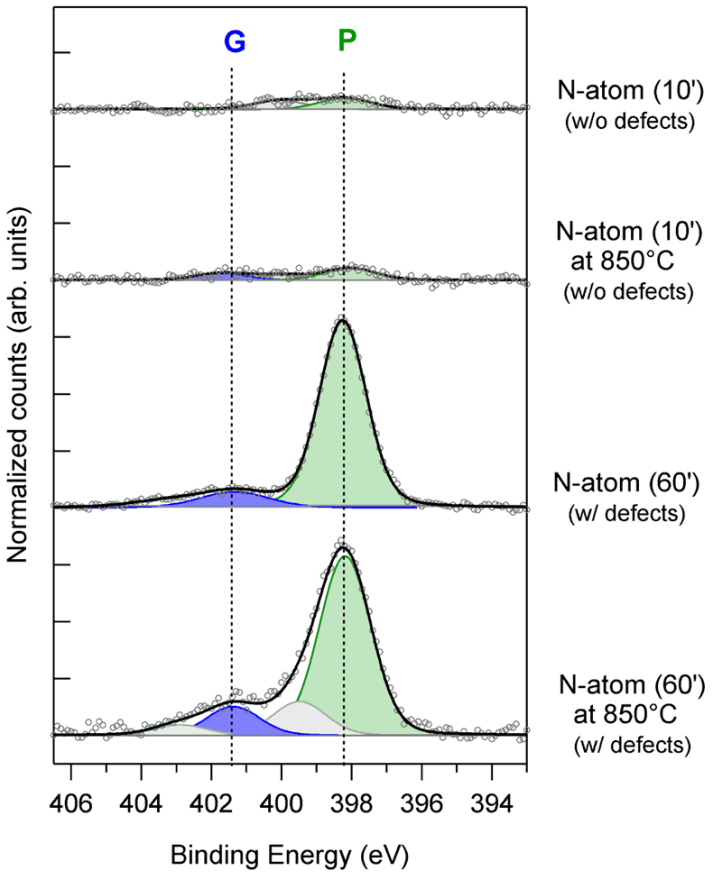

Figure 4.2: N 1*s* XPS spectra of the studied NG samples that are exposed to N-atom mode for 10 min at RT, 10 min at 850°C, 60 min at RT and 60 min at 850°C, from the top to the bottom.

concentrations *wrt* the carbon atoms in a monolayer graphene, *i.e.* assuming all incorporated N atoms are confined in the topmost graphene layer. The N 1*s* spectra of NG exposed to N-atom for 60 min exhibit a much higher doping nitrogen concentration. The concentrations of pyridinic-N attain 13.4 % and 11.5%, in addition to 1.7% and 2% of graphitic-N, for the RT and 850°C processed samples, respectively. Besides graphitic-N and pyridinic-N, there are also some other components that can be assigned to pyrrolic-N and N-O species. Being rather a minority *wrt* other components, their impact on the graphene properties are considered to be negligible.

The doping processes at RT or at high temperature of 850°C shows little difference in the resulting XPS spectra and the doping concentration of pyridinic-N. On the other hand, the total nitrogen concentrations in the NG samples exposed to N-atom for 60 min (15.7 % and 16.4%) seems too high to be solely dose-related, when compared to the samples exposed for 10 min (0.8% and 0.7%). As the N-atom dose of the former increases about six times (60 min vs. 10 min), the resulting nitrogen concentration increases more than 10 times, much larger than expected. Furthermore, the large nitrogen concentrations in the former (60 min) NG samples are principally found in pyridinic-N configuration.

Since pyridinic-N is defect-related and the thermalized N atoms should have insufficient energy to create defects, the most plausible cause is that the amount of pre-existing defects are larger in the PG samples before the 60 min N-atom exposure. Indeed, these two NG samples were prepared at an earlier stage of this thesis, when we were using a more rapid way for the growth of monolayer graphene on SiC(0001), *i.e.* a shorter period but higher annealing temperature. We assume that this brutal annealing process results in the creation of more pre-existing defects. In the later stage of this thesis, the PG samples were grown with a much longer and smoother annealing process to reduce the density of defects in the PG.

The Raman spectra of the PG grown with the "rapid annealing" and the "slow annealing", shown in figure 4.3, confirm this scenario. The Raman spectrum of a defect-less PG, grown in the slow way, exhibits a negligible defect-related D band. In contrast, the spectrum of a rapid-grown PG shows a much pronounced D band, indicating a large number of defects despite the fact that it also shows a well pronounced G and 2D band, which indicates a good quality of graphene in sp^2 structure. The Raman spectra of NG exposed to 60 min N-atom shows the vanishing of 2D band, indicating that the doping nitrogen actually strongly disturbed the graphene structure. Nevertheless, these results confirm that the formation of pyridinic-N is favored with the presence of pre-existing defects.

Similar nitrogen doping mechanisms were reported in the literature by performing a thermal annealing of the graphene in a partial pressure of NH_3 [99, 100]. The nitrogen doping level due to the NH_3 increases with the oxidation level of the graphene. Another work also shows the doping of nitrogen by annealing graphene in a NH_3 ambient with the presence of preexisting defects created by N^+ ion irradiation at 3 keV [54]. NH_3

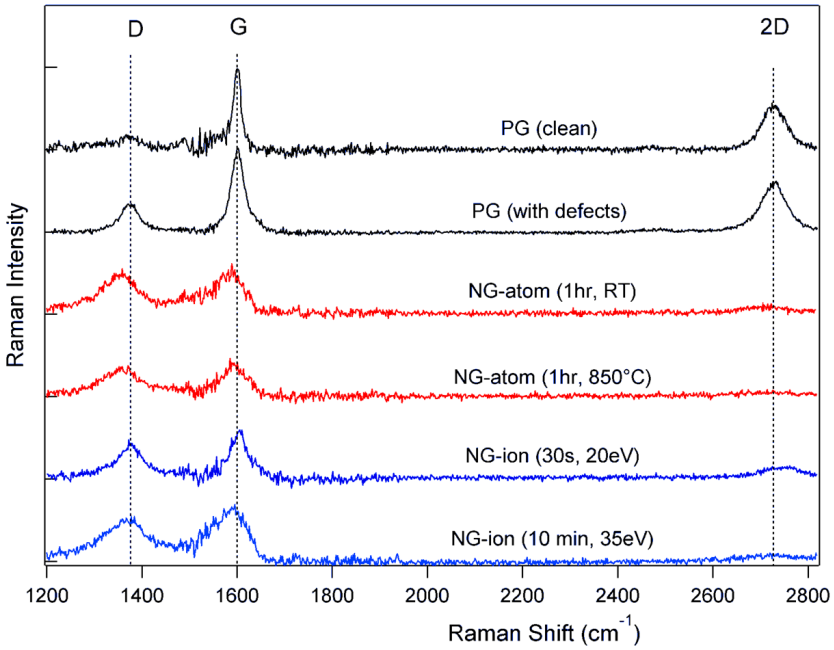

Figure 4.3: The Raman spectra of the defect-less PG, defective PG, NG exposed to N-atom for 60 min at RT and 850°C and NG exposed to N-ion.

molecules may be dissociated or activated at high temperatures to dope the graphene at its defect sites.

Unoccupied states analysis

Figure 4.4a shows the ARIPES spectra of the NG samples exposed to N-atoms for 60 min at RT. The overall spectra are still well structured after N-atom exposure, especially for the peaks related to σ^* and π^* states (peak B and D), indicating that the graphene structure is preserved after 60 min of N-atom exposure. It also indicates that the N-atoms create little defects in graphene. However, the positions of σ^* and π^* states are slightly modified. This is also shown by the dispersion of σ^* and π^* states in $\Gamma-$K of graphene BZ in figure 4.4b, based on the peak position obtained from figure 4.4a. The dispersion of σ^* states shows a small downward shift of 0.2 eV toward E_F, while the one of the π^* states shows a decrease in its dispersion slope and a very small downward shift, as compared to the pristine one.

These little modifications of the unoccupied states of graphene is assigned to a little amount of graphitic-N introduced in the graphene. Based on theoretical studies, the graphitic-N is expected to induce a n-type doping, a band-gap opening together with a decrease of π band dispersion slope, which is quite similar to the present case [101]. On the other hand, due to the high pyridinic-N concentration of 13% (equivalent to 1/8 of

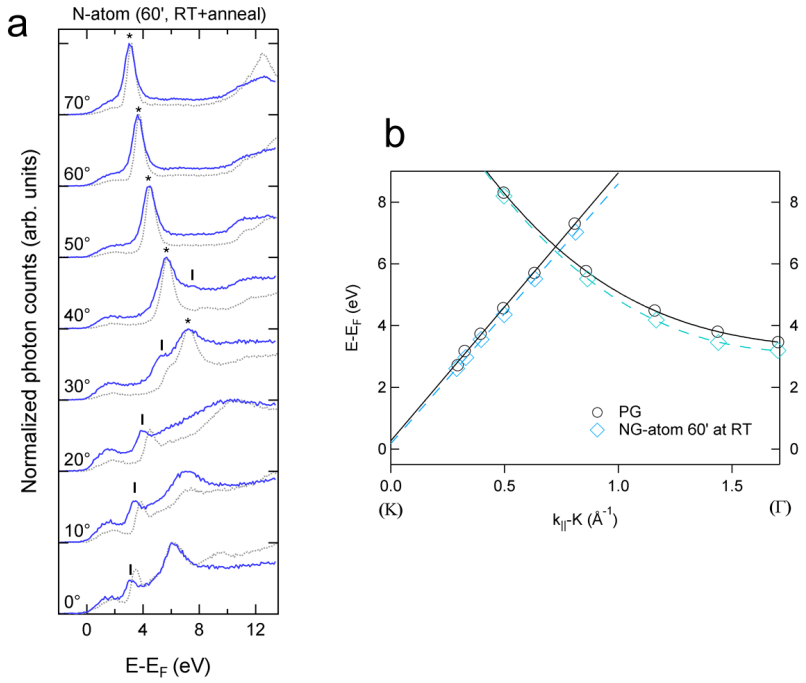

Figure 4.4: (a) ARIPES spectra of the NG sample exposed to N-atoms for 60 min at RT. σ^* and π^* states are marked with vertical bars and asterisks. (b) Dispersion of σ^* and π^* states in $\Gamma-$K of graphene BZ obtained from (a).

carbon replaced by nitrogen) and the little change of the electronic properties for this NG sample (figure 4.2), the pyridinic-N seem to be ineffective for the electronic doping of graphene [53]. More evidence to support the assumption that graphitic-N is more responsible for the unoccupied states variation than pyridinic-N are shown in the next section.

Effects of post-annealing and adsorbates

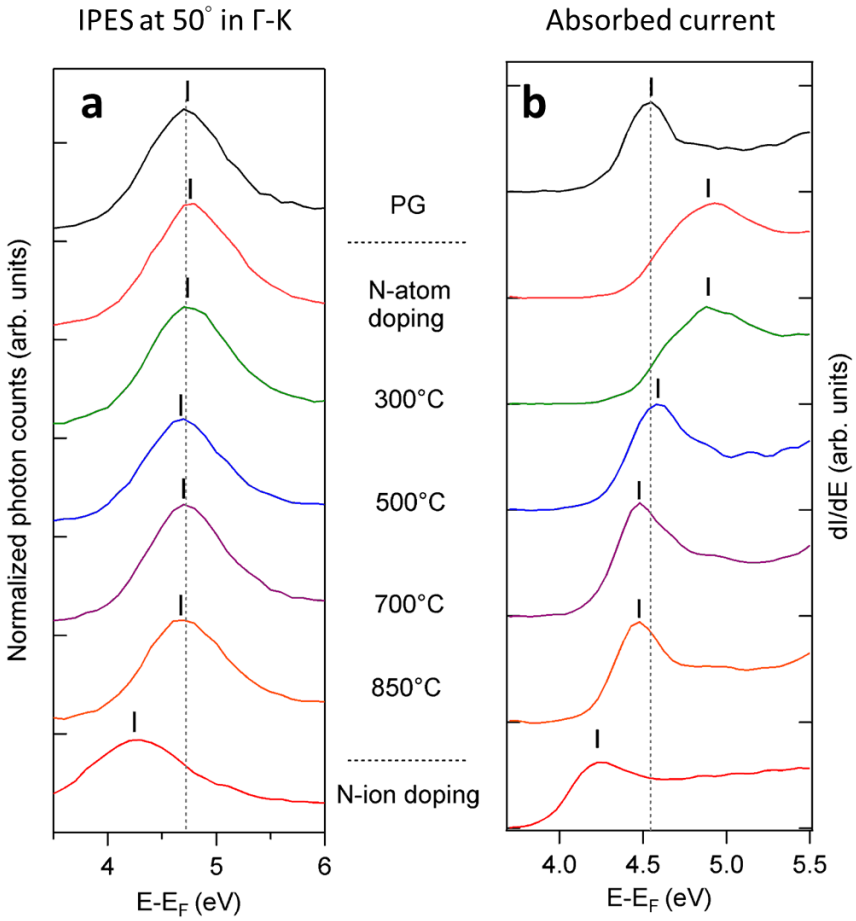

Figure 4.5: Comparison of (a) the π^* states position, obtained by IPES at 50° incidence angle along Γ-K, and (b) the derivative of absorbed current at normal incidence for the studied graphene samples. The location of the maximum of the derivative determines the work function of the sample. From top to bottom, the results are obtained from PG, NG doped by N-atom sequentially annealed to 850°C and NG doped by N-ion of 35 eV at 850°C.

Figure 4.5a and b show the evolution of the IPES spectra and adsorbed current

(TCS) of the PG exposed to nitrogen atoms and subsequently annealed at increasing temperatures. The sensitive work function of PG on SiC determined by TCS is about 4.58±0.05 eV. After the nitrogen exposure, the graphene work function rises about 0.4 eV, and then decreases with increasing annealing temperatures. After annealing at 850°C, the work function of NG-2 decreases to 0.1 eV smaller than the work function of PG. This result is similar to the value reported by Kim *et al*, where they deduced solely from work function measurements that the graphene becomes p-type after the exposure, and turns to n-type after annealing the sample at high temperature [98]. However, in our case, the π^* state measured at 50° incidence, is left unchanged after exposure, which implies a neutral doping. The π^* states then shift toward E_F (n-type doping) following the subsequent annealing at increasing temperatures.

The different behaviors between the work function and the π^* state energy may be explained by the presence of thermally unstable adsorbates after the graphene doping [95]. These adsorbates formed by neutral but activated nitrogen species may only be suppressed by annealing at temperatures larger than 800°C. This indicates a rather strong bonding, most probably a covalent one, of N atoms with graphene C atoms, plausibly nearby defect sites or regions of increased curvature. Owing to the higher electronegativity of the N atom in a C-N bond, the electronic valence charge will be displaced towards the (out-of-plane) N atom. A significant concentration of these polarized bonds may then create a net surface dipole, negatively-charged towards the vacuum, which will increase both the surface barrier height (band bending) and the work function measured by TCS or photoemission spectroscopy (at emission threshold). Similar work function increases have been reported for N adsorption on metallic surfaces [102, 103].

Annealing at high temperature causes the removal of a significant part of these adsorbates. The actual electronic properties of the NG without these surface dipoles can thus be revealed. This is confirmed by the work function and IPES results of NG doped by N-ions of 35 eV at 850°C. Since it is prepared at 850 °C, no adsorbate should remain on the surface, and thus both the work function and the π^* states vary in parallel. Therefore, any accurate determination of the electronic doping in graphene should rely on the position of E_F with respect to the Dirac point, and should not be determined solely by work function measurements [98]. Further study of the temperature effects on the nitrogen doping is shown in the next subsection.

4.1.2 Nitrogen ion doping

According to theoretical studies introduced earlier, it requires N species with higher energy than thermalized neutrals, such as low-energy N ions (>15 eV), to actively substitute carbon atoms in graphene by the incident nitrogen. This substitutional process involves two major stages: the creation of vacancies, *i.e.* knocking out a carbon atom in the graphene lattice using incident nitrogen, and the chemical doping of nitrogen, *i.e.* the formation of in-plane bonds with nearby C atoms to attain a stable configuration.

Due to the complexity of this two-stage process, proper doping and conditions have to be found if high-efficient and good quality nitrogen doping of graphene is envisioned. In this subsection, we present the study of nitrogen doping of graphene using the ion mode of the *in situ* nitrogen plasma source.

Sample temperature during N ion doping

Figure 4.6a shows the ARIPES spectra of the NG exposed to 5 eV N-ions at RT for 5 min (the plasma power is 20 mA for this particular sample). The exposed ion dose is estimated at about $3{\times}10^{15}$ cm^{-2} derived from the average ion current transmitted to both the sample and its holder multiplied by the area ratio of the sample itself. A high temperature annealing is performed after the nitrogen exposure to remove any thermally unstable species, such as physisorbed or out-of-plane bonded nitrogen atoms, as discussed in the previous subsection. At this low energy and high dose, the π^* states of the NG show a small n-type shift (toward E_F) after nitrogen ion exposition as indicated by the sharp peak of the ARIPES spectra of NG (blue curves) *wrt* the spectra of PG (black curves). It also shows a decrease and broadening of the π^*-related peak, which implies a degradation of the π-conjugated structure, possibly a structural damage of the graphene. It should be noted that the ARIPES spectra presented here are normalized to the spectra maximum, thus the relative peak intensity should be compared with the background signal. The LEED image of this NG sample (figure 4.7a) shows a quenching of $(1 \times 1)_G$ and $(6\sqrt{3} \times 6\sqrt{3})R30°$ spots of the PG and BLG, which also supports the degradation of graphene.

Upon further increasing of incident ion energy to 35 eV, with an exposure time to 10 min (at a dose of $\sim 4 \times 10^{15}$ ions/cm^{-2}), no particular feature in unoccupied states can be observed (not shown). The honeycomb structure of graphene seems to be destroyed under such doping condition even after a post-annealing step, as revealed by the absence of its LEED pattern in figure 4.7b. This should be due to the intense ion flux provided by the ECR plasma source that over-damage the honeycomb structure of graphene.

Two different methods were employed in order to reduce this plasma-induced damage: (i) applying multiple cycles of short exposition of 3 min at RT followed by a post-anneal at 850°C for 10 min in order to repair the damage after each exposition cycle; (ii) holding the sample at a high temperature of about 850°C during the N-ion exposition.

Figure 4.6b shows ARIPES spectra of the NG prepared using the first method. The π^* states can be detected but appear attenuated even when doping a 3ML thick PG. The LEED image of the NG prepared with this method shows a very blurred $(1 \times 1)_G$ pattern, as shown in figure 4.7c, indicating that the structure of graphene is still affected by defects.

Figure 4.6c shows ARIPES spectra of the NG prepared using the second method, *i.e.* N-ion exposure at 850°C. The π^* states are better developed in this case, including

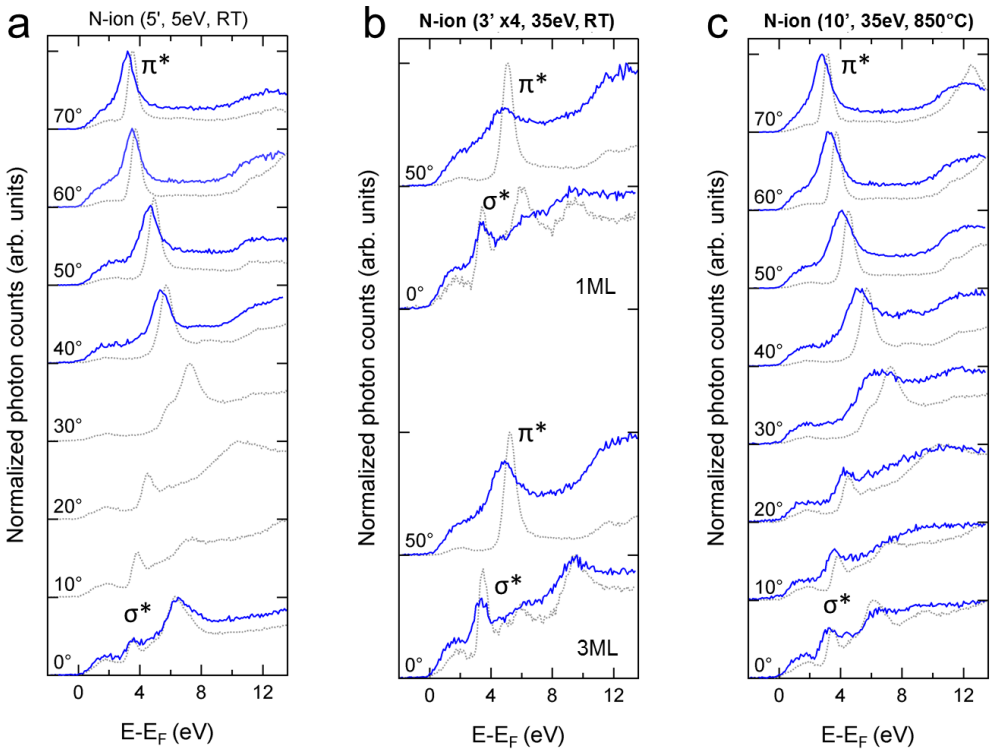

Figure 4.6: ARIPES spectra of NG (blue curves) exposed to (a) 5 eV N-ions for 5 min at RT, (b) 35 eV N-ions for 4 cycles of 3 min at RT plus post-annealing at 850°C, and (c) 35 eV N-ions for 10 min while sample is held at 850°C. ARIPES spectra of PG in black dotted curves are shown for comparison.

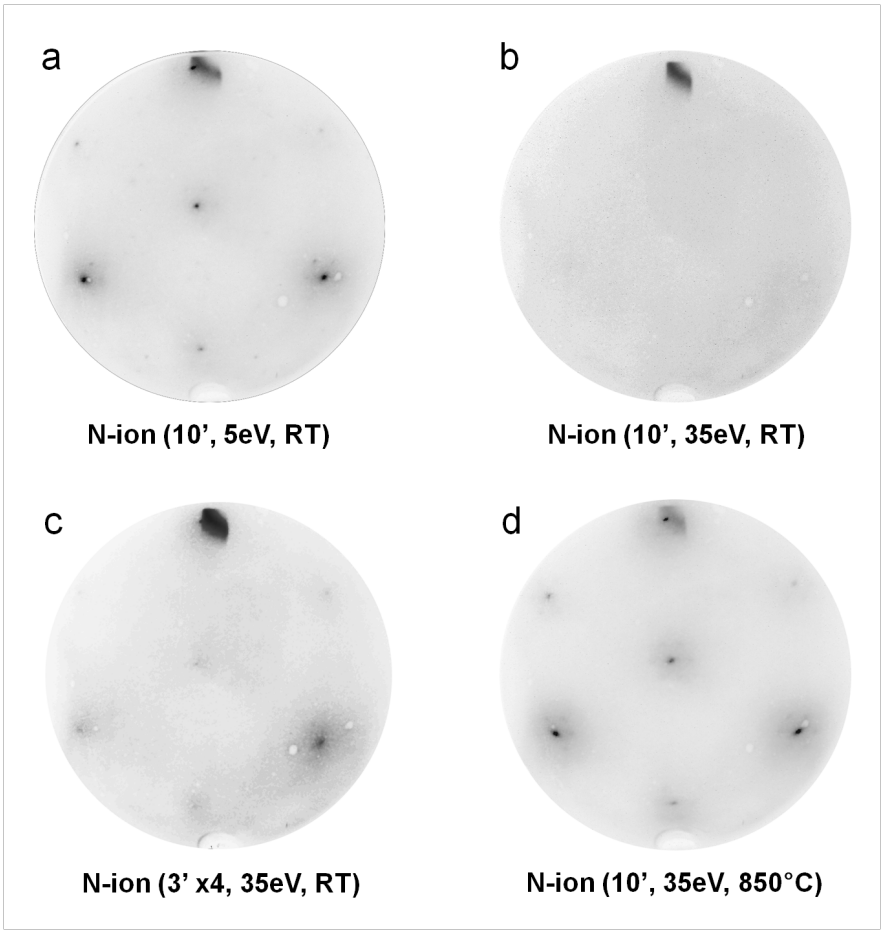

Figure 4.7: LEED images of NG exposed to (a) 5 eV N-ions for 5 min at RT, (b) 35 eV N-ion for 10 min at RT (c) 35 eV N-ions for 4 cycles of 3 min at RT plus post-annealing at 850°C, and (d) 35 eV N-ions for 10 min with sample hold at 850°C.

a broadening and a n-type shift of the entire π^* band. The LEED image of NG prepared at 850°C also confirms that the honeycomb structure is much better preserved, as shown in figure 4.7d.

These results demonstrate that using a high-temperature process for the nitrogen ion doping can help the structure of graphene to sustain such intense ion exposure. Therefore, all N-ion exposition that are mentioned in the following are proceeded at a sample temperature of 850°C.

Chemical states of doping nitrogen in graphene using N-ion doping

In order to actively substitute carbon atoms in graphene, the energy of the incident nitrogen species needs to reach a minimum displacement threshold (∼15-22 eV), as introduced earlier. At these incident energy, an incident N ion would lose most of its kinetic energy after striking out a graphene C atom. It would stay at the top graphene layer and forms in-plane bonds with neighboring C atoms. If the incident energy is above this level, N ions may not stay in the graphene and defects like vacancies are generated, which may cause the degradation of the graphene. It may also cause the generation of more complex N doping configurations. In the following, the effect of the incident energy of nitrogen ions in the doping process is investigated by revealing the chemical environment of the resultant doping nitrogen using XPS.

In this study, multiple NG samples are prepared by exposing PG monolayers hold at 850°C to a mix of neutral N species and low-energy N-ions, which ion energy is varied from 5 eV to 60 eV for different samples. Figure 4.8 shows the N 1s spectra of these NG samples doped by the nitrogen ion stream at different incident energy but at nearly equivalent dose of 3-4×10^{15} ions/cm^2. The energy of the incident N-ions for each NG sample is indicated in the brackets, in figure 4.8. Much different from the NG exposed to N-atom, which contains a majority of pyridinic-N, the N 1s spectra of the NG samples doped with low-energy ions generally show two dominant components, which N 1s peaks are located around 398.2 and 401.2 eV. The component at about 398 eV is assigned to pyridinic-N as also found in NG doped by N-atom. The other major component at higher BE of ∼401.2 eV is assigned to graphitic-N, which is bonded to three neighbor carbon atoms in sp^2 configuration. Two other components with much lower intensities are located between the two large peaks (∼399.2 eV) and at highest BE (∼403.1 eV). The former component can be attributed to pyrrolic nitrogen, whereas the latter, the high BE one, to N-O type species that remain after the pre-annealing of *ex situ* XPS measurements.

To simplify, we assume that most of the incorporated N atoms are located at the topmost monolayer of graphene at these low energy N-ion exposure (<60 eV). This is in accordance with the C 1s and Si 2p spectra, in figure 4.9, showing no particular difference at BLG-related features and no additional Si-N bonds are observed after nitrogen doping. The ARIPES spectra of these NG also show no significant differences for the substrate-related or interface-related features, indicating a negligible amount of

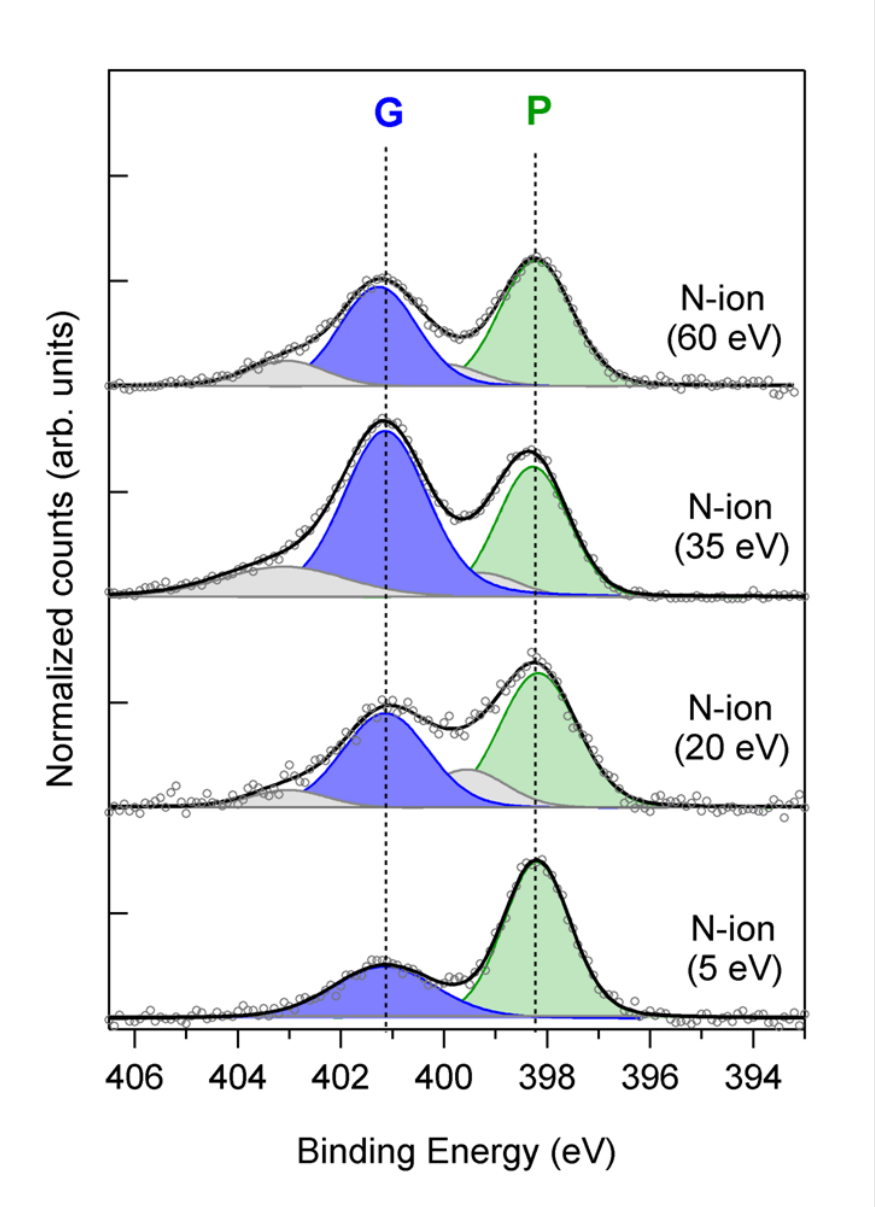

Figure 4.8: N 1s XPS spectra of the studied NG samples exposed to N-ions with energies of 5-60 eV at an equivalent dose of about 3-4$\times 10^{15}$ ions/cm^2. The experimental data (dots) are fitted with a set of Gaussians. The position of the peaks assigned to graphitic-N (blue) and pyridinic-N (green) are marked as G and P, respectively. All the N 1s spectra are normalized to the area of the corresponding Si 2p peak, which is nearly constant for all the samples.

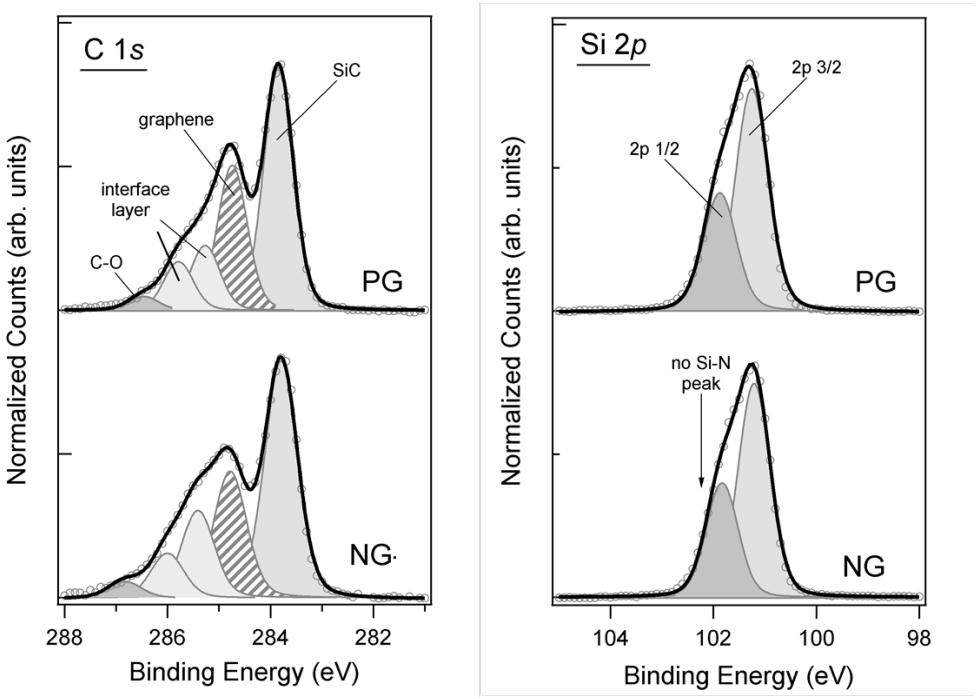

Figure 4.9: XPS C 1*s* and Si 2*p* spectra of PG and NG samples. The arrow indicates the absence of an extra peak, which would be assigned to Si-N at its expected binding energy with respect to Si-C, for both PG and NG.

incorporated nitrogen at the interface (buffer layer) and the SiC bulk. In addition, it appears that no physisorbed N_2 remain on these samples exposed to air prior to the *ex situ* XPS measurements, as revealed by the absence of any component at high BE of 405-408 eV. This is not unexpected since a 600°C annealing was made before every XPS measurement in order to desorb any physisorbed species. Furthermore, we also exclude the possibility of any intercalated N. Indeed, if intercalated N were present in our case, it should most probably decouple the buffer layer and transform the sample from a monolayer to a bilayer graphene, which should broaden and increase the intensity of the π^* states [104]. Since the π^* states intensity appears decreased after N doping, as shown in the next sub-subsection, intercalated N species likely are present in the studied case.

Figure 4.8 also shows that the relative intensity of the two components in the N 1*s* spectra varies with the incident ion energy. After a N-ion exposure at 5 eV, the concentrations of graphitic-N and pyridinic-N are 3.5% and 6.8% *wrt* the amount of carbon atoms in a monolayer graphene. At 20 eV, the resulting NG possesses 5.0% and 6.5% of graphitic-N and pyridinic-N, respectively. When increasing incident N-ion energy to 35 eV, the concentration ratio of graphitic-N (8.0%) and pyridinic-N (5.3%) increases to ∼1.5, reaching its maximum value among the studied monolayer NG. At even higher incident ion energy of 60 eV, the concentration of graphitic-N and pyridinic-N are 4.6% and 5.7%, respectively, showing a decrease of graphitic-to-pyridinic ratio. This indicates an optimum energy of about 35 eV for the generation of graphitic-N species in graphene using this MW-ECR plasma source.

Despite the creation of a majority of graphitic-N, which is expected to induce stronger electronic doping of graphene, high concentrations of pyridinic-N are also incorporated simultaneously. This maybe because the first step of the graphitic-N doping process (the creation of single vacancies) may have a higher yield than the second (the incorporation of N atoms). High density of single vacancies that are less stable may lead to the formation of more energetically-stable double-vacancies by merging two single one. These double-vacancies may then favor the formation of pyridinic-N through the addition of an activated N atom. Thus, if large numbers of vacancies are created during nitrogen exposure, pyridinic-N may be generated spontaneously. To suppress the amount of pyridinic-N and to gain the domination of graphitic-N in the resultant NG sample, the creation of defects during nitrogen plasma exposure has to be restrained. Possible paths to achieve this goal are either to remove the reactive N atoms out of the N-ion stream suppressing the formation of pyridinic-N, or to reduce the total flux of the nitrogen exposure, slowing the defect creation and allowing the formation of graphitic-N before single vacancies merges into double vacancies. However, none of these two methods has been tried during this thesis due to the limited time and especially the limitation of the experimental setup, which might need important modifications to be able to cope with the two proposed method. In contrast, we have found that the creation of pyridinic-N can be suppress in the case of a bilayer (or multilayer) graphene, as discussed later in this chapter.

Two NG samples that are exposed to N-ions are also investigated using Raman spectroscopy, as shown in figure 4.3. One sample is exposed to 35 eV N-ion for 10 min (the one presented above), the other one is exposed to 20 eV N-ion for 30 s. Their Raman spectra both show the annihilation of the 2D band, the attenuation of the G band, and the emergence of the defect-related D band. This confirms the presence of defects, most probably the doping nitrogen, in the graphene monolayer. It is also very similar to the Raman spectra of the NG sample exposed to N-atom, as discussed earlier, except that for N-ion exposure the Raman spectra show a small red-shift of the graphene modes. It implies that the incorporation of graphitic-N may induce some phonon softening. However, we are not able to identify any graphitic-N-related G' band right next to the G band, as reported in the literature [50]. This should be due to the difficulty to obtain the graphene Raman modes (G and D band) when it is grown on SiC, since these Raman modes are in superposition with the Raman modes of the SiC substrate. Despite that the graphene Raman spectrum can be extracted after subtracting the Raman spectrum of SiC substrate, its signal resolution is still limited [56].

Nevertheless, the above results indicate that, with current experimental setups and conditions, graphitic-N are formed most efficiently when exposing graphene under a ∼35 eV N-ion stream. Furthermore, by combing the nitrogen doping using thermalized neutral species, we show that it is possible to control in some way the bonding configuration of the doping nitrogen by exposing to different nitrogen species with chosen incident energy.

Unoccupied states of NG using N-ion doping

As shown in several theoretical simulations studies, the electronic structure of graphene is largely modified, especially by graphitic-N [53, 101]. Therefore, we expect that using low-energy N-ion exposition, which favors the creation of graphitic-N, the band structure of the NG would be more markedly altered. In this subsection, the unoccupied states of the NG prepared using various N-ion energy and doses are investigated.

First, we begin by the investigation of the NG samples exposed to a fixed N-ion energy of 20 eV but at different doses. We expect that the amount of graphitic-N increases with the exposition dose and plays the major role in the tailoring of unoccupied states of graphene. Here, the N-ion exposition at 20 eV is chosen because, at higher ion energy, the creation of defects/vacancies might dominate the substitutional doping and, at lower energy, the formation of pyridinic-N is favored. Figure 4.10a-c shows the ARIPES spectra of the graphene samples exposed to 20 eV N-ions at increasing doses, 2×10^{14}, 6×10^{14}, and 2×10^{15} cm^{-2}, respectively. The positions of the π^* and σ^* states show little differences at low doses (figure 4.10a and b) but exhibit obvious an n-type shift of ∼0.2 eV toward E_F when increasing the dose to 2×10^{15} cm^{-2} (figure 4.10c).

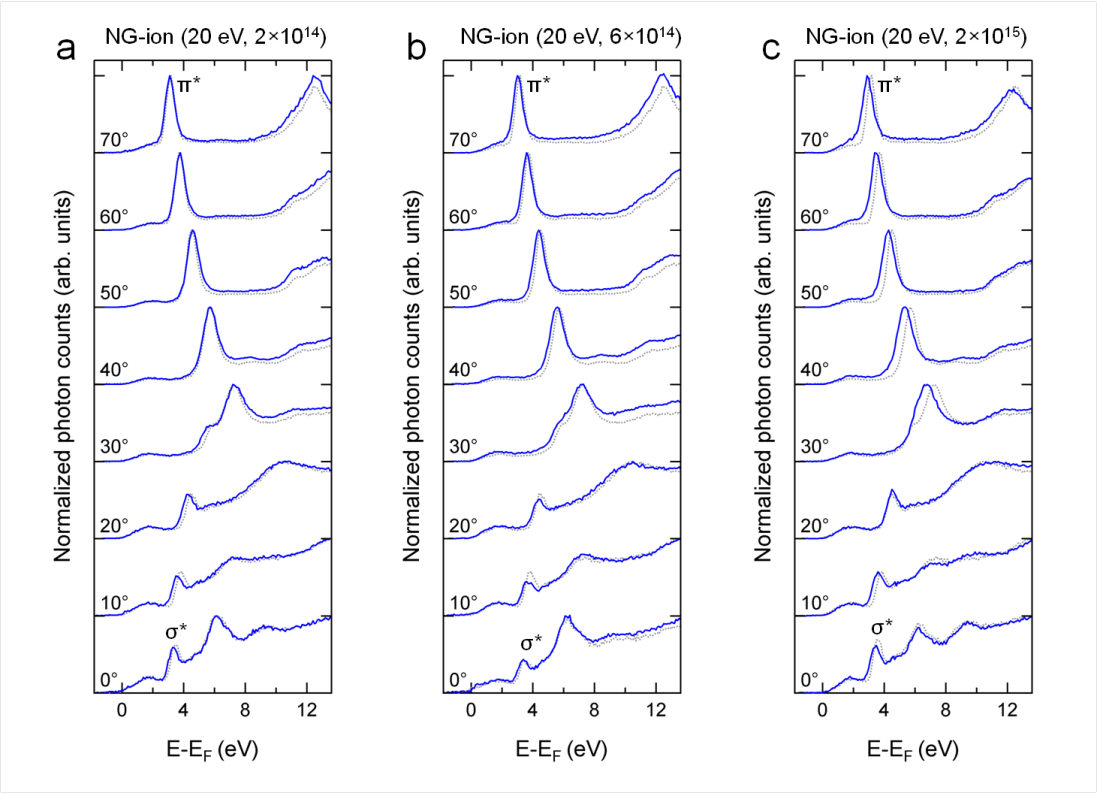

Figure 4.10: ARIPES spectra (blue curves) of the graphene samples exposed to 20 eV N-ion at (a) 2×10^{14}, (b) 6×10^{14}, and (c) 2×10^{15} ions/cm^{-2}. The ARIPES spectra of PG in gray dotted curves are also shown for comparison.

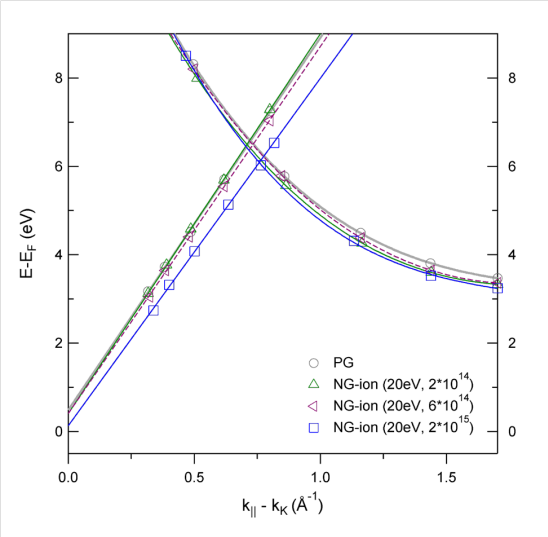

Figure 4.11: The k-dispersion of the π^* and σ^* states along $\Gamma - K$ of graphene BZ of the studied NG samples shown in figure 4.10.

The $k_{||}$ dispersion of these π^* and σ^* states are shown in figure 4.11. The symbols represent the $k_{||}$ position of the π^* and σ^* states deduced from the ARIPES spectra (figure 4.10). The approximate position of the Dirac point relative to E_F is estimated by the linear extrapolations of these π^* states, shown by the straight lines. The parabolic curves are eye-guides for the σ^* states dispersion by fitting with a second order polynomial. The respective $k_{||}$ values are obtained using equation 3.1 using the corresponding work function obtained by TCS, which is 4.53 eV for the first two samples, and 4.4 eV for the latter. The $k_{||}$ dispersions of the π^* and σ^* states of PG (black circles) and the assessed extrapolation of its band dispersion up to the K point (thick grey line) are also shown for comparison.

As far as the dispersion relation $E(k)$ of the π^*-states of pristine and N-doped graphene are concerned, several band-structure calculations have been devoted to the subject, where some of them include localized defects. For example, Rani *et al.* studied the band structure of nitrogen-doped graphene (NG) (defect-free) at various concentrations using *ab initio* calculations, considering different doping sites [101]. Recently, Hou *et al.* studied the band structure of NG with the presence of vacancies and Stone-Wales defects [53]. Both studies, as well as other similar works, show the opening of an energy gap at the Dirac point of NG, a n-type shift of the entire band structure *wrt* E_F along with a decrease in the slope of π and π^* bands of NG when the nitrogen occupies the graphitic-like doping site. These last two features are clearly seen in our results, through the experimental dispersion of the π^* states, accessible in ARIPES.

As shown in figure 4.10, the dispersions of the π^* states of NG exhibit large differences at various doses. For the lowest N-ion dose of 2×10^{14} cm^{-2} at 20 eV, the π^*

dispersion is closely identical to the pristine one. When exposed to higher N-ion dose of 6×10^{14} cm^{-2}, the slope of π^* dispersion decreases accompanied by a very little n-type shift (<0.1 eV) of the relative position of Dirac point. At much larger dose of 2×10^{15} cm^{-2}, a significant n-shift of the entire π^* band is observed and the slope of the π^* band is further decreased. The relative position of the Dirac point under this doping condition is shifted ∼0.35 eV toward E_F indicating a strong n-type character, which should be due to the doping of large amount of graphitic-N. In contrast, the σ^* states slightly shift ∼0.1-0.2 eV toward E_F for only a small dose of N-ion. The increment of this shift is barely detectable (<0.1 eV) at higher doses.

4.1.3 Discussion of *in situ* nitrogen plasma-based doping process

We further study the unoccupied states of a whole series of NG samples prepared using various energies and doses to get a global picture of the N-ion doping effects on the electronic structure of NG. Figure 4.12 shows the condition mapping of the investigated NG-ion samples. These NG are prepared by exposing PG to N-ions at energies in the range of 5 to 60 eV with estimated doses of 2×10^{14} to 4×10^{15} ions/cm^{-2}. It should be noted that the honeycomb structure of the NG keeps at relatively well under these doping conditions, as revealed by LEED (not shown). The ARIPES spectra of the samples that are not discussed above are shown in figure 4.13. The analysis results of each NG sample, including their π^* and σ^* states locations, dispersions and their work functions, are summarized in table 4.1. The shifts of the σ^* and π^* states of these NG samples are obtained *wrt* the location of σ^* and π^* states of PG. In addition to the NG doped by N-ion, the analysis results of the NG exposed to neutral nitrogen species are also listed in the same table for comparison.

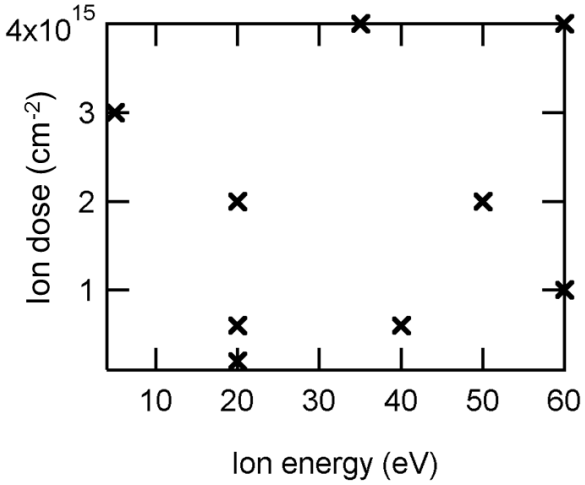

Figure 4.12: The condition mapping (energy and dose) of the investigated NG-ion samples

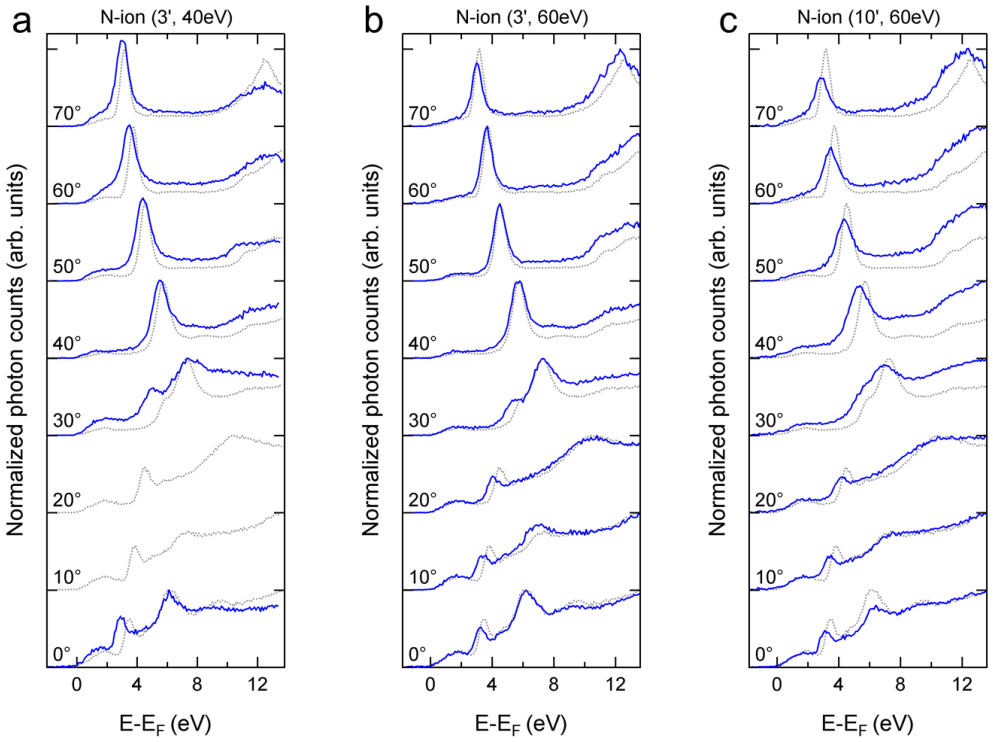

Figure 4.13: ARIPES spectra (blue curves) of the NG samples exposed to N-ions at (a) 40 eV for 3 min, (b) 60 eV for 3 min, and (c) 60 eV for 10 min. The ARIPES spectra of PG in gray dotted curves are also shown for comparison.

Table 4.1: Summary of the doping process conditions, electronic/chemical properties of the studied NG samples.

Doping process condition							Electronic/chemical property							
doping mode	expose time (min)	ion energy (eV)	estim. dose ($ions/cm^{-2}$)	estim. dose ($atoms/cm^{-2}$)	sample temp.	post anneal	σ^* at Γ point (eV)	σ^* shift (eV)	Ext. π^* at K point (eV)	π^* shift (eV)	estim. v_F (m/s)	W_Φ (eV)	N_G (%)	N_P (%)
PG	-	-	-		-	-	3.47	0.00	0.48	0.00	1.28×10^6	4.58	-	-
Atom	60'	-	-	9.0×10^{18}	850°C	-							1.8	10.1
Atom	60'	-	-	9.0×10^{18}	RT	850°C	3.4	-0.07	0.37	-0.11	1.27×10^6	4.53	2	16.9
Atom	10'	-	-	1.5×10^{18}	RT	850°C							0	0.8
Atom	10'	-	-	1.5×10^{18}	850°C	-						0.5	0.8	
Ion	5'	5	3×10^{15}	1.5×10^{18}	RT	850°C	3.37	-0.10	0.28	-0.20	1.25×10^6	4.5	3.5	6.8
Ion	1'	20	2×10^{14}	1.5×10^{17}	850°C	-	3.33	-0.14	0.42	-0.06	1.30×10^6	4.53		
Ion	3'	20	6×10^{14}	4.5×10^{17}	850°C	-	3.36	-0.11	0.40	-0.08	1.26×10^6	4.53		
Ion	4'	20	2×10^{15}	6.0×10^{17}	850°C	-	3.30	-0.27	0.13	-0.36	1.19×10^6	4.4		
Ion	15'	20	4×10^{15}	2.3×10^{18}	850°C	-							5	6.5
Ion	10'	35	4×10^{15}	1.5×10^{18}	850°C	-	3.09	-0.38	0.13	-0.35	1.20×10^6	4.3	8	5.3
Ion	3'	40	8×10^{14}	4.5×10^{17}	850°C	-	3.2	-0.27	0.40	-0.08	1.25×10^6	4.4		
Ion	3'	60	1×10^{15}	4.5×10^{17}	850°C	-	3.15	-0.32	0.31	-0.17	1.27×10^6	4.43		
Ion	10'	60	4×10^{15}	1.5×10^{18}	850°C	-	3.13	-0.34	0.13	-0.36	1.27×10^6	4.43	4.7	5.6

estim. = estimated ; temp. = temperature ; Ext. = extrapolation of ; W_Φ = work function ; N_G graphitic-N ; N_P pyridinic-N

The value of π^* and σ^* shifts are obtained *wrt* the value of PG, the estimated v_F are obtained from the slope of the π^* dispersion.

The characteristics of these NG samples, *i.e.* σ^* shift, π^* shift and the estimated Fermi velocity (v_F), are further investigated by fitting these values and their corresponding incident ion energy and dose with a 2-degree polynomial plane. Figure 4.14 shows these fitted polynomial planes, in 3D and 2D contoured representations. Figure 4.14a,b demonstrate the trend of the σ^* shift with various incident N-ion energies and doses, whereas figure 4.14c,d and e,f show their counterparts in π^* shift and the estimated v_F, respectively.

Figure 4.14a,b shows that the σ^* band generally exhibits greater negative shifts (n-type shift) with increasing ion doses. At lower doses $< 1 \times 10^{15}$ cm^{-2}, N-ions with an energy of about 40 eV induce the greatest σ^* shift, while at a higher dose of 4×10^{15} cm^{-2}, the σ^* shifts are larger with increasing incident N-ion energy.

The shifts of the π^* states show similar trend, *i.e.* the n-type shift of the π^* states increases with exposition dose, as shown in figure 4.14c,d. Though, for a certain dose, the maximum π^* shift seems to occur around 35 eV and 40 eV for lower and higher doses, respectively.

The values of the Fermi velocity (v_F) of these PG and NG samples are also estimated based on the slopes of the π^* band dispersions, which are obtained from the linear fitting of the π^* states dispersion in ARIPES spectra. By assuming a linear dispersion of the π^* band at these $k_{\|}$, we use the equation $v_F = dE/(\hbar\sqrt{dk_x^2 + dk_y^2})$ (which we simplified by $k_x = k_{\|}$ in Γ-K and k_y=0) to calculate the v_F of the PG and NG. We obtain a v_F of $\sim$1.28×10^6 m/s for the PG grown on the Si face of SiC, which is not far from the reported value of 1.1×10^6 m/s in the literature [83, 105]. The v_F of the NG samples are generally slightly lower, as shown in table 4.1.

However, one should note that these v_F values are obtained from the unoccupied π^* states away from the Dirac point. They may not represent the actual v_F of the electron near E_F and the Dirac point, which are responsible for the carrier transport in graphene. In addition, most reported v_F are experimentally obtained from the occupied π band of graphene (the lower Dirac cone), instead of the unoccupied band (the upper Dirac cone) as in this work, which is less studied so far. The theoretical and experimental studies show that v_F is sensitive to carrier concentration [106], the curvature of the graphene sheet [107], the periodic potential [108], and dielectric screening [109], due to many-body interactions such as electron-plasmon, electron-electron, and electron-phonon interactions [106]. These could be the origin of the v_F difference obtained from the occupied and unoccupied band structure of the graphene.

Nevertheless, v_F seems to decrease with increasing ion dose at lower ion energy (<40 eV), as shown in figure 4.14c. But at higher energy of >40 eV, the incident ion seems to have little effect on the v_F value. The minimum v_F occurs at about 35 eV for lower dose and $\sim$20 eV for higher dose.

By comparing the three sets of contour plots, the effectiveness of N-ion doping in σ^*-, π^*-shift and v_F, we can summarize that, at a lower dose of about 1×10^{15} ions/cm^{-2}, the N-ion energy of about 35 eV affects the electronic properties of graphene most efficiently. This conforms with (and lies between) the minimum displacement threshold

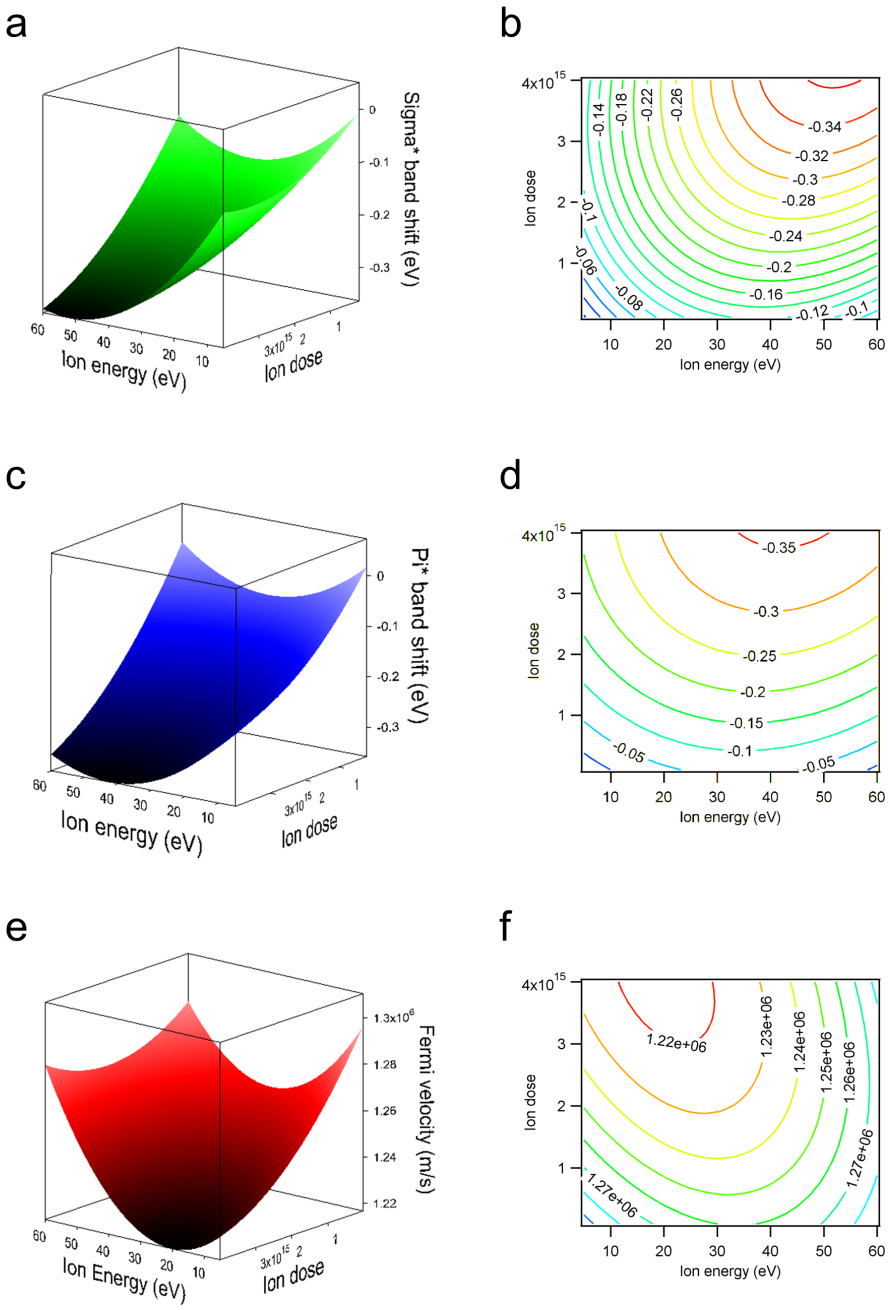

Figure 4.14: The 3D and 2D contour plots of the fitting curved plane of (a,b) σ* shift, (c,d) π* shift, and (e,f) the slope of the π* dispersion, respectively.

of 15-22 eV for a carbon atom in graphene and the optimum substitutional probability at 50 eV using N predicted by atomistic simulations [96, 110]. It also confirms that graphitic-N species are responsible for the n-type doping, as a maximum concentration of graphitic-N is found for NG prepared at 35 eV.

However, after exposing to a large N-ion dose of $\sim 4 \times 10^{15}$ cm^{-2}, the σ^* shift, π^* shift and v_F vary differently. The σ^* shift is more important at higher N-ion energy but the v_F decreases more significantly at lower N-ion energy. It is suggested that many defects are created and too many nitrogen atoms are incorporated in the graphene lattice at such high dose, which may strongly disturb the original nitrogen-substitution system. The nature of this difference may be due to the increasing formation of complex nitrogen doping configurations, *e.g.* multiple nitrogen atoms doped next to the other. They would modify the electronic structure of graphene much differently than when the doped nitrogen atoms are well separated from each other [53]. It may also be due to the formation of C-N composites (or nanoclusters) on the graphene surface. These composites may induce charge transfer without modifying the graphene lattice, similar to the case of molecular doping. Thus, they would not open a gap or decrease the v_F of the graphene. One should also consider that at higher N-ion energy some doping nitrogen may be found in the BLG, which would induce less n-doping to the topmost graphene layer but would still be counted in XPS analysis. A better understanding of this situation would require atomic scale investigations, like STM. The preliminary microscopic study of these NG actually shows the presence of both complex nitrogen doping configuration and large surface impurities (see chapter 7). The surface imaging was however very difficult due to large amount of surface impurity and maybe some oxidation of the defective NG during *ex situ* transportation. An *in situ* STM analysis may be envisioned for further studies.

Theoretically, by knowing the density of states (DOS) distribution of graphene, the magnitude of its electronic doping (the shift of its E_F) can be obtained by calculating the number of states that can be filled (or emptied) by the total additional charge transferred from the dopant to the graphene (or *vice versa*). Since the electronic states of graphene near E_F construct the linearly dispersive Dirac cone, the relationship between the Dirac point energy (E_D) *wrt* E_F and the charge-carrier concentration n can be described using the following equation: $\Delta n = \frac{\Delta E_D^2}{\pi(\hbar v_F)^2}$ where $\hbar$ is the Planck's constant h divided by 2π, and v_F is the Fermi velocity (describing the dispersion slope of the Dirac cone). The change of charge-carrier concentration before and after doping indicates the total charge transferred from the dopant to the graphene. By knowing the atomic (or molecular) concentration of the dopant, we can calculate the mobile charge contribution of a single dopant (by assuming all the dopants are in the same doping configuration).

Zhao *et al.* have shown that a n-type doping of -0.27 eV of graphene is induced by 0.34% of graphitic-N, based on STM/STS measurements. By assuming $v_F = 1 \times 10^6$ m/s and an undoped pristine graphene, they estimate a charge transfer of 0.42 electron per N atom [41]. Joucken *et al.* have claimed a charge transfer of 0.8 electron for a

single graphitic-N, which induces a -0.42 eV shift of the E_F at a total N concentration of 0.6% [52]. On the other hand, their theoretical studies predict a charge transfer of 0.55 electron per N atom at the same concentration. An earlier theoretical work of Lherbier *et al.*, also predicts a -0.4 E_D for a 0.5% of randomly doping nitrogen, compatible with a charge-transfer of 0.6 electron per graphitic-N [58].

In this study, the graphene grown on SiC(0001) is initially *n*-doped due to substrate-induced doping. The E_F is found at about 0.35-0.4 eV above the Dirac point (E_D=0.35-0.4 eV), and the intrinsic carrier density of PG on SiC(0001) is estimated to be about 1×10^{13} e/cm^2. This initial condition of graphene is much different than in the literature, where generally a quasi-undoped graphene decoupled from the substrate is studied, *e.g.* graphene grown on the C-face SiC or deposited on SiO_2/Si wafer. When considering the nitrogen doping in this case, we have to consider a lower initial position of E_D and larger charge-carrier density. Taking the NG sample exposed to 35 eV N-ions for example (figure 4.8), if we assume that 8% of graphitic-N are ideally substituted in the graphene grown on SiC(0001), while each N atom contributes 0.6 mobile carrier electron, the E_F should be brought to 1.62 eV above Dirac point (assuming $v_F = 1\times10^6$ m/s), corresponding to a *n*-type shift of ∼1.2 eV due to the doping nitrogen. The actual *n*-shift obtained by the extrapolation of the π^* states (∼0.35 eV) is much smaller than the expected value of 1.2 eV. If we try to compute the charge transfer of a doping nitrogen using our experimental value (*e.g.* for the NG exposed to 35 eV N-ions the v_F=1.2×10^6 m/s, E_F shift=-0.35 eV, and 8% of graphitic-N), the value would be around 0.06-0.1 electron per doping nitrogen (for a graphitic-N concentration of >3.5%), much smaller than expected.

Many reasons may be at the origin of this discrepancy with the values reported in the literature. First, some of the graphitic-N may actually be in a much complex doping configuration at such high N concentration, *e.g.* multiple graphitic-N inside a hexagonal ring or a graphitic-N near a pyridinic-N. Theoretical simulations show that the graphitic-N in these complex doping sites may contribute less electrons to the graphene, thus, the actual effect on E_D would be much smaller than if they are separated in single doping sites. Secondly, the electronic doping via the incorporation of nitrogen actually differs from the substrate-induced doping, the adsorbed molecule or metal doping and the field effect doping. In the case of the other types of doping, the electronic structure of graphene remains close to the pristine one but merely exhibits a rigid *n*-shift of the E_F *wrt* its band structure. By contrast, the chemical doping of nitrogen actually changes the electronic properties of graphene, especially at higher doping concentration than 0.5%. A band gap may be created and a decrease of v_F is expected, which should greatly modify the DOS of the graphene near E_F [101]. The actual relationship between the concentration of doping nitrogen and the position of E_F would thus be different. Furthermore, at sufficiently high doping concentration (>2%), quantum interference and localization effects start to influence the carrier transport inside the graphene [58]. This also implies the onset of a coupling effect (probably a repulsive one) between different dopants, which may attenuat the actual charge transfer

from the doping graphitic-N to the graphene. It attenuates the effective doping, thereby promoting a smaller band shift *wrt* E_F. Finally, the electronic properties, *e.g.* v_F, E_D, of the studied NG are obtained in this work from the unoccupied states away from Dirac point, as revealed by ARIPES. This may not be accurate enough to describe the actual electronic structure near the Dirac point, as also discussed earlier, especially as the Dirac point is below E_F. All the above effects may contribute to the rather inefficient electronic doping (E_D shift) by the doping graphitic-N in the studied NG. A better understanding of the real causes would need a thorough investigation of the electronic band structure near E_F and a detailed microscopic study of the actual N doping configuration, which are unfortunately not yet completed to date due to the limited time and resources allocated to this thesis.

Thickness dependence

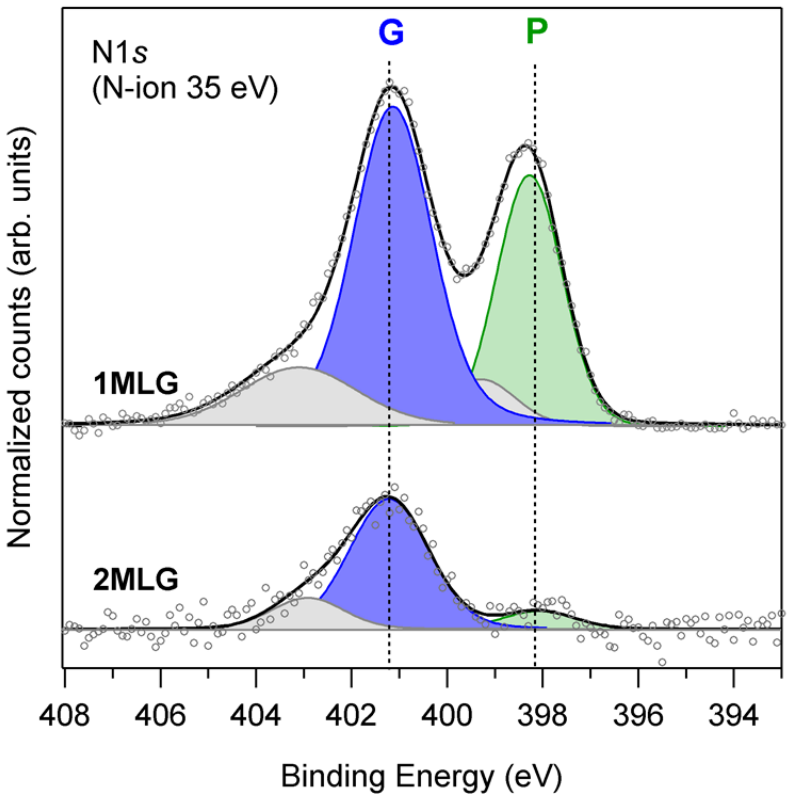

Figure 4.15: XPS N 1*s* spectra of monolayer NG and bilayer NG, exposed to 35 eV N-ion using *in situ* MW-ECR plasma source.

The above results of *in situ* nitrogen doping are obtained using PG samples of 1-1.5 ML. Though, at the later stage of this thesis, studying *ex situ* doping processes (see section 4.3), a graphene thickness dependence on the bonding configuration of the doping nitrogen is found. This thickness-dependent behavior is also confirmed using *in situ* plasma source. As shown in figure 4.15, the N 1*s* spectra of monolayer NG and bilayer NG exposed to 35 eV N-ion at an equivalent dose of 4×10^{15} cm^{-2} show that much less pyridinic-N are created on bilayer graphene ($\sim$0.4%, instead of 5.7% for monolayer NG). On the other hand, the formation of graphitic-N, though slightly decreased, is still effective in the bilayer NG, with a final concentration of 3% (while it is 8% for monolayer NG). It clearly indicates that defects and defect-related N-species (*e.g.* pyridinic-N) are more easily created on the monolayer graphene. The bilayer graphene seems more robust by suppressing the incorporation of nitrogen atoms, especially the defect-related pyridinic-N.

A similar effect has been observed using hydrogen plasma etching of graphene [111]. They found that the H-plasma etching rate on monolayer graphene is much faster and isotropic. For bilayer (or multilayer) graphene, the etching rate is slower, anisotropic and pre-existing-defect-dependent. This may be due to a different chemical reactivity between monolayer and multilayer graphene that might be related to the thermodynamically unstable nature of the 2D mono-atomic layered structure. The actual cause(s) of this thickness-dependence in the plasma-based doping process remains elusive to date [98].

The unoccupied band structure of the NG prepared from the bilayer PG is also studied by ARIPES. Figure 4.16 shows the ARIPES spectra of this sample (2ML-NG) and its corresponding $k_{\parallel}$-dispersion of σ^* and π^* states. The position of σ^* at Γ point shifts 0.36 eV toward E_F *wrt* the PG one, which magnitude is very close to the result obtained on 1MLG (0.38 eV). The position of the estimated Dirac point shifts 0.52 eV toward E_F and the v_F is decreased to 1.1×10^6, which are even more significantly than for 1ML-NG (0.35 eV, 1.2×10^6). The corresponding charge transfer of the 3% of graphitic-N obtained using the above values is 0.34 electron per N atom, which is much closer to the reported value (0.5-0.6). This indicates a more efficient electronic doping for bilayer NG and implies that the doping nitrogen may be mostly single graphitic-N sites rather than complex doping sites.

4.1.4 Summary

In summary, in order to perform nitrogen doping of graphene "actively" using N-ion exposure, especially with the goal of obtaining a majority of graphitic-N for the electronic doping of graphene, an average N-ion energy of 20-35 eV seems to be the most efficient condition. The use of bilayer (or multilayer) graphene may further improve the electronic doping efficiency by suppressing the formation of defects and pyridinic-N. On the other hand, a monolayer graphene with pre-existing (or pre-created) defects favors the incorporation of pyridinic-N. Furthermore, a high temperature doping process

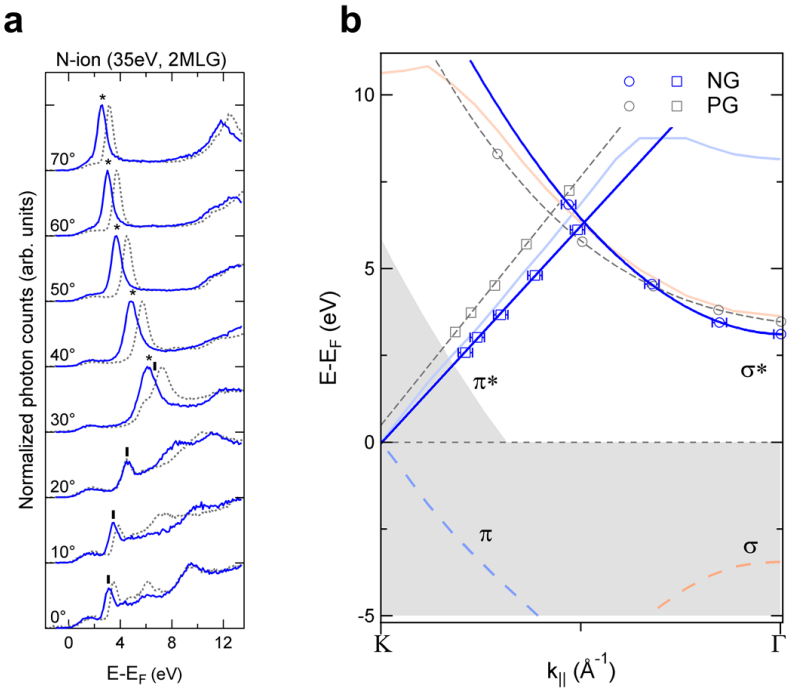

Figure 4.16: (a) ARIPES spectra of the bilayer graphene exposed to N-ions at 35 eV. σ* and π* states are marked with vertical bars and asterisks. (b) Dispersion of σ* and π* states in $\Gamma-$K of graphene BZ obtained from (a).

(∼850°C) may enable a higher doping level of graphene, while maintaining the integrity of the sp^2 honeycomb thanks to its self-repair mechanism.

4.2 *In situ* nitrogen doping of graphene grown on C-face SiC

The same *in situ* plasma-based nitrogen doping procedure was also carried out on the graphene grown on SiC(000$\bar{1}$) at 850°C. As discussed earlier in section 3.2, the pristine graphene grows by stacks of multi-layers with various orientations on the SiC C-face. Figure 4.17a shows the LEED image of the pristine multilayer graphene grown on SiC(000$\bar{1}$) showing a mix of graphene (1×1) spots and arcs due to the disorientation of graphene layers. The LEED image is obtained with sample rotated 15° *wrt* the Γ-M azimuth of SiC(000$\bar{1}$) (Γ-M$_{SiC}$), corresponding to the Γ-K direction of the most intense graphene (1×1) arc of the studied sample (the vertical direction of the LEED images). Due to its high diffraction intensity, we assume that the graphene aligned in this direction is dominant in the top layer. Figure 4.17b shows the same sample after exposing to 30 eV N-ion for 10 min. The LEED image of the nitrogen-doped graphene shows closely identical diffraction pattern to the pristine one. The relative intensity of the (1×1) spots due to the SiC substrate is slightly increased *wrt* the graphene (1×1) intensity. This implies some limited damages to the top graphene layers but the honeycomb structure of graphene is generally preserved. It should be mentioned that the $(1\times1)_SiC$ spots of this PG are more intense than its PG counterpart presented in section 3.2. This is because either the graphene thickness of this sample (used for the study of nitrogen doping) is thinner than the one studied in section 3.2, or the SiC surface may be not entirely covered by graphene for the latter. The thinner graphene may also lead to slightly different results in other analysis, *e.g.* its IPES or TCS spectra.

The multi-layers of graphene on SiC(000$\bar{1}$) exhibit each the properties of an isolated graphene monolayer due to the staking disorder between each layer. By changing the analyzing azimuth during ARIPES, we can investigate the unoccupied states of differently oriented graphene layers after the nitrogen doping. Figure 4.18 shows the ARIPES spectra of NG on the SiC C-face taken along two representative direction: Γ-M of SiC(000$\bar{1}$) and rotated 15° *wrt* Γ-M$_{SiC}$. The graphene layers in these two orientations are named as GR0 and GR15 in the following. The former refers to the graphene (1×1) spots in the LEED pattern, which Γ-K direction is parallel to Γ-M$_{SiC}$. The later refers to the most intense graphene (1×1) arcs, which Γ-K is rotated 15° *wrt* Γ-M$_{SiC}$. The thin dotted curves in the figure show the ARIPES spectra of the PG on SiC(000$\bar{1}$). In accordance with the results presented in section 3.2, the π^* states of the graphene oriented at 15° *wrt* Γ-M$_{SiC}$ are much intense than the π^* states of the graphene oriented at Γ-M$_{SiC}$. After nitrogen exposure, the π^* states of both graphene layers are much

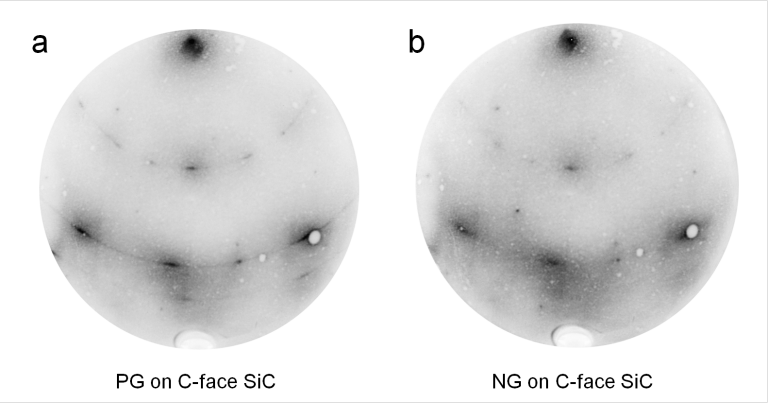

Figure 4.17: LEED images of (a) pristine and (b) nitrogen doped graphene grown on SiC(000$\bar{1}$) (the white circle at the right side of the LEED images is due to a defect on the LEED screen, rather due to the electron diffraction of the sample).

suppressed, similar to the ARIPES spectra of NG on SiC(0001). Interestingly, the *n*-shift of the π* states after nitrogen doping looks larger for the GR15 than the other one, GR0.

Figure 4.19 shows the $k_{\|}$ dispersion of the σ* and π* states obtained from ARIPES spectra of figure 4.18. The $k_{\|}$ dispersion is shown along the Γ-K direction of each graphene BZ, GR0 and GR15, as shown in the sketch at the right side of the figure. The $k_{\|}$ values are obtained from equation (3.1) using the corresponding work function measured by TCS, which is 4.81 and 4.61 eV for the studied PG and NG on SiC(000$\bar{1}$). The work function of the PG on SiC(000$\bar{1}$) is slightly different than the value presented in section 3.2. This might be due to the thinner graphene thickness or incomplete graphene coverage of the studied sample. Nevertheless, the π* states dispersions in $k_{\|}$ of NG on SiC(000$\bar{1}$) show quite different results for the graphene layer in the two orientations, GR0 and GR15. The π* states of GR15 exhibit a much larger shift toward E_F; as for GR0, the π* states dispersion remains similar to the PG. In contrast, the dispersion of the σ* states shows little difference between pristine and nitrogen-doped for both GR0 and GR15. This is because the dispersion of σ* states starting from the Γ point of graphene BZ is nearly identical close to Γ point in all directions, either in Γ-K, Γ-M or other non-symmetric directions, as shown in figure 1.2. In other words, the position of the σ* states is mainly dependent on the magnitude of $k\|$ *wrt* the Γ point, while the direction of the $k\|$ is negligible. The obtained σ* peak would be the contribution of all the graphene sheets in different orientation. Therefore, it is almost impossible to differentiate the σ* states of GR0 and GR15 using ARIPES as they will always be in superposition regardless of the azimuth probed in ARIPES.

The large difference in the π* states dispersion for GR0 and GR15 indicates that the GR15 should be dominant in the top graphene layer, which is much affected by the nitrogen exposure by showing a strong n-type doping. As for GR0, it should be an

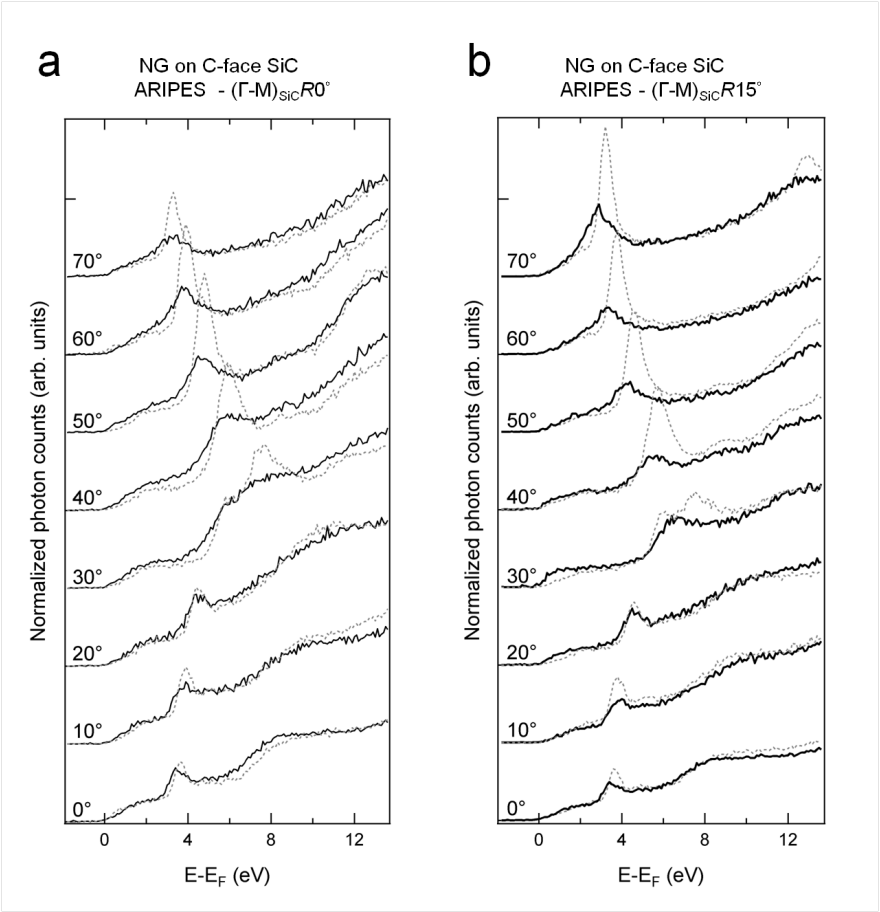

Figure 4.18: ARIPES spectra of NG on SiC(000$\bar{1}$) taken at different azimuth. Along (a) Γ-M$_{SiC}$ and (b) rotated 15° *wrt* Γ-M$_{SiC}$. The thick curves show the spectra after nitrogen doping, and the dotted curves represent the spectra of the pristine sample.

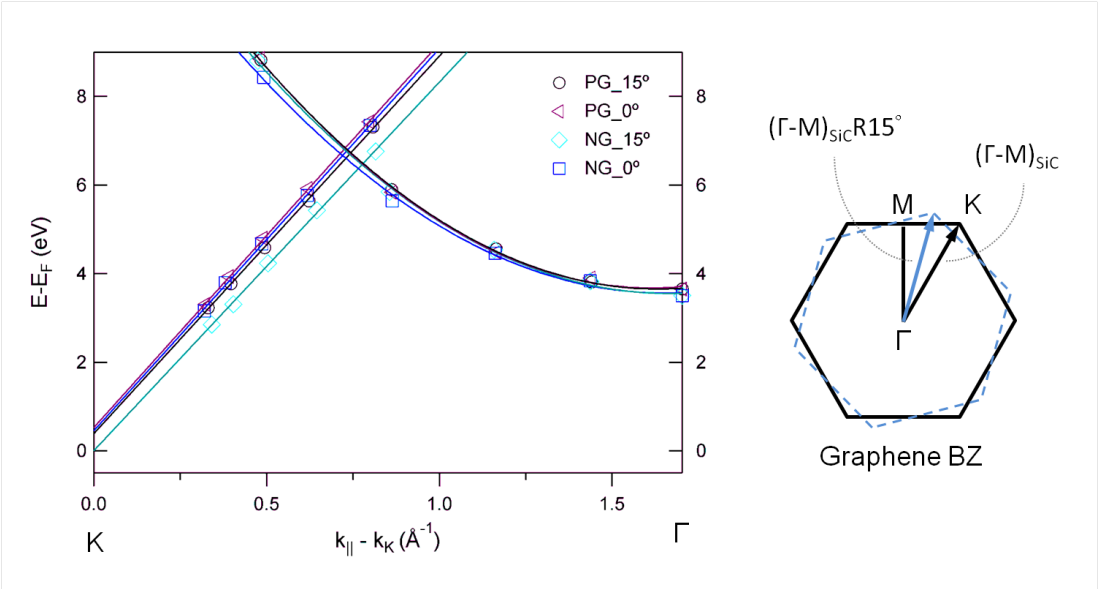

Figure 4.19: The $k_{\parallel}$ dispersion of the σ* and π* states obtained from the ARIPES spectra of figure 4.18 along the Γ-K direction of graphene BZ. Straight lines are linear extrapolation of the π* states up to the K point of graphene BZ, which direction is represented by the sketch at the right side showing the graphene BZ and its Γ-K direction(s) for the two differently oriented graphene sheets.

under-layer graphene remaining undoped after nitrogen exposure. From these results, we may also deduce that this *in situ* nitrogen doping process remains effective only to the top layer(s), such as GR15. On the other hand, judging by the decrease of its π^* states intensity, either the damage to the graphene structure caused by the nitrogen exposure affects the under-layer graphene, GR0, or some residual impurities are produced on the surface, suppressing the IPES signal of the under-layer graphene.

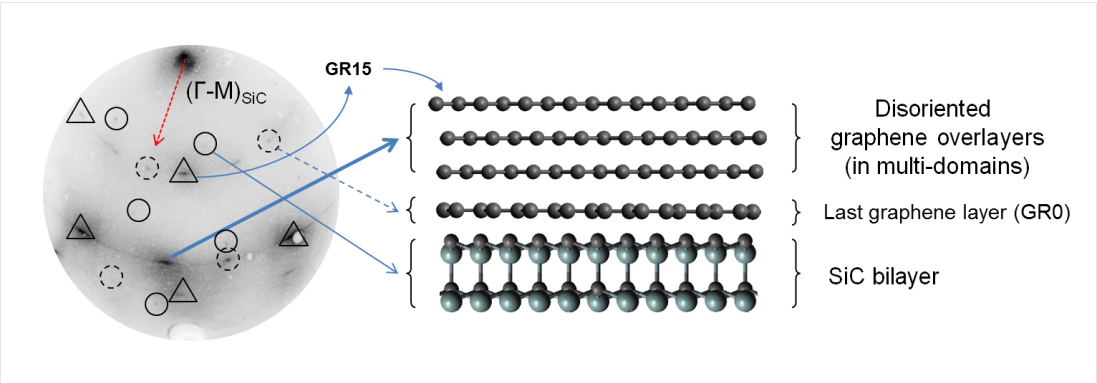

Figure 4.20: Schematic representation of the possible multi-layer graphene structure on SiC(000$\bar{1}$). Right side shows the LEED image of PG on SiC(000$\bar{1}$). The different sets of diffraction patterns are referred to the different layer(s) in the graphene/SiC structure, including the SiC bilayer (solid lines), the first graphene layer (dashed lines), and the disoriented graphene overlayers (thick lines).

The above scenario seems in better accordance with the disoriented multi-layer structure model, rather than the multi-domain one, for the mechanism of graphene epitaxy on SiC(000$\bar{1}$). We may visualize that the graphene on the SiC C-face grows by stacks of multi-layer graphene, as shown in figure 4.20. The graphene layer closest to SiC (last graphene layer in the figure) may prefer to be oriented according to the symmetry of the SiC surface structure, thus like GR0. The overlayers, which are away from the SiC substrate and have little interaction with the first graphene layer, would have no particularly preferred orientation, resulting in a rather random disorientation, like GR15.

Even though the disoriented-multilayer model seems to be reasonable, these overlayers graphene may still form multi-domains each with randomized orientations, because the disorientation of only a few layers will not be able to exhibit an arc-like LEED pattern. Due to the complexity of the graphene structure on the SiC C-face, and the limited resolution in both azimuthal and energy using the actual ARIPES set up, we were unable to further investigate the nitrogen doping effect of each orientation. However, since the overlayers are randomly oriented, the result of nitrogen doping on GR15 may be representative to generally describe the nitrogen doping effects on the overlayer(s) of graphene on the C-face.

4.3 *Ex situ* nitrogen doping of graphene

This section reports the study of nitrogen doping of graphene using the *ex situ* plasma-based nitrogen doping processed by a low-energy RF-plasma-based implanter at IBS. To generate low-energy species (<50 eV) for this study, the design of the implanter setup is different comparing to a conventional implanter. The general idea is to expose the target sample directly to unpolarized RF-plasma, which plasma potential is around 25-30 eV. The actual incident energy and exposure time (dosage) are controlled by varying sample self-bias. For example, to expose to 30 eV ions for a certain dose, the sample is grounded for a specific duration for the ion exposure, then it is polarized to higher voltage, *e.g.* +50 V, to push away the ions, preventing excess exposure during the rest of the process.

The principal difference between the *in situ* and the *ex situ* doping process is the way that the plasma is generated. The *ex situ* RF plasma has a lower density, in which the molecules are less dissociated. According to the plasma analysis report of IBS, the N_2 plasma consists mostly of ionized molecules (N_2^+), electrons, and excited N_2 molecules. This difference in the exposing species may lead to contrasting results or may induce other side-effects during the process. Although, similar to the ion mode of the *in situ* doping, the *ex situ* RF-plasma process also exposes the sample to a mix of charged (ions) and neutral species.

The PG monolayer samples grown on SiC(0001) were prepared using the same process as described before, *i.e.* via Si sublimation in UHV at 1150°C for 15 min. Their quality was examined *in situ* by LEED and ARIPES before nitrogen exposure. The investigation of the implanted NG focus on their unoccupied band structure using ARIPES and chemical states using XPS. It should be mentioned that no annealing step was performed during the *ex situ* doping due to the restrained experimental conditions of the employed equipment. It was only performed prior the ARIPES and some XPS measurements to limit the effect of adsorbates during analysis.

Six graphene samples (#0-#5) have been exposed to low-energy nitrogen plasma. The implantation processes are carried out at RT, because of which we limit the maximum exposition doses at $<1\times10^{15}$ cm^{-2} in order to prevent serious damage of graphene. The specific conditions for the nitrogen plasma exposures and their respective PG thicknesses as determined by IPES are listed below:

- #0: 30 eV, dose = 1×10^{14} cm^{-2}, PG = ∼2ML
- #1: 15 eV, dose = 5×10^{14} cm^{-2}, PG = ∼1.5ML
- #2: 30 eV, dose = 1×10^{14} cm^{-2}, PG = ∼1.5ML
- #3: 30 eV, dose = 5×10^{14} cm^{-2}, PG = ∼1.5ML
- #4: 30 eV, dose = 1×10^{15} cm^{-2}, PG = ∼1.5ML
- #5: 45 eV, dose = 5×10^{14} cm^{-2}, PG = ∼1.5ML

4.3.1 Unoccupied states of NG via *ex situ* N-doping

In the first part, we focus on the analysis of their unoccupied electronic states using ARIPES. From these spectra we can follow the shift, if any, of the different electronic bands, and estimate the actual n- or p-type doping, as also shown in previous sections. We can also assess the integrity of the honeycomb lattice of graphene from the shape and relative intensity of the π^* states.

The ARIPES spectra of the six nitrogen-exposed graphene samples are shown in figure 4.21 (thick blue curves). They are taken along the Γ-K direction of the graphene BZ. The ARIPES spectra of the PG (light dashed curves) are also shown for comparison. As stated before, the small peaks dispersing from low to higher energy with increasing incident angle are assigned to the σ^* states, and the sharp peaks dispersing toward lower energy at larger incident angle are due to the π^* states. By comparing the blue spectra to the dashed gray spectra in figure 4.21, one can observe that, for all NG sample, the nitrogen implantation using IBS's implanter has a limited effect on the position of the π^* states of graphene. Though, some samples exhibit a small n-shift of its σ^* states. For example, a ∼0.1 eV shift toward E_F is observed for sample #0, as also shown by the $k_{\|}$ dispersion (in Γ-K) of its unoccupied states of figure 4.22.

In addition to the little shift of unoccupied states, we observed an obvious attenuation of the σ^* and π^* states for sample #2, #3 and #4. This is probably due to a physical etching effect at higher exposition energy of 30 eV that over damaged the graphene structure. Figure 4.23a compares the IPES spectra of the studied samples acquired at normal incidence. For sample #1 to #4, the pristine graphene sample was close to ∼1.5ML graphene, whereas #0 is rather a bilayer. After nitrogen exposure, #1 remains a monolayer structure according to its IPES spectrum. However, for sample #2, #3 and #4, their IPES spectra reveal a surface close to a buffer-layer graphene (BLG) or even a (1×1)-SiC surface, as shown in figure 4.23b. The larger the dose to which graphene is exposed to, *e.g.* sample #4, the less graphene remains on the surface.

Figure 4.23c shows the schematic representation of these surface structures. This indicates that the nitrogen exposure at 30 eV actually damage the graphene while doping it. The sample #5 is expected to exhibit similar behavior, i.e. large damage to the graphene, but the IPES spectra show that the graphene remains rather undamaged and nearly undoped. As discussed in the next subsection, we observed that a thicker graphene seems to be stronger and hosts fewer defects during the plasma exposure. Since the XPS spectra reveal a thicker graphene for sample #5 (∼1.4 ML) than for sample #3 and #4 (∼1ML) after nitrogen exposure, we assume that the actual thickness of the pristine graphene in sample #5 may be thicker than expected. Being more resistant to plasma damage, the thicker pristine graphene may be the reason why sample #5 still exhibits the characteristics of a monolayer graphene after a nitrogen plasma exposure at 45 eV.

Another striking result that we observed is the big difference between the IPES spectra of #0 and #2, for which the same exposition (30 eV, dose: 1×10^{14} cm^{-2}) has been performed (although the exposition time and the polarization conditions,

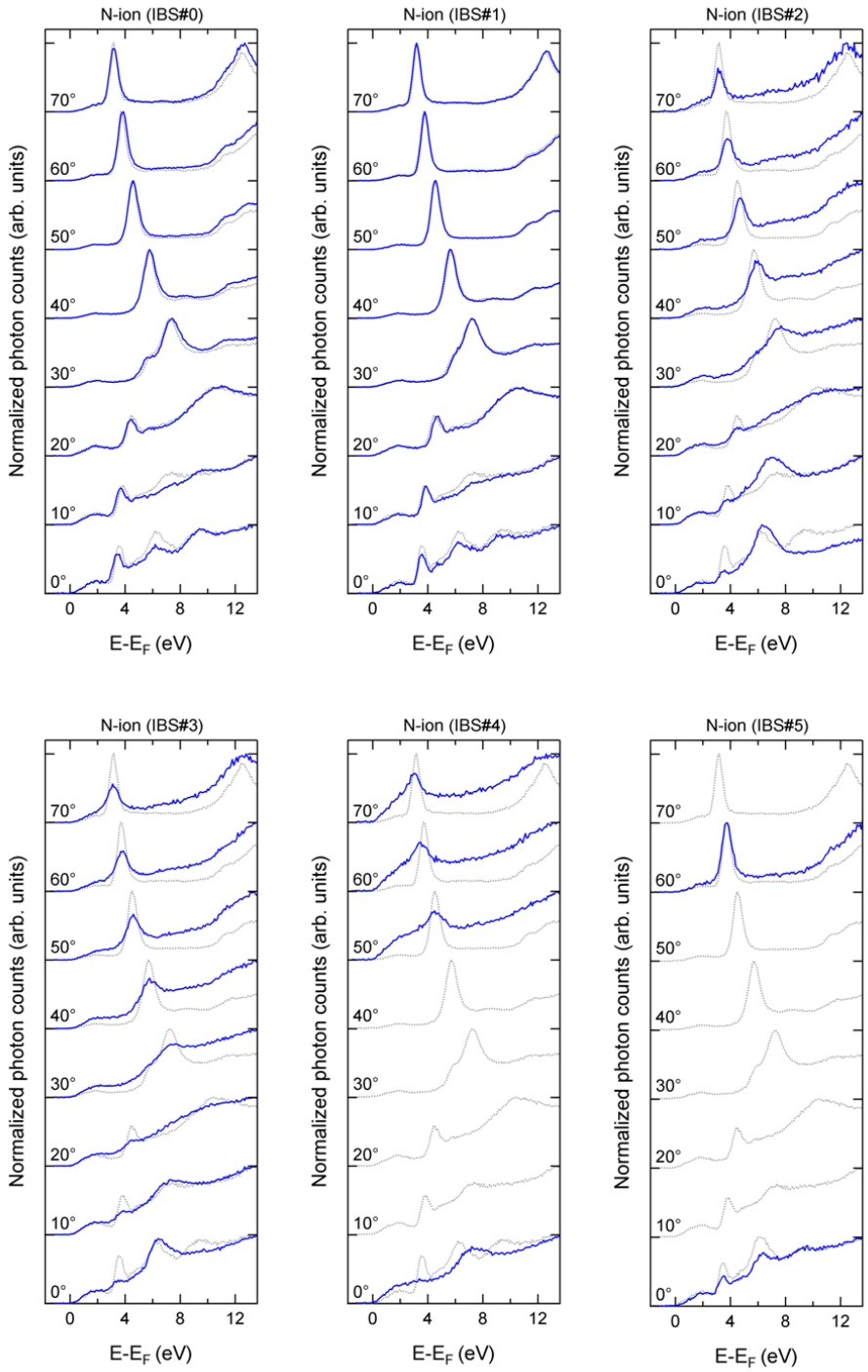

Figure 4.21: ARIPES spectra of the nitrogen-exposed graphene samples (blue) performed at IBS compared to the spectra of pristine graphene (dashed).

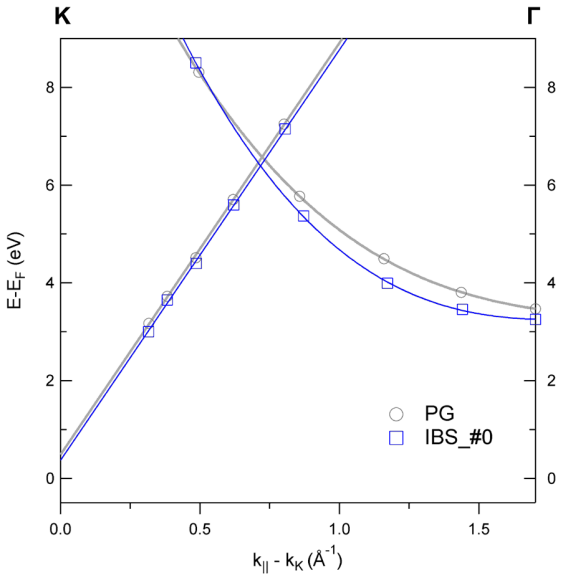

Figure 4.22: Dispersion of σ^* and π^* states of pristine (gray) and nitrogen doped (blue) graphene (sample #0). Symbols represent the σ^* and π^* states obtained from ARIPES spectra in figure 1. Straight lines and parabolic curves are linear and parabolic approximation of the dispersion of these σ^* and π^* states.

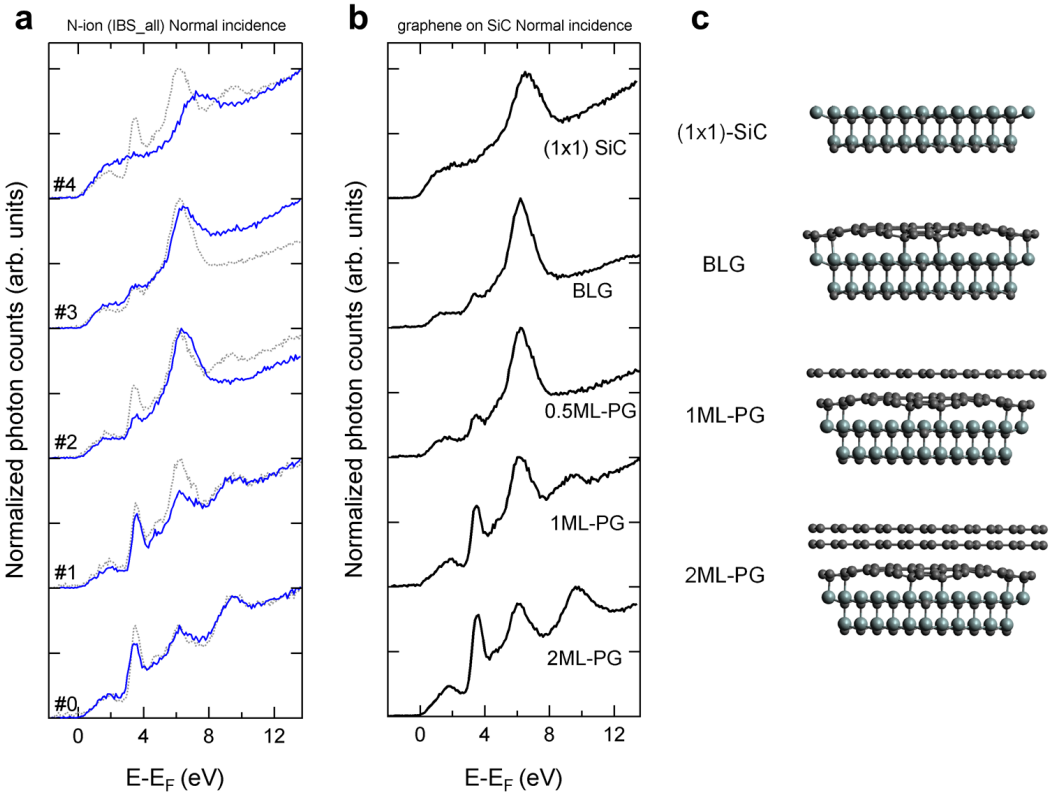

Figure 4.23: (a) IPES spectra of the nitrogen-exposed graphene acquired at normal incidence. (b) IPES spectra of SiC surface during graphene growth. From top to bottom are (1×1)-SiC surface, BLG, 0.5ML, 1ML and 2ML graphene. (c) Schematic view of the above mentioned surface structure.

according to IBS, were different: unpolarized for #0 and 5V for #2). For sample #0, the IPES spectrum shows that the graphene layer(s) remains well-structured after the exposition. As for #2, the graphene is damaged. This also might be related to the thickness of pristine graphene before nitrogen implantation, which is discussed in more details in the next subsection.

4.3.2 Chemical states of NG via *ex situ* N-doping

Due to the limited accessibility of our XPS instrument, the core level spectra of NG samples processed via IBS implanter were analyzed separately using two different setups. The one situated at IM2NP is equipped with an Omicron EA125 analyzer, which is the same used for *in situ* N-doping experiments. The other is located at CIMPACA at ST Rousset and is equipped with a KRATOS AXIS Nova spectrometer. A pre-annealing at 600°C for 10 min was proceeded for the samples analyzed at IM2NP, #0, #2 and #4. The other NG samples analyzed at CIMPACA, including #0 again, were investigated without any annealing.

Figure 4.24 shows the C 1*s* spectra of the studied NG samples. The decomposition of these spectra shows several chemical states of C atoms. Five different peaks, located at about 283.9 eV, 284.8 eV, 285.5 eV 286.0 eV and 286.9 eV, can be found in each C 1*s* spectrum, which are attributed to C atoms in SiC, graphene layer, buffer layer in sp^3 configuration, buffer layer in sp^2 configuration and some C-O species, respectively. The relative peak area of the graphene-related feature indicates the actual thickness of the graphene. By comparing with our previous studies, the thicknesses of sample #0-#5 after plasma exposure are determined to be about 1.7 ML, 1.6 ML, 1.0 ML, 0.9 ML, 0.4 ML and 1.4 ML, respectively. The graphene thicknesses seem reduced after the nitrogen doping at higher energy of 30 eV and 45 eV (sample #0, #2-#5), which was estimated to be ∼1.5ML for sample #1-#5 and ∼2ML for sample #0 before exposure based on their IPES spectra at normal incidence (figure 1). This shows a physical etching effect induced by the nitrogen plasma, especially at high doses like for sample #4. Although we have judged from the decrease of π^* states in ARIPES spectra that the graphene layer is damaged for #2, the graphene-related peaks of #2 and #3 indicate that the carbon atoms in sp^2 configuration are still close to 1ML. This may be not controversial since it may require only a small concentration of defects to severely alter the electronic property of graphene, while still exhibiting a large amount of carbon atoms in sp^2 hybridization in XPS spectra.

It should be mentioned that the thickness estimated by IPES is based on the intensity of a thickness-dependent state, located at 9 eV above E_F. This estimation should be quite accurate for defect-less graphene but could be underestimated if the sp^2 conjugation is perturbed by defects. In contrast, the graphene thickness determined by XPS counts all carbon atoms in sp^2 configuration even with the presence of defects. So, it could overestimate the thickness of graphene. For example, BLG exhibits significant amount of C atoms in sp^2 configuration but do not behaves like isolated graphene at

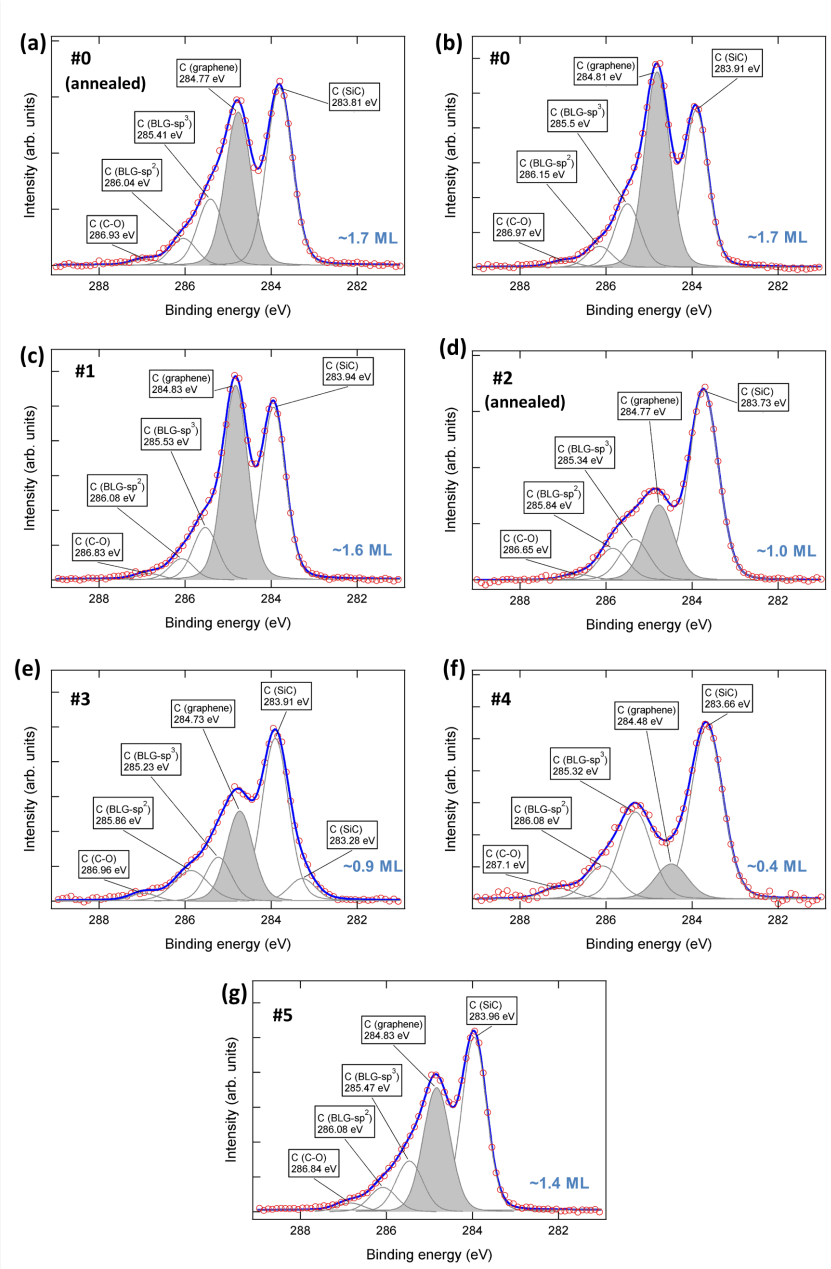

Figure 4.24: XPS C 1s spectra of the studied NG samples: (a) sample #0 after annealing, and (b) before annealing, (c) sample #1 before annealing, (d) #2 after annealing, (e-f) #3 and #5 before annealing.

all. However, this only implies that the thickness reduction due to N plasma exposure may be even larger.

Figure 4.25 shows the N 1s spectra of the studied NG samples. It shows that every sample is more or less nitrogen enriched, confirming that it is possible to incorporate N in graphene using this plasma exposition process. The area of each component shown in figure 4.25 indicates the atomic concentration in a monolayer graphene assuming all N are confined in the top most graphene layer. From sample #1, #3 and #5 (figure 4.25 c, e-f), which were exposed to 5×10^{14} cm^{-2} of N-ion at an energy of 15, 30 and 45 eV, respectively, the total concentration of the incorporated nitrogen are 0.2%, 3.7% and 3.4%, showing an optimal efficiency between 30 and 45 eV. In contrast, the N incorporation using N_2^+ is very limited at lower ion energy of 15 eV by showing a 0.2% of doping nitrogen for an exposition dose of 5×10^{14} cm^{-2}(figure 4.25c, sample #1).

Figure 4.25a and b show the N 1s spectra of #0 obtained before and after annealing. Four components are found before annealing, while only three components are present after annealing. The two peaks located at lowest (398 eV) and highest binding energies ($\sim$403 eV) are assigned to pyridinic-N and N-O species. The peak areas and locations of these two peaks are closely identical before and after the annealing process, which implies that molecules adsorbed during ambient air exposition do not affect the chemical states of these N species. In contrast, the two other components located at 401.3 eV and 399.4 eV seem to merge into a single feature at 401.3 eV after annealing, because the area summation of the former two peaks (figure 4.25a) is very close to the area of the later (figure 4.25b). Since the N 1s component at 401.3 eV is attributed to graphitic-N species in graphene, which possess locally a higher electron density, we suggest that some molecules adsorb at the graphitic-N sites and modify their chemical state. For instance, some adsorbed H_2O molecules may form hydrogen bonds with electron-rich graphitic-N, changing the local electron density and inducing a chemical shift to the N 1s peak of these nitrogen species. Thus, we assign the N 1s component located at 399.4 eV to graphitic-N species interacting with an adsorbate, which can be removed by thermal annealing. It also implies that, for the other N 1s spectra acquired without annealing, the actual graphitic-N concentration in the graphene lattice should include the contribution of both components at 401.3 eV and 399.4 eV, from which it can be deduced notwithstanding the lack of annealing prior to XPS measurements.

Following the above deduction, the incorporated nitrogen in the graphene in samples #3 and #5 are about $\sim$2/3 in graphitic-N configuration and $\sim$1/3 in pyridinic-N *wrt* the total nitrogen concentration. On the other hand, the samples #0 and #1 show a majority of graphitic-N, and the sample #2 contains an equivalent amount of the two types of nitrogen species. The difference of the graphitic-N-to-pyridinic-N ratio in these NG samples does not seem significantly related to the plasma condition (ion energy or dose) but rather depends on the thickness of the PG. This can be examined by comparing the two graphene samples exposed to a similar nitrogen exposure (30 eV, 1×10^{14} cm^{-2}): a bilayer PG (#0) and a monolayer PG (#2). The N 1s spectra of the two samples, figure 4.25b and d, show that the nitrogen plasma exposure induces

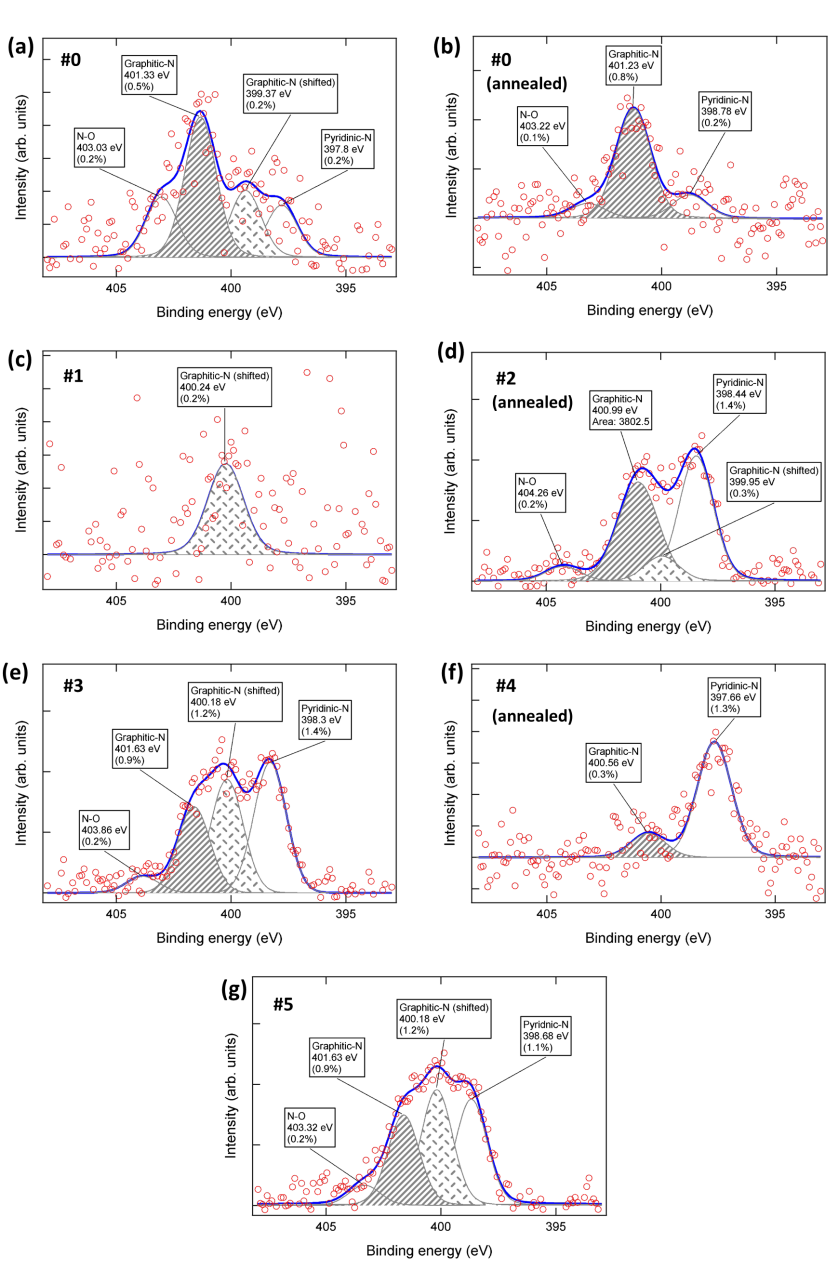

Figure 4.25: XPS N 1*s* spectra of the studied NG samples: sample #0 (a) before and (b) after annealing, (c) sample #1 before annealing, (d) #2 after annealing, (e-f) #3 and #5 before annealing. The percentage of each component indicates its atomic concentration in a monolayer graphene.

different nitrogen doping configurations in these two graphene. For bilayer graphene (#0), most of the incorporated nitrogen are in graphitic-N configuration (0.8%), while pyridinic-N are at a level of 0.2%. For monolayer graphene (#2) instead, both pyridinic-N (1.4%) and graphitic-N (1.3%) are mainly present, accompanied by a small amount of pyrrolic-N (0.3%) and N-O species 0.2%. Such thickness-dependent behavior has been observed by Kim *et al.* using a nitrogen ion source to irradiate graphene [98]. They also found that graphitic-N favorably form on multilayer graphene, and pyridinic-N on monolayer one. Since the formation of pyridinic-N requires the presence of vacancy defects, it implies that more defects are created when exposing a monolayer graphene to such nitrogen ion (or plasma) source. The monolayer graphene looks actually more fragile and more sensitive to N plasma through C vacancy incorporation than multilayer graphene, as we observe a majority of graphitic-N on the later.

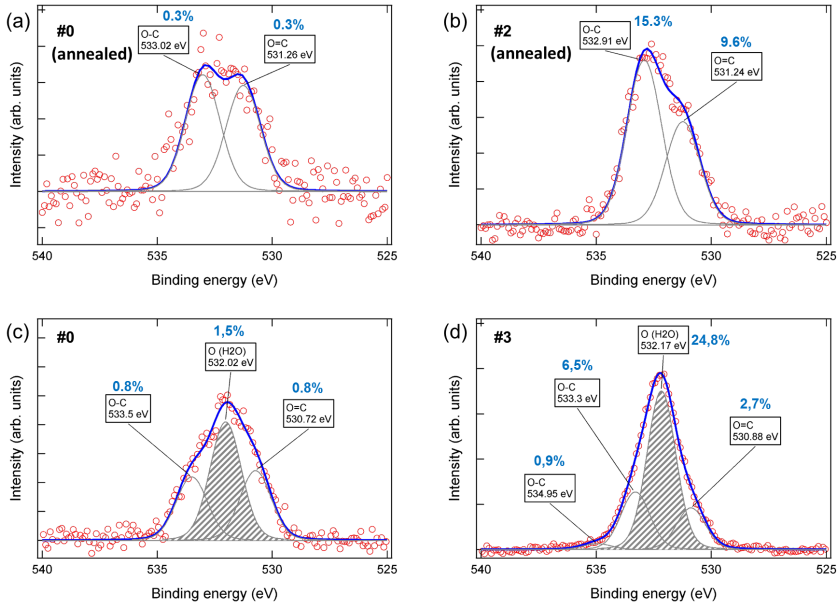

Figure 4.26: XPS O 1*s* spectra of (a) sample #0 and (b) #2 after annealing and (c) sample #0 and (d) #3 before annealing. The percentages of each components indicates its atomic concentration *wrt* the number of C atoms in a monolayer graphene.

Figure 4.26 shows the O 1*s* spectra of samples #0 and #2 after annealing at 600°C. Two prominent components are observed in both spectra. One located at about 531 eV is attributed to double-bonded oxygen, and the other at about 533 eV is attributed to single-bonded oxygen. These covalently bound oxygen are due to the atmospheric exposition of the samples for the *ex situ* ion doping as well as the XPS analysis, and are usually formed at graphene edges and defect sites. Their quantitative analysis shows that the oxygen concentration of #2, ∼25% in total, is much larger than the 0.6% of oxygen on #0. It confirms that a larger defect concentration is generated on

monolayer (#2) leading to the chemisorption of a large amount of oxygen-containing species. As for multilayer #0, much less oxygen species are chemisorbed. The O 1*s* spectra of #0 and #3 before annealing representing the typical O 1*s* spectra of the NG sample before annealing (figure 4.26c,d) show a similar tendency. The major spectral difference between the spectra obtained before and after annealing is the presence of the component at ∼532 eV (hatched area in figure 4.26c,d), which is suppressed after the annealing. It is attributed to the oxygen in molecules, like H_2O, adsorbed at the defect sites of the graphene surface. Its presence testifies our previous assumption stating that the peak shifting of the graphitic-N component is due to some adsorbed H_2O molecules.

4.3.3 Summary of *ex situ* nitrogen plasma-based doping

In conclusion, the nitrogen plasma implantation at IBS generally introduces both graphitic-N and pyridinic-N substitutional species in the graphene lattice. The optimum ion energy seems to lie between 30 and 45 eV (e.g. 3.7% of incorporated nitrogen using a dose 5×10^{14} ions/cm^2 at 30 eV), whereas, at 15 eV, a smaller amount of nitrogen is incorporated under an equivalent dose. The relative concentration of different nitrogen doping configurations, graphitic-N or pyridinic-N, seems to be related to the thickness of the pristine graphene that was exposed to the plasma. The thicker the graphene, the more the incorporated nitrogen are in the graphitic form and the less in pyridinic, and *vice versa*. This implies that the monolayer graphene may be more fragile and consequently more defects are created by the implantation, as evidenced by the larger O 1*s* peak for monolayer NG, leading to the generation of defect-related pyridinic-N. We also observe a chemical shift at the N 1*s* peak of graphitic-N component (from ∼401 eV to ∼399 eV), which we attribute to graphitic-N sites that are modified by adsorbed molecules like H_2O.

The incorporated nitrogen, however, has little influence on the unoccupied states of graphene, as investigated by ARIPES. We can barely observe a difference in the position of the $\pi*$ states, i.e. sample #0 in figure 4.21a, which may be induced by the 0.8% of graphitic-N. This is compatible with our previous work, the nitrogen doping using a versatile MW-ECR plasma source, where we observed only small shift of the unoccupied bands of graphene for a 1.7% doping of graphitic-N when exposed to thermalized atomic nitrogen species. A more significant tailoring of the electronic structure of the graphene would require higher graphitic-N concentration. However, since a plasma etching effect was observed due to high energy ion bombardment, it would also require a doping process at higher temperature to recover the damage on the graphene (self-healing effect) when increasing the exposition dosage.

Nevertheless, this first trial of nitrogen incorporation using the IBS implantation technique is promising. It not only shows the presence of incorporated nitrogen but also gives us a good idea of the proper plasma conditions for the actual doping of graphene, which should also be applicable for other plasma-based doping of graphene, such as boron or NH_3. However, the actual bonding configurations of the incorporated

nitrogen seem to be more complex than expected, which would contribute differently to the electronic and chemical property of graphene than a single graphitic-N. In order to have a better understanding of the characteristics of the present NG, a more detailed study of the STM images and even some additional measurements are suggested for further investigation. On the other hand, the impossibility of using high temperature implantation process with the IBS implanter, which limits the self-repair mechanism during the nitrogen incorporation, restrains the maximum exposition dose that can be applied. A plasma source equipped with a substrate heating element would be necessary, if a NG with higher nitrogen concentration is demanded.

4.4 Conclusions

In this chapter, a general study of the nitrogen incorporation of graphene monolayer(s) on SiC using various plasma-based methods is presented. The study is focused on activated nitrogen species with a low energy of 0-50 eV. The investigation of core-level chemical shifts of the incorporated nitrogen using XPS shows that the doping nitrogen in graphene are found in various bonding configurations, mainly graphitic-N and pyridinic-N.

More interestingly, the resulting doping configurations can be controlled via the exposition to different nitrogen species, such as N atoms, N^+ ions and N_2^+ ions. For example, pyridinic-N species are favorably generated when exposed to thermalized N atom with the presence of defects, *i.e.* ∼16% of pyridinic-N are found after 60 min of N-atom exposure using the atom mode of the *in situ* MW-ECR plasma source. Substitutional graphitic-N species are more efficiently created using N-ions, which show an optimum doping efficiency at about 20-35 eV, in good agreement with theoretical simulations [96, 97]. The NG sample exposed to 35 eV N-ion for 10 min actually possess high concentration of graphitic-N of 8%, accompanied by 5.3% of pyridinic-N probably due to the defect creation during N-ion exposure. In addition, the creation of different doping species, graphitic-N or pyridinic-N, seems to depend on the initial thickness of the PG when using plasma-based nitrogen doping methods, for both the *in situ* and the *ex situ* one. For example, using *in situ* plasma source, 3% graphitic-N are found in bilayer graphene, while pyridinic-N is restrained at 0.4% A thicker graphene favors the creation of graphitic-N, as a thinner graphene seems to favor the creation of pyridinic-N and vacancy defects.

Concerning the chemical states of the incorporated N, we observe a chemical shift of the graphitic-N related feature with the presence of adsorbed molecules like H_2O, from ∼401.3 eV to ∼399.4 eV, especially when *ex situ* XPS measurements are performed without pre-annealing. It shows that adsorbates are actually involved in the chemical states of surface atoms, and should be taken into consideration even if these adsorbed molecules (or atoms) may be not chemically bonded to the surface.

A *n*-type doping and a decrease of the Fermi velocity are found for most NG samples, as revealed by ARIPES. According to the XPS studies, the *n*-type doping as well as

the lowering of Fermi velocity should be principally induced by graphitic-N species giving extra mobile electrons to the graphene, in accordance to theoretical studies. For example, a 0.4 eV n-shift of the E_F is estimated for 8% of graphitic-N. In contrast, the pyridinic-N species seem to induce little effect to the electronic properties of graphene in the present case. A n-type doping of ∼0.1 eV is observed for a NG, exposed to 60 min of N-atom, possessing ∼17% of pyridinic-N and 2% of graphitic-N, where we attribute the small n-type doping to the small amount of graphitic-N instead of pyridinic-N. Further investigation of the ARIPES spectra of a series of NG samples shows that the tendency of n-doping and v_F are different, implying that at least two different species are affecting the electronic properties. Moreover, the average charge transfer of graphitic-N to graphene is estimated to be about 0.06-0.1 electron per N atom (for a graphitic-N concentration of >3.5%) in monolayer NG, which is much lower than the value (∼0.6 electron per N) found at lower nitrogen concentration (∼0.5%) reported in the literature. This also implies the presence of more complex doping species, *e.g.* a doping configuration with multiple graphitic-N. Further investigation about the presence of complex doping configuration would need a detailed atomic-scale inspection, such as STM. The opening of a gap at the Dirac point, which is expected for a graphene doped with graphitic-N, would require the investigation of the occupied band structure, *e.g.* using angle-resolved photoemission spectroscopy.

Nitrogen plasma-based doping is also studied using the multilayer (but possessing monolayer character) graphene grown on the C-face of SiC. A n-type doping of the π^* states is found by ARIPES for the disoriented topmost graphene layer(s) (*e.g.* GR15), while the graphene layer aligned to the orientation of SiC (GR0) remains much less affected after nitrogen doping. According to these findings, we suggest that the top graphene layer(s) should be those that are disoriented and directly exposed to nitrogen plasma, while the bottom layer, in contact with the SiC substrate may be aligned according to the orientation of SiC substrate. It also indicates that the plasma-based N-ion implantation mostly dopes the top graphene layer(s) at low incident ion energy of <35 eV.

We also show that the honeycomb structure of graphene can be severely damaged if exposed to a large dose of N-ion at RT. By holding the sample at high temperature of ∼850°C during nitrogen plasma exposure, the N-ion induced damage can be restrained even at a large dose of $\sim 4\times10^{15}$ cm^{-2}. Thus, a high nitrogen concentration of NG prepared at a larger dose can be envisioned using this high temperature process. Some thermally unstable nitrogen adsorbates may also exist on the graphene after exposition to the nitrogen plasma source, and may modify the electronic structure of the doped graphene, in particular its work function, unless a high temperature annealing is performed.

The *ex situ* nitrogen incorporation using an industrial RF plasma-based implanter (manufactured by IBS) also appears to be successful, even though this plasma source emits principally N_2^+ ions rather than N^+ ions for the *in situ* MW-ECR plasma source. The studied NG samples are prepared at smaller exposition doses of 1-10$\times10^{14}$ cm^{-2}

due to the lack of heating element inside the instrument. Despite their little effect to the electronic structure of graphene related to the low N ion dose, the XPS spectra reveal the presence of incorporated nitrogen up to a total concentration of ∼3%. The optimum incorporation efficiency may lie around an ion energy of 30 eV. The lower electronic doping efficiency may be related to the use of N_2^+ ions, which may favor the creation of complex nitrogen doping sites.

Nevertheless, we show that the nitrogen doping configuration can be controlled via the species and energies of the exposing nitrogen, and that a high nitrogen concentration can be obtained using high temperature process. The unoccupied band structures of the resultant NG samples confirm n-type doping of the graphene, which is closely related to the amount of graphitic-N. We also studied the role of adsorbates to the apparent electronic properties of the NG. The general understanding of these nitrogen incorporation processes should facilitate the study of chemical doping of graphene using different sources, and elements, especially using an industrial-familiar plasma-based technique.

Chapter 5

Hydrogenation of buffer-layer graphene on SiC

Hydrogen is also a potential additive element to alter the properties of graphene in versatile ways. Different to the nitrogen inducing substitutional doping in the graphene lattice, the hydrogen atoms are usually covalently bounded on the graphene surface like an adatom. The formation of an additional C-H bond converts the carbon atom from sp^2 to sp^3 hybridization, and modifies the electronic properties of graphene. Hydrogenated graphene could be obtained by exposing graphene flakes to activated hydrogen at lower temperature, as reported in some recent works [47, 112–114]. Even though being observed in small quantity, covalently-bound hydrogen is actually difficult to obtain on the full sp^2-configured graphene due to its low desorption energy, high reaction barrier and an unfavorable final state of the two step hydrogenation process, as proposed by Ao *et al.* [115].

The graphene in a complete hydrogenated configuration, namely graphane, has been theoretically predicted since 2007 as a stable, insulating material with a wide band-gap [116]. More than being useful in low-dimensional electronic applications [116], it is expected to be a superconducting material when p-doped [117]. The formation of graphane requires the chemical adsorption of hydrogen at both sides of graphene. Every carbon atom in graphene turns into sp^3 hybridization and a band gap of $\sim$5.4 eV opens [48]. Elias *et al.* have reported evidences about the presence of graphane by hydrogenating a suspended monolayer of graphene flake at room temperature (RT) [47]. However, graphane is difficult to obtain in practice since the graphene is usually supported by a substrate. Indeed, H atoms can hardly reach the back side of graphene at low temperature (<600°C), and the C-H bonds on graphene are unstable at higher temperature.

Another way to alter graphene properties using hydrogen is to modify the substrate induced doping. For graphene grown on SiC(0001), H atoms may intercalate between the carbon-rich $(6\sqrt{3} \times 6\sqrt{3})R30^\circ$ reconstruction (also known as BLG) and the bulk

SiC at higher temperature (> 700°C). It results in a graphene monolayer decoupled from the SiC substrate, namely QFSG, as introduced in section 1.2. On the other hand, the BLG is a good candidate for studying the hydrogen adsorption on graphene. Since the C atoms in BLG are a mix of sp^2 and sp^3 configuration, the adsorbed hydrogen may be more stable on BLG than on purely sp^2 bonded PG [118–120].

In this chapter, we investigate the effects of hydrogenation of BLG on SiC by revealing its electronic structures using IPES supported by TCS, LEED and AES. In the BLG, a significant concentration of Si DBs remains, as evidenced by a Mott-Hubbard state in IPES. These Si DBs are saturated upon hydrogenation at RT, possibly by additional C-Si bonds at the BLG/SiC interface. The RT-hydrogenated BLG (H-BLG) shows a good stability and behaves similarly to a graphane-like material. The SiC/BLG interface is also studied by inspecting the spectral characters of QFSG obtained after a high temperature hydrogenation, which shows a interface similar to a $(\sqrt{3}\times\sqrt{3})R30°$ reconstruction of SiC(0001). On the basis of the high stability and the distinct electronic properties of both H-BLG and QFSG, we suggest that the hydrogenation processes of BLG may be exploited for the engineering of graphene-based devices, and a procedure is proposed.

5.1 Experimental methods

The preparation of BLG samples is actually quite delicate, because the upper graphene layer may start to form on the SiC surface before it is fully covered by BLG. There is only a small temperature range to separate the preparation of these two surfaces. In order to obtain the best BLG coverage on SiC surface, we use a slower epitaxial rate at a lower temperature, *i.e.* gradually increase the temperature from ∼950°C to ∼1050°C and hold at ∼1050°C for about 15-20 min. The quality of the BLG sample is verified using LEED, showing a $(6\sqrt{3}\times 6\sqrt{3})R30°$ pattern, and IPES, by revealing the absence of π^* states (see chapter 3).

Hydrogenated samples are then prepared by exposing the pristine BLG to atomic hydrogen at various temperatures. The H atoms result from the decomposition of H_2 molecules by a tungsten filament heated over 2000°C, positioned about 50 mm in front of the sample, as detailed in section 2.2.2. The atomic H dose is controlled by the exposition time and the partial pressure of H_2, which we fixed at 1×10^{-5} mbar for the experiments presented in this chapter. Hydrogenated BLG (H-BLG) sample is obtained by an atomic hydrogen exposure of 10 min at RT. Hydrogen intercalated QFSG is obtained by exposing BLG to H atoms at high temperature (700°C) for 40 min. A MLG on SiC sample is also prepared for comparative study. For ease of comprehension, schematic representation of these four structures is shown in figure 5.1a-d.

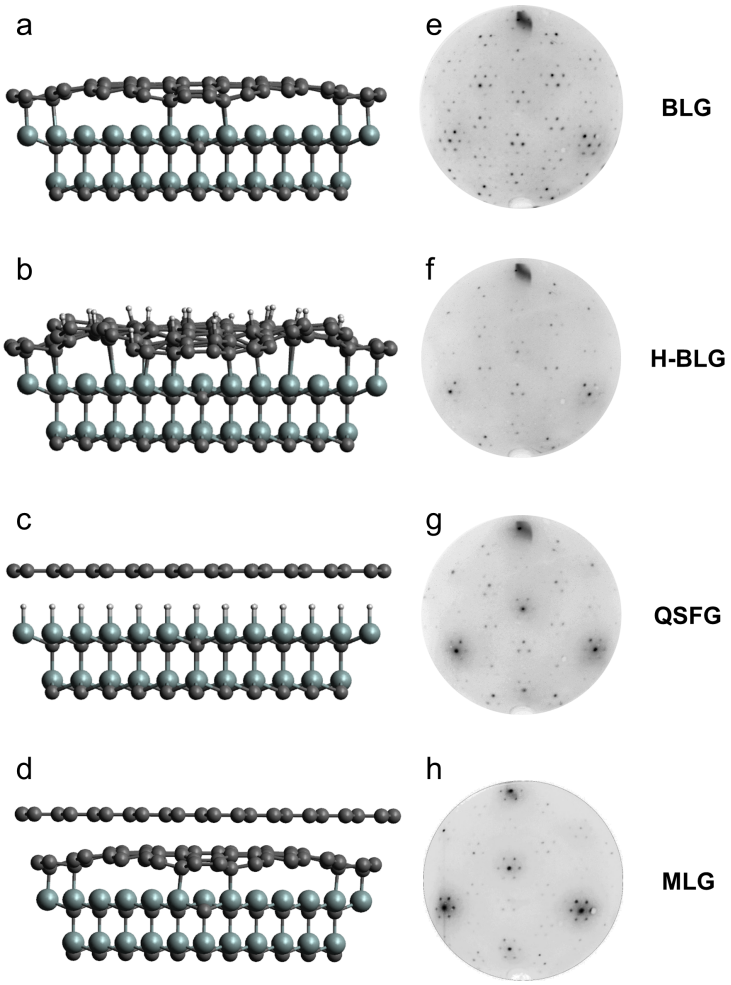

Figure 5.1: (a, b, c) Schematic representation of BLG, H-BLG and QFSG on SiC(0001) surface, respectively. Light gray balls represent Si atoms, dark gray ones represent C atoms and the small balls are the H atoms. (d, e, f) LEED images of the three studied sample, BLG, H-BLG and QFSG on SiC(0001). Images are taken at 45° incidence and a primary energy of 100 eV.

5.2 Results

5.2.1 Surface structures of BLG

The surface structures of each prepared sample are firstly examined using LEED, as shown in figure 5.1e-h. The LEED picture of pristine BLG on SiC shows a well-developed $(6\sqrt{3} \times 6\sqrt{3})R30°$-SiC diffraction pattern (figure 5.1e) [43]. After the hydrogenation of BLG at RT (H-BLG), most of the diffraction spots are attenuated, as shown in figure 5.1f. However, the (1×1)-graphene spots and some of the nearby $(6\sqrt{3} \times 6\sqrt{3})R30°$ spots are still present. It implies that the honeycomb-like structure of BLG is preserved and still correlates to the SiC but less well structured. The (1×1) spots of graphene are further enhanced when the BLG is hydrogenated at 700°C, as shown in figure 5.1g, which implies the formation of the decoupled QFSG layer [43]. The LEED image of the MLG sample shows a similar pattern to the QFSG one, except a higher intensity at some $(6\sqrt{3} \times 6\sqrt{3})R30°$ spots, due to the contribution of the underlying BLG.

5.2.2 Chemical environments

Figure 5.2a shows the AES spectra of the four studied samples. From the bottom to the top are the spectra of BLG, H-BLG, QFSG and MLG, respectively. Figure 5.2b and c show the superpositions of their Si LVV and C KLL features for comparison. The AES spectra of the BLG show a Si LVV Auger feature at 91 eV and a C KLL Auger feature at 276 eV. The Si:C intensity ratio is close to 2:1. It also shows a graphene-related peak structure at ∼253 eV, marked with a hash symbol [121]. As the BLG is hydrogenated (H-BLG) or decoupled from SiC (QFSG), both the structures of Si and C Auger features slightly modify with a slight shift of Si LVV feature for H-BLG and QFSG. The chemical shift of Si peak should be related to the band bending, which is much better resolved in IPES spectra discussed in detail in the following section. For H-BLG, the Si feature becomes thinner as pointed out by the arrow, with the main changes of the peak structure marked by an asterisk. This might indicate a change of the chemical environment of surface Si atoms. Its C KLL feature also shows a slight decrease of sp^2-related feature (as shown by hash symbol) from the pristine BLG ones. When the BLG/SiC interface is passivated by intercalated hydrogen to form the QFSG, the Si Auger feature further modifies. It becomes even thinner with a more obvious change in the peak structure. Most interestingly, the graphene-related peak (hash) of QFSG increases as the main SiC-related peak decrease. This indicates that the C atoms in the H-BLG transform from sp^3 configuration into sp^2 when the interface is hydrogenated, an evidence of QFSG formation. It should be mentioned that the hydrogenation (and H-intercalation) are reversible and their corresponding Auger spectra are reproducible. The AES spectra of MLG shows a Si:C Auger ratio of about 1:1 with an essentially more intense sp^2-related C KLL feature comparing to the QFSG one, as shown in figure 5.2c. Though, differently to the QFSG spectrum, its Si LVV

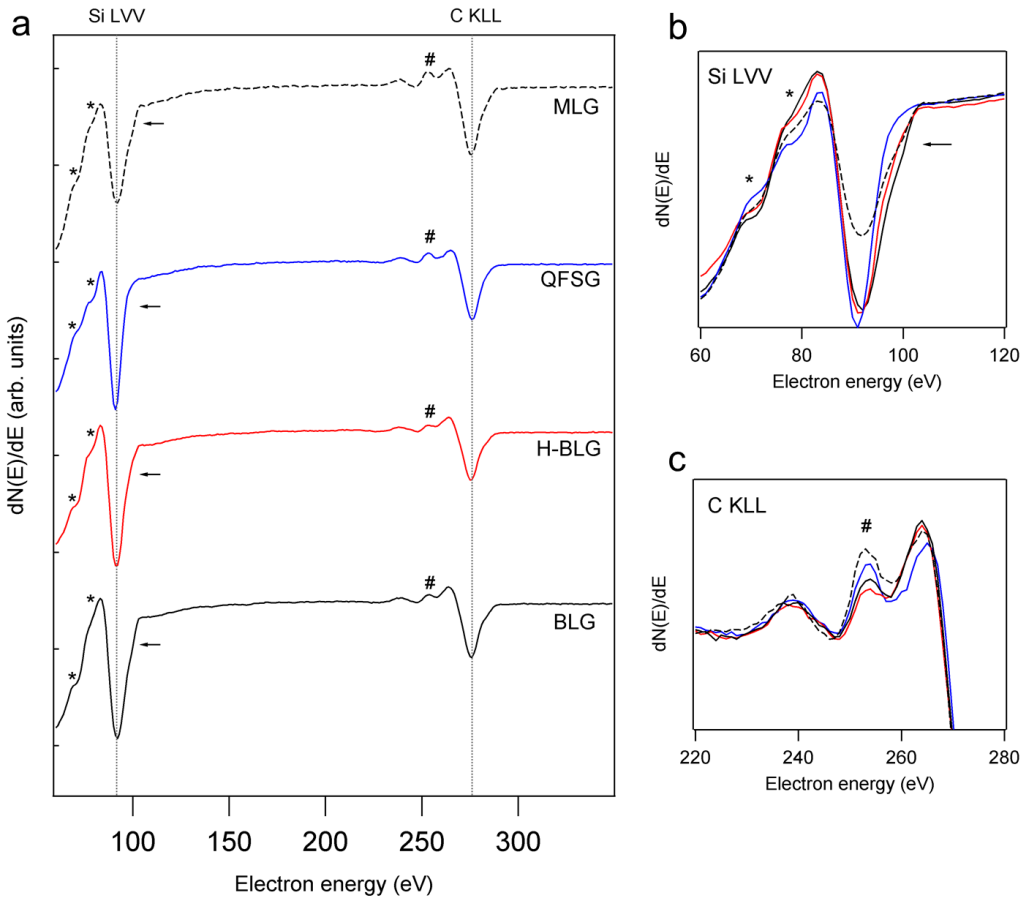

Figure 5.2: AES spectra of the studied samples, BLG (black), H-BLG (red) QFSG (blue), and MLG (dashed), in differential form. The inset shows the superposition of the Si LVV and C KLL peaks of the three spectra. The asterisks, arrows and hash symbols indicates the major differences between the three spectra.

feature is much broader. It is much similar to the BLG spectrum, which should be due to the contribution of the interface Si atoms.

5.2.3 Electronic structures

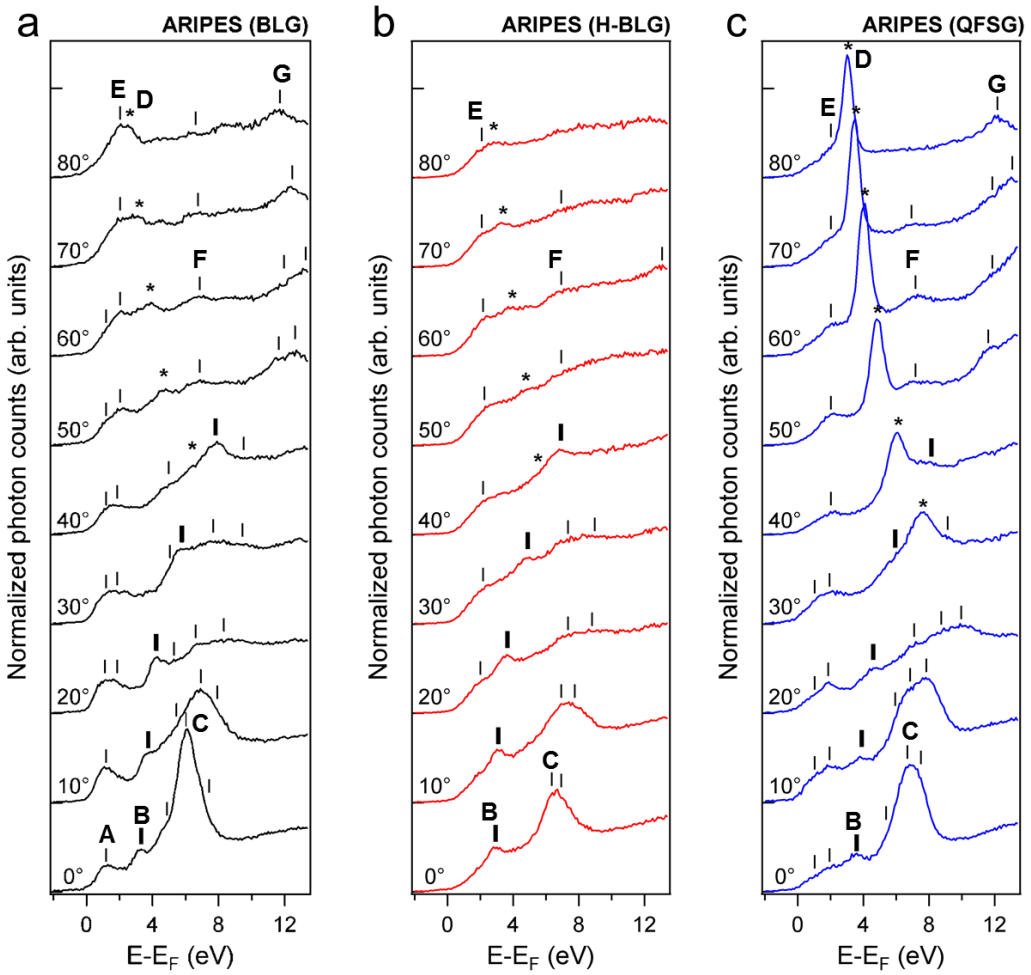

Figure 5.3: ARIPES spectra obtained from (a) BLG, (b) H-BLG, and (c) QFSG samples as a function of the polar angle θ along the Γ-K direction of the graphene Brillouin zone. The angle dispersion of peak B and D for QFSG are marked with vertical thin bars and asterisk, respectively.

Figure 5.3a shows the angle-resolved IPES (ARIPES) spectra of a pristine BLG measured at various incidence angles θ along Γ-K in the graphene BZ, as also shown in chapter 3. The spectrum taken at normal incidence (0°) shows three main features, A, B and C. As stated before, peak A, located at 1.1 eV above E_F, is assigned to the

interface states due to remaining Si DBs at BLG/SiC interface [81, 122, 123]. Peak B, located at 3.3 eV above E_F, is assigned to the σ^* bands of the BLG [14]. Finally, peak C is assigned to the SiC substrate [14]. The broadening of peak C at 10-20° incidence indicates that it may be composed of at least two components.

Figure 5.3b shows the equivalent ARIPES spectra of the H-BLG, the BLG exposed to activated hydrogen at RT. Three major distinct spectral differences are observed comparing to the spectra of pristine BLG. The first one is the lack of the interface-related peak A at all angles. The second is a shift of the entire σ^* band, peak B, toward E_F ($\sim$0.4 eV). The third is a shift toward higher energy accompanied by an intensity-decrease of the SiC substrate-related peak C. It should be noticed that the hydrogen appear covalently bound to the BLG because the electronic structure of H-BLG is kept unchanged (through the IPES spectrum) after an annealing up to 500°C. This result is also in good agreement with a recent theoretical prediction for H adsorption on BLG [120].

The intercalation of hydrogen at the BLG/SiC interface further modifies the electronic properties of this graphene layer. The ARIPES spectra of the QFSG, figure 5.3c, show an emerging sharp peak at large incidence ($> 30°$), namely peak D. It disperses to lower energy at increasing incidence angle in the Γ-K direction. As reported earlier, this peak is assigned to the π^* band of graphene [14, 124]. This intense π^* band indicates the presence of an extended graphene structure in complete sp^2 configuration, *i.e.*, in this case, the formation of the QFSG by H-intercalation. Besides the development of the π^* band (peak D), the dispersion of the σ^* band (peak B) shows a small rigid shift ($\sim$0.2 eV) to higher energy compared to the pristine BLG. The interface-related states peak A remains attenuated and the substrate-related peak C is more pronounced compared to H-BLG.

Apart from the four major features mentioned above, several small features in these ARIPES spectra are observed (marked by thin bars), especially at large incidence, namely peak H, F and G (from smaller to higher energy). Peak H, located at about 2 eV, is assigned to an indirect transition to the high DOS at M point of graphene BZ (see subsection 3.1.2). Peak F, at $\sim$7.5 eV, is better distinguishable above 50°. The shapes and positions of peak F remain unchanged regardless the surface structures of the three samples, BLG, H-BLG and QFSG, hence it may be assigned to a contribution of the bulk SiC. On the other hand, peak G, observed above 50° and located around 12 eV, depends on the surface structure. Being more pronounced in QFSG, it is assigned to the contribution of several graphene states.

5.3 Discussion

From the above results, we show that the hydrogenation of the BLG at RT or at higher temperature (700°C) modifies the electronic properties of the BLG quite differently. Actually, the electronic properties of BLG are strongly related to its surface

structure, which is, despite numerous efforts, not yet fully understood. One of its structural property that is generally accepted is the corrugation of BLG with a periodicity of $(6\sqrt{3} \times 6\sqrt{3})R30°$ to commensurate with the SiC(0001) lattice via the formation of C-Si covalent bonds between BLG and SiC substrate. This scenario was both predicted to be energetically stable and observed experimentally by STM, X-ray reflectivity and diffraction [125–130].

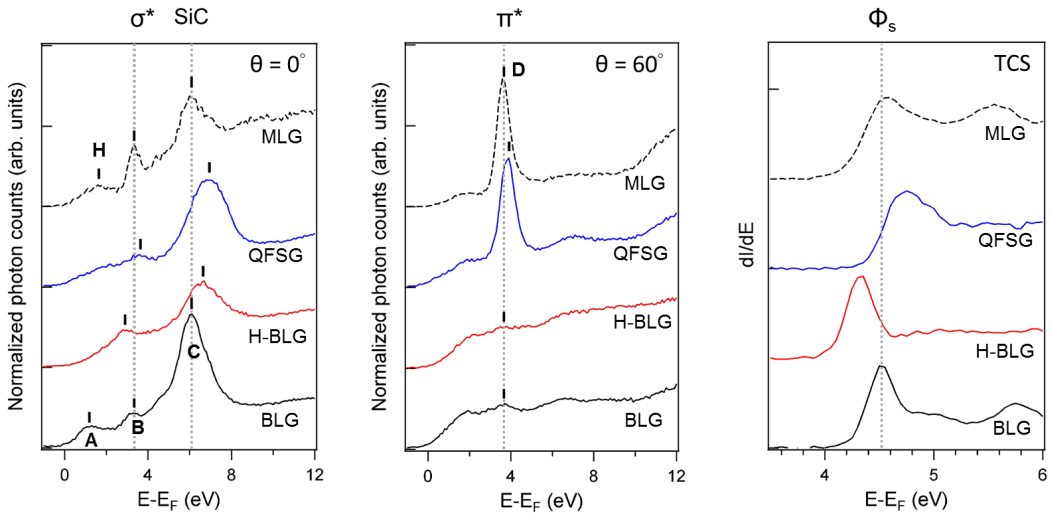

Figure 5.4: Spectral comparison of the three studied samples, BLG, H-BLG and QFSG: (a) IPES at normal incidence, (b) IPES at 60° incidence, and (c) the derivative of absorbing current based on TCS measurements *wrt.* E_F.

A remaining issue still in debate is the actual density and configuration of these C-Si bonds, also related to the reconstruction of SiC subsurface and to the possible presence of remaining Si DBs. Due to the large lattice parameter of BLG, most of earlier theoretical studies were limited to a simplified $(\sqrt{3} \times \sqrt{3})$ model where the BLG is stretched by about 8% [123]. In this oversimplified model, 1/3 of the Si atoms are not bonded to a C atom in BLG, thus would be left with one DB. Some recent experimental studies show contrasted results. Based on quantitative analysis of the C1*s* XPS spectrum, Emtsev *et al.* claimed that *every Si atom* at the interface is bonded to BLG since they found that the density of C atoms in a sp^3 configuration is equivalent to the density of Si atoms at the surface [81]. Similarly, using X-ray standing wave spectroscopy, Emery *et al.* claimed that C atoms in sp^3 are closer to SiC and are in equivalent quantity that the surface Si atoms, confirming that each Si atom are saturated by a C atom [131]. However, a puzzling difference can be found between these two works, which attribute the C-sp^3 and C-sp^2 in BLG to two different C1*s* components. More specifically, two C1*s* components related to BLG, S1 and S2 located at ∼285 and ∼285.7 eV, are found in both studies. In Ref. [81], S1 is assigned to C

atoms in sp^3 configuration, and its peak area is much smaller than S2. Contrary, in Ref. [131], it is the component S2 that is assigned to C atoms in sp^3. The peak area of S1 and S2 is also reversed (smaller S2). The contradict peak assignments and the difference in the composition of S1 and S2 indicate that the assumptions made in these two studies may not represent the actual structure of BLG, which may actually be more complex. For example, the carbon atoms in the BLG may be at three or more different chemical states, instead of two (S1 and S2). These controversial results imply that the actual structure of BLG and the chemical state of its C atoms may be more complex than it seems. Besides the simplified covalently-bonded stretched graphene model, different C-rich interface structures may actually exist [132], which complicate the study of the C1*s* spectrum of BLG. A recent theoretical work [133], which employed the full $(6\sqrt{3}\times 6\sqrt{3})$ BLG lattice lying on (1×1) SiC, shows that only 26% of C atoms in BLG are bound to Si, equivalent to about 80% of Si atoms on the (1×1) SiC surface. For the remaining 20% of Si, a DB remains. In brief, the complex structure of BLG is not fully understood. There is still some doubts about the presence of Si DB, which would significantly affect the electronic properties and reactivity of BLG, as obtained in this work.

The electronic properties, the role of hydrogen atoms in the formation of H-BLG and QFSG, and their links with the interface structure of the BLG are revealed in the following by a more detailed inspection of their IPES spectra. Figures 5.4a and b compare the IPES spectra of the BLG, H-BLG, QFSG and MLG on SiC samples at normal and 60° incidence along Γ-K, respectively. As mentioned above, the peak A of BLG is strongly attenuated after the hydrogenation, for both H-BLG and QFSG. A plausible origin for peak A of BLG could be a remaining density of Si DBs at the BLG/SiC interface since its location is similar to the DB-related states found on the (3×3) and $(\sqrt{3}\times\sqrt{3})R30°$ reconstruction of SiC(0001) [14, 134–137]. Besides, the respective IPES spectra show that the relative intensity of these DB-related states on BLG is visually close to its counterpart on the (3×3) surface, which is consistent with a similar DB density on both surfaces. Indeed, on the (3×3) surface, the DB density is equivalent to 11% of Si on the (1×1) surface, which is comparable with the theoretical by predicted 20% for BLG [133], especially taking into account the attenuation due to the short mean free path of the strongly interacting low-energy electrons in the outer carbon layer. As the DB-related state is attenuated in H-BLG and QFSG, the structures of their Si LVV features are modified comparing to the pristine BLG ones (figure 5.2). This implies a saturation of the Si DBs at the BLG/SiC surface for both H-BLG and QFSG, which attenuates the interface states and modifies the chemical state of the interface Si atoms.

It could be objected that electronic states associated with DB should be intrinsically half-filled. In accordance with the small overall bandwidth W (estimated < 0.1 eV) of peak A, which can be followed in ARIPES throughout the whole (1×1) SBZ (see figure 5.3a), it is expected that as in the case of the (3×3) and $(\sqrt{3}\times\sqrt{3})R30°$ reconstructions of SiC [134, 136], strong correlation effects may perturb the DB-derived

electronic states [138]. Indeed, these half-filled states should normally cross the E_F, as predicted by DFT-LDA calculations based on the simplified, stretched BLG ($\sqrt{3} \times \sqrt{3})R30°$ model, which conclude to a metallic reconstruction [122]. In accordance with angle-resolved photoemission spectroscopy (ARPES) results [81], we do not find any E_F crossing in ARIPES, and the BLG is clearly insulating. For a large on-site correlation energy such that the Hubbard parameter U_{eff} >>W, many-body effects are able to split the DB-derived states into two components, one filled and one empty, separated by a bandgap U_{eff}. We associate the upper single-electron band of this Mott-Hubbard insulator to peak A observed in the unoccupied states of the BLG using IPES. Its occupied counterpart *g1* has been observed using ARPES [81], with a limited dispersion and overall bandwidth, located at 0.5 eV below E_F. The estimated separation between both states, around ≈1.5 eV, gives an estimation for the effective Hubbard parameter U_{eff} of these DB-derived states. Being larger that the limited bandwidth W, it justifies the strong correlation limit and the fact that the BLG is another example of a Mott-Hubbard insulator, as its Si-rich (3×3) and $(\sqrt{3} \times \sqrt{3})R30°$ counterparts. The experimental value of the effective interaction parameter U_{eff} ≈1.6 eV is found halfway between the respective value for (3×3) (U_{exp} ≈1.25 eV[137], U_{Calc} ≈1 eV [139]) and the $(\sqrt{3} \times \sqrt{3})R30°$ (U_{exp} ≈2.3 eV [134, 137], U_{Calc} ≈2.1 eV [139]) reconstructions.

The area of Peak A, derived from the DB-related electronic states, vanishes after hydrogen treatment, for H-BLG and QFSG. Meanwhile, in AES, the structure of their Si LVV features appears modified compared to the pristine BLG one (figure 5.2). For the QFSG, we have argued that the Si DBs are saturated by the hydrogen atoms diffusing through the graphene layer at high temperature, as shown in figure 5.1. On the other hand, for RT hydrogenation, as in the case of H-BLG, hydrogen should not be able to reach the interface of Si DBs due to the tightly bound honeycomb structure of graphene, known to block the diffusion of species as small as H atoms [140, 141]. Indeed, Bocquet *et al.* have recently shown the absence of Si-H vibration modes in the hydrogenated BLG on SiC, using high-resolution electron energy loss spectroscopy (HREELS) [114]. Though, they observe both the presence of C-H bonds and some signs of the disappearance of the interface states.

The most plausible explanation is that the formation of C-H bonds above the BLG forces nearby C atoms to form additional C-Si bonds with the remaining Si DBs underneath. Thus, the interface states are indirectly annihilated, not by the incident hydrogen atoms but by buckled C atoms in the BLG [114]. Initially, some C atoms in the BLG are not bonded to the SiC due to the corrugated structure of the BLG [130]. The formation of a surface C-H bond that induces a local sp^3 character to the bonded C atom creates a local corrugation of the BLG layer, moving nearby C atom downward, closer to the Si atoms of the first SiC bilayer, and favoring the formation of additional C-Si bonds, as shown in figure 5.1b. The existence of these additional C-Si bonds, which saturate the remaining DBs, is supported by the downward shift of the

σ^* band and the upward shift of the SiC bulk states (peak C), which are discussed in the following.

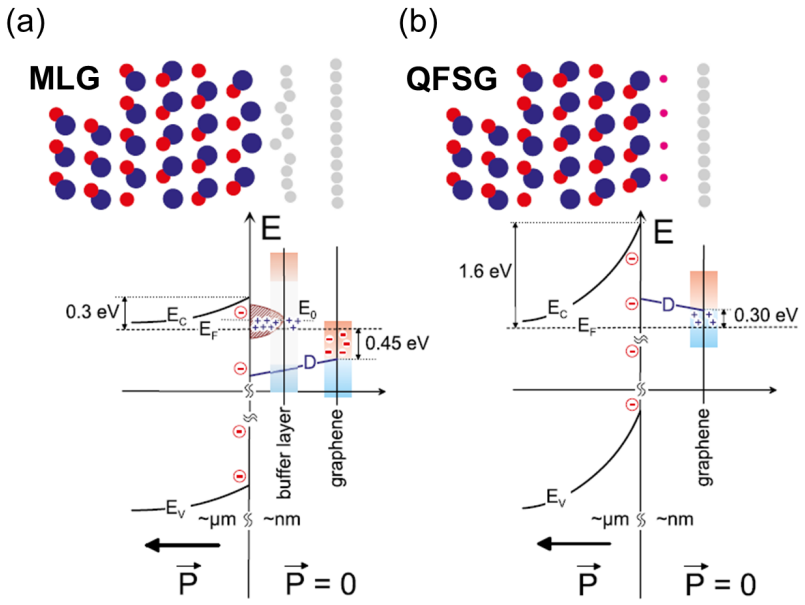

Figure 5.5: Sketch and schematic band diagram for the (a) MLG and (b) QFSG interface with 6H-SiC(0001). Large and small circles represent Si and C atoms, respectively, and the very small circles in (b) stand for hydrogen. The polarization vector inside and outside of the SiC is indicated at the bottom of the figure. Pseudo charges are marked by circles to discern from real charge. Figure reprinted from Ref. [142].

As shown in figure 5.4a, the SiC bulk-related peak C is located at lower energy in BLG and MLG (6.1 eV) and is shifted to higher energy in QFSG (6.9 eV) and H-BLG (6.6 eV). These changes of the bulk-related states are due to the band bending of the SiC substrate, as observed in previous photoemission spectroscopic studies [43]. For BLG and MLG, the bands are pinned by the donor type surface states related to the Si DB, located close to the bottom of the SiC conduction band [81], maintaining a slight upward bending of ∼0.3 eV (for n-type SiC), as shown in figure 5.5a [142]. When Si DBs are saturated by hydrogen, as in QFSG, the bands are no longer pinned and exhibit strong upward bending due to spontaneous polarization induced by the pyroelectric property of the 6H-SiC substrate, as shown in figure 5.5b [142]. In the case of H-BLG IPES spectra, the SiC bulk state (peak C) is close to QFSG, indicating that the bands are no longer pinned, as Si DB are mostly saturated, in accordance with the quenching of the Si DB-related peak A. The band bending in H-BLG is slightly smaller than in QFSG, possibly due to some remaining DBs or the compensation of C-Si bonds at the interface possessing an opposite polarization.

Although both H-BLG and QFSG exhibit larger band bending, the position of the graphene-related states, especially the σ^* states, are much different. As shown in figure 5.4a, the σ^* band of H-BLG shifts ∼0.4 eV toward lower energy comparing to the BLG one, indicating a stronger n-type character for H-BLG than for the pristine BLG. In contrast, both the σ^* band at normal incidence and the π^* band at 60° incidence of the QFSG exhibit a p-type shift (∼0.3 eV) *wrt* the BLG and MLG counterparts, as shown in figure 5.4a and b, which indicates that QFSG is quasi-undoped [43]. Since the remaining Si DB are saturated by H atoms in H-BLG, the σ^* states are expected to follow its upward band bending and should show a p-type shift *wrt* the BLG. However, the σ^* states of H-BLG actually shift to lower energy, another indication that Si DB are saturated by additional C-Si bonds, which induce a n-type doping of H-BLG. As BLG is bonded to SiC, negative charges (electrons) are transferred from Si to C due to the electronegativity (χ) difference in the C-Si bond ($\chi_C = 2.55$, $\chi_{Si} = 1.9$). This increases the electron density in BLG, resulting in a n-type character. By increasing the number of C-Si bonds, such as in H-BLG, more electrons are transferred to C atoms and the layer is more n-doped. In contrast, for QFSG, there are no C-Si bonds anywhere and no charge transfer between SiC and QFSG, in agreement with its quasi-undoped character.

Figure 5.4c shows the TCS spectra, the first derivative of the absorbed current versus the incident electron energy *wrt* the sample E_F of the studied samples in the range of their surface work function. The position of the maximum at the low-energy threshold indicates the work function value of each surface. As shown in the figure 5.4c, the work function of H-BLG (∼4.3 eV) looks decreased, while the QFSG counterpart (∼4.8 eV) is increased compared to the work function of the pristine BLG (Φ_s) located at ∼4.5 eV, and MLG at 4.58 eV. The reduction of work function for the H-BLG is attributed to the reduction of the electron affinity due to the small dipole of C-H (-+) bonds on H-BLG surface and to the increased inhomogeneous charge distribution in the corrugated H-BLG. In the corrugated BLG, the C atoms close to the SiC collect more charges from C-Si bonds and those away from SiC bulk are less charged,[129] resulting in a dipole (-+) in the BLG toward the surface. For H-BLG, the density of C-Si bonds is increased and may enhance this dipole, which further reduces the surface electron affinity.

In brief, the covalently-bound hydrogen atoms on the H-BLG surface induce the formation of additional C-Si bonds, which annihilate the interface states related to Si DBs and also induce an increased n-type doping of the hydrogenated buffer layer. On the other hand, the hydrogen atoms at the QFSG/SiC interface saturate both initial C-Si bonds and Si DBs and remove the substrate-induced doping, leaving the QFSG undoped.

Noteworthy, the electronic structure of the H-BLG should be similar to a graphane-like structure as one side of graphene is bound to hydrogen and the other side to interface Si atoms. Apart from revealing a stronger n-doping, the ARIPES spectra show the absence of any feature related to unoccupied surface states near E_F (figure 5.3b), which implies the formation of a large energy gap for the H-BLG. Closest to

E_F, the σ^* states at the Γ point located at ∼2.9 eV determine the position of the conduction band bottom. Considering the interface states related to C-Si bonds and the position of the top of σ band that may be located at about 0.5-1 eV and 5 eV below E_F, respectively [81, 118], the energy gap of H-BLG may be as large as ∼8 eV with localized interface states inside the band gap. One should note that the positions of the valence bands/states are estimated basing on the experimental value obtained on BLG reported in Ref. [81, 118] (the valence band structure of H-BLG has not yet been reported).

Although the H-BLG is not a real graphane, its strong insulating character might be very useful for the fabrication of graphene-based devices, due to its high thermal stability (up to 500°C). Here, we propose an original method to fabricate graphene-based devices based on the hydrogenation of BLG. By controlling the local annealing temperature (*e.g.* using for instance laser-based annealing) during the hydrogenation of BLG, we can obtain high-mobility QFSG patterns at the higher-temperature region. Simultaneously, at the lower-temperature regions, the large band-gap H-BLG forms. An alternative way may be to use a STM tip to assist the desorption of hydrogen, which has been demonstrated to pattern hydrogenated bilayer graphene [143]. We can thus "pattern" the graphene without etching it but instead using a local differential hydrogenation, which could be used for the fabrication of graphene-based circuits. We suggest this concept as a new route for the engineering of graphene-based devices.

Besides the presence of C-Si bonds and Si DB, the nature of the reconstruction of the SiC subsurface below BLG is also not fully understood. Most of the studies suggest that it is a (1×1) SiC surface, in good accordance with experimental results [81]. Though, a few studies show some signs of a $(\sqrt{3} \times \sqrt{3})R30°$ reconstruction beneath the BLG [14, 114]. Concerning this SiC subsurface, the IPES spectra of QFSG and BLG actually provide valuable information. Figure 5.6 shows the normal incidence IPES spectra of BLG and QFSG compared to a $(\sqrt{3} \times \sqrt{3})R30°$ surface reconstruction of SiC[14, 134], and its hydrogenated counterpart, H-$(\sqrt{3} \times \sqrt{3})R30°$. The H-$(\sqrt{3} \times \sqrt{3})R30°$ surface is obtained after a hydrogenation of $(\sqrt{3} \times \sqrt{3})R30°$ at 600°C for 10 min to simulate the procedure used to obtain QFSG. The IPES spectrum of $(\sqrt{3} \times \sqrt{3})R30°$ shows several surface states related features and a large and broad peak at ∼6.8 eV, which is related to SiC bulk [136, 137, 144]. For H-$(\sqrt{3} \times \sqrt{3})R30°$, the IPES spectrum shows no surface states near E_F but the SiC bulk related peak, at ∼6.8 eV, appears broadened. It is obviously very similar, in the peak width, shape and position, to the peak C of QFSG. Since the QFSG sample is composed of a single QFSG layer with a hydrogenated SiC substrate, we can deduce that the hydrogenated SiC substrate beneath is close to a H-$(\sqrt{3} \times \sqrt{3})R30°$ surface. This is also supported by the common features shown in the $(\sqrt{3} \times \sqrt{3})R30°$ spectrum and the BLG one. Although the bulk-related feature is not at the same energy for the two surface due to different band bending and taking into account the DB-related peak attenuated by the limited electron mean free path, two common features, located at ∼1 and 4.5 eV, related to surface states are found in both BLG and $(\sqrt{3} \times \sqrt{3})R30°$ spectra, as marked by asterisks in figure 5.6. This implies

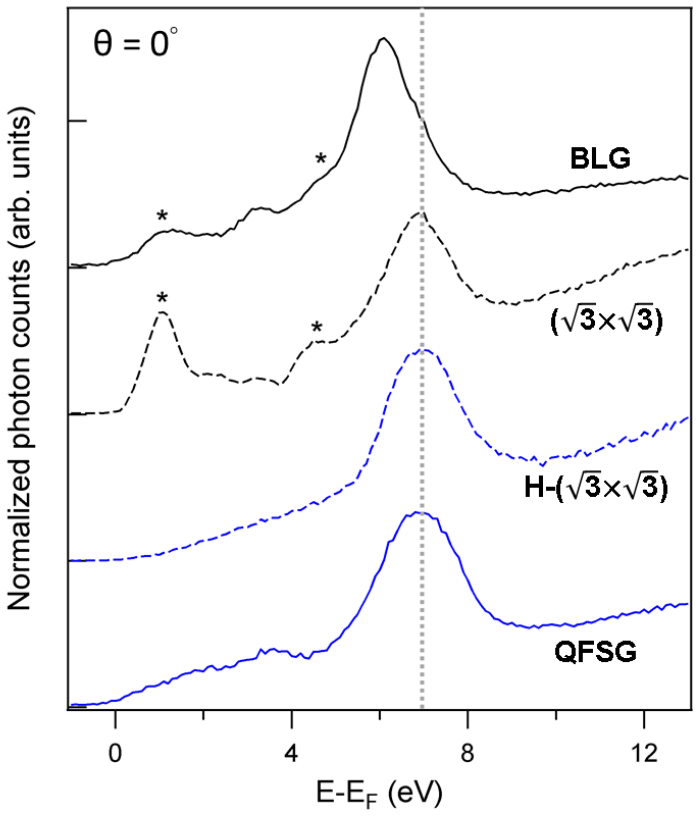

Figure 5.6: IPES spectra of QFSG taken at normal incidence compared to those of the $(\sqrt{3} \times \sqrt{3})R30°$ reconstruction of SiC surface and the H-$(\sqrt{3} \times \sqrt{3})R30°$ surface.

that at least a remnant of the adatom-based $(\sqrt{3} \times \sqrt{3})R30°$ reconstruction may exist at the SiC subsurface beneath the BLG.

5.4 Summary

We have shown the effects of activated hydrogen exposure onto the BLG on SiC(0001) substrate at various temperature. A significant concentration of remaining dangling bonds related to unsaturated Si atoms at the SiC subsurface beneath the BLG plane is evidenced in the IPES. They give rise to a peak around 1 eV above E_F, associated with the upper single-electron states of a Mott-Hubbard insulator, which vanishes upon hydrogenation.

At high temperature ($> 700°C$), the BLG transforms into a QFSG on a hydrogenated SiC surface close to a H-$(\sqrt{3} \times \sqrt{3})R30°$-SiC reconstruction. The interface states attributed to the remaining Si DBs are passivated by the intercalation of hydrogen atoms removing the substrate-induced n-type doping, as revealed by its AES and IPES spectra.

At lower temperature ($< 500°C$), hydrogen atoms are covalently bound to carbon atoms at the surface of BLG. These C-H bonds induce the formation of additional C-Si bonds with the underneath Si DB, annihilating the interface states, which is evidenced by the quenching of the DB-related peak and the upward band bending of the substrate. The n-type doping of H-BLG *wrt* the pristine BLG supports the presence of additional C-Si bonds. The significant influence of the DB-related states on the BLG and H-BLG electronic properties shows that more complex structures and chemical states should be considered for the BLG/SiC interface, including a significant density of remaining Si DB, up to $\sim$20% of the subsurface Si atoms. Moreover, the absence of unoccupied states near E_F implies a graphane-like electronic structure for the H-BLG on SiC.

Finally, based on our findings, we propose a concept for the fabrication of graphene-based devices using the hydrogenation of BLG (or hydrogen intercalation) at various temperatures: starting from an hydrogenated and highly insulating H-BLG, conducting tracks of QFSG may be directly patterned by locally increasing the annealing temperature during hydrogenation, *e.g.* by a focused laser beam.

Chapter 6

Interactions between molecules and graphene

In the previous chapters, we have demonstrated the functionalization of graphene via chemical doping of nitrogen and hydrogenation, which have successfully modified the intrinsic electronic properties of the graphene. Beside these two methods, the electronic properties of graphene can be also modified using molecular doping. It is performed by employing donor or acceptor-type molecules that give or withdraw electrons from the graphene when being adsorbed on the surface. For example, p-type F_4-TCNQ molecules are employed to compensate the SiC substrate-induced n-doping of the graphene [10], as also introduced in section 1.2. Excess electrons induced by the SiC substrate to the graphene monolayer are transferred to the adsorbed F_4-TCNQ molecules, bringing the Dirac point of graphene back to E_F. Besides electronic doping, the interaction between molecules and graphene is also an important subject concerning the application of graphene in organic electronics.

In this chapter, we show the preliminary studies of the unoccupied states of three different molecules adsorbed on graphene, namely fullerene (C_{60}), perylene-tetracarboxylic-dianhydride (PTCDA) and perylene-tetracarboxylict-diimide (PTCDI). Their molecular (chemical) structures are illustrated in figure 6.1. The C_{60} possesses similar carbon-based structure to graphene and is largely employed in organic photovoltaics, thus it is interesting to understand its behavior when in contact to graphene. The study of PTCDA and PTCDI is also interesting due to their electron acceptor nature, which we hope would exhibit an enhanced reactivity on an n-type NG surface. In addition, the adsorption of these three molecules has been previously studied on pristine graphene, especially by STM, which reveals both their self-arrangement and electronic properties when being deposited on graphene. The physisorbed C_{60} monolayer seems to arrange closed packed on graphene [145]. On the other hand, because of intermolecular hydrogen bonds, PTCDA and PTCDI monolayers self-assemble on the graphene surface in herring-bone and 1D-lines structures, respectively [146, 147]. Though having a stronger

intermolecular interaction, the molecule-surface interactions still remain weak. Further details about the study of these three molecular monolayers on graphene are introduced in the following.

In addition to the study of the unoccupied structures of these three molecular systems using IPES, we focused on the electronic properties and reactivity of these three molecules on the N-incorporated graphene surface. We expect that the previously functionalized graphene would exhibit enhanced general and/or local reactivity due to the incorporated dopant, especially near the incorporated nitrogen atoms, which increase locally the electron density of graphene.

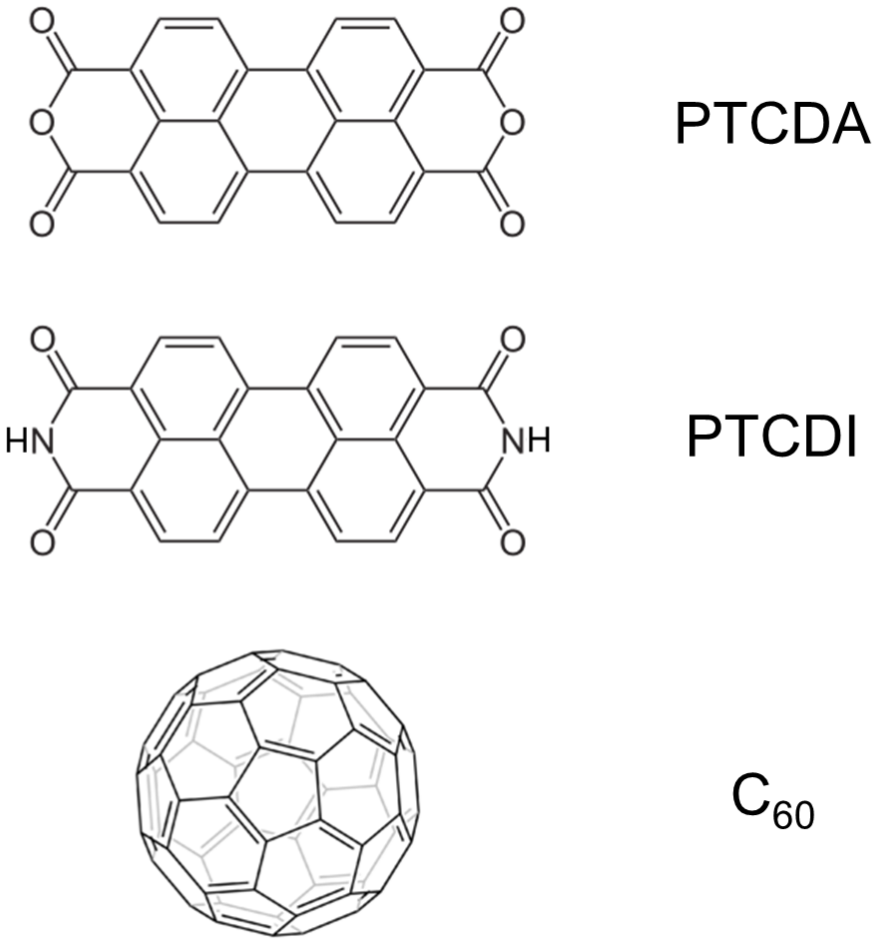

Figure 6.1: Schematic representation of the three molecules used for the study of adsorption on pristine and functionalized graphene. From top to bottom are PTCDA, PTCDI and C_{60}.

C_{60} on graphene

C_{60} molecules have been widely employed in the study of molecular self-organization mechanisms and in electronic devices such as organic photovoltaic cells. Monolayer of C_{60} deposited on graphene have been studied by STM and STS techniques [145, 148]. STM study reveals that the C_{60} molecules are closed packed on graphene surface without preferred aligning orientation. They are physisorbed on graphene as revealed by their weak interaction with the surface. High resolution images of the LUMO and HOMO of C_{60} shows that it is in contact with graphene by a hexagonal ring, suggesting that the C_{60} monolayer may be stabilized on graphene by a weak π-π coupling. The LUMO and HOMO positions of C_{60} adsorbed on graphene on SiC(0001) determined by STS are about 0.8 eV and -2.7 [145]. C_{60} was also deposited on a graphene-based transistor, demonstrating a weak *p*-type doping of graphene induced by C_{60} [149].

PTCDA on graphene

PTCDA may be the most studied molecules on graphene surface because it self-assembles in a 2D periodic structure and is expected to induce *p*-type doping of graphene. PTCDA monolayer on graphene at low temperature (4.7K) shows a brick wall structure, while a herring-bone structure is found at RT [146, 150, 151]. The herring-bone structure of PTCDA is stable and can be defect-free in hundred nanometer scaled domains, regardless the presence of graphene step edges or corrugation due to the underneath BLG. The intermolecular interactions seem much important than the interactions with graphene, and the charge transfer between PTCDA monolayer and graphene is small, as revealed by STS [146]. The LUMO and HOMO levels of the PTCDA monolayer on graphene on SiC(0001) obtained from its STS spectrum are located at about 1.1 and -1.8 eV [146].

PTCDI on graphene

The self-assembly of imidic-perylene derivative, PTCDI, has also been studied on graphene surface. The PTCDI molecules assemble in 1D linear structures on graphene, similar to their behavior on Ag(111) [147]. The formation of the linear structure is due to the formation of intermolecular hydrogen bonds between its imide group. It is also expected to slightly dope graphene into *p*-type. In order to stabilize PTCDI and to obtain a 2D-like self-assembled monolayer, PTCDI derivatives were studied and deposited on graphene. These derivative are designed by adding alkane chain groups and modifying lateral intermolecular interactions to favor the formation of 2D arrangements [152]. A dimer defect was observed in the DHH-PTCDI monolayer on graphene, which shows sign of covalent bonding of PTCDI and graphene on defect sites.

6.1 Experimental methods

The pristine and nitrogen-incorporated graphene substrates used for the deposition of molecules are prepared *in situ* in our preparation chamber, as introduced in chapter 2. Monolayer graphene samples are first prepared via Si sublimation in UHV according the procedure described in chapter 3. Nitrogen-incorporated graphene sample are fabricated by exposing a PG sample to N-ions at 20 eV for 10 min (equivalent to a dose of about 2-3$\times 10^{15}$ ions/cm^2, see chapter 4). The quality of the PG and NG is controlled by examining their structure and electronic properties using LEED and IPES. The concentration of the incorporated nitrogen in the NG used in this study is not measured (due to the limited quantitative resolution of *in-situ* AES) but is estimated to be about 3-5% of graphitic-N according to the previous studies shown in chapter 4. If the doping nitrogen atoms are uniformly distributed (or separated), every adsorbed molecule with a size similar to those studied here may interact with one graphitic-N in the graphene lattice at this graphitic-N concentration (3-5%). Even though the nitrogen are actually less uniformly distributed, the effect of the incorporated nitrogen to the adsorbed molecule monolayer is expected to be important enough to be observed.

The deposition of molecules on graphene samples are performed after the quality inspection of PG and NG. The molecule powders are loaded in a molybdenum crucible and sublimated toward the target sample. More details about the molecular source are presented in subsection 2.2.4. C_{60} molecules are sublimated at 395°C at a deposition rate of ∼10 min per monolayer. PTCDA and PTCDI molecules are sublimated at 290°C and 325°C for 10 min and 3 min, respectively, to obtain one monolayer on graphene. The molecular monolayers are then investigated by IPES at normal incidence complemented by LEED and AES measurements. The transmitting current of the IPES was reduced to under 0.4 μA for the investigation of PTCDA and PTCDI molecules, to avoid a rapid degradation of the molecules when using higher emission current (usually around 3 μA), which will be discuss later in this chapter.

6.2 Results and Discussions

Unoccupied states of C_{60} on PG and NG

Mono- and multi-layers of C_{60} are deposited on pristine and functionalized (N-doped) graphene. Except for a lower intensity of all molecule-related features, the IPES spectra of monolayer and multilayer of C_{60} on the PG and NG shows no difference in their peak positions or their relative peak-to-peak intensities, thus, only the spectra of the multilayer are shown for representation. Figure 6.2 shows the IPES spectra of C_{60} multilayer deposited on PG and NG, compared to the spectra of the clean PG and NG. The IPES spectrum of C_{60} on NG exhibits a rigid shift of about 0.4 eV of the entire spectrum toward E_F comparing to its counterpart on PG. More precisely, as shown in figure 6.2, all four molecular feature, $L_0 - L_4$ (corresponding to the LUMO, LUMO+1,

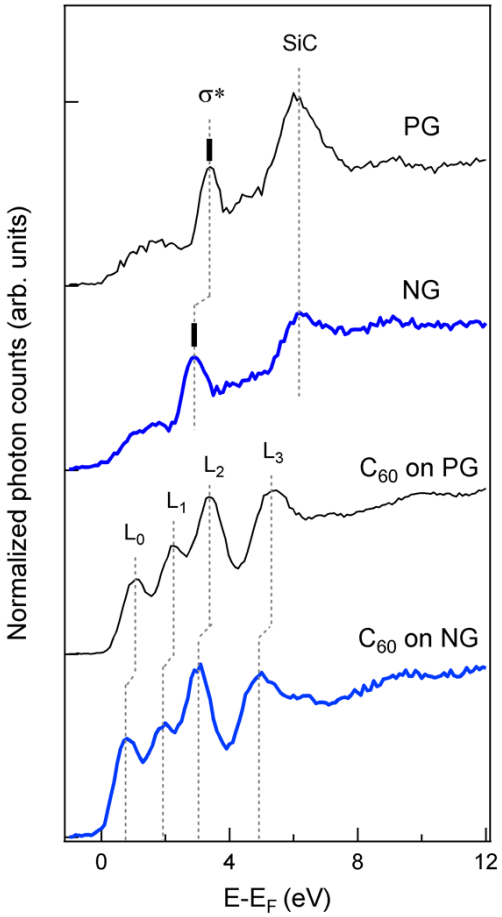

Figure 6.2: IPES spectra of PG (thin black curve), NG(thin blue curve), C_{60} on PG (thick black curve) and C_{60} NG (thick blue curve), respectively.Vertical dashed lines shows the corresponding peaks positions and their shifts.

2, 3 of C_{60}) exhibit the same shift (∼0.4 eV). This shifting magnitude is comparable to the *n*-shift of the σ^* of NG *wrt* PG (∼0.4 eV). It implies that the C_{60} levels follow the variation of the graphene levels.

In one of our previous studies concerning C_{60} on SiC-(3 × 3) reconstruction, we assigned a similar rigid peaks shift, observed on the C_{60} on hydrogenated (3 × 3) surface, to the change of band bending [144]. In the actual case, C_{60} on PG and NG, it is not the same scenario. The rigid shift observed here should not be due to the substrate band bending. This is because the position of the SiC bulk-related peak remains the same in both PG and NG, as indicated by the right vertical dashed line, which, as discussed in chapter 5, indicates the relative magnitude of the band bending. The position of the C_{60}-related peak is consistent with weakly interacting molecules electronically decoupled from the graphene. The lack of any charge transfer at the interface means that there is no surface dipole [153], therefore the molecules and the substrate align their vacuum levels. The position of unoccupied levels of the molecules *wrt* E_F becomes sensitive to any variation of the substrate electron affinity.

Despite the shift of the molecular states, C_{60} molecules remain physisorbed on PG and NG. Clean graphene surfaces are recovered after desorption of C_{60} at ∼500°C. No chemical reactions between C_{60} and NG (or PG) are stimulated by thermal annealing or low- or high-energy incident electrons.

Unoccupied states of PTCDA on PG and NG

The IPES spectra of figure 6.3a reveal the unoccupied states of a PTCDA monolayer on PG and NG comparing to those of clean PG and NG surfaces. The IPES spectrum of PTCDA on PG shows three major features near E_F. Nearest to the E_F, the peak located at 0.8 eV is attributed to the LUMO of PTCDA, namely L_0 in figure 6.3a, which is in good agreement with the position obtained by STS in the literature [146]. The second peak, located at 2 eV, is attributed to the LUMO+1 state of PTCDA (L_1). The third peak at highest energy of 3.5 eV is attributed to the σ^* states of graphene, because it locates close to the σ^* state of graphene at normal incidence (∼3.4 eV). More precisely, it actually shows a slight *p*-type shift of 0.1 eV with the presence of PTCDA. When the PTCDA monolayer is deposited on NG, a similar p-type doping of the N-doped graphene is observed. The σ^* state of NG (3.0 eV) shifts 0.1 eV higher with the adsorption of PTCDA (3.1 eV). Both results on PG and NG indicate that the acceptor character of PTCDA induces a *p*-type doping of the graphene. Worth mentioning, the LUMO and LUMO+1 positions of PTCDA roughly remain the same whether the monolayer is deposited on PG or NG, while the position of the σ^* peak follows the *n*-type doping of the NG (from 3.5 eV on PG to 3.1 eV on NG).

The *p*-type doping of graphene due to the adsorbed PTCDA monolayer indicates that there is a charge transfer between them. The electrons of both PG and NG are transferred to the PTCDA molecules, which result in a surface dipole (+-) toward the surface outwards. This surface dipole actually increases the work function of the

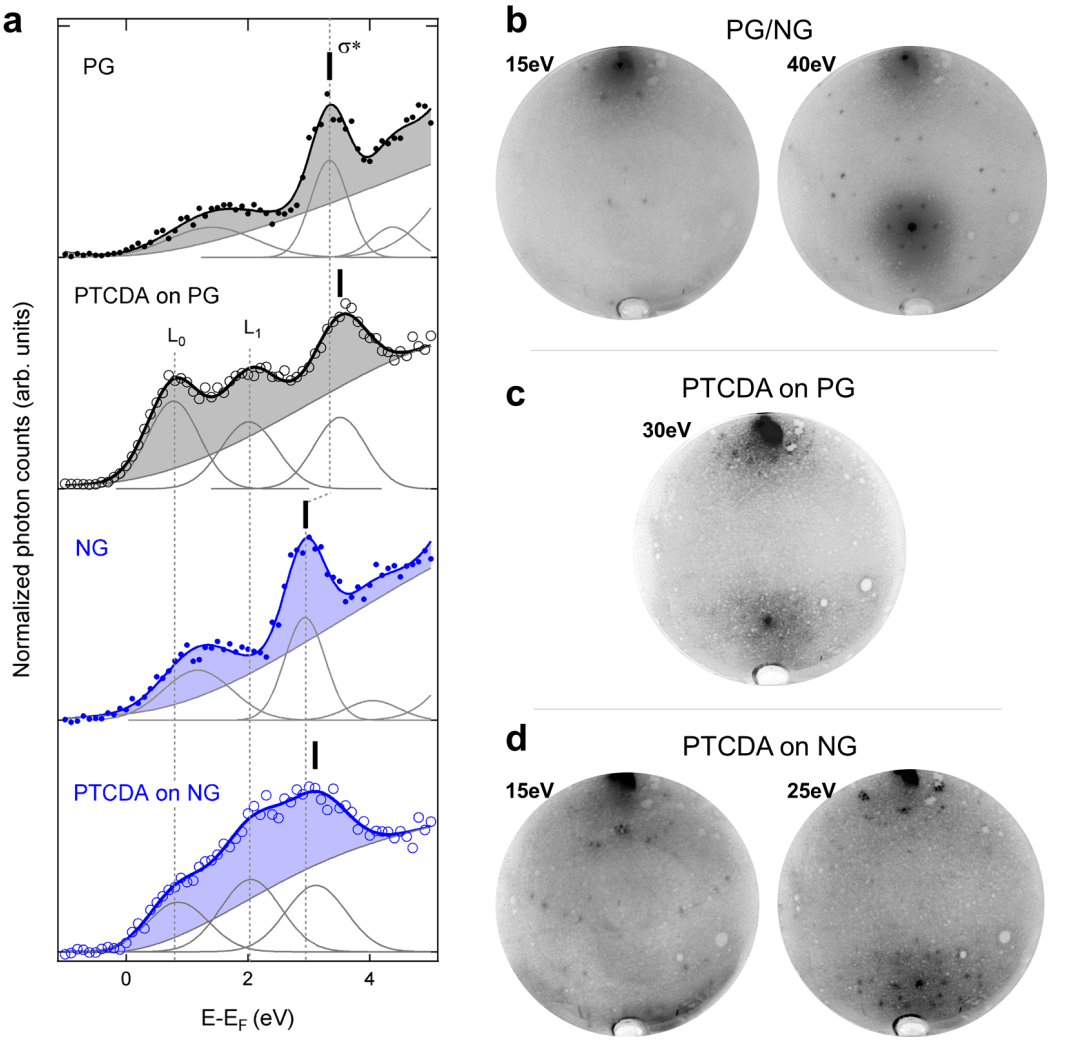

Figure 6.3: (a) IPES spectra of (from top to bottom) PG, PTCDA monolayer on PG, NG, and PTCDA monolayer on NG. The spectra are fitted using a series of Gaussian curves to reveal the position of each unoccupied states. Vertical thick bars indicate the positions of the σ^* states of graphene in each sample. Vertical dashed lines are shown as eye-guides to compare the locations of each unoccupied states, LUMO and LUMO+1 of PTCDA and σ^* of graphene. (b) LEED images of NG, PTCDA monolayer on PG and on NG. LEED images are acquired at various electron energies, as indicated beside each image.

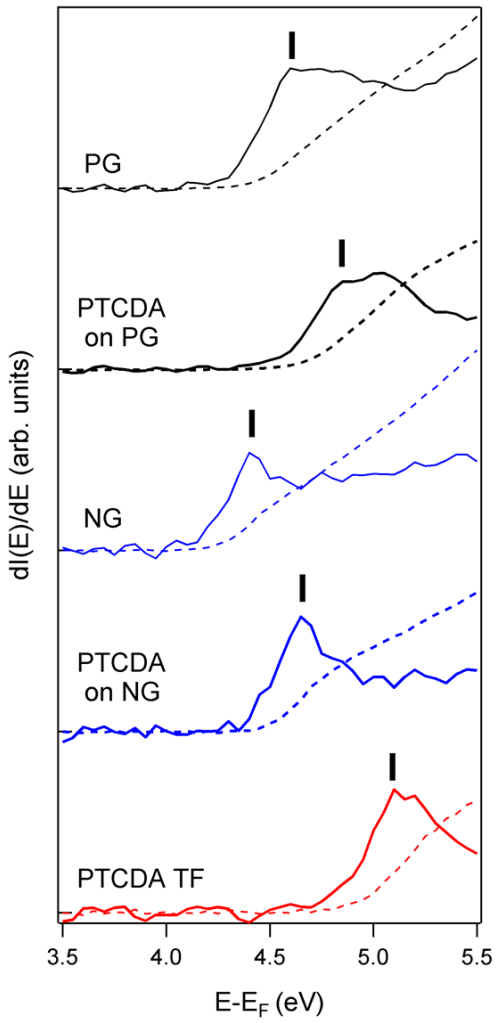

Figure 6.4: TCS spectra (solid curves) of PG, PTCDA monolayer on PG, NG, PTCDA monolayer on NG, PTCDA multilayer (or thick film, TF). Dashed curves are the respective absorbed current *wrt* incident electron energy. Vertical thick bars indicate the work function values of each sample.

sample [153], as evidenced in their TCS spectra. As shown in figure 6.4, the electron affinity increases when PTCDA monolayer is adsorbed on PG and NG surface due to the charge-transfer-induced surface dipole. For PG, the work function increases from ∼4.6 eV to ∼4.85 eV. And for NG, it increases from ∼4.4 eV to ∼4.65 eV. One may notice that the TCS spectrum of PTCDA on PG shows a second dI(E)/dE maximum at about 5.05 eV, which implies that some PTCDA molecules are adsorbed on the PTCDA monolayer, which exhibit an electron affinity close to the counterpart for multilayer of PTCDA. The PTCDA on PG may be slightly thicker than a monolayer.

Concerning the LUMO and LUMO+1 states of PTCDA, these two molecular states behave quite differently on PG and NG surfaces. whereas the LUMO+1 seems to show little difference on both surfaces, the former LUMO is much attenuated when PTCDA lies on NG. This implies a stronger coupling between graphene and the LUMO of PTCDA when the graphene is doped with nitrogen. There are several causes that would lead to the modification of molecular electronic states, such as charge transfer and covalent bonding. Covalent bonds seem not involved in this case, because, as mentioned before, PTCDA can be desorbed below 600°C. The most plausible explanation for this quenching of the LUMO feature is a larger charge transfer between PTCDA and NG.

As mentioned before, the adsorption of PTCDA induces a *p*-type shift of the σ^* band of graphene, as shown in figure 6.3a. Although the magnitudes of this shift are the same in both PG and NG cases, the levels of the charge transfer are different. This is because the DOS of graphene near the Dirac point increases quasi-linearly away from the Dirac point, due to the linear dispersion of the π^* band (figure 1.2). For a highly *n*-doped (or *p*-doped) graphene like NG, a larger DOS is found near E_F. Thus, it requires to introduce (or extract) more charges in order to induce the same level of band shifting. For a less doped graphene with a smaller DOS near E_F, such as PG, a smaller charge transfer is enough to induce the same shift.

The large charge transfer between PTCDA and NG should also produce a stronger surface dipole. Though, this is not directly observed in the modifications of their work functions, which are sensitive to the variation of surface dipole. Indeed, in figure 6.4, the adsorption of PTCDA increase the work function of ∼0.25 eV for both PG and NG. However, it should be noticed that the nitrogen doping also influences the surface dipole of NG. The doping nitrogen increases the electron density in graphene, shifting its unoccupied states ∼0.4 eV toward E_F. Simultaneously, the nitrogen doping also induces a surface dipole (+-) that intend to increase the work function, which opposes to the *n*-type doping that intend to decrease the work function. The compensation of the two results in a smaller decrease in the work function of NG, *i.e.* -0.2 eV *wrt* the PG counterpart. When the PTCDA monolayer is adsorbed on NG, part of the charge transfer is used to compensate the existing surface dipole (and the *n*-type doping). Thus, although having a larger charge transfer than on PG, the apparent work function is not much increased. In other words, if the surface dipole due to the doping nitrogen was not present, the work function of NG should be 0.2 eV lower, and the work function increased by the PTCDA would be larger, in accordance with the larger charge transfer.

Figure 6.3b-d shows the LEED images of NG, PTCDA on PG and PTCDA on NG sample. Since the LEED image of PG is closely identical to the NG, only the LEED image of NG is shown here (figure 6.3b). The contrast of each image has been enhanced differently to reveal the structure of the surface. The images of those with adsorbed molecules exhibit fainter diffraction spots and needed a larger enhancement to be able to identify the diffraction spots. The LEED images of NG are obtained at electron energies of 15 and 40 eV, which show both an intense graphene (1×1) spots along with some less intense spots related to the $(6\sqrt{3} \times 6\sqrt{3})R30°$ reconstruction of BLG. The LEED image of PTCDA on PG is obtained at an electron energy of 30 eV, as shown in figure 6.3c. It shows multiple spots around the (0,0) spot, different to those of $(6\sqrt{3} \times 6\sqrt{3})R30°$, which indicates that the PTCDA monolayer is actually well arranged and periodically aligned following the lattice of graphene. Figure 6.3d shows the LEED images of PTCDA on NG obtained at 15 and 25 eV. They still exhibit a large series of spots different to those of NG, indicating that the self-arrangement of PTCDA still remains on NG. Since the presence of doping N has little influence on its self-assembly, we assume that the PTCDA-NG interaction remains weak, while the intermolecular interactions still dominate. By annealing the sample up to about 600°C, all PTCDA molecules are desorbed from both graphene surfaces and a clean PG or NG surface is recovered by showing a clean (1×1) LEED pattern. These results agree with the suggestion deduced from the IPES studies that PTCDA molecules do not form strong chemical bonds with NG, and the quenching of its LUMO feature should be due to a stronger charge transfer.

We were not able to further investigate the PTCDA monolayer on PG and NG (*e.g.* the dispersion of its unoccupied states and detailed LEED pattern) due to several reasons. First, the use of a fluorescent screen of LEED limits the spatial resolution of the LEED spots. In contrast, a detailed study of the LEED pattern of PTCDA on graphene reported recently has used a 2D micro-channel plate to obtain high spatial resolution and high sensitivity of the diffracted electrons [154]. Second, the PTCDA molecules degrade after exposing to a certain dose of electrons, as discussed in more detail in the next section. Since all of our *in situ* analysis techniques involve incident electrons onto the target sample, either at low energy (5-100 eV for IPES and LEED) or high energy (1200 eV for AES), we had to limit the total acquisition time and the emission current of these measurements in order to prevent the degradation of PTCDA. The few results presented here are the most we could obtain from the same sample before a significant degradation of PTCDA occurred.

Nevertheless, the unoccupied states of a monolayer of PTCDA on graphene shows that its LUMO seems to experience a stronger coupling with graphene when the graphene layer is doped with nitrogen. A more important charge transfer between PTCDA and NG is evidenced by the IPES and TCS results. The LEED images confirm that a PTCDA monolayer self-assembles on graphene, and they also reveal that this arrangement is not disturbed by the presence of incorporated nitrogen. The PTCDA

molecules can also be desorbed from both PG and NG surface if not degraded, indicating that PTCDA is rather physisorbed with a charge transfer on both surfaces and no predominant covalent bonding between PTCDA and NG (or PG) exists.

Unoccupied states of PTCDI on PG and NG

Figure 6.5a shows the IPES spectra of PTCDI on PG and NG. Similar to PTCDA on graphene, as shown in figure 6.5b, the IPES spectra of PTCDI on PG and NG also show three major features, which are assigned to LUMO, LUMO+1 and σ^* of graphene. The LUMO of PTCDI on PG is located at about 0.9 eV, slightly higher than the LUMO of PTCDA (0.8 eV). The LUMO+1 of PTCDI on PG (at 2.45 eV) is also higher than the PTCDA counterpart (2 eV). The σ^* states of PG, while a PTCDI monolayer is deposited on the surface, is located similar to the position found for PTCDA, at 3.6 eV.

When PTCDI is deposited on NG, the LUMO of PTCDI seems unchanged (both location and intensity) but the LUMO+1 is shifted toward E_F and is also slightly attenuated. The σ^* states of NG is shifted to 3.2 eV due to the n-type doping of nitrogen, similar to the case of PTCDA. The presence of nitrogen in graphene seems to affect the LUMO+1 state of PTCDI rather than the LUMO, as for PTCDA. Since PTCDI can be desorbed from both PG (and NG) at 600°C, it implies that no covalent bonding is formed between PTCDI and PG (or NG). The reason that LUMO+1 is affected rather than LUMO may be due to the different arrangement and adsorption configuration of PTCDI on graphene compared to the PTCDA counterpart. As introduced earlier, the former align in long parallel lines due to strong hydrogen bonds between imide groups, and the latter in herring-bone structure. The electron diffraction of the expected linear arrangement of PTCDI is not observed in the LEED image (no diffraction is observed), thus is not shown here.

As mentioned earlier, the PTCDI molecules (as well as PTCDA) are easily degraded under low energy electron exposure. The IPES spectrum of PTCDI, no matter on PG or NG, is rapidly modified into the bottom spectrum in figure 6.5a. It is assigned to the degraded PTCDI molecules as its LUMO and LUMO+1 features are strongly attenuated, and no significant feature can be resolved. Similar degradation is observed for PTCDA monolayer on graphene, as shown in figure 6.5b. The dose of low-energy-electrons producing such degradation is about 3-5 μA for 10 min, which is much too short to acquire any useful information. By decreasing the emission current by a factor of 10, to about 0.4 μA, the degradation of molecules due to incident electron is slowed-down, and the reliable measurement period can be extended to over 1 hour.

The low energy electrons are suggested to be the major cause of the PTCDI degradation. It is because the low energy electrons of 5-20 eV bring the molecules to excited states by filling unoccupied states close to E_F. The excited molecules would be much reactive at such circumstance and may react with neighbor molecules or graphene or

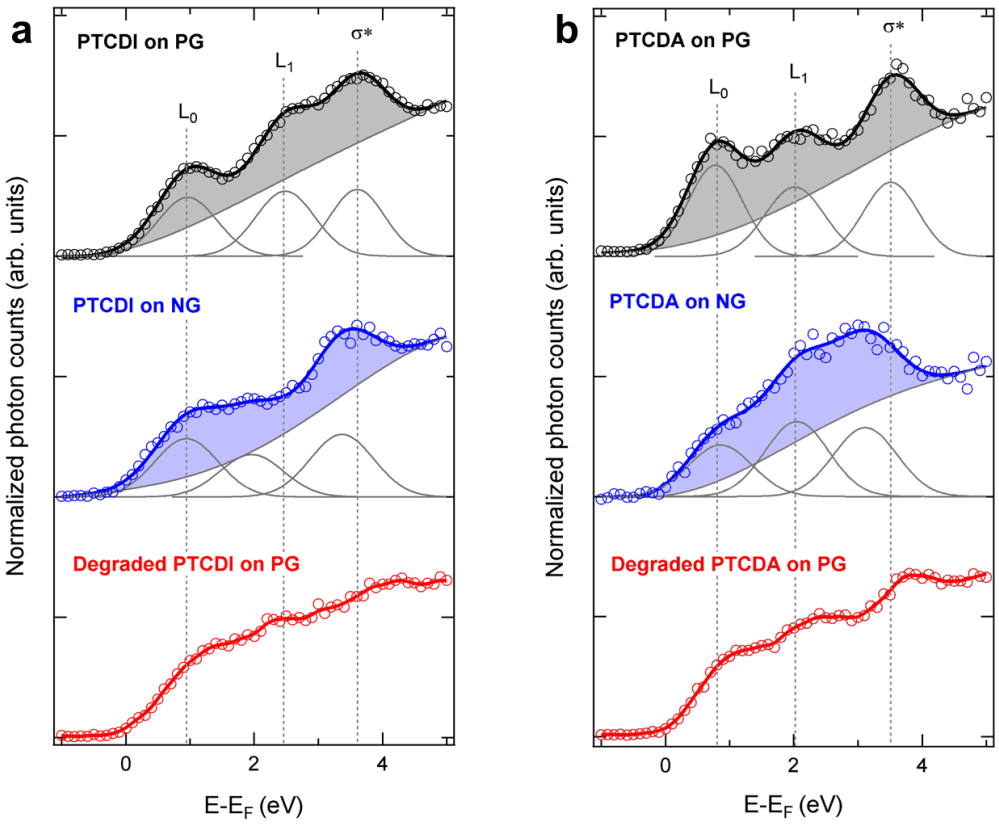

Figure 6.5: (a) IPES spectra of PTCDI monolayer on PG (black) and NG (blue). The spectra are fitted using a series of Gaussian curves to reveal the position of each unoccupied states. The bottom spectra compare the degraded PTCDI layer after exposing to high dose of low energy electrons. (b) Comparative IPES spectra of PTCDA monolayer on PG (black), NG (blue) and after degradation.

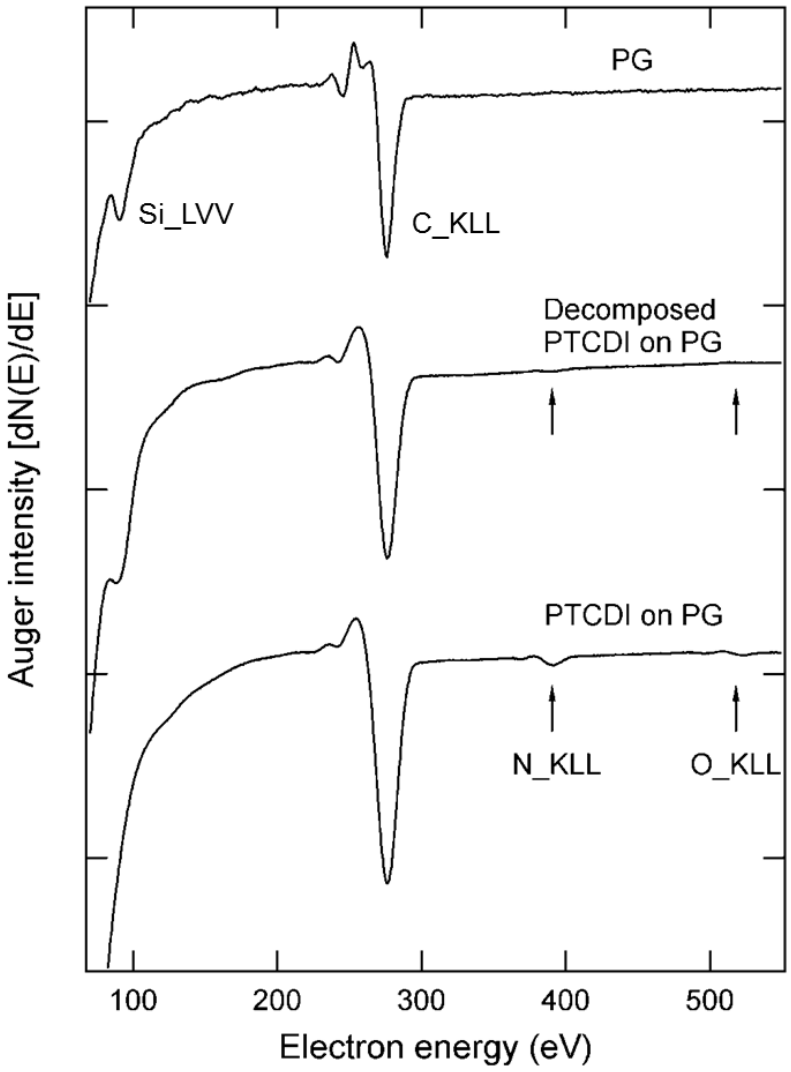

Figure 6.6: AES spectra of PG, decomposed PTCDI on PG and self-assembled PTCDI on PG.

become decomposed into carbon-based composites. Figure 6.6 shows the Auger electron spectra of PTCDI on PG compared to a monolayer of decomposed PTCDI on PG and a clean PG. Worth noticing, the condition of the AES measurement of PTCDI samples are different to that for PG. The emission current is reduced and the modulation signal for lock-in amplifier is increased to 7V (instead of 5V for PG), in order to keep a correct signal-to-noise ratio. When PTCDI molecules are just deposited on PG, their AES spectrum shows a small N_{KLL} and O_{KLL} feature, and the Si_{LVV} feature is strongly attenuated compared to the AES spectrum of PG. The N_{KLL} and O_{KLL} feature indicate that the adsorbed PTCDI molecules are in their pristine structure. After the PTCDI monolayer on PG is exposed to a large dose of low energy electrons, a large amount of PTCDI are degraded as revealed by IPES. These degraded molecules cannot be removed by thermal annealing (even as high as 850°C). The middle AES spectrum shows the chemical composition of the decomposed PTCDI on PG. It clearly shows that almost no oxygen or nitrogen remain on the surface, which implies that PTCDI molecules have lost their oxygen and nitrogen-related function group. The higher C_{KKL} to Si $_{LVV}$ ratio than the PG counterpart also indicates that some carbon-rich composites remain on the surface, which we attribute to decomposed PTCDI. These carbon composites seem to be covalently bonded to graphene since they still remain on the surface at 850°C. We are not sure if this degradation effect is surface related, since these observations are identical for PTCDI on NG. We did not observe any difference in the chemical reactivity of PTCDI and PTCDA on the PG and NG at these magnitudes.

6.3 Summary

We have studied three different molecules deposited on PG and NG surfaces, namely C_{60}, PTCDA and PTCDI. All three molecules can be successfully desorbed from both PG and NG surfaces if they are not degraded, indicating that no covalent bonds are formed between molecules and graphene, as deposited. A weak physisorption is suggested for C_{60} on graphene, no matter the latter is doped or not. For PTCDA and PTCDI on graphene, a stronger physisorption with a charge transfer seems to take place.

The unoccupied states of PTCDA and PTCDI are more modified on NG surface than on PG counterpart. The LUMO of PTCDA is reduced on NG and a stronger charge transfer can be deduced from the IPES and TCS spectra, indicating stronger molecule-graphene interactions with the presence of incorporated nitrogen. For PTCDI, the LUMO+1, instead of LUMO, is more significantly affected by the incorporated N by showing a downward shift and a quenching when adsorbed on NG. The difference of the affected molecular orbital for PTCDA and PTCDI on NG may be attributed to their difference in the adsorption configuration and molecular arrangement. Though, further study is needed to confirm this assumption.

On the other hand, we have observed degradations of PTCDA and PTCDI, when exposed to large dose of low-energy electrons. Molecules are decomposed, losing their

oxygen- and nitrogen-containing function groups, as revealed by AES. The remaining carbon composites seems to remain covalently bonded to graphene even at temperature as high as 850°C.

Despite that the high-electron-density sites of N do not appear to promote a higher chemical reactivity of NG with the three studied molecules, the unoccupied states of the perylene-derived molecules are still affected by a stronger charge transfer. The degradation of PTCDA and PTCDI on both PG and NG, when exposed to large amount of low-energy electrons, demonstrate the possibility to realize chemical reaction between the molecules and the graphene. In addition, as shown in chapter 4, a modification of the chemical state of graphitic-N was also observed with the adsorption of H_2O (or other oxygen-containing) molecules. These results imply that the local reactions between molecules and graphene stimulated by tip induced tunneling current are possible, if adequate molecules and processes are employed. In addition, the nitrogen doping of graphene may also enhance this reactivity at a certain level. However, this study is still in progress and has not been accomplished to date.

Chapter 7

Conclusions and perspectives

This thesis presents several studies involving the interesting field of "the functionalization of graphene". These studies include: (i) the fabrication and characterization of the epitaxial graphene grown on SiC(0001) and SiC(000$\bar{1}$), (ii) the functionalization of the graphene, which is demonstrated via plasma-based nitrogen doping, hydrogenation, and (iii) the interaction between molecules and the functionalized graphene. The pristine and functionalized graphene monolayers are investigated in various aspects. Their electronic properties are studied through their unoccupied band structures using ARIPES. Their chemical properties, such as atomic compositions and chemical environments, are investigated using XPS and AES. Their structural characters are revealed by LEED.

The dispersion of the σ^* and π^* bands of monolayer graphene on SiC(0001) is revealed by ARIPES for the first time. The experimental results primitively agree with the calculated band structure using GW approximation. Although the access to the Dirac point at the K point of graphene BZ is forbidden due to current experimental setup, a reliable linear extrapolation of the π^* states away from K is used to determine the relative shift of the E_F *wrt* the Dirac point and to estimate the Fermi velocity variation. The IPES spectra of the graphene also give information about its thickness by the emergence of a thickness-dependent peak at 9 eV above E_F, which is attributed to interlayer interaction. It is shown to be reliable and precise for the determination of the actual thickness of the epitaxial graphene.

The epitaxial graphene on SiC(000$\bar{1}$), the C-face of SiC, grows by stacks of multilayers and is shown to be quasi-undoped as compared to the graphene on the Si-face. This multilayer graphene is randomly oriented with a preferred angle of 4-17° or 30° *wrt* SiC (1×1), where each layer exhibits the character of single-layer graphene. Upon nitrogen plasma exposure, the graphene layer(s) randomly oriented become n-doped, implying that the top graphene layer(s) may be mostly constituted by these disoriented graphene layers. The graphene aligned at 30° *wrt* SiC is suggested to be the bottom graphene layer, being in contact with SiC.

The functionalization of graphene is principally focused on the incorporation of nitrogen via plasma-based methods. The plasma exposure using the two nitrogen sources, *i.e. in situ* MW-ECR plasma source and *ex situ* plasma implanter owned by IBS, both show successful nitrogen incorporation. The total nitrogen concentration can be attained up to about 4-15% for the former and 0.2-3% for the latter. The smaller nitrogen incorporation using the *ex situ* plasma source is due to the lack of heating elements in the implanter. Actually, we show that, if the doping process is proceeded at high temperature, the graphene may sustain higher exposition dose of N ions, thus incorporate more N without degradation.

We have also shown that the bonding configuration of the incorporated nitrogen in graphene can be controlled by the incident species and the thickness of PG. For example, pyridinic-N (nitrogen doping site with a neighbor vacancy) are favorably incorporated using thermalized nitrogen atoms with the presence of pre-existing defects. Graphitic-N (substitutional nitrogen bonded to three neighbor C atoms) are incorporated by exposing to low-energy N ions (5-60 eV), with an optimum energy of about 35 eV. Moreover, defect-dependent pyridinic-N are still created when doping a monolayer graphene with N-ion, but can be much suppressed if doping a bilayer (or multilayer) graphene. The ratio of graphitic-N:pyridinic-N in the resulting NG may increase from 1:1 for monolayer graphene to over 10:1 for bilayer graphene. This thickness dependency may be related to a higher reactivity of monolayer graphene, and/or a physically more rigid structure of bilayer graphene. Similar ion-energy and thickness dependencies for the incorporation of graphitic-N are also found when using the *ex situ* plasma implanter of IBS.

Furthermore, graphitic-N dopants are shown to induce n-type doping of graphene. For example, a 0.4 eV n-shift of the E_F is estimated for 8% of graphitic-N after a 35 eV N-ion exposure for 10 min. A slight decrease of Fermi velocity is also observed. This is compatible with theoretical simulation, which expects a n-doping and a decrease of v_F of graphene with graphitic-N. An opening of a band gap was also predicted at K points but should be located below E_F and would require ARPES measurement to confirm its presence. Unfortunately, the ARPES measurement is not preceded yet because the instrument, owned by the collaborating laboratory at IS2M, where we planned to carry out the measurements, was not functional till recently. These measurements should be planned in the follow-up work.

Concerning the doping efficiency of the incorporated graphitic-N, a charge transfer is estimated to be about 0.06-0.1 electron per graphitic-N in monolayer graphene, which is much smaller than the value reported in the literature, 0.5-0.6, obtained by the STS technique. This implies that the actual doping configurations of these graphitic-N are more complex than randomly distributed single graphitic-N. Doping sites containing multiple graphitic-N, which would induce less average charge transfer should be considered. The different trends in the π^*-shift and v_F decrease *wrt* N-ion dose and energy also support this assumption. Actually, the preliminarily STM images of the

NG prepared using *ex situ* plasma implanter validate the presence of complex N-doping sites.

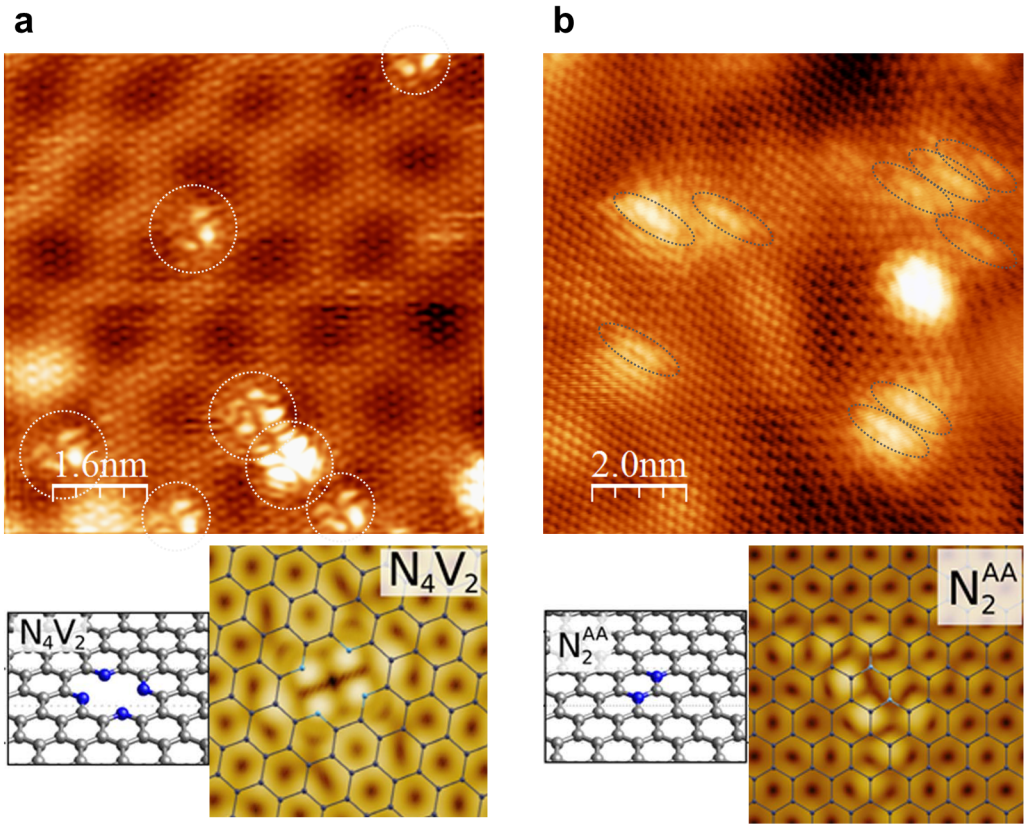

Figure 7.1: Preliminarily LT-STM images of the NG prepared using *ex situ* plasma implanter. Image obtained from (a) N-doped monolayer graphene (V_{bias}=-1.4 V, 500 pA) (b) N-doped bilayer graphene (V_{bias}=-0.14 V, 500 pA) at substrate temperature of 77 K.

Figure 7.1 shows two examples of the nitrogen doping sites on graphene observed by STM. Figure 7.1a shows "flower-like" features with four "leaves", as indicated by white dashed circles. They may be assigned to pyridinic-N doping sites with a double vacancy considering their similar symmetry. The represented bonding configuration and the simulated STM image reprinted from Ref. [51] are shown at the bottom of the figure. Figure 7.1b shows another type of doping site consisting of four features linearly aligned, as encircled by black dashed lines. These doping sites are assigned to two graphitic-N in a single hexagonal ring of graphene in the same lattice point, namely N_2^{AA}. This doping configuration is also reported and simulated in Ref. [51] as shown in the bottom inset. Besides these two types of features, other doping sites with different shapes were also observed but are not successfully resolved in atomic scale, thus are not

shown here. Most doping sites observed by STM seem to result from complex N-doping configurations, which are less well-known. This also complicates the analysis of these defect- and dopant-relative features in STM images. The presence of large-size impurity on the NG surface also severely complicates the STM imaging. Further measurements on lightly doped NG samples would be considered in the follow-up study. Comparative studies using *in situ/ex situ* plasma source and mono/multi-layered graphene may be also considered.

On the other hand, the hydrogenation of the BLG demonstrates a different way to achieve the functionalization of graphene. At RT, hydrogen atoms are covalently bound on the surface, forming the H-BLG. The chemisorbed hydrogen induces the formation of additional C-Si bonds at BLG/SiC interface, saturating the remaining Si dangling bonds, as revealed by IPES and AES. The surface states related to these dangling bonds are thus annihilated "indirectly" by the hydrogenation. It further creates a wide band gap near E_F of H-BLG, tuning it to a strongly insulating 2D material. As most of the C atoms in H-BLG are bonded to H at the surface or to Si at the bottom interface, the H-BLG is claimed to be graphane-like. The hydrogenation of BLG at high temperature decouples the BLG into a QFSG via hydrogen intercalation, as also reported in previous works. By combining the highly conductive QFSG and the semi-insulating H-BLG, a new concept for the engineering of graphene-based device is proposed. It has the advantage to pattern graphene without the need to etch the graphene layer. It requires only to tailor the electronic properties of BLG via the patterning of covalently bonded area (H-BLG) and non-bonded area (QFSG), by controlling the surface temperature during the hydrogenation of BLG, *e.g.* via a focused laser beam.

Finally, the interaction between π-conjugated molecules and the functionalized (or pristine) graphene is investigated. The unoccupied states of C_{60}, PTCDA and PTCDI on PG and NG are investigated. The C_{60} unoccupied states are rigidly shifted to lower energy toward E_F to align its vacuum levels to the substrate when deposited on NG (*wrt* PG counterpart), indicating a weak interaction. The C_{60} molecules remain physisorbed on NG and PG after low- and high- electron exposure. On the contrary, the LUMO of PTCDA monolayer is suppressed when deposited on NG (compared to PG), while it is the LUMO+1 of PTCDI that is more affected on NG. The modifications of these molecular states are attributed to a stronger molecule-graphene charge transfer with the incorporation of nitrogen. The different behaviors of PTCDA and PTCDI are suggested to be related to the arrangement of these molecules on NG. A modification of the chemical state of graphitic-N is also observed by XPS with the presence of some adsorbed molecules (such as H_2O) after ambient air exposure. These results indicate that the interaction between molecules and graphene is modified after the functionalization of graphene via nitrogen doping.

However, we were not able to determine whether the chemical reactivity of the functionalized graphene is enhanced or not. All molecules deposited on NG remain relatively weakly coupled with graphene and can be removed from the surface via thermal annealing at 500°C, if they are not degraded. An exposure to low-energy electrons

of PTCDA and PTCDI monolayers on graphene actually degrade the molecules and may create covalent bonding of molecular fragments with the graphene, regardless they are deposited on PG or NG. No distinct difference in the rate of degradation on PG and NG can be determined, and the electron dose seems to be the major dependence of the degradation. Nevertheless, we have shown the possibility to generate chemical reactions between molecules and graphene using low-energy electrons, and we have shown an enhanced interaction between molecules and the functionalized graphene. We believe that with proper methods, molecules and conditions, the final goal of the "ChimiGraphN" project, *i.e.* to initiate local chemical reaction of dienophile molecules with a more reactive functionalized graphene via tip-induced tunneling current, can be achieved in the near future with the contribution of this work.

Appendix

AES acquisition program based on Igor Pro

```
\#pragma rtGlobals=1  // Use modern global access method.
// Yu-Pu LIN Fev. 2012
\#pragma IndependentModule = AugerSpectro_Module
////////////////////////////// Menu ////////////////////////////////
Menu "--Photoemission--"
 "Auger Electron Spectorscopy/F10", AugerSpectro_Module\#AugerSpec()
end
////////////////////////////// Init ////////////////////////////////
Function AugerSpec()
 NewDataFolder /O/S root:AugerSpec
 NewDataFolder /O/S root:AugerSpec:Data
 SetDataFolder root:AugerSpec
 ASInitVar() // Recover global variables or creates them
 AugerSpecWindow() // Creates the main panel
end
////////////////////// Init Variables //////////////////////////
Function ASInitVar()
 SetDataFolder root:AugerSpec
 NVAR/Z VarStabTime
 NVAR/Z VarAverage
 NVAR/Z VarSingle
 NVAR/Z VarMin
 NVAR/Z VarMax
 NVAR/Z VarIncrement
 NVAR/Z InputChannel // Channel for reading input
 NewPath/O AES "D:na.manipipe:Data:AugerSpec:"
 SVAR /Z Var_SavingFolder
 NVAR /Z Var_FileNb
 SVAR /Z Var_FileName
 SVAR/Z Note1
 SVAR/Z Note2
 NVAR/Z VarcurrentKE
 NVAR /Z VarsweepNb
 Variable /G Varcurrentsweepnb=1
 Variable/G isPaused=0 // 0 means not paused
 Variable/G Varcounter=0
 WAVE /Z currentwave
 WAVE /Z energywave
 WAVE /Z SumWave
 Variable /G SweepRunning=0 // Not running
 Variable /G SettingRunning=0 // Not running
 Variable /G CurrentSettingRunning=0 // Not running
 Variable /G CtrlTab=0
 Variable /G anythingChanged = 0 // ==1 when either Emin, Emax, Increment changes
 //Variable /G SweepTab=0
 SVAR /Z Varspecname
 SVAR /Z Var_sample
 NVAR /Z Var_Ef
 SVAR /Z Var_deposition
```

```
SVAR /Z Var_prepa
NVAR /Z Varcurrent

if (!SVAR_Exists(Var_sample))
 String/G Var_sample="SiC"
endif
if (!NVAR_Exists(Var_Ef))
 Variable/G Var_Ef=0
endif
if (!SVAR_Exists(Var_deposition))
 String/G Var_deposition="H*"
endif
if (!SVAR_Exists(Var_prepa))
 String/G Var_prepa=""
endif
if (!SVAR_Exists(Note1))
 String/G Note1="Note"
endif
if (!SVAR_Exists(Note2))
 String/G Note2="Note suivante"
endif
if (!SVAR_Exists(Var_FileName))
 String/G Var_FileName="AESpec"
endif
if (!NVAR_Exists(Var_FileNb))
 Variable/G Var_FileNb=1
endif
if (!SVAR_Exists(Var_SavingFolder))
 pathinfo AES
 String/G Var_SavingFolder=S_path//"D:manip:AugerSpec"
endif
if (!NVAR_Exists(InputChannel))
 Variable/G InputChannel=1 // ?? input ??
endif
if (!NVAR_Exists(VarStabTime))
 Variable/G VarStabTime=0.1
endif
if (!NVAR_Exists(VarAverage))
 Variable/G VarAverage=100
endif
if (!NVAR_Exists(VarSingle))
 Variable/G VarSingle=4.2 // don't need?
endif
if (!NVAR_Exists(VarMin))
 Variable/G VarMin=50  // Min
endif
if (!NVAR_Exists(VarMax))
 Variable/G VarMax=300  // Max
endif
if (!NVAR_Exists(VarIncrement))
 Variable/G VarIncrement=0.1
endif
if (!NVAR_Exists(VarcurrentKE))
 Variable/G VarcurrentKE=0
endif
if (!NVAR_Exists(Varsweepnb))
 Variable/G Varsweepnb=5
endif
if (!NVAR_Exists(Varcurrent))
 Variable/G Varcurrent=0
endif

////////////////////// Same thing in the StartButtonProcedure
Variable/G currentwavelength = ceil(((VarMax-VarMin)/VarIncrement))//+1
VarIncrement = ceil((VarMax-VarMin)*1000 / currentwavelength) /1000
if (!WaveExists(currentwave))
 Make/N=(currentwavelength) currentwave=0
 SetScale/P x, VarMin, VarIncrement, currentwave
endif
if (!WaveExists(energywave))
```

```
  Make/N=(currentwavelength) energywave=0
  SetScale/P x, VarMin, VarIncrement, energywave
 endif
 if (!WaveExists(SumWave))
  Make/N=(currentwavelength) SumWave=0
  SetScale/P x, VarMin, VarIncrement, SumWave
 endif
 if (!SVAR_Exists(Varspecname))
  String/G Varspecname="Spec"
 endif
End

////////////////////////////// Main Panel ////////////////////////////////////
Function AugerSpecWindow() : Panel
 SetDataFolder root:AugerSpec
 NVAR VarStabTime
 NVAR VarAverage
 NVAR VarSingle
 NVAR VarMin
 NVAR VarMax
 NVAR VarIncrement
 NVAR VarcurrentKE
 WAVE currentwave
 WAVE SumWave
 SVAR Var_SavingFolder
 SVAR Var_FileName
 NVAR Var_FileNb
 NVAR VarsweepNb
 NVAR VarStabTime
 NVAR Varcurrent

 PauseUpdate; Silent 1  // building window...
 NewPanel /K=0 /W=(90,64,1018,585) as "AES Control and acquisition"
 ModifyPanel cbRGB=(60928,60928,60928)
 //ShowTools/A
 String PanelName = WinName(0,64)
 TabControl UPSTab,pos={7,12},size={252,277},proc=CtrlProcAES
 TabControl UPSTab,labelBack=(57344,57088,58112),tabLabel(0)="Scan Controls"
 TabControl UPSTab,tabLabel(1)="Sample",value= 0 //,tabLabel(2)="Miscellaneous",value= 0
 SetVariable saveFolder,pos={22,39},size={229,16},bodyWidth=170,title="Data Folder", proc=AESSaveFolderProc
 SetVariable saveFolder,value=Var_SavingFolder, disable=0, help={"Use a semicolomn instead of a \"/\""}
 SetVariable specname,pos={30,62},size={111,16},bodyWidth=60,title="FileName:"
 SetVariable specname,frame=1, value= Var_FileName
 SetVariable specnb,pos={170,62},size={45,16},bodyWidth=60,title="-"
 SetVariable specnb,frame=1, value=Var_FileNb, limits={0,999,1}
 SetVariable sweepnb,pos={54,86},size={87,20},bodyWidth=60,title="Sweep Nb"
 SetVariable sweepnb,limits={1,300,1},value=VarsweepNb
 SetVariable sweepnb proc=SweepNbProcAES
 SetVariable emin,pos={54,115},size={87,20},bodyWidth=60,title="E\\Bmin",frame=1
 SetVariable emin value=VarMin, proc=MaxMinIncProcAES
 SetVariable emin limits={0,1500,0.1}
 SetVariable emax,pos={51,143},size={90,20},bodyWidth=60,title="E\\Bmax",frame=1
 SetVariable emax value=VarMax, proc=MaxMinIncProcAES
 SetVariable emax limits={0, 2000,0.1}
 SetVariable increment,pos={30,167},size={111,16},bodyWidth=60,title="Increment"
 SetVariable increment,frame=1,limits={0,10,0}
 SetVariable increment , value=VarIncrement, proc=MaxMinIncProcAES
 SetVariable countingtime,pos={30,186},size={111,16},bodyWidth=60,title="Stab. time"
 SetVariable countingtime,limits={0.01,10,0},value=VarStabTime
 SetVariable count,pos={25,322},size={225,40},title="\\Z16dN/dE:"
 SetVariable count,fSize=35, valueColor=(0,0,0), disable=0
 SetVariable count,limits={0,1,0},value=Varcurrent,noedit=1
 SetVariable currentenergy,pos={35,404},size={215,40},bodyWidth=60,title="\\Z16Current Energy:"
 SetVariable currentenergy,limits={0,1000,0},barmisc={0,1000}, valueColor=(65280,0,0)
 SetVariable currentenergy value=VarcurrentKE, fSize=35,bodyWidth=100
 SetVariable currentenergy disable=0,noedit=1, proc=CurrentEnergyVarProcAES
 SetVariable currentsweep,pos={36,445},size={174,32},bodyWidth=60,title="\\Z16Current Sweep:"
 SetVariable currentsweep,fSize=25,limits={0,0,0},barmisc={0,1000}
 SetVariable currentsweep,value=Varcurrentsweepnb
 SetVariable currentsweep disable=0,noedit=1
```

```
 SetVariable sample,pos={39,41},size={209,16},bodyWidth=170,title="Sample"
 SetVariable sample,value=Var_sample, disable=1
 SetVariable prepa,pos={20,97},size={228,16},bodyWidth=170,title="Preparation"
 SetVariable prepa,value=Var_prepa, disable=1
 SetVariable deposition,pos={17,122},size={231,16},bodyWidth=138,title="Deposition species"
 SetVariable deposition,value=Var_deposition, disable=1
 SetVariable Note1,pos={30,148},size={218,16},bodyWidth=170,title="Note1"
 SetVariable Note1,value=Note1, disable=1
 SetVariable Note2,pos={30,173},size={218,16},bodyWidth=170,title="Note2"
 SetVariable Note2,value=Note2, disable=1
 Button stopaftersweepbutton,pos={63,496},size={120,20},title="Stop after sweep"
 Button stopaftersweepbutton proc=StopAfterSweepButtonProcAES
 Button stopaftersweepbutton,fSize=14
 Button stopbutton,pos={8,496},size={50,20},disable=1,title="Stop",fSize=14
 Button stopbutton proc=StopButtonProcAES
 Button startbutton,pos={8,496},size={50,20},title="Start",fSize=14
 Button startbutton proc=StartButtonProcAES
 Button pausebutton,pos={185,496},size={72,20},proc=PauseButtonProcAES,title="Pause", disable=2
 Button pausebutton,fSize=14
 Button resumebutton,pos={185,496},size={72,20},proc=ResumeButtonProcAES,title="Resume",disable=1
 Button resumebutton,fSize=14
 TabControl plots,pos={261,6},size={1387,943}, proc=GraphProcAES
 TabControl plots,tabLabel(0)="Sum", tabLabel(1)="Sweeps" //, tabLabel(2)="Set Counts up"

 Display/W=(266,27,1620,947)/HOST=\# SumWave
 Label bottom "Energy (eV)"
 Label left "dN/dE"
 SetDrawLayer UserFront
 ModifyGraph frameStyle=2, nticks(bottom)=10, zapTZ(left)=1
 SetAxis/A left 0,*
 SetAxis bottom 50,*
 RenameWindow \#,SumWindow
 SetActiveSubwindow \#\#
  Display/W=(266,27,1620,947)/HOST=\# /HIDE=1 SumWave as "Sweep cheking Window"
 Label bottom "Energy (eV)"
 Label left "dN/dE"
 SetDrawLayer UserFront
 ModifyGraph frameStyle=2, nticks(bottom)=10, zapTZ(left)=1
 SetAxis left 0,*
 SetAxis bottom 50,*
 RenameWindow \#,SweepWindow
 RemoveFromGraph SumWave
 SetActiveSubwindow \#\#
 return 0
End

//////////////////////////// Saving Folder ////////////////////////////////
Function AESSaveFolderProc(sva) : SetVariableControl
 STRUCT WMSetVariableAction &sva
 switch( sva.eventCode )
  case 1: // mouse up
  case 2: // Enter key
   SetDataFolder root:AugerSpec
   SVAR Var_SavingFolder
   NewPath/O AES Var_SavingFolder
  case 3: // Live update
   Variable dval = sva.dval
   String sval = sva.sval
   break
 endswitch
 return 0
End

//////////////////////////// Sweep Function ////////////////////////////////
Function SweepNbProcAES(sva) : SetVariableControl
 STRUCT WMSetVariableAction &sva
 SetDataFolder root:AugerSpec
 NVAR VarsweepNb
 NVAR Varcurrentsweepnb
 switch( sva.eventCode )
```

```
  case 1: // mouse up
  case 2: // Enter key
  case 3: // Live update
   Variable dval = sva.dval
   String sval = sva.sval
    // Checking that you don't put a SweepNb too small !!!
    if ( Varsweepnb < Varcurrentsweepnb)
     Varsweepnb = Varcurrentsweepnb
    endif
   break
 endswitch
 return 0
End

////////////////////////////// MaxMinInc ////////////////////////////////////
// If Emin, Emax ou Inc changes, it's remembered so that the wave lenght
// will change in due time
Function MaxMinIncProcAES(sva) : SetVariableControl
 STRUCT WMSetVariableAction &sva
 SetDataFolder root:AugerSpec
 NVAR anythingChanged
 switch( sva.eventCode )
  case 1: // mouse up
  case 2: // Enter key
  case 3: // Live update
  anythingChanged =1
   break
 endswitch
 return 0
End

//////////////////////////// StopAfterSweepButton ////////////////////////////
Function StopAfterSweepButtonProcAES(ba) : ButtonControl
 STRUCT WMButtonAction &ba
 SetDataFolder  root:AugerSpec
 NVAR Varsweepnb
 NVAR Varcurrentsweepnb
 switch( ba.eventCode )
  case 2: // mouse up
   Varsweepnb = Varcurrentsweepnb
   break
 endswitch
 return 0
End

////////////////////////////// StopButton //////////////////////////////////
Function StopButtonProcAES(ba) : ButtonControl
 STRUCT WMButtonAction &ba
SetDataFolder  root:AugerSpec
 switch( ba.eventCode )
  case 2: // mouse up
   JustStopAES()
 endswitch
 return 0
End

//////////////////////////// StartButton ////////////////////////////////////
Function StartButtonProcAES(ba) : ButtonControl
 STRUCT WMButtonAction &ba
 ba.blockReentry=1 // should not allow to double click until this is finished.
 switch( ba.eventCode )
  case 2: // mouse up
   SetDataFolder root:AugerSpec
   NVAR SweepRunning
   NVAR VarMin
   NVAR VarMax
   NVAR VarIncrement
   NVAR currentwavelength
   NVAR CtrlTab
   NVAR SettingRunning
```

```
    NVAR anythingChanged
    WAVE currentwave
    WAVE SumWave
    //WAVE LastSumWave
    String/G PanelName = ba.win
    SweepRunning=1 // Running
    Button startbutton disable=1
    Button stopbutton disable=0
    Button resumebutton disable=1
    Button pausebutton disable=0
    if( CtrlTab == 0)
     SetVariable emax disable=2 // No user input
     SetVariable emin disable=2
     SetVariable increment disable=2
     SetVariable countingtime disable=2
    endif
    if( anythingChanged == 1 )
     currentwavelength = ceil(((VarMax-VarMin)/VarIncrement))//+1
     VarIncrement = ceil((VarMax-VarMin)*1000 /currentwavelength) /1000
     Make/O/N=(currentwavelength) currentwave=0
     SetScale/P x, VarMin, VarIncrement, currentwave
     anythingChanged = 0
    endif
    currentwave = 0
    Duplicate/O currentwave SumWave LastSumWave energywave // To make sure of the sizes
    Variable/G myincrement=0
// Cleaning the Sweeps Tab:
    Variable i
    String nameEE
    For( i=0; i< 10 ; i+=1)
     nameEE = "\#" + num2str(i)   //W_WaveList[i][0]
    // //RemoveFromGraph /W=$(PanelName + "\#SweepWindow")  W_WaveList[i][0] //$nameEE
     RemoveFromGraph /W=$(PanelName + "\#SweepWindow") /Z $""
    Endfor
    AppendToGraph /W=$(PanelName + "\#SweepWindow") root:AugerSpec:currentwave
    CtrlNamedBackground goCountAES, period=1, proc=TheAESCounter
    CtrlNamedBackground goCountAES, start
    break
 endswitch
 return 0
End

//////////////////////////// PauseButton ////////////////////////////////
Function PauseButtonProcAES(ba) : ButtonControl
 STRUCT WMButtonAction &ba
 SetDataFolder  root:AugerSpec
 NVAR isPaused // 0 means not paused!
 switch( ba.eventCode )
  case 2: // mouse up
   if (isPaused==0)
    CtrlNamedBackground goCountAES, stop
    SetVariable currentenergy valueColor=(65535,65535,65535), valueBackColor=(26112,26112,0)
    Button resumebutton disable=0
    Button pausebutton disable=1
    isPaused=1
   else
    DoAlert 0, "Something strange with Pause function..."
    return -1
   endif
   break
 endswitch
 return 0
End

//////////////////////////// ResumeButton ////////////////////////////
Function ResumeButtonProcAES(ba) : ButtonControl
 STRUCT WMButtonAction &ba
 SetDataFolder  root:AugerSpec
 NVAR isPaused // 0 means not paused!
 switch( ba.eventCode )
```

```
  case 2: // mouse up
   if (isPaused==1)
    CtrlNamedBackground goCountAES, start
    SetVariable currentenergy valueColor=(65280,0,0),valueBackColor=0
    Button resumebutton disable=1
    Button pausebutton disable=0
    isPaused=0
   else
    DoAlert 0, "Something strange with Resume function..."
    return -1
   endif
   break
 endswitch
 return 0
End

////////////////////////////// Graph ////////////////////////////////
Function GraphProcAES(tca): TabControl
 STRUCT WMTabControlAction &tca
 if (tca.eventCode != 2)
  return 0
 endif
 String/G panel = tca.win
 String tabControlName = tca.ctrlName
 Variable tabNb= tca.tab
 Variable isTab0= tabNb==0
 Variable isTab1= tabNb==1
 Variable isTab2= tabNb==2
 Variable isTab3= tabNb==3
 SetDataFolder root:AugerSpec
 NVAR SettingRunning
 NVAR CurrentSettingRunning    // note: disable=0 means "show", disable=1 means "hide"
 SetWindow $(panel + "\#SumWindow") hide= (!isTab0), needUpdate=1
 SetWindow $(panel + "\#SweepWindow") hide= (!isTab1), needUpdate=1
End

////////////////////////// CurrentEnergyVar ////////////////////////////////
Function CurrentEnergyVarProcAES(sva) : SetVariableControl
 STRUCT WMSetVariableAction &sva
 switch( sva.eventCode )
  case 1: // mouse up
  case 2: // Enter key
  case 3: // Live update
   Variable dval = sva.dval
   GiveAESTension(dval)
   break
 endswitch
 return 0
End

////////////////////////////// TheAESCounter ////////////////////////////////
// Runs a multiple sweeps in the background
// Gives proper tensions on Output0,1,2 and 3 ; counts on Counter0
Function TheAESCounter(BackGnd)
 STRUCT WMBackgroundStruct &BackGnd
 SetDataFolder  root:AugerSpec
 NVAR VarAverage
 NVAR VarStabTime
 NVAR VarMin
 NVAR VarMax
 NVAR VarcurrentKE
 NVAR myincrement
 SVAR Varspecname
 SVAR Var_savingFolder
 NVAR Var_FileNb
 NVAR Varcurrentsweepnb
 NVAR Varsweepnb
 WAVE currentwave
 WAVE SumWave
 NVAR Varcurrent
```

APPENDIX

```
NVAR VarIncrement
String Device = "Dev1" //GetDeviceName()
Variable InputChannel = 1
Variable type=1
Variable edgeslopewhen=0
//-------------------------------------------------//
try
 variable ener = VarMin + VarIncrement*myincrement
 GiveAESTension(ener)
//-------------------------------------------------//
 if( myincrement == 0) // sweep starting delay
  DAQmx_CTR_OutputPulse/DEV=Device /FREQ={1/VarStabTime,.999999} /NPLS=1 /DELY=10 1; AbortOnRTE
 else     // Delay used for the tensions to stabilize: /DELY=0.01 (in seconds)
  DAQmx_CTR_OutputPulse/DEV=Device /FREQ={1/VarStabTime,.999999} /NPLS=1 /DELY=0.01 1; AbortOnRTE
 endif
catch
 print "Pb with counters... " + fDAQmx_ErrorString()
 JustStopAES()
 return 2 // Error: Stop Backgroundtask
endtry
Do // Wait for the elapsed time to evaporate...
While( fDAQmx_CTR_IsFinished(Device, 1) == 0)
Variable av=0
Variable Varcu =0
for( av=0; av<VarAverage ; av+=1)
 Varcu += fDAQmx_ReadChan(Device,InputChannel, -10,10, 1)
endfor
Varcu /= VarAverage // VarAverage = 100
Varcurrent = Varcu // fDAQmx_ReadChan(Device,Channel,-2,2,0)
fDAQmx_CTR_Finished(Device, 1)
currentwave[myincrement] = Varcurrent
SumWave[myincrement] = (Varcurrent + (Varcurrentsweepnb-1)*SumWave[myincrement] ) / Varcurrentsweepnb
//-------------------------------------------------//
if( myincrement == DimSize(currentwave,0)-1) // sweep is over
 // Save current sweep data
 SetDataFolder root:AugerSpec
 SVAR PanelName
 WAVE energywave
 String FileN = Varspecname+"-"+num2str(Var_FileNb)+"_"+num2str(Varcurrentsweepnb)
 duplicate root:AugerSpec:currentwave root:AugerSpec:data:$FileN
 String FileNTXT = FileN + ".txt"
 String EnergyN = "E_"+FileN
 duplicate root:AugerSpec:energywave root:AugerSpec:data:$EnergyN
 Save/G/M="\r\n"/W/P=AES root:AugerSpec:data:$EnergyN, root:AugerSpec:data:$FileN as FileNTXT
 AppendToGraph /W=$(PanelName + "\#SweepWindow") root:AugerSpec:data:$FileN
 myincrement=0
 Varcurrentsweepnb+=1
// Last sweep or not ??? ----------------------//
 if ( Varcurrentsweepnb <= Varsweepnb )
  currentwave=0
  return 0 // Go for next sweep
 else
  String/G FileName = Varspecname+"-"+num2str(Var_FileNb)
  duplicate root:AugerSpec:SumWave root:AugerSpec:data:$FileName
  String FileNameTXT = FileName + ".ixt"
  String EnergyName = "E_"+FileName
  duplicate root:AugerSpec:energywave root:AugerSpec:data:$EnergyName
  GiveNotesAES()
  Save/T/M="\r\n"/W/P=AES root:AugerSpec:data:$EnergyName,
  root:AugerSpec:data:$FileName as FileNameTXT
  Varcurrentsweepnb = 1
  Var_FileNb += 1
  JustStopAES()
  beep; sleep/S 1;beep; sleep/S 1;beep
  return 1 // Finish the Backgroundtask
 endif
else // Sweep not over yet
 myincrement += 1
 return 0 // Continue Backgroundtask
endif
```

```
End

////////////////////////// GiveAESTension ////////////////////////
Function GiveAESTension(ener)
 Variable ener
 SetDataFolder  root:AugerSpec
 NVAR VarcurrentKE
 NVAR myincrement // Interger value: row nb of wave
 WAVE energywave
 VarcurrentKE =ener
 Variable G = VarcurrentKE*.005   // 0-10V for 0-2kV
 energywave[myincrement] = VarcurrentKE
 if( G > 10 )
  print "too much output! 10Volts is the maximum"
  //return 2 // Error: Stop Backgroundtask
 endif
 String String_T = "" + num2str(G) + ",0"
 String Device = "Dev1"
 DAQmx_AO_SetOutputs/DEV=Device String_T   // output control for AES high pass grid
 // use output "0" for AES (also for MassSpec)
 return 0
End

////////////////////////// CtrlProcAES ////////////////////////////
Function CtrlProcAES(tca): TabControl
 STRUCT WMTabControlAction &tca
//(ctrlName,tabNum) : TabControl
// String ctrlName
 String panel = tca.win
 String tabControlName = tca.ctrlName
 Variable tabNum= tca.tab
 Variable isTab0= tabNum==0
 Variable isTab1= tabNum==1
 Variable isTab2= tabNum==2
 SetDataFolder root:AugerSpec
 NVAR SweepRunning
 NVAR CtrlTab
 CtrlTab = !isTab0
 // note: disable=0 means "show", disable=1 means "hide", 2 means "no user input"
 if( tabNum!=0) // hide them
  ModifyControl increment disable= !isTab0 // hide if not Tab 0
  ModifyControl emax disable= !isTab0
  ModifyControl emin disable= !isTab0
  ModifyControl countingtime disable= !isTab0
 else // show them back
  if(SweepRunning==1)
   ModifyControl increment disable=2
   ModifyControl emax disable=2
   ModifyControl emin disable=2
   ModifyControl countingtime disable=2
  else
   ModifyControl increment disable= !isTab0 // hide if not Tab 0
   ModifyControl emax disable= !isTab0
   ModifyControl emin disable= !isTab0
   ModifyControl countingtime disable= !isTab0
  endif
 endif

 ModifyControl specname disable= !isTab0
 ModifyControl specnb disable= !isTab0
 ModifyControl sweepnb disable= !isTab0
 ModifyControl saveFolder disable= !isTab0
 ModifyControl sample  disable= !isTab1
 ModifyControl prepa  disable= !isTab1
 ModifyControl deposition  disable= !isTab1
 ModifyControl Note1  disable= !isTab1
 ModifyControl Note2  disable= !isTab1
 SetVariable Note1,pos={30,173},size={218,16},bodyWidth=170,title="Note1"
 SetVariable Note1,value=Var_Note1
 SetVariable Note2,pos={30,148},size={218,16},bodyWidth=170,title="Note2"
```

```
 SetVariable Note2,value=Var_Note2
 SetVariable deposition,pos={17,122},size={231,16},bodyWidth=138,title="Deposition species"
 SetVariable deposition,value=Var_deposition
 SetVariable prepa,pos={20,97},size={228,16},bodyWidth=170,title="Preparation"
 SetVariable prepa,value=Var_prepa
 SetVariable sample,pos={39,41},size={209,16},bodyWidth=170,title="Sample"
 SetVariable sample,value=Var_sample
end

////////////////////////////// JustStop ////////////////////////////
Function JustStopAES()
 SetDataFolder root:AugerSpec
 NVAR isPaused
 NVAR SweepRunning
 NVAR CtrlTab
 NVAR myincrement
 NVAR Varcurrentsweepnb
 myincrement=0
 CtrlNamedBackground goCountAES, stop
 SweepRunning=0 // Stopped
 Button startbutton disable=0
 Button stopbutton disable=1
 if( CtrlTab == 0)
  SetVariable emax disable=0 // No user input
  SetVariable emin disable=0
  SetVariable countingtime disable=0
  SetVariable increment disable=0
 endif
 Button pausebutton disable=2
 Button resumebutton disable=2
 isPaused=0
 SetVariable currentenergy valueColor=(65280,0,0),valueBackColor=0
 Varcurrentsweepnb = 1 // back to 1st sweep, by YP
End

////////////////////////////// GiveNotes ////////////////////////////
Function GiveNotesAES()
 SetDataFolder root:AugerSpec
 SVAR FileName
 SVAR Var_sample
 NVAR VarMin
 NVAR VarMax
 NVAR VarIncrement
 NVAR VarStabTime
 NVAR /Z Var_FileNb
 SVAR /Z Var_FileName
 SVAR Var_deposition
 SVAR Var_prepa
 SVAR/Z Note1
 SVAR/Z Note2
 Note root:AugerSpec:Data:$FileName ("Emin= "+ num2str(VarMin))
 Note root:AugerSpec:Data:$FileName ("Emax= "+ num2str(VarMax))
 Note root:AugerSpec:Data:$FileName ("Step= "+ num2str(VarIncrement))
 Note root:AugerSpec:Data:$FileName ("Counting Time per step= "+ num2str(VarStabTime))
 Note root:AugerSpec:Data:$FileName ("Sample: "+ Var_sample)
 Note root:AugerSpec:Data:$FileName ("Preparation: "+ Var_prepa)
 Note root:AugerSpec:Data:$FileName ("Deposition species: "+ Var_deposition)
 Note root:AugerSpec:Data:$FileName (Note1)
 Note root:AugerSpec:Data:$FileName (Note2)
End

//////////////////////THE//////////////////////
//////////////////////END//////////////////////
```

Electron trajectory simulation in a hemispherical analyzer

The following shows the codes of the primitive simulation of electron trajectory inside the hemispherical analyzer of UPS under a homogeneous, small magnetic field(B). The demonstrated conditions are pass energy, KE = 25 eV, mean hemisphere radius, R_C = 50 mm, residual magnetic field, Bx = 0 ; By = Bz = 50 mG. The numerical computation has been done using GNU Octave language.

```
% initial condition
KE=25;
% system condition
Rin=36;
Rext=63;
Rc=50;
q=1.6E-19;
me=9.11E-31;
Vmax=(KE*q/me).^0.5;
theta=[0,0,1];
Vxx=theta(1)*Vmax;
Vyy=theta(2)*Vmax;
Vzz=theta(3)*Vmax;

% example from web
for k=1:5

        Vmax=(KE*q/me).^0.5;
        angle=2
        ang=angle*pi/180;
        theta=[0,0,1;sin(ang),0,cos(ang);-sin(ang),0,cos(ang);
                0,sin(ang),cos(ang);0,-sin(ang),cos(ang)];

        Vxx=theta(k,1)*Vmax;
        Vyy=theta(k,2)*Vmax;
        Vzz=theta(k,3)*Vmax;

        function dr = dr_hemi(t,r)
                % initial condition
                KE=25;
                Bx=0*0.0000001;
                By=50*0.0000001;
                Bz=50*0.0000001;
                % system condition
                Rin=36;
                Rext=63;
                Rc=50;
                Vin=23.5;
                Vext=10;
                q=1.6E-19;
                me=9.11E-31;
                E=-1000*(Vin-Vext)/(Rext-Rin);
                F=q*E;
```

```
        x = r(1);
        y = r(2);
        z = r(3);
        vx = r(4);
        vy = r(5);
        vz = r(6);
        ax = (E*(x./(x.^2+y.^2+z.^2).^0.5) + By*vz + Bz*vy)*q/me;
        ay = (E*(y./(x.^2+y.^2+z.^2).^0.5) + Bx*vz + Bz*vx)*q/me;
        az = (E*(z./(x.^2+y.^2+z.^2).^0.5) + Bx*vy + By*vx)*q/me;
        dr = [vx,vy,vz,ax,ay,az];
    endfunction

    deltax=[0,0.0005,-0.0005,0,0]
    deltay=[0,0,0,0.0005,-0.0005]
    X0 = (-Rc/1000) + deltax(k);
    Y0 = deltay(k);
    Z0 = 0;
    VX0 = Vxx;
    VY0 = Vyy;
    VZ0 = Vzz;

    initialVector = [ X0, Y0, Z0, VX0, VY0, VZ0]

    StartT= 0 %s
    StopT = 0.0011*pi*Rc/Vzz %s

    options = odeset('RelTol',1E-4,
        'AbsTol',1E-4,
        'InitialStep',StopT/100,
        'MaxStep',StopT/100)
    switch (k)
        case 1
        [T,Path1] = ode45( @dr_hemi,[StartT, StopT], initialVector , options )
        figure(2)
            plot(T, Path1(:,4),'.',
            T, Path1(:,5),'x',
            T, Path1(:,6),'o');
            xlabel 'time / s'
            ylabel 'velocity / (m/s)'
            legend('vx','vy','vz')
        case 2
        [T,Path2] = ode45( @dr_hemi,[StartT, StopT], initialVector , options )
        case 3
        [T,Path3] = ode45( @dr_hemi,[StartT, StopT], initialVector , options )
        case 4
        [T,Path4] = ode45( @dr_hemi,[StartT, StopT], initialVector , options )
        case 5
        [T,Path5] = ode45( @dr_hemi,[StartT, StopT], initialVector , options )
    endswitch
end

r=-0.064:0.0001:0.064;
```

```
R1 = (-(r.^2 - (0.001*Rin)^2)).^0.5;
R2 = (-(r.^2 - (0.001*Rext)^2)).^0.5;

figure(1)
subplot (2, 2, 1)
  plot3(Path1(:,1),Path1(:,2),Path1(:,3),
                Path2(:,1),Path2(:,2),Path2(:,3),
                Path3(:,1),Path3(:,2),Path3(:,3),
                Path4(:,1),Path4(:,2),Path4(:,3),
                Path5(:,1),Path5(:,2),Path5(:,3));%, r, R1, r, R2);
  xlabel 'x position / m'
  ylabel 'y position / m'
  zlabel 'z position / m'
  daspect ([1 1 1]);
  pbaspect ([1 1 1]);
  grid("on");
subplot (2, 2, 2)
  plot(Path1(:,1),Path1(:,2),
                Path2(:,1),Path2(:,2),

        Path3(:,1),Path3(:,2),
                Path4(:,1),Path4(:,2),
                Path5(:,1),Path5(:,2));%, r, R1, r, R2);
  xlabel 'x position / m'
  ylabel 'y position / m'
  axis ([1,2],"equal","square");
  grid("on");
  rectangle("position",[0.0495,-0.0005,0.001,0.001],"curvature",1);
subplot (2, 2, 3)
  plot( Path1(:,1),Path1(:,3),
                Path2(:,1),Path2(:,3),
                Path3(:,1),Path3(:,3),
                Path4(:,1),Path4(:,3),
                Path5(:,1),Path5(:,3), r, R1, r, R2);
  xlabel 'x position / m'
  ylabel 'z position / m'
  axis ([1,2],"square","equal");
  grid("on");
  rectangle("position",[0.0495,-0.0002,0.001,0.0002]);
subplot (2, 2, 4)
  plot( Path1(:,2),Path1(:,3),
                Path2(:,2),Path2(:,3),
                Path3(:,2),Path3(:,3),
                Path4(:,2),Path4(:,3),
                Path5(:,2),Path5(:,3));%, r, R1, r, R2);
  xlabel 'y position / m'
  ylabel 'z position / m'
  axis ([1,2],"square","equal");
  grid("on");
  rectangle("position",[-0.0005,-0.0002,0.001,0.0002]);
```

Glossary

List of frequently employed abbreviation:

PG	pristine graphene
NG	nitrogen-doped graphene
MLG	monolayer graphene
BLG	buffer layer graphene
QFSG	quasi-free standing graphene
H-BLG	hydrogenated buffer layer graphene
UHV	ultra-high vacuum
ARIPES	angle-resolved inverse photoemission spectroscopy
TCS	target current spectroscopy
LEED	low energy electron diffraction
AES	Auger electron spectroscopy
XPS	X-ray photoemission spectroscopy
STM	scanning tunneling microscopy
STS	scanning tunneling spectroscopy
DOS	density of states
BZ	Brillouin zone

References

[1] K. S. Novoselov, A. K. Geim, S. V. Morozov, D. Jiang, Y. Zhang, S. V. Dubonos, I. V. Grigorieva, and A. A. Firsov. **Electric field effect in atomically thin carbon films**. *Science*, **306**(5696):666–669, 2004. 4, 8, 13

[2] M. Scarselli, P. Castrucci, and M. D. Crescenzi. **Electronic and optoelectronic nano-devices based on carbon nanotubes**. *J. Phys.: Condens. Matter*, **24**(31):313202, 2012. 4

[3] M. D. Stoller, S. Park, Y. Zhu, J. An, and R. S. Ruoff. **Graphene-based ultracapacitors**. *Nano Lett.*, **8**(10):3498–3502, 2008. 4, 70

[4] C. Lee, X. Wei, J. W. Kysar, and J. Hone. **Measurement of the elastic properties and intrinsic strength of monolayer graphene**. *Science*, **321**(5887):385–388, 2008.

[5] A. A. Balandin, S. Ghosh, W. Bao, I. Calizo, D. Teweldebrhan, F. Miao, and C. N. Lau. **Superior thermal conductivity of single-layer graphene**. *Nano Lett.*, **8**(3):902–907, 2008. 4

[6] P. R. Wallace. **The band theory of graphite**. *Phys. Rev.*, **71**:622–634, 1947. 4, 5, 6

[7] P. C. Hohenberg. **Existence of long-range order in one and two dimensions**. *Phys. Rev.*, **158**:383–386, 1967. 4

[8] A. K. Geim and K. S. Novoselov. **The rise of graphene**. *Nat. Mater.*, **6**(3):183–191, 2007. 4, 5

[9] K. S. Novoselov, A. K. Geim, S. V. Morozov, D. Jiang, M. I. Katsnelson, I. V. Grigorieva, S. V. Dubonos, and A. A. Firsov. **Two-dimensional gas of massless dirac fermions in graphene**. *Nature*, **438**(7065):197–200, 2005. 5

[10] C. Riedl, C. Coletti, and U. Starke. **Structural and electronic properties of epitaxial graphene on SiC(0001): a review of growth, characterization, transfer doping and hydrogen intercalation**. *J. Phys. D: Appl. Phys.*, **43**(37):374009, 2010. 6, 7, 12, 13, 35, 56, 59, 135

[11] M. Y. Han, B. Özyilmaz, Y. Zhang, and P. Kim. **Energy band-gap engineering of graphene nanoribbons**. *Phys. Rev. Lett.*, **98**:206805, 2007. 5

[12] Z. H. Ni, T. Yu, Y. H. Lu, Y. Y. Wang, Y. P. Feng, and Z. X. Shen. **Uniaxial strain on graphene: Raman spectroscopy study and band-gap opening**. *ACS Nano*, **2**(11):2301–2305, 2008.

[13] S. Y. Zhou, G.-H. Gweon, A. V. Fedorov, P. N. First, W. A. de Heer, D.-H. Lee, F. Guinea, A. H. Castro Neto, and A. Lanzara. **Substrate-induced bandgap opening in epitaxial graphene**. *Nat. Mater.*, **6**(10):770–775, 2007. 5, 12

[14] I. Forbeaux, J.-M. Themlin, and J.-M. Debever. **Heteroepitaxial graphite on 6H-SiC(0001): interface formation through conduction-band electronic structure**. *Phys. Rev. B*, **58**(24):16396–16406, 1998. 7, 54, 56, 125, 127, 131

[15] C. Riedl, U. Starke, J. Bernhardt, M. Franke, and K. Heinz. **Structural properties of the graphene-SiC(0001) interface as a key for the preparation of homogeneous large-terrace graphene surfaces**. *Phys. Rev. B*, **76**:245406, 2007. 7

[16] C. Riedl, A. A. Zakharov, and U. Starke. **Precise in situ thickness analysis of epitaxial graphene layers on SiC(0001) using low-energy electron diffraction and angle resolved ultraviolet photoelectron spectroscopy**. *Appl. Phys. Lett.*, **93**(3):033106, 2008. 7, 12, 49, 50, 54

[17] J. Hass, R. Feng, T. Li, X. Li, Z. Zong, W. A. de Heer, P. N. First, E. H. Conrad, C. A. Jeffrey, and C. Berger. **Highly ordered graphene for two dimensional electronics**. *Appl. Phys. Lett.*, **89**(14):143106, 2006. 7

[18] W. Norimatsu, J. Takada, and M. Kusunoki. **Formation mechanism of graphene layers on SiC(000$\bar{1}$) in a high-pressure argon atmosphere**. *Phys. Rev. B*, **84**(3):035424, 2011. 8, 60

[19] P. Blake, P. D. Brimicombe, R. R. Nair, T. J. Booth, D. Jiang, F. Schedin, L. A. Ponomarenko, S. V. Morozov, H. F. Gleeson, E. W. Hill, A. K. Geim, and K. S. Novoselov. **Graphene-based liquid crystal device**. *Nano Lett.*, **8**(6):1704–1708, 2008. 8

[20] M. Lotya, Y. Hernandez, P. J. King, R. J. Smith, V. Nicolosi, L. S. Karlsson, F. M. Blighe, S. De, Z. Wang, I. T. McGovern, G. S. Duesberg, and J. N. Coleman. **Liquid phase production of graphene by exfoliation of graphite in Surfactant/Water solutions**. *J. Am. Chem. Soc.*, **131**(10):3611–3620, 2009. 8

[21] A. A. Green and M. C. Hersam. **Solution phase production of graphene with controlled thickness via density differentiation**. *Nano Lett.*, **9**(12):4031–4036, 2009. 8

[22] P. R. Somani, S. P. Somani, and M. Umeno. **Planer nano-graphenes from camphor by CVD**. *Chem. Phys. Lett.*, **430**(13):56–59, 2006. 9

[23] K. S. Kim, Y. Zhao, H. Jang, S. Y. Lee, J. M. Kim, K. S. Kim, J.-H. Ahn, P. Kim, J.-Y. Choi, and B. H. Hong. **Large-scale pattern growth of graphene films for stretchable transparent electrodes**. *Nature*, **457**(7230):706–710, 2009. 9

REFERENCES

[24] S. Bhaviripudi, X. Jia, M. S. Dresselhaus, and J. Kong. **Role of kinetic factors in chemical vapor deposition synthesis of uniform large area graphene using copper catalyst**. *Nano Lett.*, **10**(10):4128–4133, 2010. 9

[25] X. Li, W. Cai, L. Colombo, and R. S. Ruoff. **Evolution of graphene growth on Ni and Cu by carbon isotope labeling**. *Nano Lett.*, **9**(12):4268–4272, 2009. 9

[26] A. Malesevic, R. Vitchev, K. Schouteden, A. Volodin, L. Zhang, G. V. Tendeloo, A. Vanhulsel, and C. V. Haesendonck. **Synthesis of few-layer graphene via microwave plasma-enhanced chemical vapour deposition**. *Nanotech.*, **19**(30):305604, 2008. 9

[27] S. Stankovich, D. A. Dikin, G. H. B. Dommett, K. M. Kohlhaas, E. J. Zimney, E. A. Stach, R. D. Piner, S. T. Nguyen, and R. S. Ruoff. **Graphene-based composite materials**. *Nature*, **442**(7100):282–286, 2006. 9

[28] V. Singh, D. Joung, L. Zhai, S. Das, S. I. Khondaker, and S. Seal. **Graphene based materials: Past, present and future**. *Progress in Materials Science*, **56**(8):1178–1271, 2011. 9

[29] F. Banhart, J. Kotakoski, and A. V. Krasheninnikov. **Structural defects in graphene**. *ACS Nano*, **5**(1):26–41, 2010. 10, 11, 73

[30] L. Li, S. Reich, and J. Robertson. **Defect energies of graphite: Density-functional calculations**. *Phys. Rev. B*, **72**:184109, 2005. 10

[31] X. Peng and R. Ahuja. **Symmetry breaking induced bandgap in epitaxial graphene layers on SiC**. *Nano Lett.*, **8**(12):4464–4468, 2008. 10

[32] A. A. El-Barbary, R. H. Telling, C. P. Ewels, M. I. Heggie, and P. R. Briddon. **Structure and energetics of the vacancy in graphite**. *Phys. Rev. B*, **68**(14):144107, 2003. 11, 15

[33] J. Wu, H. A. Becerril, Z. Bao, Z. Liu, Y. Chen, and P. Peumans. **Organic solar cells with solution-processed graphene transparent electrodes**. *Appl. Phys. Lett.*, **92**(26):263302–263302–3, 2008. 11

[34] S. Yang, X. Feng, X. Wang, and K. Müllen. **Graphene-Based carbon nitride nanosheets as efficient Metal-Free electrocatalysts for oxygen reduction reactions**. *Angew. Chem. Inter. Ed.*, **50**(23):5339–5343, 2011. 70

[35] F. Schedin, A. K. Geim, S. V. Morozov, E. W. Hill, P. Blake, M. I. Katsnelson, and K. S. Novoselov. **Detection of individual gas molecules adsorbed on graphene**. *Nat. Mater.*, **6**(9):652–655, 2007. 13

[36] F. Darkrim Lamari and D. Levesque. **Hydrogen adsorption on functionalized graphene**. *Carbon*, **49**(15):5196–5200, 2011. 11

[37] A. H. Castro Neto, F. Guinea, N. M. R. Peres, K. S. Novoselov, and A. K. Geim. **The electronic properties of graphene**. *Rev. Mod. Phys.*, **81**:109–162, 2009. 12

[38] A. Das, S. Pisana, B. Chakraborty, S. Piscanec, S. K. Saha, U. V. Waghmare, K. S. Novoselov, H. R. Krishnamurthy, A. K. Geim, A. C. Ferrari, and A. K. Sood. **Monitoring dopants by raman scattering in an electrochemically top-gated graphene transistor**. *Nat. Nanotechn.*, **3**(4):210–215, 2008. 12

[39] W. Chen, S. Chen, D. C. Qi, X. Y. Gao, and A. T. S. Wee. **Surface transfer p-type doping of epitaxial graphene**. *J. Am. Chem. Soc.*, **129**(34):10418–10422, 2007. 12

[40] T. Ohta, A. Bostwick, T. Seyller, K. Horn, and E. Rotenberg. **Controlling the electronic structure of bilayer graphene**. *Science*, **313**(5789):951–954, 2006. 12

[41] L. Zhao, R. He, K. T. Rim, T. Schiros, K. S. Kim, H. Zhou, C. Gutiérrez, S. P. Chockalingam, C. J. Arguello, L. Pálová, D. Nordlund, M. S. Hybertsen, D. R. Reichman, T. F. Heinz, P. Kim, A. Pinczuk, G. W. Flynn, and A. N. Pasupathy. **Visualizing individual nitrogen dopants in monolayer graphene**. *Science*, **333**(6045):999–1003, 2011. 12, 15, 95

[42] C. Coletti, C. Riedl, D. S. Lee, B. Krauss, L. Patthey, K. von Klitzing, J. H. Smet, and U. Starke. **Charge neutrality and band-gap tuning of epitaxial graphene on SiC by molecular doping**. *Phys. Rev. B*, **81**(23):235401, 2010. 12

[43] C. Riedl, C. Coletti, T. Iwasaki, A. A. Zakharov, and U. Starke. **Quasi-free-standing epitaxial graphene on SiC obtained by hydrogen intercalation**. *Phys. Rev. Lett.*, **103**(24):246804, 2009. 12, 13, 54, 58, 122, 129, 130

[44] T. O. Wehling, K. S. Novoselov, S. V. Morozov, E. E. Vdovin, M. I. Katsnelson, A. K. Geim, and A. I. Lichtenstein. **Molecular doping of graphene**. *Nano Lett.*, **8**(1):173–177, 2008. 13

[45] J. S. Burgess, B. R. Matis, J. T. Robinson, F. A. Bulat, F. Keith Perkins, B. H. Houston, and J. W. Baldwin. **Tuning the electronic properties of graphene by hydrogenation in a plasma enhanced chemical vapor deposition reactor**. *Carbon*, **49**(13):4420–4426, 2011. 14

[46] M. H. F. Sluiter and Y. Kawazoe. **Cluster expansion method for adsorption: Application to hydrogen chemisorption on graphene**. *Phys. Rev. B*, **68**:085410, 2003. 14

[47] D. C. Elias, R. R. Nair, T. M. G. Mohiuddin, S. V. Morozov, P. Blake, M. P. Halsall, A. C. Ferrari, D. W. Boukhvalov, M. I. Katsnelson, A. K. Geim, and K. S. Novoselov. **Control of graphene's properties by reversible hydrogenation: Evidence for graphane**. *Science*, **323**(5914):610–613, 2009. 14, 119

[48] S. Lebègue, M. Klintenberg, O. Eriksson, and M. I. Katsnelson. **Accurate electronic band gap of pure and functionalized graphane from GW calculations**. *Phys. Rev. B*, **79**(24):245117, 2009. 14, 119

[49] D. Wei, Y. Liu, Y. Wang, H. Zhang, L. Huang, and G. Yu. **Synthesis of N-doped graphene by chemical vapor deposition and its electrical properties**. *Nano Lett.*, **9**(5):1752–1758, 2009. 14, 15, 16, 70

[50] H. Wang, T. Maiyalagan, and X. Wang. **Review on recent progress in nitrogen-doped graphene: Synthesis, characterization, and its potential applications**. *ACS Catalysis*, **2**(5):781–794, 2012. 15, 16, 87

[51] R. Lv, Q. Li, A. R. Botello-Mendez, T. Hayashi, B. Wang, A. Berkdemir, Q. Hao, A. L. Elias, R. Cruz-Silva, H. R. Gutierrez, Y. A. Kim, H. Muramatsu, J. Zhu, M. Endo, H. Terrones, J.-C. Charlier, M. Pan, and M. Terrones. **Nitrogen-doped graphene: beyond single substitution and enhanced molecular sensing**. *Scientific Reports*, **2**, 2012. 15, 153

[52] F. Joucken, Y. Tison, J. Lagoute, J. Dumont, D. Cabosart, B. Zheng, V. Repain, C. Chacon, Y. Girard, A. R. Botello-Méndez, S. Rousset, R. Sporken, J.-C. Charlier, and L. Henrard. **Localized state and charge transfer in nitrogen-doped graphene**. *Phys. Rev. B*, **85**(16):161408, 2012. 15, 70, 96

[53] Z. Hou, X. Wang, T. Ikeda, K. Terakura, M. Oshima, and M.-a. Kakimoto. **Electronic structure of n-doped graphene with native point defects**. *Phys. Rev. B*, **87**(16):165401, 2013. 15, 16, 69, 78, 87, 89, 95

[54] B. Guo, Q. Liu, E. Chen, H. Zhu, L. Fang, and J. R. Gong. **Controllable n-doping of graphene**. *Nano Lett.*, **10**(12):4975–4980, 2010. 15, 70, 75

[55] Y.-C. Lin, C.-Y. Lin, and P.-W. Chiu. **Controllable graphene n-doping with ammonia plasma**. *Appl. Phys. Lett.*, **96**(13):133110–133110–3, 2010. 15

[56] J. Röhrl, M. Hundhausen, K. V. Emtsev, T. Seyller, R. Graupner, and L. Ley. **Raman spectra of epitaxial graphene on SiC(0001)**. *Appl. Phys. Lett.*, **92**(20):201918, 2008. 16, 51, 87

[57] L. Qu, Y. Liu, J.-B. Baek, and L. Dai. **Nitrogen-doped graphene as efficient metal-free electrocatalyst for oxygen reduction in fuel cells**. *ACS Nano*, **4**(3):1321–1326, 2010. 16

[58] A. Lherbier, X. Blase, Y.-M. Niquet, F. Triozon, and S. Roche. **Charge transport in chemically doped 2D graphene**. *Phys. Rev. Lett.*, **101**(3):036808, 2008. 16, 96

[59] Y. Shao, S. Zhang, M. H. Engelhard, G. Li, G. Shao, Y. Wang, J. Liu, I. A. Aksay, and Y. Lin. **Nitrogen-doped graphene and its electrochemical applications**. *J. Mater. Chem.*, **20**(35):7491–7496, 2010. 16

[60] D. Pan, S. Wang, B. Zhao, M. Wu, H. Zhang, Y. Wang, and Z. Jiao. **Li storage properties of disordered graphene nanosheets**. *Chem. Mater.*, **21**(14):3136–3142, 2009. 16, 70

[61] R. Podila, J. Chacón-Torres, J. T. Spear, T. Pichler, P. Ayala, and A. M. Rao. **Spectroscopic investigation of nitrogen doped graphene**. *Appl. Phys. Lett.*, **101**(12):123108, 2012. 17

[62] R. Anton, T. Wiegner, W. Naumann, M. Liebmann, C. Klein, and C. Bradley. **Design and performance of a versatile, cost-effective microwave electron cyclotron resonance plasma source for surface and thin film processing**. *Rev. Sci. Instrum.*, **71**(2):1177–1180, 2000. 23, 71

[63] J. B. Pendry. **Theory of inverse photoemission**. *Journal of Physics C: Solid State Physics*, **14**(9):1381, 1981. 25

[64] V. Dose. **Momentum-resolved inverse photoemission**. *Surf. Sci. Rep.*, **5**(8):337–378, 1985. 26

[65] F. J. Himpsel. **Inverse photoemission from semiconductors**. *Surf. Sci. Rep.*, **12**(1):3–48, 1990. 26

[66] I. Schäfer, M. Schlüter, and M. Skibowski. **Conduction-band structure of graphite studied by combined angle-resolved inverse photoemission and target current spectroscopy**. *Phys. Rev. B*, **35**:7663–7670, 1987. 27

[67] F. C. BOCQUET. **Du fullerène au graphène : Etudes spectroscopiques de l'interaction de systémes π-conjugués avec des surfaces solides**. *Thesis, Aix-Marseille Université*, 2012. 27, 30, 40

[68] N. V. Smith. **Inverse photoemission**. *Rep. Prog. Phys.*, **51**(9):1227, 1988. 28, 29

[69] P. W. Erdman and E. C. Zipf. **Low-voltage, high-current electron gun**. *Rev. Sci. Instrum.*, **53**(2):225, 1982. 29

[70] S. Komolov and L. Chadderton. **Total current spectroscopy**. *Surf. Sci.*, **90**(2):359–380, 1979. 31

[71] D. Dai, X. Wang, J. Hu, and Y. Ge. **Total-current-spectroscopy studies of the electron states of the clean si(100)2×1 and hydrogen-chemisorbed si(100)1×1 surfaces**. *Phys. Rev. B*, **46**(16):10284–10288, 1992. 31

[72] S. C. Jain and K. S. Krishnan. **The thermionic constants of metals and semi-conductors. i. graphite**. *Proc. R. Soc. Lond. A*, **213**(1113):143–157, 1952. 32

[73] N. Barrett, E. E. Krasovskii, J.-M. Themlin, and V. N. Strocov. **Elastic scattering effects in the electron mean free path in a graphite overlayer studied by photoelectron spectroscopy and LEED**. *Physical Review B*, **71**(3):035427, 2005. 34

[74] A. C. Ferrari, J. C. Meyer, V. Scardaci, C. Casiraghi, M. Lazzeri, F. Mauri, S. Piscanec, D. Jiang, K. S. Novoselov, S. Roth, and A. K. Geim. **Raman spectrum of graphene and graphene layers**. *Phys. Rev. Lett.*, **97**(18):187401, 2006. 43

[75] L. Malard, M. Pimenta, G. Dresselhaus, and M. Dresselhaus. **Raman spectroscopy in graphene**. *Phys. Reports*, **473**(56):51–87, 2009. 43, 44

[76] R. Saito, M. Hofmann, G. Dresselhaus, A. Jorio, and M. S. Dresselhaus. **Raman spectroscopy of graphene and carbon nanotubes**. *Adv. in Phys.*, **60**(3):413–550, 2011. 43

[77] T. Junno, K. Deppert, L. Montelius, and L. Samuelson. **Controlled manipulation of nanoparticles with an atomic force microscope**. *Appl. Phys. Lett.*, **66**(26):3627–3629, 1995. 45

REFERENCES

[78] D. S. Lee, C. Riedl, B. Krauss, K. von Klitzing, U. Starke, and J. H. Smet. **Raman spectra of epitaxial graphene on SiC and of epitaxial graphene transferred to SiO_2**. *Nano Lett.*, **8**(12):4320–4325, 2008. 51, 52

[79] T. Ohta, A. Bostwick, J. L. McChesney, T. Seyller, K. Horn, and E. Rotenberg. **Interlayer interaction and electronic screening in multilayer graphene investigated with angle-resolved photoemission spectroscopy**. *Phys. Rev. Lett.*, **98**(20):206802, 2007. 54

[80] P. E. Trevisanutto, C. Giorgetti, L. Reining, M. Ladisa, and V. Olevano. **Ab initio *GW* many-body effects in graphene**. *Phys. Rev. Lett.*, **101**:226405, 2008. 55, 56, 57

[81] K. V. Emtsev, F. Speck, T. Seyller, L. Ley, and J. D. Riley. **Interaction, growth, and ordering of epitaxial graphene on SiC(0001) surfaces: A comparative photoelectron spectroscopy study**. *Phys. Rev. B*, **77**(15):155303, 2008. 56, 125, 126, 128, 129, 131

[82] P. Plochocka, C. Faugeras, M. Orlita, M. L. Sadowski, G. Martinez, M. Potemski, M. O. Goerbig, J.-N. Fuchs, C. Berger, and W. A. de Heer. **High-energy limit of massless dirac fermions in multilayer graphene using magneto-optical transmission spectroscopy**. *Phys. Rev. Lett.*, **100**:087401, 2008. 57

[83] D. A. Siegel, C.-H. Park, C. Hwang, J. Deslippe, A. V. Fedorov, S. G. Louie, and A. Lanzara. **Many-body interactions in quasi-freestanding graphene**. *Proceedings of the National Academy of Sciences*, **108**(28):11365–11369, 2011. 57, 93

[84] B. Shan and K. Cho. **First principles study of work functions of single wall carbon nanotubes**. *Phys. Rev. Lett.*, **94**(23):236602, 2005. 57

[85] D. Ferrah, J. Penuelas, C. Bottela, G. Grenet, and A. Ouerghi. **X-ray photoelectron spectroscopy (XPS) and diffraction (XPD) study of a few layers of graphene on 6H-SiC(0001)**. *Surf. Sci.*, **615**:47–56, 2013. 59

[86] M. Sprinkle, D. Siegel, Y. Hu, J. Hicks, A. Tejeda, A. Taleb-Ibrahimi, P. Le Févre, F. Bertran, S. Vizzini, H. Enriquez, S. Chiang, P. Soukiassian, C. Berger, W. A. de Heer, A. Lanzara, and E. H. Conrad. **First direct observation of a nearly ideal graphene band structure**. *Phys. Rev. Lett.*, **103**(22):226803, 2009. 62, 63

[87] M. Orlita, C. Faugeras, P. Plochocka, P. Neugebauer, G. Martinez, D. K. Maude, A.-L. Barra, M. Sprinkle, C. Berger, W. A. de Heer, and M. Potemski. **Approaching the dirac point in high-mobility multilayer epitaxial graphene**. *Phys. Rev. Lett.*, **101**(26):267601, 2008. 62

[88] J. Hass, F. Varchon, J. E. Millán-Otoya, M. Sprinkle, N. Sharma, W. A. de Heer, C. Berger, P. N. First, L. Magaud, and E. H. Conrad. **Why multilayer graphene on 4H-SiC(000$\bar{1}$) behaves like a single sheet of graphene**. *Phys. Rev. Lett.*, **100**(12):125504, 2008. 62, 63

[89] L. I. Johansson, S. Watcharinyanon, A. A. Zakharov, T. Iakimov, R. Yakimova, and C. Virojanadara. **Stacking of adjacent graphene layers grown on C-face SiC**. *Phys. Rev. B*, **84**(12):125405, 2011. 62

[90] Luxmi, N. Srivastava, G. He, R. M. Feenstra, and P. J. Fisher. **Comparison of graphene formation on C-face and Si-face SiC(0001) surfaces**. *Phys. Rev. B*, **82**(23):235406, 2010. 63

[91] U. Starke and C. Riedl. **Epitaxial graphene on SiC(0001) and SiC(000$\bar{1}$) : from surface reconstructions to carbon electronics**. *J. Phys.: Condens. Matter*, **21**(13):134016, 2009. 65

[92] H. M. Jeong, J. W. Lee, W. H. Shin, Y. J. Choi, H. J. Shin, J. K. Kang, and J. W. Choi. **Nitrogen-doped graphene for high-performance ultracapacitors and the importance of nitrogen-doped sites at basal planes**. *Nano Lett.*, **11**(6):2472–2477, 2011. 70

[93] Y. Wang, Y. Shao, D. W. Matson, J. Li, and Y. Lin. **Nitrogen-doped graphene and its application in electrochemical biosensing**. *ACS Nano*, **4**(4):1790–1798, 2010. 70

[94] K.-J. Kim, H. Lee, J. Choi, H. Lee, M. C. Jung, H. J. Shin, T.-H. Kang, B. Kim, and S. Kim. **Surface property change of graphene using nitrogen ion**. *J. Phys.: Condens. Matter*, **22**(4):045005, 2010. 70

[95] A. Kumar, A. Ganguly, and P. Papakonstantinou. **Thermal stability study of nitrogen functionalities in a graphene network**. *J. Phys.: Condens. Matter*, **24**(23):235503, 2012. 70, 79

[96] O. Lehtinen, J. Kotakoski, A. V. Krasheninnikov, A. Tolvanen, K. Nordlund, and J. Keinonen. **Effects of ion bombardment on a two-dimensional target: Atomistic simulations of graphene irradiation**. *Phys. Rev. B*, **81**(15):153401, 2010. 70, 95, 116

[97] E. H. Ahlgren, J. Kotakoski, and A. V. Krasheninnikov. **Atomistic simulations of the implantation of low-energy boron and nitrogen ions into graphene**. *Phys. Rev. B*, **83**(11):115424, 2011. 70, 116

[98] K.-j. Kim, S. Yang, Y. Park, M. Lee, B. Kim, and H. Lee. **Annealing effects after nitrogen ion casting on monolayer and multilayer graphene**. *The Journal of Physical Chemistry C*, **117**(5):2129–2134, 2013. 73, 79, 98, 114

[99] X. Wang, X. Li, L. Zhang, Y. Yoon, P. K. Weber, H. Wang, J. Guo, and H. Dai. **N-doping of graphene through electrothermal reactions with ammonia**. *Science*, **324**(5928):768–771, 2009. 75

[100] X. Li, H. Wang, J. T. Robinson, H. Sanchez, G. Diankov, and H. Dai. **Simultaneous nitrogen doping and reduction of graphene oxide**. *J. Am. Chem. Soc.*, **131**(43):15939–15944, 2009. 75

[101] P. Rani and V. K. Jindal. **Designing band gap of graphene by b and n dopant atoms**. *RSC Advances*, **3**(3):802–812, 2012. 76, 87, 89, 96

[102] A. M. Black-Schaffer and K. Cho. **First-principles study of the work function of nitrogen doped molybdenum (110) surface**. *J. Appl. Phys.*, **100**(12):124902, 2006. 79

[103] A. Soon, L. Wong, M. Lee, M. Todorova, B. Delley, and C. Stampfl. **Nitrogen adsorption and thin surface nitrides on Cu(111) from first-principles**. *Surf. Sci.*, **601**(21):4775–4785, 2007. 79

[104] Z.-j. Wang, M. Wei, L. Jin, Y. Ning, L. Yu, Q. Fu, and X. Bao. **Simultaneous n-intercalation and n-doping of epitaxial graphene on 6H-SiC(0001) through thermal reactions with ammonia**. *Nano Research*, **6**(6):399–408, 2013. 86

[105] K. R. Knox, S. Wang, A. Morgante, D. Cvetko, A. Locatelli, T. O. Mentes, M. A. Nio, P. Kim, and R. M. Osgood. **Spectromicroscopy of single and multilayer graphene supported by a weakly interacting substrate**. *Phys. Rev. B*, **78**(20):201408, 2008. 93

[106] A. Bostwick, T. Ohta, J. L. McChesney, T. Seyller, K. Horn, and E. Rotenberg. **Renormalization of graphene bands by many-body interactions**. *Solid State Commun.*, **143**(12):63–71, 2007. 93

[107] X. Du, I. Skachko, A. Barker, and E. Y. Andrei. **Approaching ballistic transport in suspended graphene**. *Nat. Nanotech.*, **3**(8):491–495, 2008. 93

[108] C.-H. Park, L. Yang, Y.-W. Son, M. L. Cohen, and S. G. Louie. **Anisotropic behaviours of massless dirac fermions in graphene under periodic potentials**. *Nat. Phys.*, **4**(3):213–217, 2008. 93

[109] C. Hwang, D. A. Siegel, S.-K. Mo, W. Regan, A. Ismach, Y. Zhang, A. Zettl, and A. Lanzara. **Fermi velocity engineering in graphene by substrate modification**. *Scientific Reports*, **2**, 2012. 93

[110] N. Al-Aqtash, K. M. Al-Tarawneh, T. Tawalbeh, and I. Vasiliev. **Ab initio study of the interactions between boron and nitrogen dopants in graphene**. *J. Appl. Phys.*, **112**(3):034304–034304–7, 2012. 95

[111] G. Diankov, M. Neumann, and D. Goldhaber-Gordon. **Extreme monolayer-selectivity of hydrogen-plasma reactions with graphene**. *ACS Nano*, **7**(2):1324–1332, 2013. 98

[112] D. Haberer, D. V. Vyalikh, S. Taioli, B. Dora, M. Farjam, J. Fink, D. Marchenko, T. Pichler, K. Ziegler, S. Simonucci, M. S. Dresselhaus, M. Knupfer, B. Büchner, and A. Grüneis. **Tunable band gap in hydrogenated quasi-free-standing graphene**. *Nano Lett.*, **10**(9):3360–3366, 2010. 119

[113] F. C. Bocquet, R. Bisson, J.-M. Themlin, J.-M. Layet, and T. Angot. **Reversible hydrogenation of deuterium-intercalated quasi-free-standing graphene on SiC(0001)**. *Phys. Rev. B*, **85**:201401, 2012.

[114] F. C. Bocquet, R. Bisson, J.-M. Themlin, J.-M. Layet, and T. Angot. **Deuterium adsorption on (and desorption from) SiC(0001)-(3×3), $(\sqrt{3}\times\sqrt{3})r30^\circ$, $(6\sqrt{3}\times 6\sqrt{3})R30^\circ$ and quasi-free-standing graphene obtained by hydrogen intercalation**. *J. Phys. D: Appl. Phys.*, **47**(9):094014, 2014. 119, 128, 131

[115] Z. M. Ao, A. D. Hernández-Nieves, F. M. Peeters, and S. Li. **Enhanced stability of hydrogen atoms at the graphene/graphane interface of nanoribbons**. *Appl. Phys. Lett.*, **97**(23):233109, 2010. 119

[116] J. O. Sofo, A. S. Chaudhari, and G. D. Barber. **Graphane: A two-dimensional hydrocarbon**. *Phys. Rev. B*, **75**(15):153401, 2007. 119

[117] G. Savini, A. C. Ferrari, and F. Giustino. **First-principles prediction of doped graphane as a high-temperature electron-phonon superconductor**. *Phys. Rev. Lett.*, **105**(3):037002, 2010. 119

[118] N. P. Guisinger, G. M. Rutter, J. N. Crain, P. N. First, and J. A. Stroscio. **Exposure of epitaxial graphene on SiC(0001) to atomic hydrogen**. *Nano Lett.*, **9**(4):1462–1466, 2009. 120, 131

[119] B. Lee, S. Han, and Y.-S. Kim. **First-principles study of preferential sites of hydrogen incorporated in epitaxial graphene on 6H-SiC(0001)**. *Phys. Rev. B*, **81**(7):075432, 2010.

[120] G. Sclauzero and A. Pasquarello. **First-principles study of H adsorption on graphene/SiC(0001)**. *Physica status solidi (b)*, page 123123123, 2013. 120, 125

[121] A. Van Bommel, J. Crombeen, and A. Van Tooren. **LEED and auger electron observations of the SiC(0001) surface**. *Surf. Sci.*, **48**(2):463–472, 1975. 122

[122] A. Mattausch and O. Pankratov. **Abinitio study of graphene on SiC**. *Phys. Rev. Lett.*, **99**(7):076802, 2007. 125, 128

[123] F. Varchon, R. Feng, J. Hass, X. Li, B. N. Nguyen, C. Naud, P. Mallet, J.-Y. Veuillen, C. Berger, E. H. Conrad, and L. Magaud. **Electronic structure of epitaxial graphene layers on SiC: effect of the substrate**. *Phys. Rev. Lett.*, **99**(12), 2007. 125, 126

[124] Y.-P. Lin, Y. Ksari, J. Prakash, L. Giovanelli, J.-C. Valmalette, and J.-M. Themlin. **Nitrogen-doping processes of graphene by a versatile plasma-based method**. *Carbon*, **73**:216–224, 2014. 125

[125] S. Kim, J. Ihm, H. J. Choi, and Y.-W. Son. **Origin of anomalous electronic structures of epitaxial graphene on silicon carbide**. *Phys. Rev. Lett.*, **100**(17):176802, 2008. 126

[126] P. Lauffer, K. V. Emtsev, R. Graupner, T. Seyller, L. Ley, S. A. Reshanov, and H. B. Weber. **Atomic and electronic structure of few-layer graphene on SiC(0001) studied with scanning tunneling microscopy and spectroscopy**. *Phys. Rev. B*, **77**(15):155426, 2008.

[127] J. Hass, J. E. Millán-Otoya, P. N. First, and E. H. Conrad. **Interface structure of epitaxial graphene grown on 4H-SiC(0001)**. *Phys. Rev. B*, **78**(20):205424, 2008.

[128] J.-Y. Veuillen, F. Hiebel, L. Magaud, P. Mallet, and F. Varchon. **Interface structure of graphene on SiC: an ab initio and STM approach**. *J. Phys. D: Appl. Phys.*, **43**(37):374008, 2010.

[129] G. Sclauzero and A. Pasquarello. **Stability and charge transfer at the interface between SiC(0001) and epitaxial graphene**. *Microelectron. Eng.*, **88**(7):1478–1481, 2011. 130

REFERENCES

[130] L. H. de Lima, A. de Siervo, R. Landers, G. A. Viana, A. M. B. Goncalves, R. G. Lacerda, and P. Häberle. **Atomic surface structure of graphene and its buffer layer on SiC(0001): a chemical-specific photoelectron diffraction approach**. *Phys. Rev. B*, **87**(8):081403, 2013. 126, 128

[131] J. D. Emery, B. Detlefs, H. J. Karmel, L. O. Nyakiti, D. K. Gaskill, M. C. Hersam, J. Zegenhagen, and M. J. Bedzyk. **Chemically resolved interface structure of epitaxial graphene on SiC(0001)**. *Phys. Rev. Lett.*, **111**(21):215501, 2013. 126, 127

[132] W. Norimatsu and M. Kusunoki. **Transitional structures of the interface between graphene and 6H-SiC(0001)**. *Chem. Phys. Lett.*, **468**(13):52–56, 2009. 127

[133] G. Sclauzero and A. Pasquarello. **Carbon rehybridization at the graphene/SiC(0001) interface: Effect on stability and atomic-scale corrugation**. *Phys. Rev. B*, **85**(16):161405, 2012. 127

[134] J.-M. Themlin, I. Forbeaux, V. Langlais, H. Belkhir, and J.-M. Debever. **Unoccupied surface state on the $(\sqrt{3} \times \sqrt{3})R30^\circ$ of 6H-SiC(0001)**. *Europhys. Lett.*, **39**(1):61, 1997. 127, 128, 131

[135] L. S. O. Johansson, L. Duda, M. Laurenzis, M. Krieftewirth, and B. Reihl. **Electronic structure of the 6H-SiC(0001)-3×3 surface studied with angle-resolved inverse and direct photoemission**. *Surf. Sci.*, **445**(1):109–114, 2000.

[136] R. Ostendorf, K. Wulff, C. Benesch, H. Merz, and H. Zacharias. **Unoccupied mott-hubbard state on the $(\sqrt{3}\times\sqrt{3})r30^\circ$ reconstructed 4h-sic(0001) surface**. *Phys. Rev. B*, **70**(4):205325, 2004. 127, 131

[137] C. Benesch, M. Fartmann, and H. Merz. **k-resolved inverse photoemission of four different 6H-SiC(0001) surfaces**. *Phys. Rev. B*, **64**:205314, 2001. 127, 128, 131

[138] A. Charrier, R. Pérez, F. Thibaudau, J.-M. Debever, J. Ortega, F. Flores, and J.-M. Themlin. **Contrasted electronic properties of Sn-adatom-based (3×3)R30° reconstructions on Si(111)**. *Phys. Rev. B*, **64**(11):115407, 2001. 128

[139] J. Furthmüller, F. Bechstedt, H. Hüsken, B. Schröter, and W. Richter. **Si-rich SiC(111)/(0001)3×3 and 3×3 surfaces: A Mott-Hubbard picture**. *Phys. Rev. B*, **58**(20):13712–13716, 1998. 128

[140] I. Deretzis and A. La Magna. **Interaction between hydrogen flux and carbon monolayer on SiC(0001): graphene formation kinetics**. *Nanoscale*, **5**(2):671, 2013. 128

[141] M. Yang, A. Nurbawono, C. Zhang, R. Wu, Y. Feng, and Ariando. **Manipulating absorption and diffusion of h atom on graphene by mechanical strain**. *AIP Advances*, **1**(3):032109, 2011. 128

[142] J. Ristein, S. Mammadov, and T. Seyller. **Origin of doping in quasi-free-standing graphene on silicon carbide**. *Phys. Rev. Lett.*, **108**(24):246104, 2012. 129

[143] P. Sessi, J. R. Guest, M. Bode, and N. P. Guisinger. **Patterning graphene at the nanometer scale via hydrogen desorption**. *Nano Lett.*, **9**(12):4343–4347, 2009. 131

[144] F. C. Bocquet, Y. Ksari, Y. P. Lin, L. Porte, and J.-M. Themlin. **Interaction of C_{60} with clean and hydrogenated SiC-(3×3) probed through the unoccupied electronic states**. *Phys. Rev. B*, **88**:125421, 2013. 131, 140

[145] J. Cho, J. Smerdon, L. Gao, O. Süzer, J. R. Guest, and N. P. Guisinger. **Structural and electronic decoupling of C_{60} from epitaxial graphene on sic**. *Nano Lett.*, **12**(6):3018–3024, 2012. 135, 137

[146] Q. H. Wang and M. C. Hersam. **Room-temperature molecular-resolution characterization of self-assembled organic monolayers on epitaxial graphene**. *Nature Chemistry*, **1**(3):206–211, 2009. 135, 137, 140

[147] A. J. Pollard, E. W. Perkins, N. A. Smith, A. Saywell, G. Goretzki, A. G. Phillips, S. P. Argent, H. Sachdev, F. Müller, S. Hüfner, S. Gsell, M. Fischer, M. Schreck, J. Osterwalder, T. Greber, S. Berner, N. R. Champness, and P. H. Beton. **Supramolecular assemblies formed on an epitaxial graphene superstructure**. *Angew. Chem. Inter. Ed.*, **49**(10):17941799, 2010. 135, 137

[148] H. T. Zhou, J. H. Mao, G. Li, Y. L. Wang, X. L. Feng, S. X. Du, K. Müllen, and H.-J. Gao. **Direct imaging of intrinsic molecular orbitals using two-dimensional, epitaxially-grown, nanostructured graphene for study of single molecule and interactions**. *Appl. Phys. Lett.*, **99**(15):153101, 2011. 137

[149] R. Wang, S. Wang, X. Wang, J. A. S. Meyer, P. Hedegrd, B. W. Laursen, Z. Cheng, and X. Qiu. **Charge transfer and current fluctuations in single layer graphene transistors modified by self-assembled C_{60} adlayers**. *Small*, **9**(14):2420–2426, 2013. 137

[150] H. Huang, S. Chen, X. Gao, W. Chen, and A. T. S. Wee. **Structural and electronic properties of PTCDA thin films on epitaxial graphene**. *ACS Nano*, **3**(11):3431–3436, 2009. 137

[151] P. Lauffer, K. V. Emtsev, R. Graupner, T. Seyller, and L. Ley. **Molecular and electronic structure of PTCDA on bilayer graphene on SiC(0001) studied with scanning tunneling microscopy**. *Physica status solidi (b)*, **245**(10):2064–2067, 2008. 137

[152] H. Yang, A. J. Mayne, G. Comtet, G. Dujardin, Y. Kuk, P. Sonnet, L. Stauffer, S. Nagarajan, and A. Gourdon. **STM imaging, spectroscopy and manipulation of a self-assembled PTCDI monolayer on epitaxial graphene**. *Phys. Chem. Chem. Phys.*, **15**(14):4939–4946, 2013. 137

[153] F. Flores and J. Ortega. *The Molecule-Metal Interface*, chapter Basic Theory of the Molecule-Metal, pages 15–49. Wiley-VCH Verlag GmbH & Co. KGaA, 2013. 140, 143

[154] M. Meissner, M. Gruenewald, F. Sojka, C. Udhardt, R. Forker, and T. Fritz. **Highly ordered growth of PTCDA on epitaxial bilayer graphene**. *Surf. Sci.*, **606**(2122):1709–1715, 2012. 144

Publications and Communications List

The publications and the communications related to this thesis are listed below.

Publications:

1. Y. P. Lin, Y. Ksari, and J. M. Themlin, Hydrogenation of buffer-layer graphene on SiC: A route for the engineering of graphene-based device (submitting for publication) **2014**.
2. Y. P. Lin, Y. Ksari, J. Prakash, L. Giovanelli, J.-C. Valmalette and J. M. Themlin, Nitrogen-doping processes of graphene by a versatile plasma-based method *Carbon*, 73, 216, **2014**.
3. Y. P. Lin, O. Ourdjini, L. Giovanelli, S. Clair, T. Faury, Y. Ksari, J. M. Themlin, L. Porte, and M. Abel, Self-Assembled Melamine Monolayer on Cu(111) *J. Phys. Chem. C*, 117 (19), 9895-9902, **2013**.
4. F. C. Bocquet, Y. Ksari, Y. P. Lin, L. Porte, and J.-M. Themlin, Interaction of C60 with clean and hydrogenated SiC-(3x3) probed through the unoccupied electronic states *Phys. Rev. B*, 88, 125421, **2013**.

Conferences:

1. Y. P. Lin, Y. Ksari, J. Prakash, L. Giovanelli, J.-M. Themlin, Controllable nitrogen doping of graphene via a versatile plasma-based technique European Workshop on Epitaxial Graphene and 2D Materials, **2014**.
2. Y. P. Lin, Y. Ksari, J. Prakash, L. Giovanelli, J.-M. Themlin, Nitrogen-doping processes of graphene by a versatile plasma-based method E-MRS, **2014** spring (oral presentation).
3. Y. P. Lin, Y. Ksari, J. Prakash, L. Giovanelli, J.-M. Themlin, A versatile plasma-based method for the nitrogen doping of graphene 4th Graphene conference, **2014**.
4. Y. P. Lin, T. Faury, O. Ourdjini, M. Abel, L. Giovanelli, Y. Ksari, L. Porte, and J. M. Themlin, Ordered Structure of Melamine Species adsorbed on Cu(111) JMC13 Montpelier, **2012** (oral presentation).

Abstract

In order to promote 2D materials like graphene to their numerous applications, new methods altering their electronic and chemical properties have to be mastered. In this thesis, the processes of chemical doping and hydrogenation of monolayer graphene grown on SiC are investigated. Nitrogen atoms are successfully substituted in the graphene lattice using plasma-based methods. The bonding configurations of the incorporated N can be controlled via the nature and energy of exposing species and the thickness of the pristine graphene. An *n*-type doping, revealed by angle-resolved inverse photoemission spectroscopy (ARIPES), is found in most N-doped graphene and is assigned to the presence of graphitic-N. Hydrogenations of the buffer layer of graphene (BLG) on SiC at ambient or high temperatures saturate the remaining Si dangling bonds at BLG/SiC interface in two different ways, either by inducing additional C-Si bonds or by H intercalation. This results in 2D materials with distinct characters, an insulating, graphane-like H-BLG or a quasi-free-standing graphene, which may be used as a new concept for the engineering of graphene-based devices. The interactions between π-conjugated molecules and the functionalized graphene are also investigated. The unoccupied states of molecules are altered by the presence of incorporated N, but the degradation of molecules due to low-energy electron exposure seems not enhanced by the doping nitrogen under the studied conditions. Nevertheless, the functionalization of graphene is demonstrated and its electronic and chemical properties are carefully studied, which should facilitate further applications employing functionalized graphene.

Keywords: graphene, SiC, epitaxy, chemical doping, plasma, hydrogenation, spectroscopy

---

Résumé

Cette étude de la fonctionnalisation du graphène se base principalement sur la monocouche de graphène épitaxiée sur SiC, dont nous avons notamment modifié les propriétés électroniques via le dopage par exposition à un plasma d'azote et par l'hydrogénation. Les propriétés électroniques, structurales et la composition chimique du graphène fonctionnalisé sont étudiées *in situ* et *ex situ* par des techniques de spectroscopies électroniques, principalement la photoémission inverse résolue angulairement (ARIPES). L'incorporation d'azote dans le graphène réalisée par l'exposition à un plasma d'azote entraîne un décalage des niveaux inoccupés du graphène vers le niveau de fermi. Ce dopage-n est attribué à la présence d'atomes d'azote substitutionnels entourés de trois voisins carbone (N-graphitique). D'autres centres azotés, associés à des lacunes, sont présents dans le graphène, sous forme d'azotes pyrroliques et pyridinique, mais la configuration majoritaire peut tre contrlée efficacement par l'énergie du plasma, les espèces d'azote incidentes (atomes ou/et ions), et l'épaisseur de la couche de graphène de départ. Nous étudions ensuite l'hydrogénation de la couche tampon de graphène (BLG) sur SiC en fonction de la température. A l'ambiante, l'hydrogène adsorbé sur le graphène sature les liaisons pendantes de Si de l'interface par un processus indirect impliquant la formation de nouvelles liaisons C-Si. Le BLG ainsi hydrogéné est un isolant dont la bande interdite (E_{GAP} 5 eV) est proche de celle du graphane, alors que le BLG est un isolant de Mott-Hubbard (E_{GAP} 1.6 eV). A haute température, l'hydrogène s'intercale sous le BLG, exposant ainsi une monocouche de graphène quasi-flottante (QFSG) non-dopée, les liaisons pendantes du substrat étant complètement saturées par l'hydrogène intercalé. Sur la base de ces propriétés, nous proposons un nouveau concept de fabrication de dispositifs à base de graphène sur SiC. Enfin, nous avons également étudié la réaction entre des molécules pi-conjuguées et les graphène vierge ou dopé à l'azote. Les états inoccupés des molécules dérivées du pérylène (PTCDA, PTCDI) sont légèrement modifiés sur le graphène dopé N à cause d'un renforcement du transfert électronique vers la molécule. Des réactions chimiques entre ces molécules et le graphène sont observées après exposition aux électrons de basse énergie. En résumé, cette étude permettra une meilleure maîtrise des propriétés électroniques des matériaux 2D comme le graphène, et facilitera le développement de nouvelles applications à base de graphène, notamment en nano-électronique.

Mots-clés: graphène, 6H-SiC, dopage chimique, plasma, hydrogénation, IPES, XPS